Imperial College London
Department of Physics
EPSRC Center of Doctoral Training in Theory and Simulation of Materials

Theory and simulation of electronic and optical properties of thin film barium strontium titanate

Jawad Mohamed Taher Qasim Mohamed Alsaei

June 2015

A thesis submitted for the degree of
Doctor of Philosophy
and the
Diploma of Imperial College

ما الفضلُ إلا لأهل العلم إنهمُ *** على الهدى لمن استهدى أدلّاءُ
وقيمة المرء ما قد كان يحسنه *** والجاهلون لأهل العلم أعداء
فقم بعلمٍ ولا تطلب به بدلاً *** فالناس موتى وأهل العلم أحياء

من الديوان المنسوب لأمير المؤمنين علي بن أبي طالب (عليه السلام)

To my family

Preface

The work presented in this dissertation contains the research carried out between November 2011 and February 2015 at Imperial College London. I certify that this thesis is the result of my own work, and that all else is appropriately acknowledged.

Jawad Alsaei
June 2015

Abstract

In this thesis, we investigate, from first-principles, various means by which the energy gaps and the refractive index of $BaTiO_3$, $SrTiO_3$ and $Ba_xSr_{1-x}TiO_3$ may be tuned, including epitaxial strain, alloying, and anionic doping.

We start by discussing some limitations in the experimental spectroscopic ellipsometry technique that could affect the reliability of the measured optical spectra.

Then, we investigate the effects of strain and alloying on the energy gaps of these materials. Interesting features in the gaps are observed as a function of strain, where it decreases and increases for small and high strains, respectively. These features are correlated with the spontaneous polarization of the system, whose behaviour is sensitive to the value of strain. The polarization also affects the behaviour of the bandgap of $Ba_xSr_{1-x}TiO_3$ as a function of Sr content, which shows a non-monotonic trend.

On the other hand, the refractive index of $Ba_xSr_{1-x}TiO_3$ shows similar features with strain and alloying to those of the bandgaps. Strain is found to induce a decrease of up to $\sim 8\%$ in the refractive index and a birefringence of up to ~ 0.14, whereas alloying has a smaller effect. Ferroelectric distortions are found to have a major role in decreasing the index, where much less effect is observed when they are inhibited. However, we show that the refractive index is insensitive to the ordering of Sr atoms in $Ba_xSr_{1-x}TiO_3$.

Finally, we investigate the effect of F and N codoping in $BaTiO_3$. The refractive index is sensitive to the atomic ordering of the dopant atoms, which prefer to be aligned in linear chains of F$-$Ti$-$N. The component of the index along the chain shows a dramatic increase with respect to pure $BaTiO_3$, while the other components are almost unaffected. Also, we show that the index can be further tuned by strain and doping concentration.

Acknowledgement

First of all, I would like to express my deep thanks to my principle supervisor Arash Mostofi, who was a great source of knowledge and support. I am also deeply grateful to my second supervisor Paul Tangney, whose ideas and criticism were invaluable.

Special thanks go also to Dangyuan Lei, for a lot of useful discussion about spectroscopic ellipsometry. Useful discussion with Peter Petrov, David Tompsett and Nick Bristowe is also much appreciated.

I would like also to thank my sponsor, the University of Bahrain, for a full financial support.

I do not forget to thank all my family, with a special mention to my parents, for their unceasing encouragement and support.

Finally, I want to express a great gratitude and appreciation to my wife for her invaluable support during my entire course of study.

Copyright Declaration

The copyright of this thesis rests with the author and is made available under a Creative Commons Attribution Non-Commercial No Derivatives licence. Researchers are free to copy, distribute or transmit the thesis on the condition that they attribute it, that they do not use it for commercial purposes and that they do not alter, transform or build upon it. For any reuse or redistribution, researchers must make clear to others the licence terms of this work.

Contents

Abstract **7**

1 Introduction **31**
1.1 Ferroelectric materials and perovskites 33
1.2 $BaTiO_3$ and $SrTiO_3$ 34
1.2.1 BTO 35
1.2.2 STO 36
1.3 Origin of ferroelectricity in perovskite oxides 36
1.3.1 Goldschmidt tolerance factor 36
1.3.2 The nature of the ferroelectric transition 38
1.3.3 The origin of ferroelectricity 40
1.4 Reduced sizes and thin films 41
1.4.1 Ferroelectric Thin Films 42
1.5 Tuning the optical properties of BST thin films 44
1.6 Outline of thesis 46

2 Spectroscopic ellipsometry **49**
2.1 Overview 49
2.2 Introduction to spectroscopic ellipsometry 50
2.3 Theory of light polarization upon reflection 51
2.4 What is measured in SE? 56
2.5 SE data analysis 57
2.6 Models for the refractive index 60
2.6.1 Lorentz model 61
2.6.2 Sellmeier model 62
2.6.3 Cauchy model 63
2.6.4 Drude Model 63

2.7 Models for the film structure 63
2.8 Depolarizing films 67
2.9 Criticism 68
2.10 Motivations 72

3 Density functional theory **75**
3.1 Overview 75
3.2 The many-body Schrödinger equation 76
3.2.1 Born-Oppenheimer approximation 77
3.3 The formulation of density functional theory 78
3.3.1 Hohenberg-Kohn theorems 78
3.3.2 The Kohn-Sham framework 80
3.3.3 The exchange-correlation functional 83
3.3.4 Bloch's theorem 86
3.4 Technical details 91
3.4.1 Choosing a basis set 91
3.4.2 K-point sampling 94
3.4.3 Pseudopotentials 97
3.5 The virtual crystal approximation 101
3.6 Geometry optimization 104

4 Strain-induced changes in BST bandgaps **109**
4.1 Overview 109
4.2 The band gap problem in DFT 110
4.3 The simulation of epitaxial strain 113
4.4 Computational details 115
4.5 Structure and electronic structure 116
4.6 Effect of strain on BTO bandgaps 117
4.7 Effect of strain on STO bandgaps 123
4.7.1 Comparison with the work in the literature 132
4.8 Effect of alloying on E_g of BST solid solutions 138
4.8.1 Structural properties of BST 138
4.8.2 Strain induced changes in E_g of BST 139
4.8.3 Effect of Sr content of the gaps of BST 142
4.9 Summary 144

5 Optical properties of BST **149**
5.1 Overview . . . 149
5.2 Theoretical framework . . . 150
5.3 Optical spectra of bulk BTO and STO . . . 153
5.4 Effect of strain on the refractive index of BTO . . . 154
5.4.1 Quantifying the results . . . 158
5.5 Effect of strain on the refractive index of STO . . . 159
5.6 The refractive index of bulk BST . . . 161
5.7 Summary . . . 167

6 Effect of doping BTO with F and N **169**
6.1 Overview . . . 169
6.2 Computational details . . . 170
6.3 Properties of bulk $BaTiO_{2.8}F_{0.1}N_{0.1}$ . . . 171
6.3.1 Structural properties . . . 171
6.3.2 Electronic and optical properties . . . 175
6.4 Properties of thin film $BaTiO_{2.8}F_{0.1}N_{0.1}$ . . . 179
6.4.1 Structural properties . . . 180
6.4.2 Electronic and optical properties . . . 182
6.5 Most stable configuration . . . 189
6.5.1 Electronic and optical properties . . . 195
6.5.2 Refractive index averaging . . . 197
6.6 Properties of bulk $BaTiO_{2.92}F_{0.04}N_{0.04}$ . . . 200
6.7 Summary . . . 202

7 Conclusions **205**
7.1 Future work . . . 208

Bibliography **226**

Appendices **227**

A Experimental methods **229**
A.1 Abelés method . . . 229
A.2 Prism coupling technique . . . 230

B Permissions **233**

List of Figures

1.1 The hysteresis loop of bulk $BaTiO_3$, a typical ferroelectric material. This figure is reproduced, with permission, from Ref. [1], see App. B. 32

1.2 **(a):** The crystal structure of a typical perovskite in the cubic paraelectric phase. The 'A' cation (green) is at the origin, the 'B' cation (blue) is at the body centre, and the oxygen atoms (red) are at the face centres. The oxygen octahedron is represented by the blue transparent faces. **(b):** The corresponding atomic displacements (exaggerated) that break the inversion symmetry when the material is polarized along the [001] direction. With respect to the 'A' cation, the 'B' cation moves in an opposite direction to the oxygen anions. Atomic displacements are along the polarization direction. 34

1.3 A view along the [001] direction of the high temperature (a) and the low temperature (b) phases of STO. Panel (b) illustrates the rotations of the oxygen octahedra about the [001] direction. Orange atoms represent the Sr species. 37

1.4 HRTEM images of BTO/STO/SiO_2/Si stacks (left) and BTO film grown on $LaAlO_3$ substrate (right). One can notice the edge dislocations at the BTO/STO interface in the left image and the 90° domain boundaries of the BTO film in the right image. Left and right images are reproduced, with permission, from Refs [2] and [3], respectively. See App. B. 44

2.1 Schematic diagram for a linearly polarized electromagnetic wave incident on a planar interface from medium 0 to medium 1. The components of the electric field parallel and perpendicular to the plane of incidence are denoted p and s, respectively. ϕ_0 is the angle of incidence and ϕ_1 is the angle of refraction. 52

2.2 Schematic diagram showing the interaction of the incident light with a thin film of thickness d deposited on an infinitely thick substrate. Media (0,1,2) represent the ambient environment (air), the film, and the substrate, respectively, with corresponding refractive indices N_0, N_1 and N_2. 58

2.3 Schematic diagram showing some of the possible structural models of different complexity that are adopted for the film in order to extract its optical spectra from the raw SE data. 64

2.4 A schematic diagram illustrating the idea of the effective medium approach. In this example, the surface roughness layer is modelled by assuming that it is consisting of the film material embedded with spherically-shaped voids of the ambient environment. 66

2.5 The fitted curves of ψ and Δ as compared to the measured values. A 4-phase and a 5-phase models are adopted in (a) and (b), respectively. The corresponding MSE value for the two cases is given in the main text. 70

2.6 The extracted refractive indices of the constituent layers of the 4-phase and the 5-phase models. 71

2.7 The fitted and measured values of ψ and Δ **(a)**, and the corresponding refractive indices **(b)** of a 5-phase model. In this figure, the fitting parameters reached alternative local minimum of the MSE, slightly higher than that of the earlier fit shown in Fig. 2.5, but lower than the 4-phase model fit. In spite of the excellent fit, the refractive indices are non-physical and significantly different than those obtained from the earlier fit. 73

3.1 Schematic diagram of a periodic simulation cell (bounded by the dashed line) that includes **(a)** a defect, and **(b)** a surface. The use of periodic boundary conditions imposes fictitious interactions between the defect or the surface with its periodic images. The characteristic length (L) should be large enough to reduce the interactions and to converge the correct physical quantity that one is interested in. 94

3.2 Illustration to the all-electron method versus the PP approximation method. In the core region ($r < r_c$), the strong ionic potential Z_{eff}/r is replaced by a weaker pseudopotential V_{PP}, and the multi-node oscillatory wavefunction ψ^{ae} is replaced by a smooth nodeless pseudo wavefunction ψ^{pp}. Beyond the designated cutoff radius r_c, ψ^{pp} and ψ^{ae} must agree. The wavefunction shown in this figure corresponds to the Ba 5s orbital. The pseudopotential is generated via the OPIUM code [4]. 98

3.3 **(Top):** The simulation cell that corresponds to pure single crystal bulk cubic BTO. **(Bottom):** A supercell formed by a 2×2×2 cubic extension of the BTO primitive cell. In this supercell, one of the Ba atoms is replaced by a Sr atom, forming the solid solution of $Ba_{0.875}Sr_{0.125}TiO_3$. Larger supercells are needed for more dilute concentrations of Sr. Green, orange, blue and red atoms correspond to Ba, Sr, Ti and O species, respectively. . . . 102

4.1 Illustration of the application of biaxial strain on a cubic perovskite unit cell. **(Middle):** Strain-free system. **(Left):** System under compressive strain. **(Right):** System under tensile strain. The amount of strain is exaggerated for illustration purposes. 114

4.2 The calculated electronic band structure of BTO (a) and STO (b) along high symmetry directions in the Brillouin zone. The highest valence and the lowest conduction states are only shown. The valence band maximum is set at zero energy. 117

4.3 Effect of epitaxial strain on the direct ($\Gamma - \Gamma$) and the indirect ($R-\Gamma$) bandgaps of pure BTO, represented by the blue and the red curves, respectively. The region surrounded by the rectangle is enlarged in the inset. The unshaded region highlights the range of strain where the gap is decreased by increasing strain. The opposite trend is highlighted by the shaded region. . 118

4.4 Strain-induced changes in the band edges of BTO at Γ and R. The v and c subscripts refer to the valence and the conduction bands, respectively. 119

4.5 The magnitude (a) and the direction (b) of $\mathbf{Q}$, defined in Eq. 4.10, for pure BTO. The angle θ_Q is measured from the c axis. Panel (c) illustrates the rotation of the polarization vector for the values of strains represented by the unshaded region, where the magnitude is exaggerated for clarity. The relative dimensions of the (110) plane correspond to the strain-free structure. The corresponding vector of the strain-free system is extrapolated by the dashed line. Panel (d) shows the c/a ratio of the system as a function of strain. 120

4.6 Effect of epitaxial strain on the direct ($\Gamma - \Gamma$) and the indirect ($R-\Gamma$) bandgaps of pure STO, represented by the blue and the red curves, respectively. Region surrounded by the rectangle is enlarged in the inset. The unshaded and shaded regions highlight the strain ranges within which the gap decreases and increases, respectively. k_1 and k_2 indicate observed kinks in the gaps within the tensile and compressive strains range, respectively. 124

4.7 The magnitude (a) and direction (b) of $\mathbf{Q}$, defined in Eq. 4.10, for pure STO. 124

4.8 Effect of epitaxial strain on the tetragonality ratio (a) and the volume per unit cell (b) of pure STO. 126

4.9 The data sets and the corresponding fits that are used to evaluate $\partial E_g/\partial\eta$ (a) and $\partial E_g/\partial\widetilde{V}$ (b) that appear in Eq. 4.11. The data points are obtained from DFT calculations. $\widetilde{V}$ and η are held fixed in (a) and (b), respectively. The slopes of the best fit lines are tabulated in Table 4.3. All data correspond to pure STO system. 127

4.10 A comparison of the strain-induced changes in E_g^i (a) and E_g^d (b) between direct DFT calculations (red) and Eq. 4.11 (green). The individual effects of the volume and the tetragonality are also illustrated by the blue and purple curves, respectively. Energies are given in units of eV. All data correspond to pure STO system. 129

4.11 The lowest three Ti $3d$ conduction states at selected values of tensile strains. The curve of E_g^i versus strain is shown in the inset, where we have circled the corresponding point for which the states are shown. The minima of the states at Γ are all set to the same reference for convenience. An extremely high resolution of k-points along the X−Γ−R path is used to allow a straightforward disentangling of the bands. 131

4.12 Strain-induced changes in the bandgaps of STO at the experimental lattice parameters. 136

4.13 A supercell of $1\times1\times2$ unit cells corresponding to $Ba_{0.5}Sr_{0.5}TiO_3$ at -3% strain, used as a reference to check the validity of the VCA approach. 139

4.14 Strain-induced changes in the direct and the indirect energy gaps of BST at different Sr content. Sr concentration is printed on each panel. 141

4.15 Effect of strain on the magnitude of the atomic displacements of BST that are represented by the quantity $\mathbf{Q}$, defined in Eq. 4.10. Each panel corresponds to a different Sr concentration in BST. . 142

4.16 Effect of Sr concentration on the direct and the indirect gaps of free-standing BST thin films. The shaded region highlights the range of concentrations for which the gaps are decreased. 144

5.1 The calculated real (a) and imaginary (b) parts of the frequency dependent dielectric function of the high temperature phase of BTO (red) and STO (blue). 153

5.2 The calculated refractive index dispersion of bulk BTO (red) and STO (blue) at their high temperature phases. 154

5.3 Strain-induced changes in the xx and zz components of the refractive index of ferroelectric and paraelectric BTO (represented by the solid and the dashed lines, respectively). The green line corresponds to paraelectric BTO under isotropic strain. The unshaded and shaded regions cover the same range of strains as in Fig. 4.5. 155
5.4 Strain-induced changes in the xx and zz components of the refractive index of STO thin films. The shaded region covers the same range of strains as in Fig. 4.6. 160
5.5 The corresponding configurations of Sr atom in BST at 50% concentration of Sr for which the refractive indices in Fig. 5.6 are calculated. Supercells of sizes $1 \times 1 \times 1$, $2 \times 2 \times 1$ and $2 \times 2 \times 2$ are used for the configurations $C^{(1)}$, $C^{(2)}$ and $C^{(3)}$, respectively. Ba and Sr species are represented by the green and orange atoms, respectively. Ti and O species are not shown for clarity. 162
5.6 The refractive index of bulk $Ba_{0.5}Sr_{0.5}TiO_3$ for different atomic configurations of Sr atoms that are shown in Fig. 5.5. $C^{(3)}$ is isotropic, so only the xx component is shown. 163
5.7 A comparison between the supercell (SC) approach and the virtual crystal approximation (VCA) approach in calculating the refractive index of bulk BST solid solutions in their cubic paraelectric phase. The supercells used in these calculations are shown in Fig. 5.8. The indicated percentage refers to the Sr content in BST. The refractive indices of pure BTO and STO are also shown for reference. 164
5.8 The supercells that are used for the calculations of the refractive indices of BST solid solutions at 12.5% (a) and 50% (b) Sr concentration. See Fig. 5.7. Ti and O species are not shown for clarity. 165
5.9 Effect of Sr content on the refractive index of free standing BST thin films. 166
5.10 A comparison between the effects of volume and Sr content on the refractive index of BST. Bulk cubic paraelectric phase is adopted for all systems. 167

6.1 An illustration of the $2 \times 2 \times 2$ supercell used for the calculation of $BaTiO_{2.8}F_{0.1}N_{0.1}$. The positions of the seven nitrogen atoms (blue) with respect to the fluorine atom (yellow) indicate the seven symmetry inequivalent sites described in the main text. The corresponding labels are printed on each N atom. 172

6.2 The three components of the refractive index that correspond to the seven symmetry-inequivalent atomic configurations of the F and N dopant atoms in $BaTiO_{2.8}F_{0.1}N_{0.1}$. Panels **(a)**-**(g)** correspond to configurations of $C^{(1-7)}$ shown in Fig. 6.1, respectively. The refractive index of pure rhombohedral BTO (green line) is shown on each panel for comparison. 176

6.3 The calculated electronic band structures of **(a)** $C^{(1)}$ and **(b)** $C^{(6)}$ of $BaTiO_{2.8}F_{0.1}N_{0.1}$ as depicted in Fig. 6.1. Only the top valence and the bottom conduction states are shown. The corresponding band structure of pure rhombohedral BTO is also shown in panel **(c)** for comparison. The N and F states are coloured blue and green, respectively, in panel **(b).** 178

6.4 Total **(a)** and partial **(b)**−**(d)** electronic density of states of $BaTiO_{2.8}F_{0.1}N_{0.1}$ ($C^{(1)}$). Panels **(b)**, **(c)**, and **(d)** show the partial density of states of the O $2p$, N $2p$, and F $2p$ electrons, respectively. Energies are given with respect to the valence band maximum, which is set to zero. 179

6.5 $BaTiO_{2.8}F_{0.1}N_{0.1}$ under compressive strain. Two symmetry-inequivalent alignments of the linear F−Ti−N motif are shown, one perpendicular $C^{(\perp)}$ and one parallel $C^{(\parallel)}$ to the strained (001) plane. 181

6.6 The total energy of the perpendicular (red) and the parallel (blue) configurations, depicted in Fig. 6.5, of strained $BaTiO_{2.8}F_{0.1}N_{0.1}$. The tetragonality ratio of $C^{(\perp)}$ ($c^{\perp}/a$) is also shown by the black curve. The energies are given with respect to the minimum point in the curves, which corresponds to $C^{(\perp)}$ at -1% strain. The shaded area corresponds to the range of strains where ($c^{\perp}/a$) is less than 1. 182

6.7 Effect of biaxial strain on the xx component of the refractive index of $BaTiO_{2.8}F_{0.1}N_{0.1}$ thin films. The refractive indices of $C^{(\perp)}$ and $C^{(\parallel)}$ (shown in Fig. 6.5) are illustrated by the red and blue curves, respectively. For comparison, the refractive index of pristine BTO is shown by the green curve. The value of strain is printed on each panel. 183

6.8 Effect of biaxial strain on the yy component of the refractive index of $BaTiO_{2.8}F_{0.1}N_{0.1}$ thin films. The refractive indices of the $C^{(\perp)}$ and $C^{(\parallel)}$ configurations (shown in Fig. 6.5) are illustrated by the red and blue curves, respectively. For comparison, the refractive index of pristine BTO is shown by the green curve. The value of strain is printed on each panel. 184

6.9 Effect of biaxial strain on the zz component of the refractive index of $BaTiO_{2.8}F_{0.1}N_{0.1}$ thin films. The refractive indices of $C^{(\perp)}$ and $C^{(\parallel)}$ configurations (shown in Fig. 6.5) are illustrated by the red and blue curves, respectively. For comparison, the refractive index of pristine BTO is shown by the green curve. The value of strain is printed on each panel. The black arrows indicate a characteristic peak in the refractive index of $C^{(\perp)}$. . . 185

6.10 The zz component of the imaginary part of the dielectric constant $\varepsilon^{(2)}$ at a strain of -4% for $C^{(\perp)}$ (red curve) and $C^{(\parallel)}$ (blue curve). The corresponding curve of BTO is also shown by the green curve. $(\varepsilon^2_{zz})^{\perp}$ has an extra characteristic peak at ~ 400 nm, denoted by P_0. 187

6.11 The refractive index (at 1000 nm) of $C^{(\perp)}$ **(a)** and $C^{(\parallel)}$ **(b)** (represented by solid circles) as affected by epitaxial strain. Panel **(c)** shows the refractive index of the lowest energy configuration at each value of strain, as given by Fig. 6.6. The xx, yy and zz components of the refractive index are represented by the red, green and blue curves, respectively. The refractive index of pristine BTO is also shown for comparison (represented by the open squares). 188

6.12 Seven symmetry-inequivalent atomic configurations of $BaTiO_{2.8}F_{0.1}N_{0.1}$ that are achieved by considering a $2 \times 4 \times 2$ supercell. 191

6.13 Five symmetry-inequivalent atomic configurations of $BaTiO_{2.8}F_{0.1}N_{0.1}$ constructed by considering a $2 \times 2 \times 4$ supercell. The Ba and the O atoms are not shown for clarity. 194
6.14 The zz component of the refractive indices of configurations a – e **(a)** and configurations α – ξ **(b)** referred to in the main text. $C^{(\perp)}$ of the $2 \times 2 \times 2$ supercell is represented by the dashed black line in the two panels for reference. 196
6.15 An illustrative figure addressing the possibility of reproducing the refractive index of the system on the left by averaging the refractive indices of the "sub-systems" on the right. 198
6.16 The three components of the refractive indices of the systems shown in Fig. 6.15. The averaged refractive index of $C^{(dc)}$ and pristine BTO, which we denote as $\bar{n}$, is represented by the dashed line. 199
6.17 Effect of the concentration of F and N on the xx **(a)** and zz **(b)** components of the refractive index. $C^{(l)}$ refers to the system of low dopant concentrations of $BaTiO_{2.92}F_{0.04}N_{0.04}$. The weighted average of refractive index of $C^{(1)}$ and BTO is represented by the dashed line. 202

List of Tables

2.1 The fitted thicknesses (in nm) of the constituent layers of the 4-phase and the 5-phase models. ℓ_1 and ℓ_2 stand for layer 1 and layer 2 of the film, respectively, as depicted in Fig. 2.3. The sum of the thicknesses of the constituent layers is given in the last row. The second and the third columns correspond to the fits shown in Fig. 2.5, while the last column correspond to the fit shown in Fig. 2.7. 72

4.1 The lattice constants a (in Å), the bulk moduli B (in GPa), and the direct $E_{\rm g}^{\rm d}$ and indirect $E_{\rm g}^{\rm i}$ gaps (in eV) of BTO and STO, as compared between the present work and literature results. . . 116

4.2 The changes (in eV) in the direct and the indirect gaps of BTO as affected by epitaxial strain. The differences are calculated with respect to the gaps of BTO as 0% strain. All strains considered in this table belong to the shaded region depicted in Fig. 4.3. 122

4.3 The numerical values of the Taylor expansion coefficients appearing in Eq. 4.11, calculated from the best-fit lines shown in Fig. 4.9. The corresponding gradients of both $E_{\rm g}^{\rm i}$ and $E_{\rm g}^{\rm d}$ are quoted. The slopes are given in units of eV. All data correspond to pure STO system. 128

4.4 The changes (in eV) in the direct and the indirect gaps of STO as affected by epitaxial strain. The differences are calculated with respect to the gaps of STO as 0% strain. 132

4.5 The equilibrium DFT-LDA lattice parameter of strain-free STO a_0 and the critical values of compressive and tensile strains at which the ferroelectric transition is induced. The data are obtained from three different references and compared to this work. We explicitly quote the corresponding values of the strained in-plane lattice parameter a in the last column. 133

4.6 The critical values (denoted by an asterisk) of a, c, and the volume V at which the ferroelectric transition occurs in STO under different strain regimes. 135

4.7 A comparison between the VCA and the supercell approaches for a selected set of physical quantities corresponding to the $Ba_{0.5}Sr_{0.5}TiO_3$ system. The atomic displacements are given in fractional coordinates. The subscripts of the O atoms refer to the arrangement in Fig. 4.13. For the supercell calculation, the value reported for c is half the supercell lattice parameter in the [001] direction, and the atomic displacements in the two unit cells that make up the supercell are averaged to maintain consistency in comparison. 140

4.8 The equilibrium lattice constant a_0 of BST at 0% strain as affected by Sr concentration. The values are obtained from the VCA approach. The interpolated lattice constants according to Vegard's law are shown in the last column for comparison. . . . 140

4.9 The values of the critical lattice parameter a^* ($\approx c^*$), at which the ferroelectric transition occurs, of BST system at different Sr concentrations. The equilibrium lattice parameters are also indicated for reference. 143

5.1 The percentage differences in the xx and the zz components of the refractive index of ferroelectric BTO at different values of epitaxial strain as compared to the corresponding values of unstrained BTO. The birefringence is quoted in the last column. 158

5.2 The percentage differences in the xx and the zz components of the refractive index of STO ferroelectric thin films at different values of epitaxial strains as compared to the corresponding values of free standing STO film. The birefringence is quoted in the last column. 161

6.1 The interatomic distance between F and N, and the alignment of the Ti−N bond of the seven configurations shown in Fig. 6.1. 172

6.2 The structural parameters and the corresponding relative energies of the seven symmetry-inequivalent atomic configurations of the supercell of $BaTiO_{2.8}F_{0.1}N_{0.1}$ shown in Fig. 6.1. The relative energy ΔE (per $2\times2\times2$ supercell) is defined as $\Delta E = E_i - E_1$, where E_i is the energy of the i^{th} configuration with i running from 1 to 7, and E_1 is the total energy of $C^{(1)}$. The lattice parameters, the angles, the volumes and the energies are given in units of angstroms, degrees, Å^3 and eV, respectively. The corresponding calculated quantities of pure rhombohedral BTO are shown in the last row. 173

6.3 The direct energy gaps (at Γ) of the seven configurations of $BaTiO_{2.8}F_{0.1}N_{0.1}$ depicted in Fig. 6.1. The corresponding bandgap of rhombohedral BTO is given in the last row. ΔE_{g} is the difference in the bandgap with respect to pristine BTO. All the energies are given in units of eV. 177

6.4 The percentage difference in the refractive index Δn (at 1000 nm) between thin films of pristine BTO and the equilibrium structure of $BaTiO_{2.8}F_{0.1}N_{0.1}$ at each value of epitaxial strain. 190

6.5 The energy difference of $BaTiO_{2.8}F_{0.1}N_{0.1}$ between the configurations shown in Fig. 6.12 and $C^{(\perp)}$ shown in Fig. 6.5a at 0% strain. All configurations are more energetically favourable, apart from $C^{(\text{g})}$. Energies are given per $2\times2\times2$ supercell. . . . 192

6.6 The energy difference of $BaTiO_{2.8}F_{0.1}N_{0.1}$ between the configurations shown in Fig. 6.13 and $C^{(\perp)}$ shown in Fig. 6.5a at 0% strain. All configurations are less energetically favourable than $C^{(\perp)}$. Energies are given per $2\times2\times2$ supercell. 195

6.7 The direct energy gaps (at Γ) of the different configurations of $BaTiO_{2.8}F_{0.1}N_{0.1}$ at 0% strain depicted in Figs. 6.12 and 6.13. The corresponding bandgaps of $C^{(\perp)}$ and cubic BTO at 0% strain are given in the last two rows for comparison. ΔE_g is the difference in the bandgap with respect to BTO. All energies are given in units of eV. 197

6.8 The changes in the volume and the lattice constants of pure BTO (in percent) due to doping of F and N at two different concentrations. 201

Chapter 1

Introduction

Since ferroelectricity was first discovered in Rochelle salt in 1921 [5, 6], researchers have been attracted to this interesting physical property. Much research has been conducted since then, to try to explain, formulate, and deepen the knowledge of this phenomenon, and in addition, design useful device components using ferroelectric materials.

The word "ferroelectricity" is chosen as an analogue to the word "ferromagnetism", as the two phenomena have similarities. A ferroelectric material is one that can sustain a finite electric dipole moment that can be switched by means of an external electric field of sufficient strength. In other words, for a material to be classified as a ferroelectric, it must obey two conditions: 1. it can be spontaneously polarized (by spontaneously we mean in the absence of an external electric field) in multiple polarization states, and 2. it must be possible to switch between the polarization states by means of an applied external electric field [7, 8]. Therefore, a ferroelectric material generally exhibits hysteresis behaviour as shown in Fig. 1.1.

The polarization switching and the hysteresis loop of a ferroelectric material can be experimentally measured by several techniques, such as the Sawyer-Tower circuit [9]. Theoretically and computationally, there exists a rigorous formulation to define and calculate polarization as a bulk intensive quantity. The theory is known as the Modern Theory of Polarization, or the Berry-phase theory of polarization. [10, 11]. Whilst a detailed description of these methods and theories is beyond the scope of this thesis, the interested reader is directed to Ref. [7].

In fact, what makes ferroelectric materials very attractive is that they gen-

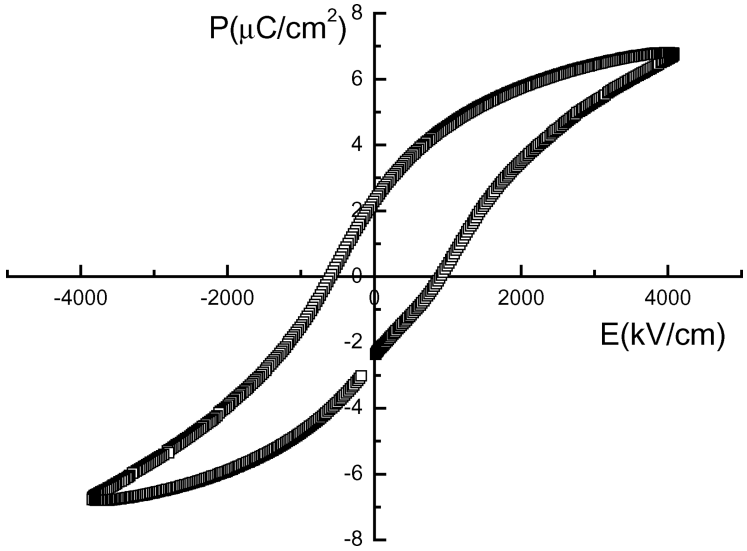


Figure 1.1: The hysteresis loop of bulk $BaTiO_3$, a typical ferroelectric material. This figure is reproduced, with permission, from Ref. [1], see App. B.

erally show interesting physical properties besides ferroelectricity, as shall be discussed in Sec. 1.2. For example, all ferroelectric materials are also pyroelectric, that is, the spontaneous polarization of the system can be changed by varying the temperature, inducing an electric voltage across the system. Furthermore, all pyroelectric materials are piezoelectric, which means that the polarization vector is affected by the application of mechanical strain to the sample. The opposite is not true, however. For instance, some materials (such as quartz [12]) can show piezoelectricity while they are not ferroelectric [13] .

From a crystallographic perspective, a ferroelectric crystal must break inversion symmetry. This is a necessary, but not a sufficient, requirement for ferroelectricity. Among the 32 crystallographic point groups, 11 of them possess inversion symmetry and cannot be ferroelectric. Out of the 21 remaining point groups, 20 exhibit piezoelectricity. Only 10 of the piezoelectric point groups have a unique polar axis that make them candidates for possessing a spontaneous polarization vector, making them pyroelectric materials. If, and only if, it becomes possible to switch the polarization vector between different states, then the material is classified as being ferroelectric [14].

1.1 Example of ferroelectric materials, introducing perovskites

There exist a wide range of materials with different crystal structures that display ferroelectricity. The ferroelectric transition usually involves a particular rearrangement of the atoms in the material. Lines and Glass [8] quoted three categories of ferroelectrics in a classification based on the atomic rearrangements required for polarization switching. These categories are the "one dimensional" , the "two dimensional" and the "three dimensional" classes. In the first class, atoms move along the polarization axis, and this class includes materials such as $BaTiO_3$ and $KNbO_3$. In the second class, atoms move in a plane perpendicular to the polarization axis, and this class includes materials such as $BaMgF_4$ and $NaNO_2$. The third class involves atomic movements in all three dimensions and include materials such as $KNaC_4H_4O_6.4H_2O$ (Rochelle salt). It is also worth mentioning that ferroelectricity has also been observed in some liquid crystals and polymers [15].

Among all these materials and families, perovskite oxides proved to be the most important ferroelectric family, and they are used in most devices that are based on ferroelectric components [13].

Perovskite is the common name of the mineral calcium titanate ($CaTiO_3$). The name is then given to materials that, crystallographically, belong to the same family as $CaTiO_3$. The general stoichiometric formula of perovskite oxides is ABO_3, where A and B are two cations (usually of different sizes) that can have different valences, with the 'B' cation being a transition metal. The crystal structure of a typical perovskite is shown in Fig. 1.2. If the 'A' is taken as the origin, then the 'B' cation occupies the body centre of the unit cell, and the oxygen atoms occupy the face centres. This can be viewed in an alternative way: The oxygen atoms are arranged in the material such that they form vertices of octahedra, the 'B' cations are located inside and at the centre of each oxygen octahedron, and the 'A' cations are located in the interstices between the octahedra.

Fig. 1.2 (a) depicts the case where the perovskite is *paraelectric*; i.e, there is no net polarization vector and all the atoms are at their ideal high-symmetry positions. Fig. 1.2 (b) shows the same system in the ferroelectric phase. It is evident that the inversion symmetry of the cell is broken by the displacements

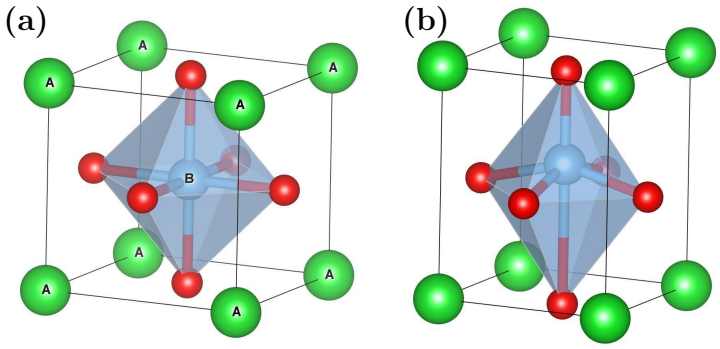


Figure 1.2: **(a):** The crystal structure of a typical perovskite in the cubic paraelectric phase. The 'A' cation (green) is at the origin, the 'B' cation (blue) is at the body centre, and the oxygen atoms (red) are at the face centres. The oxygen octahedron is represented by the blue transparent faces. **(b):** The corresponding atomic displacements (exaggerated) that break the inversion symmetry when the material is polarized along the [001] direction. With respect to the 'A' cation, the 'B' cation moves in an opposite direction to the oxygen anions. Atomic displacements are along the polarization direction.

of the atoms from their high-symmetry positions. The atomic movements required for polarization switching are along the polarization axis, making these ferroelectrics "one dimensional", according to the classification of Lines and Glass [8].

Perovskite oxides exhibit a wide variety of physical properties that make them interesting both technologically and scientifically. Besides ferroelectricity, pyroelectricity [16] and piezoelectricity [17], they also show flexoelectricity [18] (where strain gradients induce electric polarization in the material) and superconductivity [19]. In addition, the perovskite structure, having in general two different cation sizes, is amenable to a wide range of dopant additions [20], which makes it possible to make solid solutions with tuneable properties. We shall focus in this thesis on two prototypical perovskite oxides, namely $BaTiO_3$ and $SrTiO_3$, and their solid solutions.

1.2 $BaTiO_3$ and $SrTiO_3$

Barium titanate $BaTiO_3$ (BTO), strontium titanate $SrTiO_3$ (STO), and their solid solution $Ba_xSr_{1-x}TiO_3$ (BST) are prototypical examples of perovskite oxides. There is a significant body of literature on these materials in relation to

their structural, electronic and optical properties. Their interesting physical properties, which include high dielectric constant, large electro-optic coefficients, high optical nonlinearity and low optical losses, make them attractive candidates in manufacturing a number of useful devices, including electro-optic waveguides, optical modulators, tuneable microwave devices (such as filters and phase shifters), integrated capacitor structures (such as dynamic random access memories) and thermal switches. [21–27].

1.2.1 BTO

BTO appears as white powder or, when forming larger single crystals, transparent. It was the first material, within the perovskite family, that was identified to be ferroelectric. This important discovery that took place in 1945 opened the door for a wide range of applications, and stimulated the search for other ferroelectric perovskites. It also caused a dramatic change to the common understanding of the origin of ferroelectricity [28].

BTO undergoes multiple phase transitions with temperature. At low temperatures, it has a rhombohedral structure with the $R3m$ space group symmetry. The first transition occurs at 183 K, where BTO crystallizes in the orthorhombic structure with the $Amm2$ symmetry. At 278 K, it transfers to the tetragonal structure with the $P4mm$ symmetry. The third transition takes place at 393 K, where it crystallizes in a cubic phase with the $Pm\bar{3}m$ symmetry [7, 29, 30].

The first three phases are ferroelectric (note that it is ferroelectric at room temperature). Experimentally, the direction of the polarization vector was measured in Ref. [29] together with the magnitudes of the atomic distortions. The polarization direction is aligned along the [111], [011], and [001] directions in the $R3m$, $Amm2$, and $P4mm$ phases respectively. The high-temperature cubic phase is paraelectric where all the atoms are at the perfect high symmetry positions.

At high temperatures (around 1700 K), BTO can also crystallize in a hexagonal polymorph if it is fired in a hydrogen atmosphere. This transition can be enhanced by means of additives such as $MnCO_3$, or can be inhibited by impurities such as Sr and Si [31].

1.2.2 STO

Much like BTO, STO appears also as a white powder, and it is transparent when forming larger single crystals. As opposed to BTO, STO does not undergo as many phase transitions with temperature. The high temperature phase of STO is paraelectric cubic with the $Pm\bar{3}m$ symmetry. As the temperature decreases, it shows a tendency towards a ferroelectric transition, however, the transition does not occur. This is attributed to quantum fluctuations that stabilize the paraelectric phase over the ferroelectric phase making STO an "incipient ferroelectric" or "quantum paraelectric" [32]. When the O atoms in STO are substituted by their isotope ^{18}O, STO is indeed observed to undergo a ferroelectric transition at about 23K [33].

At this point, it is worth noting that isotope exchange is not the only means by which ferroelectricity can be induced in STO. It can also be achieved by means of epitaxial strain [34] or chemical substitution [35]. We shall discuss this in more detail in Chapter 4.

At about 110 K and below, STO crystallizes into a tetragonal structure with special atomic distortions taking place. The oxygen octahedra rotate about the [001] axis lowering the symmetry of the system to $I4/mcm$ [36]. This phase transition is called the "antiferrodistortive" transition. An illustration of the octahedra rotation is shown in Fig. 1.3.

1.3 Origin of ferroelectricity in perovskite oxides

Before the discovery of ferroelectricity in BTO, the common understanding was that hydrogen bonding plays an essential role for this property [28]. This understanding has changed dramatically after this discovery, and a lot of progress has been made since then towards the understanding of the ferroelectricity origin in perovskite oxides.

1.3.1 Goldschmidt tolerance factor

In 1926, Goldschmidt provided an empirical criterion for the stability of the perovskite structure based on the ionic radii of the constituent species, from

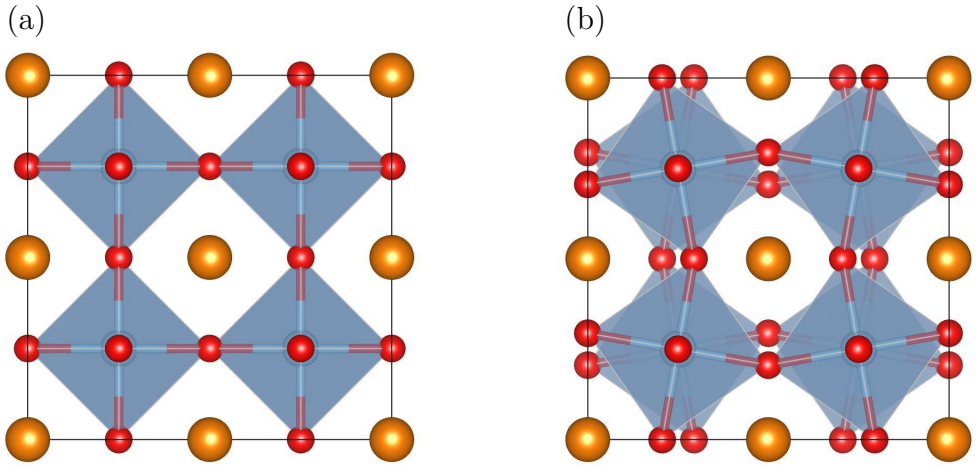


Figure 1.3: A view along the [001] direction of the high temperature (a) and the low temperature (b) phases of STO. Panel (b) illustrates the rotations of the oxygen octahedra about the [001] direction. Orange atoms represent the Sr species.

which one can have a general idea about whether or not the ferroelectric phase is favourable. In what follows we give a brief overview of this criterion summarised from Ref. [7].

Goldschmidt set up the following two rules:

- The cations in the system will be surrounded, at most, by the number of anions that can touch them.
- The anions *must touch* the cations, and the distance between them is simply given by the sum of the anion and cation radii.

When these two rules are followed, one obtains the following relation for an ideal cubic perovskite structure:

$$r_O + r_A = \sqrt{2}\,(r_O + r_B)\,, \tag{1.1}$$

where r_O, r_A, and r_B are the ionic radii of the oxygen anion, the A cation and the B cation respectively.

The Goldschmidt tolerance factor, t, is defined as the ratio

$$t = \frac{r_O + r_A}{\sqrt{2}\,(r_O + r_B)}\,. \tag{1.2}$$

When this ratio is close to one, then the perovskite structure tends to be formed and stable. If $t > 1$, this indicates that the 'B' cation is small and prefers to move off-centre resulting in a ferroelectric distortion (as in the case of BTO). On the other hand, if $t < 1$, the 'A' cation is small and can fit in the spaces between the oxygen octahedra, leading to the antiferrodistortive rotations of the octahedra (as in the case of STO).

1.3.2 The nature of the ferroelectric transition

It is generally understood that the ferroelectric transition is governed by the competition between the long-range Coulomb forces that favour the ferroelectric phase, and short range repulsive forces that favour the paraelectric phase [37]. In other words, the Coulomb interactions favour the atomic displacements in a perovskite oxide, which lead to a net polarization of the system. However, as the atoms are displaced, the repulsion between the electronic clouds with the neighbouring atoms causes the energy of the system to increase and therefore inhibits the distortions. The ferroelectric transition is favoured if there is an overall decrease in the energy of the system when the atoms displace off their high-symmetry positions.

The above reasoning gives a general governing principle about when the ferroelectric transition occurs, and explains its sensitivity to strain, chemistry and other factors. However, it does not provide information about the *nature* of the transition. There are two scenarios within which the ferroelectric transition is generally understood: the "displacive" and the "order-disorder" models. The former picture lies within the context of the lattice dynamics, where one of the lattice vibrational modes is unstable and temperature dependent. As the sample is cooled down, this mode becomes softer (decreases in frequency) until it goes to zero as the transition temperature is approached , leading to the displacements of the atoms (usually this concept is referred to as the soft-mode concept) [38]. Experimental evidence involving inelastic neutron scattering and Raman scattering measurements exists supporting the concept of the soft-mode picture and the displacive model in some ferroelectric materials.

On the other hand, the "order-disorder" description of the ferroelectric transition suggests that the "observed" direction of the polarization vector of a ferroelectric perovskite sample is actually a "time average" of other metastable

directions. To further clarify this idea: in the order-disorder scheme, it is understood that there are eight directions (or sites) along which the polarization vector has a local minimum. These directions are the [111] crystallographic directions [39]. At some finite temperature, the polarization vector hops randomly between some or all of these sites. Taking BTO as an example, the high-temperature paraelectric cubic phase has the polarization vector hopping between the all eight sites, giving a vanishing net polarization on average. In the tetragonal structure, the polarization vector hops randomly between four of these sites giving an average net polarization along [001]. The orthorhombic structure has the polarization vector hopping between two of these sites so that the average direction is [110]. Finally, the low-temperature rhombohedral structure is completely ordered so that the observed direction is along [111] direction [40].

It is not very straightforward to determine which kind of transition, among the two above, a certain ferroelectric material exhibits. Sometimes one finds contradicting views for a specific material. For example, Takesada *et al* [41] performed a Raman scattering study on STO18 (STO with a substitution of the O atoms by the isotope ^{18}O), and suggested that the transition is completely displacive with a perfect softening of the ferroelectric mode. On the other hand, Shigenari *et al* [42] drew a different conclusion from their Raman spectra stating that the transition is of order-disorder nature.

While the ferroelectric transition in some materials shows displacive nature, and order-disorder nature in others, there may exist also some ferroelectric materials in which the transition is hybrid of the two. As an example, recent neutron diffraction data of $KTiOPO_4$ suggested that the transition has both order-disorder and displacive components [43].

As for the case of BTO, it has long been uncertain what the nature of the transition is [44]. Previous X-ray absorption fine structure (XAFS) measurements suggest that the transition is of order-disorder nature [45], while inelastic neutron scattering study suggested that it is of displacive nature [46]. Ongoing recent research shows that BTO may have aspects of both models, confirmed experimentally by NMR measurements [47]. From the simulation perspective, it is also suggested that the ferroelectric transition in BTO has both components. Monte Carlo simulations based on an effective Hamiltonian fitted to *ab initio* calculations [48] show that the transition is mainly displacive

with a small component of order-disorder character. Very recent molecular dynamics simulations [49, 50], on the other hand, suggest that the order-disorder component is more dominant.

1.3.3 The origin of ferroelectricity

Apart from the nature of the ferroelectric transition, efforts have been spent to further understand the origin of ferroelectricity in perovskite oxides and particularly in BTO. It has been shown that the hybridization between the O $2p$ and the Ti $3d$ states in BTO (also in $PbTiO_3$) is essential for ferroelectricity. The paraelectric phase becomes the most stable phase if the hybridization is inhibited, as predicted by full potential linearised augmented-plane wave (FP-LAPW) calculations [37].

Ferroelectricity in BTO has been shown to have a strong dependence on the volume of the system. The first-principles calculations in Ref. [51] show that the ferroelectricity of BTO is decreased under a compressive pressure, and is completely inhibited when the volume goes below a critical threshold. The opposite is true for tensile pressure, which enhances the ferroelectricity of the system.

The electronic polarizability of the A cation in the ABO_3 crystal has been shown to have a strong correlation to the ferroelectricity. Considering $CaTiO_3$, STO, BTO and $PbTiO_3$, the polarizability increases from the Ca, Sr, Ba and Pb cations respectively, with the Pb having the highest value. This is linked to the fact that the spontaneous polarization in $PbTiO_3$ is larger than that in BTO, while STO and $CaTiO_3$ are paraelectrics [52].

Recent density functional theory calculations showed that the Coulomb repulsions between the B cation and the O anion in ABO_3 have a strong role in the ferroelectricity. In BTO in particular, the repulsion between the Ti $3s$ and $3p$ states and the O $2s$ and $2p$ states are found to be important for the Ti displacement [53].

For the sake of completeness, it is worth noting that in magnetoelectric multiferroics there exist other factors that are thought to be responsible for their ferroelectric polarization, such as charge redistribution and atomic displacements induced by spin order [54].

1.4 Reduced sizes and thin films

To meet the demand of manufacturing smaller industrial components, such as advanced integrated electronic devices, attention has been drawn to ferroelectric perovskites in nanostructure or thin film forms. Reducing the size of a ferroelectric sample affects its ferroelectric properties [55]. While the size effect on the analog ferromagnetism is generally understood, it is not obvious for the case of ferroelectricity. A lot of research has been conducted to investigate and understand finite size effects on this property.

For the case of ferromagnetism, it is generally understood that when the size of a ferromagnetic sample is reduced below a certain critical value, the energy of the magnetic anisotropy is dominated by the thermal energy. This causes the magnetic moments of the sample to flip in random directions leading to the disappearance of macroscopic net magnetisation. The resulting state is usually referred to as "superparamagnetic" [56].

The size effect on ferroelectricity is, however, not very clear yet. The presence of extrinsic effects (i.e., effects that are not inherent to the system, such as the method of fabrication and the depolarizing field) can seriously affect the reported critical sizes for stabilizing the ferroelectric phase, and, as a result, forms one of the challenges in obtaining a clear understanding of this issue.

Taking BTO as an example, thin BTO films were reported to show ferroelectric switching for film thicknesses as low as 40 nm [57]. On the other hand, Yashima *et al* [58] experimentally studied the size effect on the axial ratio c/a and the spontaneous polarization of BTO nanoparticles. The critical size was about 30 nm. Moreover, Matsui *et al* observed a switchable spontaneous polarization in BTO nanoparticles of sizes down to 6 nm [59].

Taking another example of $PbTiO_3$, different values for critical particle sizes are reported in the literature, ranging from about 12.6 nm, 10.7 nm down to 9.1 nm [55, 60, 61]. In $PbTiO_3$ thin films, it is reported that the crystal structure turns into a cubic paraelectric when the average crystallite size is below $\sim$5 nm [62]. A more recent study showed that ferroelectricity in $PbTiO_3$ films is stabilized for thicknesses down to 1.2 nm (equivalent to 3 unit cells) through the formation of ferroelectric domains [63].

These discrepancies in the reports of critical size suggest that extrinsic

effects have a non-trivial influence on ferroelectric switching. From the examples above, one notices that, in general, more recent studies report smaller sizes compared to older ones, suggesting perhaps that improvements in sample preparation might reduce limitations, such as the presence of defects and grain boundaries, that could be responsible for hindering ferroelectric switching [7].

As an attempt to further understand and predict the critical size of ferroelectric switching, scientists approached this problem from a theoretical perspective. For example, Zhong *et al* used the Landau phenomenological theory to study the effect of the particle size on the phase transition of spherical BTO and $PbTiO_3$ particles [64]. The critical size of $PbTiO_3$ was found to be 4.2 nm. However, they reported a value of 44 nm for BTO, which is an order of magnitude larger than the experimental values quoted above.

Computer simulations can also play an important role in investigating the size effect on ferroelectricity. As an example, atomistic simulations for free-standing BTO thin films showed that the critical size for the ferroelectricity is about 3.6 nm [65], which is about 10 unit cells long.

Ab initio simulations of a BTO capacitor sandwiched between two $SrRuO_3$ electrodes suggested the existence of a critical thickness of about 2.4 nm, below which ferroelectricity is lost [66]. On the other hand, the calculations of Vanderbilt *et al* on BTO and $PbTiO_3$ slabs confirmed that the ferroelectric instability can exist for very thin slabs, suggesting the absence of a critical size [67].

The above review clearly shows that reducing the size of a ferroelectric sample has a strong impact on its ferroelectric properties. The large discrepancies in the experimental and the theoretical reports of the critical sizes reflect the complexity of the problem and indicate the important role of the variety of extrinsic factors in changing the physical properties of a ferroelectric perovskite thin film or nanostructure.

1.4.1 Ferroelectric Thin Films

Reducing the size towards the nanometer scale does not only affect ferroelectric properties (such as the Curie temperature and coercive field), but also a wide range of other physical properties making them generally different from those of the bulk, including the dielectric and piezoelectric properties [68].

Focusing on thin films in particular, it is well known that the properties of thin films can significantly differ (and sometimes become superior) to bulk properties. For example, the superconducting transition temperature of $La_{1.85}Sr_{0.15}CuO_4$ can be raised by 4 degrees when grown epitaxially on $LaSrAlO_4$ substrates [69]. In addition, Gan *et al* showed that epitaxial $SrRuO_3$ thin films exhibit different electrical and magnetic properties as compared to bulk, including a lower Curie temperature and lower magnetic saturation [70]. Moreover, Ramesh *et al* reported that when $BiFeO_3$ is grown epitaxially on STO substrates, it adopts a different crystal structure compared to the bulk (monoclinic versus rhombohedral, respectively), and they also reported an enhancement of the spontaneous polarization and magnetization [71]. Furthermore, it has been shown that ferroelectricity of BTO thin films can be enhanced by around 250% compared to bulk BTO single crystals, and the Curie temperature can be raised by 500 degrees [72]. Also, although bulk STO is not ferroelectric as mentioned earlier, ferroelectricity can be induced in STO when grown epitaxially on $DyScO_3$ or other substrates [34]. Maier *et al* [73] have reported that a solid solution of $Ba_{0.5}Sr_{0.5}TiO_3$, when epitaxially deposited on pure STO, $LaAlO_3$, and $La_{0.3}Sr_{0.7}Al_{0.65}Ta_{0.35}O_3$ substrates, has different values of refractive index depending on the substrate, and all of these values differ to the bulk.

The discrepancies between thin films properties and bulk properties are generally attributed to a number of extrinsic factors. A key factor is the lattice mismatch strain that the film experiences when deposited on a substrate with a different lattice parameter [74]. Other factors include the finite thickness of the film (where surface effects can be important), the film growth direction, the presence of defects (point defects such as vacancies, line defects such as dislocations, or planar defects such as grain boundaries), the electrical boundary conditions that can be imposed to the film, stoichiometric variations of the film components, and cation substitutions. [75–77]. Fig 1.4 shows examples of high resolution transmission electron microscopy (HRTEM) images characterizing the structure of epitaxially grown BTO films on different substrates.

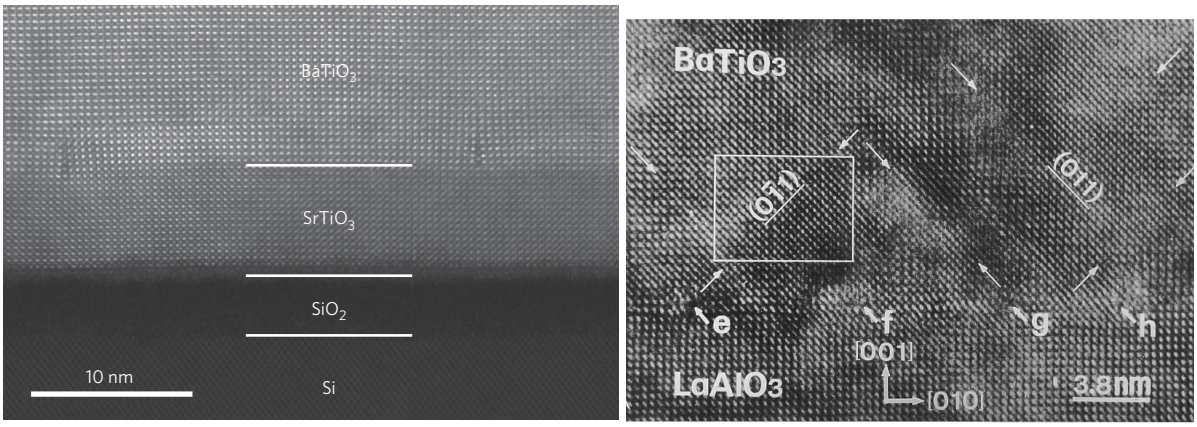


Figure 1.4: HRTEM images of BTO/STO/SiO_2/Si stacks (left) and BTO film grown on $LaAlO_3$ substrate (right). One can notice the edge dislocations at the BTO/STO interface in the left image and the 90° domain boundaries of the BTO film in the right image. Left and right images are reproduced, with permission, from Refs [2] and [3], respectively. See App. B.

1.5 Tuning the optical properties of BST thin films

We have presented so far how BTO and STO thin films are very interesting and show many physical properties that make them potential candidates in manufacturing useful devices. In particular, the novel optical properties of these materials attracted a lot of interest in developing devices such as optical waveguides, electro-optic modulators and optical switches.

It is far more interesting, though, to be able to *control* and *tune* the optical properties of these functional materials, which eventually leads to controlling the functionality of the manufactured devices. Tailoring the properties of BST thin films is usually achieved through several means, which include thermal tuning, electro-optical effects, strain engineering and compositional variations.

A lot of experimental and theoretical research was conducted to study the optical properties of BST thin films and investigate the methods by which they may be tuned. For instance, Maier *et al* [73] reported that the refractive index of $Ba_{0.5}Sr_{0.5}TiO_3$ decreases with increasing epitaxial strain, as obtained from their spectroscopic ellipsometry measurements. Spectroscopic ellipsometry investigations by Dejneka *et al* [78] also reported similar result for STO films.

Also, the effect of the Sr content in BST films have been investigated from ellipsometry measurements by Wang *et al* [79], where it was reported that the refractive index of the films generally increase with decreasing the Sr content, although the trend was not shown to be monotonic through the entire range of concentrations. Furthermore, tuning the refractive index via thermal effects and electro- optic effects has been investigated in Refs. [80] and [81], respectively, where the prism coupling method was used for the measurements of the optical properties. Investigations of other effects such as the film thickness and the annealing temperature have also been performed in Refs. [82–84].

On the other hand, many theoretical investigations, based on density functional theory, of the optical properties of BTO, STO, and BST exist in the literature. For instance, the dielectric functions of bulk BTO and STO have been calculated in Refs. [85–87], and were found to be in a good agreement with experiment. The frequency-dependent and the static dielectric constant of bulk BST solid solutions have also been investigated in Refs. [88] and [89], respectively. Khenata *et al* [90] investigated the effect of the hydrostatic pressure on the dielectric function of bulk BTO, where they reported that pressure induces an overall blueshift in the spectrum. Furthermore, the effect of selected cation substitutions on the optical properties of BTO and STO were investigated in Refs. [91, 92].

However, there is a large gap between the experimental investigations and the theoretical studies that exist in the literature. To the best of our knowledge, comprehensive first principles investigations of the optical properties of BTO, STO and BST, and their sensitivity to structural perturbations such as strain, alloying, ferroelectric distortions and doping are missing from the literature.

The importance of these investigations is two fold. Firstly, the experimental methods that are most widely used to characterize the optical properties of BST thin films (in particular, the spectroscopic ellipsometry technique) are generally indirect; that is, the raw measurements need further analysis based on pre-defined models for the optical spectra and the film structure, in order to extract the optical properties such as the refractive index or the dielectric function. This can lead to a high margin of unreliability of the calculated spectra, and a prior knowledge of the structure of the film might be necessary.

Secondly, comprehensive first principles study of the aforementioned effects can provide a wider and deeper understanding of how and to what extent they

can be used to tune the optical properties of BST. Disentangling different effects, which is not always possible experimentally, can help provide very useful suggestions to how to most effectively engineer the optical properties of the films under study, and gives fundamental insights into the microscopic mechanisms underlying the observed or predicted trends.

1.6 Outline of thesis

We have given in this chapter an introduction to the physics of ferroelectricity and ferroelectric materials, introduced the prototypical perovskites BTO and STO and provided a relevant literature review of what is already known about these materials. We have also described the technological importance of these materials in thin film form and how their properties could significantly differ from bulk. Lastly, we described the context of our work, focusing on its importance and what we can add to the literature.

The rest of this thesis is organized as follows. In Chapter 2 we give a detailed description of the experimental method known as spectroscopic ellipsometry, describing its theoretical basis and the usual procedure of calculating optical spectra from the raw measurements. We focus on the limitations of this technique and provide certain examples in which it can provide misleading results.

In Chapter 3, we provide a detailed description of density functional theory, on which all our electronic structure calculations are based. We allude to the main approximations that lead to the success and the applicability of the theory and highlight some of the limitations that accompany these approximations.

In Chapter 4, we investigate the strain-induced changes in the electronic structure and bandgaps of BTO, STO and their solid solutions. We provide a detailed discussion of the features that are observed in the energy gaps of these materials due to strain, and attempt to rationalise the factors that govern the strain-induced ferroelectric transition in these materials. We also investigate the effect of Sr concentration on the bandgap of BST.

In Chapter 5, we study the effect of biaxial strain on the refractive index of BTO and STO, linking the features that are observed in the trends with the results of Chapter 4. We also investigate the effects of the ionic displacements

and atomic configuration on the refractive indices of BST. We justify the use of the virtual crystal approximation by comparing its results with the results of supercell calculations. We finally study the effect of Sr content on the refractive indices of BST solid solutions.

We investigate in Chapter 6 another means by which the refractive index of BTO might be tuned. Anionic co-substitution of F and N in BTO with different atomic configurations and concentrations are extensively studied. We perform systematic investigations to understand the most stable configurations of the dopant atoms. We also investigate the effect of strain on the energetics of different atomic configurations and the refractive index of the codoped BTO.

Finally, in Chapter 7 we give a summary of the main results that have been obtained from the above investigations, and highlight future work that is suggested by these results.

Chapter 2

Experimental approach; Spectroscopic ellipsometry

2.1 Overview

The optical properties of thin solid films, in particular the refractive index and its dispersion (i.e. given as a function of the energy or the wavelength of the incoming light), can be investigated experimentally by means of several techniques that include the Abelés method, the prism coupling method (PC), and spectroscopic ellipsometry (SE). These methods vary in their accuracy, complexity, and applicabilities. Some of these techniques are "direct" and others are "indirect". By "indirect" we mean that the collected experimental raw data do not directly represent the refractive index of the film, but rather contain information about light reflected/transmitted from/through the film. Post analysis of these data is then necessary to extract the desired optical properties.

The data analysis may involve adopting specific models for the structure of the film and for the dispersion of the optical property in question. This means that without a prior knowledge of the film structure and its optical properties, the results could be unreliable.

As a matter of interest, a brief overview of the Abelés method and the prism coupling method is given in App. A. In this chapter, we shall give a description to the theory behind the SE method, demonstrating a key limitation of SE in relation to determining the refractive index of thin films, which is one of the

main reasons for our subsequent work on developing a deeper understanding of the optical properties of thin oxide films from first-principles.

2.2 Introduction to spectroscopic ellipsometry

Spectroscopic ellipsometry (SE) [93–95] is the most widely used technique for measuring the optical properties and thicknesses of thin films. This method has a history dating back to the late 1800s where it evolved from Paul Drude's measurements of the thicknesses of ultra thin films (several angstroms in thickness) using elliptically polarized light [95–97].

Like with the PC technique (described in App. A), SE is an indirect technique with competing measurement accuracy. However, unlike the PC method, it is contactless and therefore non destructive, it works for film thicknesses down to the angstrom scale, measurements can be taken at a wide range of wavelengths (from infrared to ultraviolet), and the imaginary part of the refractive index (in addition to its real part) can be obtained directly[1]. These can be regarded as some of the advantages of SE over the PC method.

Since its foundation, the SE method has undergone a series of developments that enhanced the measurements precision and significantly reduced the time taken to acquire the data. SE was first applied using monochromatic light (where the method used to be referred to as "ellipsometry"), but it has been improved to take measurements at wide range of wavelengths. Recently, real time SE has been developed, where the measurements are continuously taken during the film synthesis, allowing further characterizations of the thin film such as studying the initial growth processes or interface structures [98].

Spectroscopic ellipsometry has a vast range of applications in characterizing thin films structures and optical functions. Although it is an indirect method, very accurate structures may be obtained from SE measurements that reproduce those obtained from direct techniques such as transmission electron microscopy (TEM) [94, 98]. The SE method has been used, in particular, in a lot of studies to investigate the optical properties of BST thin films. Examples

[1]The imaginary part of the refractive index can be generally obtained through the Kramers–Kronig relations once the real part is known (or vice versa). Spectroscopic ellipsometry yields both the real and the imaginary parts simultaneously without the need to use the Kramers–Kronig relations.

can be found in Refs. [73, 79, 82, 83, 99–103].

The theory behind SE is somewhat complicated, and the calculations required to extract the optical properties from the raw measurements are more complex than for the PC method. Indeed, *a priori* models of the film structure and the dispersion of the optical functions must be known in order to find the desired optical properties through fitting to the raw measurements. This can lead, however, to a number of problems that can affect the realiability of the extracted data.

In what follows, we will give a brief overview of the theory on which SE is based, describing what exactly is measured and how the refractive index (and the film thickness) can be extracted from the raw data. We shall then focus on the limitations that involve the calculations of the optical properties and the film thicknesses.

2.3 Theory of light polarization upon reflection

When linearly polarized light is incident on a planar surface, part of it is reflected, and part is transmitted, as depicted in Fig. 2.1.

By applying the electrodynamic boundary conditions at the interface of the two media, one can calculate the fractions of the electric field amplitudes of the reflected (E_r) and the transmitted (E_t) light with respect to that of the incident (E_i) light:

$$\begin{aligned} r_{01} &\equiv \frac{E_\mathrm{r}}{E_\mathrm{i}}\,, \\ t_{01} &\equiv \frac{E_\mathrm{t}}{E_\mathrm{i}}\,. \end{aligned} \tag{2.1}$$

where the numerical subscripts ($\alpha\beta$) here, and henceforth in this chapter, indicate that these coefficients are calculated at the boundary between medium α and medium β, where the light is initially travelling through medium α before hitting the boundary with medium β. These ratios are referred to as the Fresnel coefficients of reflection and transmission respectively.

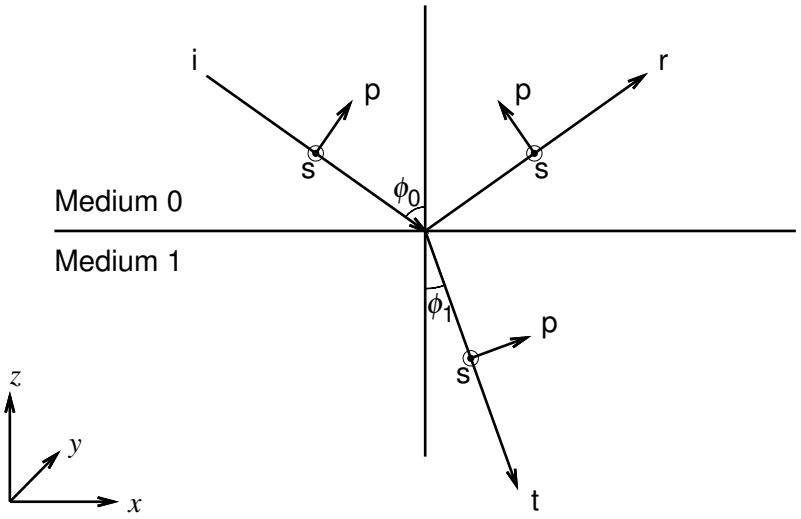


Figure 2.1: Schematic diagram for a linearly polarized electromagnetic wave incident on a planar interface from medium 0 to medium 1. The components of the electric field parallel and perpendicular to the plane of incidence are denoted p and s, respectively. ϕ_0 is the angle of incidence and ϕ_1 is the angle of refraction.

We shall now give a simplified derivation of how to express these coefficients in terms of the refractive indices of the two media and the angles of incidence and refraction. Full details can be found in many electrodynamics text books (such as [104, pp. 386–390]).

The monochromatic linearly polarized electric field of the incident light can be generally written as

$$\widetilde{\mathbf{E}}_{\mathrm{i}}(\mathbf{r},t) = \mathbf{E}_{\mathrm{i}}\, e^{i\,(\mathbf{k}_{\mathrm{i}}\cdot\mathbf{r} - w\,t)}\,, \tag{2.2}$$

with similar equations for the reflected and the transmitted waves.

The electric field vector can be decomposed into two components: one is parallel to the plane of incidence (the $x\,z$ plane) and is denoted (Fig. 2.1) with the subscript p; the other is perpendicular to the plane of incidence (pointing along the y direction) and is denoted with the subscript s. Fresnel coefficients can be derived for both components.

At the (01) boundary, the electric and the magnetic fields of the electromagnetic wave in medium 0 are related to those in medium 1 by the electrodynamic boundary conditions, which state that the fields must maintain continuity across the interface:

$$\mathbf{E}_0^{\parallel} = \mathbf{E}_1^{\parallel}, \tag{2.3a}$$

$$\frac{1}{\mu_0}\mathbf{B}_0^{\parallel} = \frac{1}{\mu_1}\mathbf{B}_1^{\parallel}\,, \tag{2.3b}$$

where the numerical subscripts indicate the *total* field in the corresponding medium.

In other words; at the (01) boundary, the total electric field parallel to the interface (parallel to the $x\,y$ plane)[2] in medium (0) must be equal to that in medium (1). The same is true for the magnetic field ($\mathbf{B}$), but weighted by the reciprocal of the magnetic permeability μ of the corresponding medium. For non-magnetic media, the permeability is almost equal to that of the free space, so the prefactors in Eq. 2.3b can be simply dropped to an excellent

[2]The parallel component here, denoted by $\parallel$, is not to be confused with the parallel component denoted by p, which mentioned elsewhere in the text. The latter is meant to be parallel to the plane of incidence (the xz plane in Fig. 2.1).

approximation.

Focusing on the parallel component of the electric field, substituting Eq. 2.2 into Eq. 2.3a yields:

$$\widetilde{E}^x_{\mathrm{i,p}}(\mathbf{r},t) + \widetilde{E}^x_{\mathrm{r,p}}(\mathbf{r},t) = \widetilde{E}^x_{\mathrm{t,p}}(\mathbf{r},t), \tag{2.4}$$

since the parallel components that are parallel to the interface are along the x-axis. Note that $\widetilde{\mathbf{E}}_{\mathrm{i}} = (\widetilde{E}^x_{\mathrm{i}}, \widetilde{E}^y_{\mathrm{i}}, \widetilde{E}^z_{\mathrm{i}})$. The subscripts (,p and ,s) here and in what follows, indicates the parallel and the perpendicular components of the fields, respectively.

In Eq. 2.4, the spatial and the temporal dependences of the electric fields are merely found in the exponential part (see Eq. 2.2), and since this boundary condition holds at any position $\mathbf{r}$ at any time t, then all the exponential factors have to be equal and can therefore be dropped from the equation. In other words, the complex amplitudes themselves must satisfy:

$$E^x_{\mathrm{i,p}} + E^x_{\mathrm{r,p}} = E^x_{\mathrm{t,p}}\,, \tag{2.5a}$$

$$\Rightarrow E_{\mathrm{i,p}}\cos\phi_0 - E_{\mathrm{r,p}}\cos\phi_0 = E_{\mathrm{t,p}}\cos\phi_1\,, \tag{2.5b}$$

where we have utilized the equality of the angles of incidence and reflection. The equality of the exponential factors lead to the three laws[3] of reflection and refraction. One of them is Snell's law, which relates the angles ϕ_0 and ϕ_1 to the refractive indices of the two media, N_0 and N_1:

$$N_0 \sin\phi_0 = N_1 \sin\phi_1\,. \tag{2.6}$$

The corresponding magnetic field of the parallel component of the electric field points along the $-y$ direction, since $\mathbf{B} = \frac{1}{v}\hat{\mathbf{k}} \times \mathbf{E}$, where v is the velocity of light in the corresponding medium, and $\hat{\mathbf{k}}$ is a unit vector pointing in the direction along which the wave is travelling. So, applying the boundary

[3]These are the well-known laws that govern the process of reflection and refraction. The first law states that the incident, the reflected, and the transmitted beams all lie in the same plane, usually referred to as the *plane of incidence*, which includes the vector normal to the interface. The second law states that the angle of incidence is equal to the angle of reflection. The third law is Snell's law, which is explained in the main text.

condition of Eq. 2.3b, one gets:

$$\frac{E_{\mathrm{i,p}}}{v_0} + \frac{E_{\mathrm{r,p}}}{v_0} = \frac{E_{\mathrm{t,p}}}{v_1}, \tag{2.7}$$

where we have substituted $B = \dfrac{E}{v}$.

The refractive index N of a medium is defined as the ratio of the speed of light in vacuum c to the speed of light in that medium v: $N \equiv \dfrac{c}{v}$. So, Eq. 2.7 can be written as

$$N_0 E_{\mathrm{i,p}} + N_0 E_{\mathrm{r,p}} = N_1 E_{\mathrm{t,p}}\,. \tag{2.8}$$

Eqs. 2.5b and 2.8 can be solved for $E_{\mathrm{r,p}}$ and $E_{\mathrm{t,p}}$ to obtain the Fresnel coefficents of reflection and transmission for the parallel component of the field:

$$(r_{01})_{\mathrm{p}} = \frac{N_1 \cos\phi_0 - N_0 \cos\phi_1}{N_1 \cos\phi_0 + N_0 \cos\phi_1}, \tag{2.9a}$$

$$(t_{01})_{\mathrm{p}} = \frac{2N_0 \cos\phi_0}{N_1 \cos\phi_0 + N_0 \cos\phi_1}\,. \tag{2.9b}$$

Similarly, one can obtain the Fresnel coefficients of the perpendicular component of the electric field. These are given by

$$(r_{01})_{\mathrm{s}} = \frac{N_0 \cos\phi_0 - N_1 \cos\phi_1}{N_0 \cos\phi_0 + N_1 \cos\phi_1}, \tag{2.10a}$$

$$(t_{01})_{\mathrm{s}} = \frac{2N_0 \cos\phi_0}{N_0 \cos\phi_0 + N_1 \cos\phi_1}\,. \tag{2.10b}$$

The Fresnel coefficients are generally complex numbers showing the effect of reflection and refraction on the amplitude and the phase of the incident wave. In order to examine this effect on the amplitude and the phase separately, they are expressed as

$$\left.\begin{aligned} r_{\mathrm{p}} &= |r_{\mathrm{p}}|\, e^{i\delta_{\mathrm{r,p}}}, \quad t_{\mathrm{p}} = |t_{\mathrm{p}}|\, e^{i\delta_{\mathrm{t,p}}} \\ r_{\mathrm{s}} &= |r_{\mathrm{s}}|\, e^{i\delta_{\mathrm{r,s}}}, \quad t_{\mathrm{s}} = |t_{\mathrm{s}}|\, e^{i\delta_{\mathrm{t,s}}} \end{aligned}\right\}, \tag{2.11}$$

where δ_{r} and δ_{t} give the phase shifts experienced by the incident wave upon reflection and transmission, respectively, and the subscripts relating to medium 0 and medium 1 have been suppressed for clarity.

2.4 What is measured in SE?

As described in the previous section, when an electromagnetic wave is incident on a surface, the polarization state of the wave is changed upon reflection and transmission. The core of SE is to measure these changes in the polarization state and to calculate the optical constants and the thickness of the film from these measurements.

In general, the perpendicular and the parallel components of the electric field can be significantly different from each other upon reflection, in both magnitude and phase. Hence, the parallel and perpendicular Fresnel coefficients (see Eqs. 2.1, 2.9 and 2.10) are in turn different.

Defining the ratio ρ as

$$\rho \equiv \frac{r_{\mathrm{p}}}{r_{\mathrm{s}}} = \left|\frac{r_{\mathrm{p}}}{r_{\mathrm{s}}}\right| e^{i(\delta_{\mathrm{r,p}} - \delta_{\mathrm{r,s}})} = \tan\psi\, e^{i\Delta}\,, \tag{2.12}$$

it follows that ψ and Δ are directly related to the raw measurement of SE, where $\tan\psi$ is the amplitude of the ratio between the parallel and the perpendicular polarizations, while Δ represents the phase difference between them, i.e.,

$$\tan\psi = \left|\frac{r_p}{r_s}\right|, \tag{2.13a}$$

$$\Delta = \delta_{\mathrm{r,p}} - \delta_{\mathrm{r,s}}\,. \tag{2.13b}$$

So, the change in the polarization state of the light upon reflection is captured by SE by measuring the variations in the parallel and the perpendicular

polarizations of the reflected light.

In transmission SE (as compared to reflection SE), ψ and Δ have analagous definitions to Eqs. 2.12 and 2.13 but in terms of the Fresnel coeficients of transmission t_{p} and t_{s}.

In general, the refractive index N of a material is a complex number:

$$N \equiv n - i\kappa, \tag{2.14}$$

where the real part n is the ratio between the speeds of light in vacuum and in the material, and the imaginary part k is the extinction coefficient, which is related to the absorption coefficient of the material α by the relation:

$$\alpha = \frac{4\pi\kappa}{\lambda}\,, \tag{2.15}$$

where λ is the wavelength of the incoming light.

Although the derivation that we followed for Eqs. 2.9 and 2.10 assumed that N is real, these equations are still valid for complex refractive indices[4].

In principle, if medium 1 in Fig. 2.1 represents the sample for which one wants to find the refractive index (e.g., a bare substrate), and medium 0 represents the ambient environment (e.g., air), then the refractive index of the sample N_1 can be calculated from the measurments of ψ and Δ using Eqs. 2.9, 2.10, 2.12 and 2.13 (where the refraction angle ϕ_1 can be eliminated using Eq. 2.6, and N_0 and ϕ_0 are obviously known). So, basically for samples of homogeneous structure and uniform refractive index, the measured ψ represents the real part of the refractive index, while Δ represents the absorption of the film to the incoming light [94]. This is in general how SE works.

2.5 SE data analysis

Clearly, the systems that we are often interested in are not as simple as a bare infinitely thick substrate as depicted in medium 1 in Fig. 2.1. When a thin

[4]Indeed, Eq. 2.2 assumes that the light is propagating through the medium without attenuation of its intensity. In the case of an absorbing medium, Eq. 2.2 is multiplied by a spatial damping exponential factor according to Beer-Lambert law. By introducing the concept of a complex refractive index, Eq. 2.2 can restore its original form and the absorption coefficient is represented by the imaginary part of the refractive index. It follows that the derivation of the Fresnel coefficient follows the same steps and similar expressions hold for a complex refractive index.

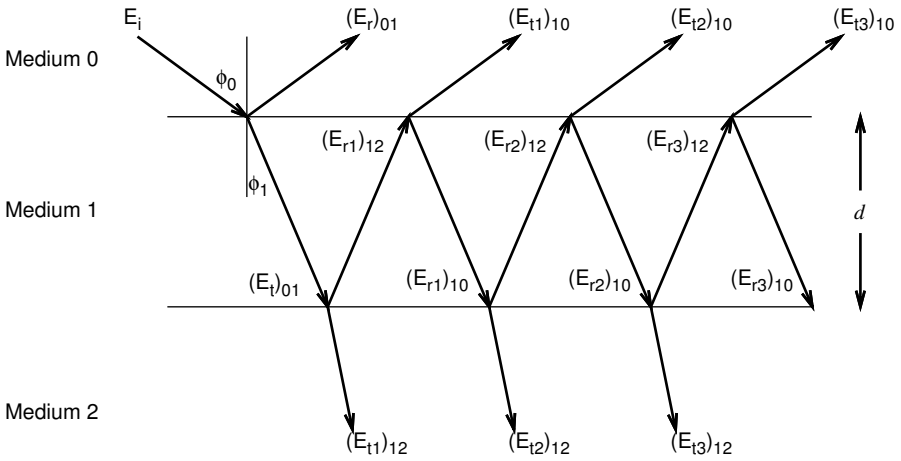


Figure 2.2: Schematic diagram showing the interaction of the incident light with a thin film of thickness d deposited on an infinitely thick substrate. Media (0,1,2) represent the ambient environment (air), the film, and the substrate, respectively, with corresponding refractive indices N_0, N_1 and N_2.

film, of finite thickness d, is deposited on the substrate, the Fresnel coefficients of the parallel and perpendicular polarizations are modified due to the presence of the film/substrate interface which adds further reflection events. Hence, the process of calculating the refractive index of the film along with its thickness becomes more complicated.

In what follows, we provide a simple derivation of the Fresnel coefficients for the air/film/substrate system, which correspond to medium 0/ medium 1/medium 2 respectively in Fig. 2.2. More details can be found, for example, in Ref. [93].

For this system, the amplitude ratio $\tan\psi$ and phase shift Δ measured in SE correspond to:

$$\frac{(R_{012})_{\rm p}}{(R_{012})_{\rm s}} = \tan\psi\, e^{i\Delta}\,, \tag{2.16}$$

where $(R_{012})_{\rm p,s}$ are the Fresnel coefficients that correspond to the *total* light reflected back to medium 0 from all of the possible paths, which include multiple reflections within medium 1. More compactly:

$$R_{012} \equiv \frac{(E_{\rm r})_{01} + \Big((E_{t1})_{10} + (E_{t2})_{10} + \cdots\Big)}{E_{\rm i}}\,, \tag{2.17}$$

where the terms have their meaning illustrated in Fig. 2.2. We have dropped the subscripts p and s for ease of notation.

From the definitions in Eqs. 2.1, one can rewrite $(E_{\rm r})_{01}$, $(E_{\rm t})_{01}$, $(E_{r1})_{12}$, $(E_{t1})_{10}$ in terms of $E_{\rm i}$:

$$(E_{\rm r})_{01} = r_{01} E_{\rm i}\,, \tag{2.18a}$$

$$(E_{\rm t})_{01} = t_{01} E_{\rm i}\,, \tag{2.18b}$$

$$(E_{r1})_{12} = r_{12}\Big((E_{\rm t})_{01}\, e^{-i\beta}\Big) = r_{12}\, t_{01}\, e^{-i\beta}\, E_{\rm i}\,, \tag{2.18c}$$

$$(E_{t1})_{10} = t_{10}\Big((E_{r1})_{12}\, e^{-i\beta}\Big) = t_{10} r_{12}\, t_{01}\, e^{-2i\beta}\, E_{\rm i}\,. \tag{2.18d}$$

The factor $e^{-i\beta}$, appearing in Eqs. 2.18c and 2.18d, is the phase shift that results from the path difference relative to the first reflected wave. β is the phase thickness of medium 1 and is given by (see, e.g., Ref. [105, p. 313])

$$\beta = \frac{2\pi d N_1 \cos\phi_1}{\lambda}\,, \tag{2.19}$$

where λ is the wavelength of the light in vacuum.

Similarly, one can find expressions for all of the waves that are transmitted back to medium 0 (air) after 2,3,4 $\cdots$ reflections at the interface between medium 1 (film) and medium 2 (substrate):

$$(E_{t2})_{10} = t_{10} r_{12}\, t_{01}\, e^{-2i\beta}\left(r_{10}\, r_{12} e^{-2i\beta}\right) E_{\rm i}\,, \tag{2.20a}$$

$$(E_{t3})_{10} = t_{10} r_{12}\, t_{01}\, e^{-2i\beta}\left(r_{10}\, r_{12} e^{-2i\beta}\right)^2 E_{\rm i}\,, \tag{2.20b}$$

and so on . . . .

Clearly, these terms form a geometric series that can be summed to give:

$$(E_{t1})_{10} + (E_{t2})_{10} + (E_{t3})_{10} + \cdots = \frac{t_{10}\, t_{01}\, r_{12}\, e^{-2i\beta}}{1 - r_{10}\, r_{12} e^{-2i\beta}}\, E_{\rm i}\,. \tag{2.21}$$

This, along with Eq. 2.18a, can be substituted in Eq. 2.17 to yield:

$$R_{012} = r_{01} + \frac{t_{10}\, t_{01}\, r_{12}\, e^{-2i\beta}}{1 - r_{10}\, r_{12} e^{-2i\beta}} = \frac{r_{01} + r_{12}\, e^{-2i\beta}}{1 + r_{01}\, r_{12}\, e^{-2i\beta}}\,, \tag{2.22}$$

where the latter equality can be reached by utilizing relations between r_{10} and r_{01}, and between t_{10} and t_{01} that may be obtained from Eqs. 2.9 and 2.10.

One can obtain a similar formula for the transmission coefficients for this system. It reads (as in Ref. [93]):

$$T_{012} = \frac{t_{01}\, t_{12}\, e^{-i\beta}}{1 + r_{01}\, r_{12}\, e^{-2i\beta}}\,. \tag{2.23}$$

The formula given for R_{012} in Eq. 2.22 is known as Airy's formula [105, p. 362]. By utilizing Snell's law (Eq. 2.6) and the two-medium Fresnel coefficients (Eqs. 2.9 and 2.10), the ratio $(R_{012})_{\mathrm{p}}/(R_{012})_{\mathrm{s}}$ can be expressed as a function of the angle of incidence ϕ_0, the film thickness d, and the refractive indices N_{0-2} of the ambient, the film and the substrate, respectively. Usually, the refractive index of the substrate is obtained independently, so it can be regarded as a known parameter. So, unless the film thickness is known from other sources, there remain three degrees of freedom which are the film thickness and the real and the imaginary parts of the film refractive index. Unlike the simplest case of a bare substrate measurement, it turns out that these cannot be determined uniquely from the measured ψ and Δ. In order to circumvent this problem, SE measurements are usually taken at a wide range of wavelengths (e.g., over the visible spectrum; 400 nm - 700 nm), hence the name "spectroscopic". We will describe this in more detail in the next section.

2.6 Models for the refractive index

The trick of extracting the refractive index and the film thickness from the SE raw measurements lies in assuming a model form for the dispersion of the refractive index (or the dielectric function) that contains a number of parameters [94]. ψ and Δ are measured as a function of the wavelength λ of the incident light. The parameters in the model, along with the film thickness if it is to be calculated too, are treated as fitting parameters so that the complex ratio $(R_{012})_{\mathrm{p}}/(R_{012})_{\mathrm{s}}$ best reproduces the spectrum of the raw measurements.

To quantify this, usually one is interested in minimising the mean squared error (MSE) between the measured data and the model, which is defined as

$$\mathrm{MSE} = \frac{1}{N-M-1}\sum_{n=1}^{N}\left(\rho_{\mathrm{exp}}(\lambda_n) - \rho_{\mathrm{model}}(\lambda_n;\{\alpha_m\})\right)^2, \tag{2.24}$$

where N is the total number of the data points, and M is the number of fitting parameters $\{\alpha_m\}$ that are in the model. So the expression $N-M-1$ gives the effective number of degrees of freedom. λ_n, ρ_{exp} and ρ_{model} are the wavelength of the n^{th} point, the measured and the modeled ratios of the Fresnel coefficients, respectively. Nonlinear fitting algorithms are commonly used in order to fit the data. Such algorithms are implemented in a number of computational packages like *Mathematica*.

If the experimental errors in the SE measurements are accessible, one can more rigorously look for a good fit by finding the parameters $\{\alpha_m\}$ that minimize instead the reduced χ^2 measure, where the summand in Eq. 2.24 is weighted by σ_n^{-2}, with σ_n being the error in $\rho_{\mathrm{exp}}(\lambda_n)$.

There is no unique model for the dispersion of the refractive index. One can find different models adopted in the literature that vary in their degree of complexity. Examples of these models include the Lorentz model, the Sellmeier model, the Cauchy model, and the Drude model; we describe each briefly below.

2.6.1 Lorentz model

The Lorentz model is based on the classical picture that the electron acts as a damped oscillator which is bound to its nucleus by a spring. The electric field of the incoming electromagnetic wave interacts with the electron as a driving force oscillating it. Within this picture, the equation of motion of the electron can be simply solved, parametrized by the damping coefficient Γ and the spring resonant frequency ω_0. Hence, the complex dielectric function (as a function of the frequency of the incoming wave) is given by [94]:

$$\varepsilon(\omega) = 1 + \frac{e^2 N_e}{\epsilon_0 m_e}\frac{1}{(\omega_0^2-\omega^2)+i\Gamma\omega}, \tag{2.25}$$

where e, N_e, ϵ_0 and m_e are the electron charge, the number of electrons per unit volume, the permittivity of free space, and the electron mass, respectively.

Practically, the model is summed over more than one oscillator and often expressed as a function of the energy E (or the wavelength) rather than the frequency of the incoming wave:

$$\varepsilon(E) = 1 + \sum_j \frac{\alpha_j}{(E_{0j}^2 - E^2) + i\Gamma_j E}\,, \tag{2.26}$$

where j is the index of the j^{th} oscillator, and α_j, E_{0j} and Γ_j are fitting parameters.

The refractive index N is related to the complex dielectric function $\varepsilon = \varepsilon_1 - i\varepsilon_2$ by

$$N = \sqrt{\varepsilon} = n - ik\,, \tag{2.27a}$$

$$\Rightarrow n = \frac{1}{\sqrt{2}}\sqrt{\sqrt{\varepsilon_1^2 + \varepsilon_2^2} + \varepsilon_1}\,, \tag{2.27b}$$

$$\Rightarrow k = \frac{1}{\sqrt{2}}\sqrt{\sqrt{\varepsilon_1^2 + \varepsilon_2^2} - \varepsilon_1}\,. \tag{2.27c}$$

2.6.2 Sellmeier model

The Sellmeier model [106] is widely used to model the dispersion of the refractive index, see for example Refs. [99, 102]. It can be expressed as [94]

$$n(\lambda) = \left(A + \sum_j \frac{B_j \lambda^2}{\lambda^2 - C_j^2}\right)^{1/2}\,, \tag{2.28}$$

with A, B_j and C_j being the fitting parameters.

This model is often used for ranges of wavelengths in which the material is transparent (i.e., absorption is negligible and the refractive index is purely real), such as the visible and near infrared range in the case of BTO. In fact, the Lorentz model reduces to the Sellmeier model when Γ_j in Eq. 2.26 is set to zero.

2.6.3 Cauchy model

The Cauchy dispersion model is one of the simplest models that is often adopted in SE data analysis, as in Refs. [73, 100, 101, 103, 107]. It is expressed as

$$n(\lambda) = A + \frac{B}{\lambda^2} + \frac{C}{\lambda^4} + \cdots , \tag{2.29}$$

with A, B and C being the fitting parameters.

Actually, this model is an approximation to the Sellmeier model, and can be obtained by performing a series expansion of Eq. 2.28.

2.6.4 Drude Model

The Drude model is widely used for materials that have free carriers (e.g. metals). It can be expressed as [95]:

$$\varepsilon(E) = 1 - \sum_j \frac{\alpha_j}{E^2 - i\Gamma_j E} . \tag{2.30}$$

This equation can be obtained from the Lorentz model by setting the spring resonant frequency to zero.

The summation in Eqs. 2.26, 2.28, 2.29 and 2.30 usually requires only few terms to reach a good fit. In the Cauchy model for example, often the summation is terminated at the quartic term.

2.7 Models for the film structure

In the schematic figure Fig. 2.2, the refractive index of each medium, including that of the film, is assumed to be spatially homogeneous. In reality, the mismatch strain that the film experiences can be relieved along the growth direction (the z direction), implying non-homogeneity of the film and, in particular, this can be pronounced in the region near the surface where surface relaxations can occur. Also, if the film is thick enough, there could exist some intermediate regions where the film has bulk-like structure. Furthermore, unlike the schematic illustration in Fig 2.2, the surface of the film may exhibit roughness, which adds to the complexity of the problem. Thus, in general, due to the non-homogeneity of the film, one should consider that the refrac-

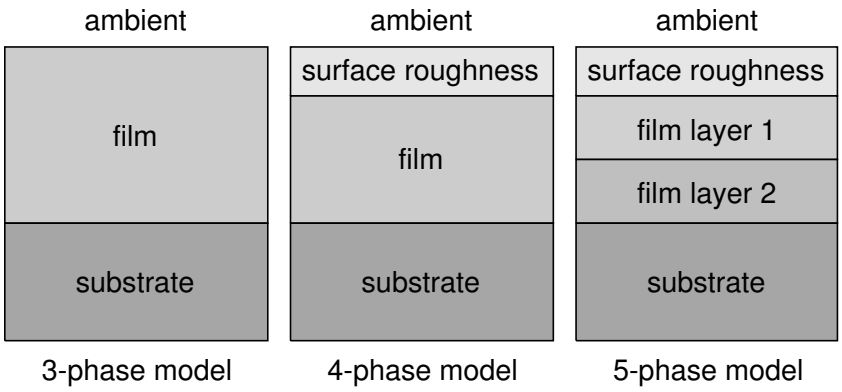


Figure 2.3: Schematic diagram showing some of the possible structural models of different complexity that are adopted for the film in order to extract its optical spectra from the raw SE data.

tive index of the film is also not homogeneous and is a function of z (or most generally, a function for $\mathbf{r}$) rather than being uniform.

So in the analysis of the SE data, an additional step is to adopt a certain structural model for the film [94] in order to increase the reliability of the calculated optical spectra. Usually a multi-phase model is adopted in the literature in which the thin film is assumed to be composed of distinct layers, see Fig. 2.3. For example, a 3-phase model is adopted in Refs. [83, 100, 108], a 4-phase model is adopted in Refs. [82, 84, 101, 103, 107], and a 5-phase model is adopted in Ref. [79].

Within the multi-phase model, each phase is assumed to have a certain thickness and a certain homogeneous value of the refractive index. As mentioned above, in order to extract the optical spectra from the raw SE measurements, a theoretical expression for the Fresnel coefficients is needed. While Eqs. 2.9 and 2.10 can be used for the case of a homogeneous infinitely thick film, and Eq. 2.22 is the generalization for a homogeneous film of finite thickness deposited on a substrate, further generalization is necessary in order to perform the data fitting for more complicated models for the film.

In fact, following the same procedure that we showed in Sec. 2.5, we have generalized Eqs. 2.22 and 2.23 and derived the Fresnel coeffiicients for an arbitrary number of layers (phases) in the multi-phase model. Let us first introduce

new notations for the Fresnel coefficients that correspond to reflection from / transmission through m layers (not counting the ambient phase (layer number 0), but counting the substrate phase (layer number m)), as follows:

$$R^{(m)} \equiv R_{0123\cdots m}\,, \tag{2.31a}$$
$$R'^{(m)} \equiv R_{m\cdots 210}\,, \tag{2.31b}$$
$$T^{(m)} \equiv T_{0123\cdots m}\,, \tag{2.31c}$$
$$T'^{(m)} \equiv T_{m\cdots 210}\,, \tag{2.31d}$$

where the subscripts have the same meaning as explained in Sec 2.3 and Sec 2.5. Then the Fresnel coefficients for m layers, can be given in terms of the coefficients for $m-1$ layers by the following recursive relations:

$$R^{(m)} = R^{(m-1)} + \frac{T^{(m-1)}\,T'^{(m-1)} r_{(m-1)m} e^{-2i\beta_{m-1}}}{1 - R'^{(m-1)} r_{(m-1)m} e^{-2i\beta_{m-1}}}\,, \tag{2.32a}$$
$$T^{(m)} = \frac{T^{(m-1)} t_{(m-1)m} e^{-i\beta_{m-1}}}{1 - R'^{(m-1)} r_{(m-1)m} e^{-2i\beta_{m-1}}}\,. \tag{2.32b}$$

$R'^{(m)}$ and $T'^{(m)}$ can be obtained from $R^{(m)}$ and $T^{(m)}$ by reversing the order of the subscripts, as defined in Eqs. 2.31b and 2.31d.

If a model with m layers is adopted, one is then interested in fitting to:

$$\rho_m \equiv \frac{R_p^{(m)}}{R_s^{(m)}} = \tan\psi\, e^{i\Delta}\,, \tag{2.33}$$

as a generalization to Eq. 2.16. Once again, the ratio ρ_m can be expressed in terms of the angle of incidence, the refractive indices of the constituent phases and their thicknesses.

In the multi-phase model, usually layer 1 (the layer in contact with the ambient) is taken to represent the surface roughness of the film, as in Ref. [73]. Different schemes are used in the literature to model the refractive index of this layer. For example, it is assumed to be independent of the wavelength of the incoming light, and hence it is just a constant obtained from the stan-

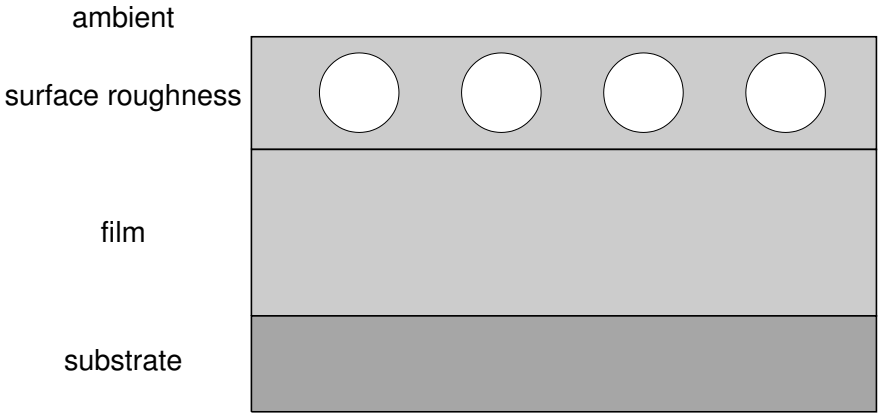


Figure 2.4: A schematic diagram illustrating the idea of the effective medium approach. In this example, the surface roughness layer is modelled by assuming that it is consisting of the film material embedded with spherically-shaped voids of the ambient environment.

dard fitting procedure, as in the previous reference. Alternatively, this layer can be treated as an effective inhomogeneous medium whose refractive index is a "mixture" of the refractive indices of the layers above and below it (See Fig. 2.4). This latter approach is referred to as the "effective medium approximation" approach and is explained in more detail in Ref. [95], and applications of it can be found for example in Ref. [109]. Generally, the average dielectric constant of the effective medium $\langle\varepsilon\rangle$ can be obtained by

$$\frac{\langle\varepsilon\rangle - \varepsilon_h}{\langle\varepsilon\rangle + \gamma\varepsilon_h} = \sum_j f_j \frac{\varepsilon_j - \varepsilon_h}{\varepsilon_j + \gamma\varepsilon_h}\,, \tag{2.34}$$

where ε_h is the dielectric constant of a chosen host medium, γ is a constant depending on the shape of the constituent media included (e.g., it equals 2 for spherically shaped constituents), and f_j is the volume fraction of the j^{th} constituent medium. Different flavours exist for this approximation depending on the choice of ε_h, these include the Lorentz-Lorentz, the Maxwell-Garnett, and the Bruggeman models.

2.8 Depolarizing films

Once a model is chosen for the film and for the optical properties (like the refractive index) for each phase within the film, the fitting procedure can be performed to find the desired optical functions and/or the thicknesses of each phase of the film. The fitting procedure is however not very straightforward and several sources of error can influence the reliability of the results [94]. For example, if the structural model (often called the optical model) of the film is too simple, it is often not possible to minimize the MSE (see Sec. 2.6) to a reasonable value. A similar problem occurs if the model for the refractive index or the dielectric function are not appropriate for the particular film (or energy window) under study.

Another source of error emerges when the sample depolarizes the light. Depolarization is attributed to several factors, such as the non-uniform thickness of the sample and the scattering of the incident wave, as in the ZnO films studied in Ref. [110]. As mentioned above, the core idea of SE is to measure the relative parallel and perpendicular polarizations of the reflected light and to fit it to a theoretical expression for the Fresnel coefficients. If the sample depolarizes the light, then the expressions for the Fresnel coefficients derived above are no longer valid. This problem is traditionally dealt with via the Mueller-Stokes formalism [95], where the polarization state of the light beam is expressed in terms of some relevant intensities and mathematically expressed as a four-component vector referred to as a Stokes vector $\mathbf{S}$, which can be expressed as

$$\mathbf{S} \equiv \begin{pmatrix} \langle E_{0x}^2 \rangle + \langle E_{0y}^2 \rangle \\ \langle E_{0x}^2 \rangle - \langle E_{0y}^2 \rangle \\ \langle 2E_{0x}E_{0y}\cos\delta \rangle \\ \langle 2E_{0x}E_{0y}\sin\delta \rangle \end{pmatrix}, \tag{2.35}$$

where E_{0x} and E_{0y} are the x and the y components of the electric field vector of an electromagnetic wave travelling parallel to the z direction, and δ is the phase difference between the two components. The symbol $\langle\rangle$ denotes the time average.

As opposed to the two-component Jones vector $\mathbf{J}$ [111], which can be expressed as

$$\mathbf{J} \equiv \begin{pmatrix} E_{0x} \\ E_{0y}e^{i\delta} \end{pmatrix}, \tag{2.36}$$

Stokes vector can describe the range of fully polarized light to non-polarized light, and hence are used to deal with depolarizing films. The analogues of Jones matrices in this case are referred to as Muller matrices, where the system (in this case, the modelled thin film) has a specific Muller matrix that describes its interaction with the incoming wave and hence can be used to obtain the corresponding Fresnel coefficients for a depolarizing film.

2.9 Criticism

As we have described in the previous sections, SE is an indirect method. Hence, even if very accurate measurements were performed, this does not necessarily lead to accurate data for the fitted optical function of the film. We have already alluded to, in Sec. 2.8, some of the error sources that are present in the calculation of the film refractive index and thickness. In fact, each step required to extract optical data from the raw measurements, namely:

1. The choice of the structural model of the film.

2. The choice of the analytical model for the refractive index or the dielectric function of each layer within the structural model.

3. Fitting the data.

has a number of limitations that can affect the reliability of the calculated data. In fact, to choose a valid structural model one needs a good guess or a prior knowledge of the structure of the film. Actually, obtaining a "good" fit does not necessarily imply the validity of the chosen models or the extracted data.

To further illustrate this idea, we consider a thin film of $Ba_{0.5}Sr_{0.5}TiO_3$ of growth thickness of 113 nm deposited on an MgO substrate. The film growth and the SE measurements of ψ and Δ are performed by a collaborating experimental group [112]. We have performed the nonlinear fitting procedure using the "NonlinearModelFit" built-in package implemented in *Mathematica*.

Eq. 2.33 has been used and two different structural models have been considered; a 4-phase model (air/surface roughness/film/substrate), and a 5-phase model (air/ surface roughness/ film(layer1)/ film(layer2)/substrate), see Fig. 2.3. The data are available for wavelengths in the range of 400-1600 nm, for which the material is transparent. Hence the refractive index of each layer of the film is modelled via the Cauchy dispersion model (Eq. 2.29). The refractive index of the surface roughness layer is assumed to be wavelength independent as in Ref. [73]. The refractive index of the substrate is measured independently and obtained from our collaborators. It is also modelled using the profile of Cauchy dispersion. We show in Fig 2.5 the fitted curves for ψ and Δ for the two models used together with the experimental data. The figure clearly shows that the fitting, in both cases, is excellent. The MSE (defined in Eq. 2.24) is calculated for both curves as follows:

$$\mathrm{MSE} = \frac{1}{N-M-1}\sum_{n=1}^{N}\left((\psi_{\mathrm{exp}}-\psi_{\mathrm{model}})^2+(\Delta_{\mathrm{exp}}-\Delta_{\mathrm{model}})^2\right). \qquad (2.37)$$

The corresponding MSE values for the 4-phase and the 5-phase models are 9.7 and 0.03, respectively, with the lower value of the latter indicating a better fit. These values are relatively good as compared to Ref. [73], where similar system and models are adopted. An even better fit can be achieved if the first couple of points in the short wavelength side are excluded[5].

The extracted optical data (shown in Fig 2.6), however, for the two cases differ a lot. In fact, the behaviour of the refractive index curve of film layer 2 in the 5-phase model shows a significant qualitative discrepancy compared to the other curves shown in the same figure, and the behaviour may even be considered to be non-physical where it increases with wavelengths beyond ~ 600 nm.

As for the extracted thicknesses (summarized in Table 2.1), the two models almost agree on the total thickness (the sum of the thicknesses of the constituent layers) as well as on the thickness of the surface layer. Both values actually almost agree with the growth thickness quoted above. This agreement may provide reassurance in the reliability of the fitted curves and the

[5]For short wavelengths, BTO starts to be absorbant. Therefore, the refractive index starts to deviate from the Cauchy model, resulting in worsening the fit.

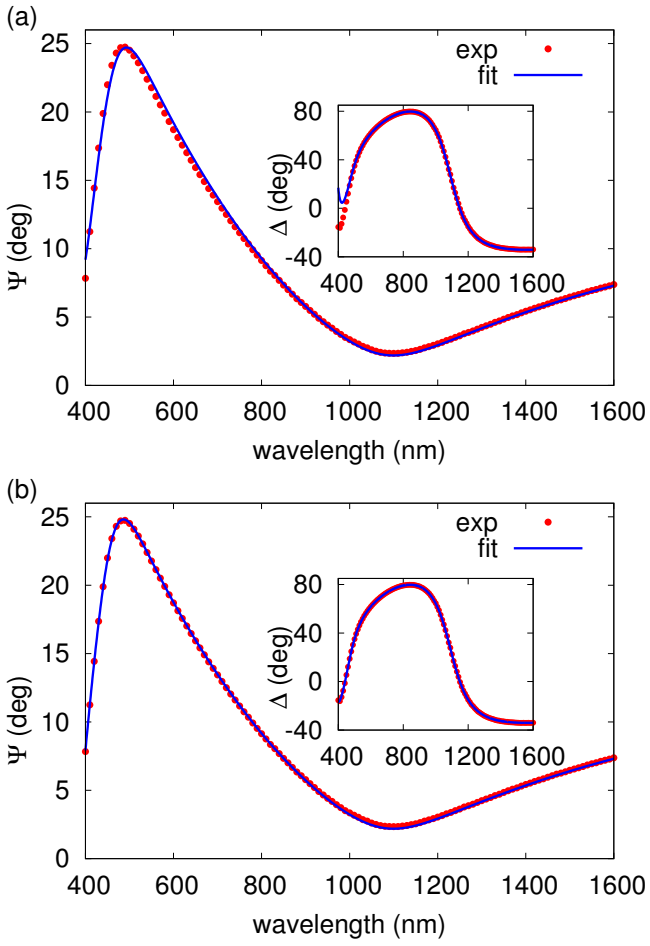


Figure 2.5: The fitted curves of ψ and Δ as compared to the measured values. A 4-phase and a 5-phase models are adopted in (a) and (b), respectively. The corresponding MSE value for the two cases is given in the main text.

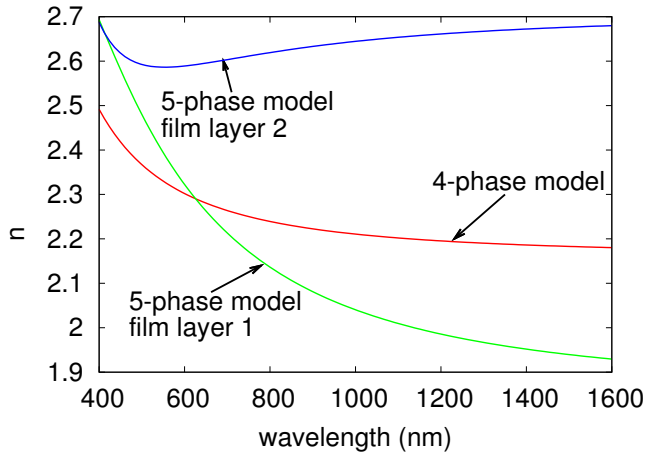


Figure 2.6: The extracted refractive indices of the constituent layers of the 4-phase and the 5-phase models.

extracted data, but we have shown that this cannot be the case in the situation that we have addressed above, as the 5-phase model, whose calculated thickness is closest to the growth thickness, results in non-physical behaviour of the refractive index, and therefore considered to be an invalid model.

To summarize: the point of the above discussion is to reiterate the idea that SE data analysis involves a number of problems and limitations. We mainly shed light on two points: 1. Obtaining a good fit does not necessarily mean that the calculated optical functions and thicknesses are correct, and 2. different structural models that well fit the SE data can lead to different optical functions for the film.

Sometimes, a "global" fit is performed in order to increase the confidence in the results by increasing the number of data points but retaining the same number of fitting parameters. For example, different sets of ψ and Δ data that correspond to different angles of incidence are fitted simultaneously using the same models and fitting parameters (as applied in Ref. [73]).

The global fit, however, is not guaranteed to eliminate the problems that we have discussed above. Actually, the fits and the corresponding refractive indices of the 5-phase model that we have shown in Figs. 2.5 and 2.6 indicate that the manifold formed by the fitting parameters is quite complicated that makes reaching a global minimum quite hard. To further support this idea, we show in Fig. 2.7 another 5-phase model fit, obtained by a different initial

	4-phase model	5-phase model	5-phase model (2^{nd} fit)
Surface roughness	33.6	28.2	40.7
Film (ℓ_1)	94.8	60.0	45.9
Film (ℓ_2)	—	23.1	11.7
Total film thickness	128.4	111.3	98.3

Table 2.1: The fitted thicknesses (in nm) of the constituent layers of the 4-phase and the 5-phase models. ℓ_1 and ℓ_2 stand for layer 1 and layer 2 of the film, respectively, as depicted in Fig. 2.3. The sum of the thicknesses of the constituent layers is given in the last row. The second and the third columns correspond to the fits shown in Fig. 2.5, while the last column correspond to the fit shown in Fig. 2.7.

guess of the fitting parameters. This fit corresponds to an MSE value of 4.3, indicating a better fit than the 4-phase-model fit shown in Fig. 2.5. However, it obviously corresponds to a case of falling at a local minimum, and it leads to refractive indices that are non-physical and significantly differ, quantitatively and qualitatively, from the other two fits, despite that the calculated total thickness of the film, tabulated in Table 2.1, do not differ a lot from the other two (though the surface roughness layer is quite thick).

Actually, certain "flavours" of global fit may indicate more problems in the process. Sometimes, datasets that correspond to films of different thicknesses are fitted simultaneously assuming that the refractive index of the film is *independent* of its thickness, as in Ref. [73]. The results obtained by this procedure may be in contradiction with the case of fitting each dataset individually, where the refractive index of the film can show a dependence on its thickness, as in Ref. [82].

2.10 Motivations for handling the problem from first-principles

The problems and limitations, discussed in the previous section, of the SE technique, which is the most widely-used experimental method in finding the optical functions of thin films, lead us to investigate the problem from first-

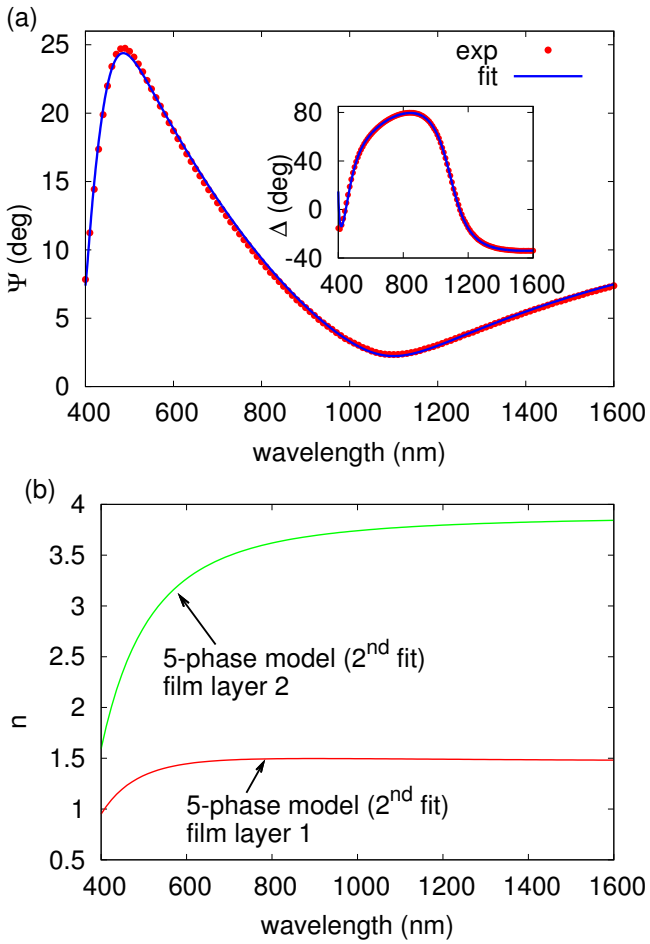


Figure 2.7: The fitted and measured values of ψ and Δ **(a)**, and the corresponding refractive indices **(b)** of a 5-phase model. In this figure, the fitting parameters reached alternative local minimum of the MSE, slightly higher than that of the earlier fit shown in Fig. 2.5, but lower than the 4-phase model fit. In spite of the excellent fit, the refractive indices are non-physical and significantly different than those obtained from the earlier fit.

principles. In *ab initio* calculations, one can model the thin film as a bulk material subjected to a number of structural perturbations such as epitaxial strain and other factors discussed earlier in Sec. 1.4.1. This treatment enables the disentanglement of the individual factors and permits us to study the effect on the optical properties of each factor independently. This will help shed more light on, and allow a deeper understanding of, the problem. A comparison study between these individual effects can provide very useful answers to how to better engineer the optical properties of the films under study. The approach of first-principles calculations has also a number of limitations that we shall address and discuss in the relevant context.

In the next chapter, we will give an overview of the density functional theory, the theory of the *ab initio* calculations that we are using throughout our work in this thesis.

Chapter 3

First Principles Approach; Density Functional Theory

3.1 Overview

Most of the properties of materials are determined by the electrons therein. Equilibrium crystal structure, electrical conductivity, superconductivity, magnetism, elastic constants, and optical properties are only a few examples [113].

It is known from the very postulates of quantum mechanics that all the properties of a system, like the ones mentioned above, are embedded in the wavefunction of the system. The role of first principles calculations is to approach the problem of "finding" this wavefunction, employing a set of approximations that, on the one hand, makes the problem tractable, and on the other hand are not specifically dependent on the system under study, and do not rely on any parameterization based on experimental measurements.

A lot of effort has been spent in order to tackle this problem, and different approaches of different applicabilities and accuracies now exist. These include the quantum Monte Carlo method (QMC) [114], Hartree-Fock theory [115], and density functional theory (DFT) [116, 117].

In this chapter, we shall focus on the latter approach, on which all the first-principles calculations performed in this thesis are based. We shall describe the theory showing the key approximations that made the problem tractable, and give an overview of the technical details that are involved in the application of this method. In later chapters, we shall describe how calculations of optical

properties may be performed based on DFT.

3.2 The many-body Schrödinger equation

In the non-relativistic limit, the time independent many-body Schrödinger equation of a system of electrons and nuclei that make up a material, such as a solid or a molecule, reads:

$$\widehat{H}\Psi = E\Psi\,, \tag{3.1}$$

where Ψ is the wavefunction of the system (which is a function of all the electronic and the nuclear positions), E is the total energy of the system, and $\widehat{H}$ is the Hamiltonian operator that is given by[1]

$$\begin{aligned}\widehat{H} = &\sum_{\alpha} -\frac{1}{2M_\alpha}\nabla^2_{\mathbf{R}_\alpha} + \sum_{i} -\frac{1}{2}\nabla^2_{\mathbf{r}_i} - \sum_{i}\sum_{\alpha}\frac{Z_\alpha}{|\mathbf{r}_i - \mathbf{R}_\alpha|} \\ &+ \frac{1}{2}\sum_{i}\sum_{j\neq i}\frac{1}{|\mathbf{r}_i - \mathbf{r}_j|} + \frac{1}{2}\sum_{\alpha}\sum_{\beta\neq\alpha}\frac{Z_\alpha Z_\beta}{|\mathbf{R}_\alpha - \mathbf{R}_\beta|},\end{aligned} \tag{3.2}$$

where the first two terms stand for the kinetic energy of the nuclei and the electrons, respectively. The remaining terms stand for the electrostatic potential energy of the electrons-nuclei, the electrons-electrons, and the nuclei-nuclei interactions, respectively. The positions of the i^{th} electron and the α^{th} nucleus are denoted by $\mathbf{r}_i$ and $\mathbf{R}_\alpha$, respectively. M_α and Z_α stand for the mass, and the atomic number of the α^{th} nucleus, respectively.

However, Eq. 3.1 is a second order inseparable differential equation that cannot be solved analytically in practice but for very simple systems (such as the hydrogen atom). Finding an exact solution to this equation for macroscopic systems is completely out of reach (e.g., a small piece of solid contains an order of Avogadro number ($\sim 10^{23}$) of electrons and nuclei) . Therefore, approximations need to be made to approach the problem. Such approximations shall be discussed in the following sections.

[1] It should be noted that Hartree atomic units are adopted in this equation and throughout this thesis, where $\hbar = e = m_e = 4\pi\varepsilon_0 = 1$.

3.2.1 Born-Oppenheimer approximation

Nuclei are much more massive than electrons. The proton to electron mass ratio is about 1836. Keeping in mind that both electrons and nuclei feel similar electrostatic forces due to their similar absolute charges, this indicates that nuclei move far slower than the electrons. Then, it is reasonable to assume, in the time scale of the electronic motion, that the nuclei are frozen at a certain configuration, and the wavefunction of the system is represented by the electronic wavefunction Φ that depends only *parametrically* on the positions of the nuclei. This approximation is referred to as the Born-Oppenheimer approximation [118], where the nuclear and the electronic degrees of freedom are separated, allowing the wavefunction of the coupled system Ψ to be approximated as

$$\Psi(\{\mathbf{r}_i\},\{\mathbf{R}_\alpha\}) = \chi(\{\mathbf{R}_\alpha\})\Phi(\{\mathbf{r}_i\};\{\mathbf{R}_\alpha\})\,, \tag{3.3}$$

with $\chi(\{\mathbf{R}_\alpha\})$ being the nuclear wavefunction. The electronic wavefunction Φ is required to be eigenstate for the "electronic" Hamiltonian ($\widehat{H}^{\mathrm{el}}$) in a static array of nuclei:

$$\begin{aligned}\widehat{H}^{\mathrm{el}} = &\sum_i -\frac{1}{2}\nabla^2_{\mathbf{r}_i} - \sum_i\sum_\alpha \frac{Z_\alpha}{|\mathbf{r}_i-\mathbf{R}_\alpha|} \\ &+ \frac{1}{2}\sum_i\sum_{j\neq i}\frac{1}{|\mathbf{r}_i-\mathbf{r}_j|} + \frac{1}{2}\sum_\alpha\sum_{\beta\neq\alpha}\frac{Z_\alpha Z_\beta}{|\mathbf{R}_\alpha-\mathbf{R}_\beta|},\end{aligned} \tag{3.4}$$

and the problem is now transferred to solving for the electronic wavefunction Φ:

$$\widehat{H}^{\mathrm{el}}\Phi\left(\{\mathbf{r}_i\};\{\mathbf{R}_\alpha\}\right) = E(\{\mathbf{R}_\alpha\})\Phi\left(\{\mathbf{r}_i\};\{\mathbf{R}_\alpha\}\right). \tag{3.5}$$

The "electronic" energy $E(\{\mathbf{R}_\alpha\})$ in the equation above depends on the nuclear degrees of freedom. In fact, the nuclear wavefunction $\chi(\{\mathbf{R}_\alpha\})$ satisfies a Schrödinger in which $E(\{\mathbf{R}_\alpha\})$ acts as the potential. Full detail can be found in e.g., Ref. [113, pp. 482-484].

Within the Born-Oppenheimer approximation, the last term in this Hamiltonian, namely the nuclear-nuclear interaction term, is just a numerical constant that depends merely on the nuclei configuration, and contributes to the

total energy as an additive constant. For simplicity, we will drop it in what follows and assume that it is included in the total energy.

Although the nuclei positions are no longer treated quantum mechanically in this approximation, it is still possible to study the dynamics of the nuclei classically (following Newtonian mechanics), thanks to the knowledge of the quantum mechanical forces that act on the atoms [119, 120]. The electrons in the system will instantaneously respond to the movements of the nuclei and stay always in their ground state, according to this approximation. This kind of study is often referred to as "quantum molecular dynamics" or "*ab initio* molecular dynamics". We shall describe later in this chapter the theory involved in calculating the quantum mechanical atomic forces.

The Born-Oppenheimer approximation is a very common and successful approximation in simplifying the problem of solving Eq. 3.1, even if it can go wrong in certain situations [121]. However, the problem of solving the many-body Schrödinger equations remains practically unsolvable even in the form of Eq. 3.5. Still more has to be done.

3.3 The formulation of density functional theory

Density functional theory [116,117] is one of the most successful theories in the field of electronic structure calculations. Since its foundation in 1964, and with the magnificent development of the algorithms and computing capabilities over the years, the application of DFT has been growing tremendously in a variety of scientific fields, from condensed matter theory to biological chemistry. There exist a number of computational packages that implement this theory with approximations of different flavours that makes its application quite accurate, robust and less computationally demanding compared to other methods such as quantum Monte Carlo. Examples of these packages include: QUANTUM ESPRESSO [122], ABINIT [123–125], CASTEP [126] and ONETEP [127].

3.3.1 Hohenberg-Kohn theorems

The key quantity of DFT is the electronic number density $n(\mathbf{r})$. For an N electron system with an electronic wavefunction of $\Phi(\mathbf{r}_1, \mathbf{r}_2, \cdots, \mathbf{r}_N)$, the electronic

density at some point $\mathbf{r}$ in the system is defined as

$$n(\mathbf{r}) = \int \left|\Phi\left(\mathbf{r}_1, \mathbf{r}_2, \cdots, \mathbf{r}_N\right)\right|^2 \sum_i \delta\left(\mathbf{r} - \mathbf{r}_i\right) d\mathbf{r}_1 d\mathbf{r}_2 \cdots d\mathbf{r}_N \,, \tag{3.6}$$

and is integrated to give the total number of electrons in the system (if the wavefunction Φ is normalized):

$$\int n(\mathbf{r}) d\mathbf{r} = N \,. \tag{3.7}$$

In 1964, Hohenberg and Kohn proved two theorems upon which DFT is based [116]. The first theorem states that for a system of interacting electrons put under the influence of some external potential $V_{\text{ext}}(\mathbf{r})$[2], the potential $V_{\text{ext}}(\mathbf{r})$ is a unique functional[3] (up to an arbitrary constant) of the ground state electronic density of the system $n_0(\mathbf{r})$. In other words, no two external potentials, that differ by more than a constant, can yield the same value of the ground state density, so, the external potential $V_{\text{ext}}[n(\mathbf{r})]$ is *uniquely* determined by $n_0(\mathbf{r})$.

In the second theorem, Hohenberg and Kohn showed that there exists an energy functional $E[n(\mathbf{r})]$ that has a global minimum value equal to the ground state energy of the system E_0, and that the global minimum occurs at the ground state density of the system: $E[n_0(\mathbf{r})] = E_0$. The energy functional is defined by

$$E[n(\mathbf{r})] \equiv F[n(\mathbf{r})] + \int V_{\text{ext}}(\mathbf{r}) n(\mathbf{r}) d\mathbf{r} \,. \tag{3.8}$$

The functional F in the above equation is a *universal* functional that represents the kinetic energy and the interaction energy of the electrons. The term "universal" means that it is independent of the external potential, so if it is known once, then, in principle, its form does not change if the external potential changes. Conveniently, one can "separate out" the self Coulomb interactions of the density from F:

[2]In the case of electrons in a solid, the external potential is the attractive Coulomb potential due to the nuclei.

[3]A "function" takes a number and maps it into another number. A "functional" takes a function and maps it into a number. So a functional can be thought of as a function of a function.

$$F[n(\mathbf{r})] = \frac{1}{2}\iint \frac{n(\mathbf{r})n(\mathbf{r}')}{|\mathbf{r}-\mathbf{r}'|}d\mathbf{r}d\mathbf{r}' + G[n(\mathbf{r})]\,, \tag{3.9}$$

where $G[n]$ is clearly a universal functional too. The first term in the right hand side of the equation above is referred to as the Hartree energy $E_H[n]$.

The virtue of the theorems above is that instead of solving for the $3N$ dimensional complex wavefunction for a system of N electrons, it suffices to solve for the three dimensional *real* electronic density, since the density fully determines the external potential and hence the Hamiltonian. It follows that all the properties of the system are contained in the ground state density, as inferred from the first Hohenberg-Kohn theorem. Furthermore, the energy functional is variational with the density, so knowledge of $E[n]$ would enable finding the ground state energy and density of the system by minimizing $E[n]$ with respect to V-representable[4] densities $n(\mathbf{r})$, as inferred from the second Hohenberg-Kohn theorem [113].

However, although the proof provided by Hohenberg and Kohn is quite simple, it does not include information about the form of the energy functional. In addition, even if one finds a way to construct $E[n]$ and minimize it to find the ground state density, it is still not clear how some of the properties of the system are to be extracted from the knowledge of density alone (such as whether or not the material has an insulating energy gap) [113, pp. 131-132].

So, DFT in the framework described so far does not provide a great help in solving the many body problem. In fact, the following work of Kohn and Sham [117] (that we shall describe in the next section) played a major role in making DFT a useful and successful theory.

3.3.2 The Kohn-Sham framework

Kohn and Sham dealt with the original problem of a many-body system of interacting particles by mapping it into another problem of *non-interacting* electrons of the same density $n(\mathbf{r})$. They first proposed that the universal

[4] $n(\mathbf{r})$ is said to be V-representable if it is a "valid" ground state density of some external potential V_{ext}. There exist some densities that cannot be a ground state density of *any* potential, in which case they are referred to as non-V-representable.

functional $G[n]$, appearing in Eq. 3.9, can be written as

$$G[n(\mathbf{r})] = T[n(\mathbf{r})] + E_{\rm xc}[n(\mathbf{r})]\,. \tag{3.10}$$

In the equation above, $T[n]$ is the sum of the kinetic energies of the *non-interacting* electrons:

$$T[n(\mathbf{r})] = -\frac{1}{2}\sum_i \langle\psi_i|\nabla^2|\psi_i\rangle\,, \tag{3.11}$$

with ψ_i being the independent particle wavefunction of the i^{th} electron. $E_{\rm xc}[n]$ is the exchange-correlation[5] functional within which all the many-body interaction effects are embedded.

Now, one is interested in minimizing $E[n]$ subject to the constraint 3.7, namely:

$$\frac{\delta}{\delta n}\left(E[n(\mathbf{r})] - \mu\int n(\mathbf{r})d\mathbf{r}\right) = 0\,, \tag{3.12}$$

where μ is a Lagrange multiplier. Substituting for $E[n]$ from Eq. 3.8, Eq. 3.9 and Eq. 3.10, one gets, after taking the functional derivative:

$$\frac{\delta T[n(\mathbf{r})]}{\delta n} + \int\frac{n(\mathbf{r}')}{|\mathbf{r}-\mathbf{r}'|}d\mathbf{r}' + V_{\rm ext}(\mathbf{r}) + \frac{\delta E_{\rm xc}[n(\mathbf{r})]}{\delta n} - \mu = 0\,, \tag{3.13}$$

or

$$\frac{\delta T[n(\mathbf{r})]}{\delta n} + V_{\rm eff}(\mathbf{r}) = \mu\,, \tag{3.14}$$

where

$$V_{\rm eff}(\mathbf{r}) \equiv \int\frac{n(\mathbf{r}')}{|\mathbf{r}-\mathbf{r}'|}d\mathbf{r}' + V_{\rm ext}(\mathbf{r}) + \frac{\delta E_{\rm xc}[n(\mathbf{r})]}{\delta n}\,. \tag{3.15}$$

In fact, if one considers a system of non-interacting electrons moving in an external potential of $V_{\rm eff}(\mathbf{r})$, The Euler-Lagrange equation of the system

[5]Electrons interact with each other in two ways: 1. through electrostatic Coulomb repulsion, which is referred to as electron *correlation*, and 2. through the Pauli exclusion principle that forbids any two electrons from occupying the same state. The latter results from the anti-symmetry of the electronic wavefunction that changes sign when two particles swap positions, and is usually referred to as the *exchange* interaction. Both exchange and correlation act in keeping the electrons away from each other.

has exactly the same form of Eq. 3.14. Hence, the density of the real system $n(\mathbf{r})$ can be obtained by simply solving the independent electron Schrödinger equations for the orbitals ψ_i:

$$\left(-\frac{1}{2}\nabla^2 + V_{\text{eff}}(\mathbf{r})\right)\psi_i(\mathbf{r}) = \varepsilon_i\psi_i(\mathbf{r})\,, \tag{3.16}$$

and the density is therefore given by

$$n(\mathbf{r}) = \sum_i |\psi_i(\mathbf{r})|^2\,. \tag{3.17}$$

So, the original many-body Schrödinger equation of a system of N interacting electrons is now mapped *exactly* to a set of N one-electron equations, usually known as the Kohn-Sham equations.

It should be noted that Eqs. 3.16 and 3.17 should be solved self-consistently. Clearly, the density defines the effective potential $V_{\text{eff}}(\mathbf{r})$ through Eq. 3.15, $V_{\text{eff}}(\mathbf{r})$ is in turn used to get the one-electron orbitals (or the Kohn-Sham orbitals) ψ_i, but these very orbitals define the density through Eq. 3.17. So, in practice, one usually starts with an initial guess to the density, call it $\tilde{n}_0$, proceeds to get the effective potential and hence the orbitals, and then calculates the output density defined by the orbitals (call this $\tilde{n}_1$). If $\tilde{n}_1$ is not consistent with $\tilde{n}_0$, one would start again with the new density (or, in practice, with a mixture between the new and the old densities [128]) and continue until the input and the output densities are consistent.

The above recipe is appealing, since solving the one-particle KS equations is tractable. In principle, one obtains the true ground state density of the "real" system of interacting electrons. Furthermore, accessibility to the independent-electron wavefunctions[6] may provide some insight into properties that have no clear relation with the density alone.

However, despite the success of the Kohn-Sham approach in separating all the many-body interaction effects into the exchange-correlation functional E_{xc}, the form of this functional, for an arbitrary density $n(\mathbf{r})$, unfortunately remains unknown. Hence, it is necessary to approximate it in order to solve the Kohn-Sham equations. This point shall be discussed in the following section.

[6]It is not to be understood, however, that the Kohn-Sham eigenstates correspond to the true eigenstates of the many-body interacting system.

3.3.3 The exchange-correlation functional

In fact, what makes the formalism of Kohn and Sham useful is that there exist quite simple approximations to $E_{\rm xc}$ that lead to remarkably accurate results, the most common of which are the local density approximation and the generalized gradient approximation.

The local density approximation

The local density approximation (LDA) was proposed by Kohn and Sham [117] for systems of slow varying density, where the exchange correlation functional $E_{\rm xc}$ at some point $\mathbf{r}$ is approximated to match that of a homogeneous electron gas of the same density at that point:

$$E_{\rm xc}[n(\mathbf{r})] \approx E_{\rm xc}^{\rm LDA}[n(\mathbf{r})] = \int n(\mathbf{r})\epsilon_{\rm xc}\left(n(\mathbf{r})\right) d\mathbf{r}\,, \tag{3.18}$$

with $\epsilon_{\rm xc}\left(n(\mathbf{r})\right)$ being the exchange-correlation energy per electron of the homogeneous electron gas at $\mathbf{r}$. Note that $\epsilon_{\rm xc}\left(n(\mathbf{r})\right)$ depends only on the density $n(\mathbf{r})$ at the neighbourhood of the point $\mathbf{r}$, hence the name *local*. The functional derivative appearing in Eq. 3.15 is then given by

$$\frac{\delta E_{\rm xc}^{\rm LDA}}{\delta n} = \epsilon_{\rm xc}\left(n(\mathbf{r})\right) + n(\mathbf{r})\frac{\partial \epsilon_{\rm xc}\left(n(\mathbf{r})\right)}{\partial n}\,. \tag{3.19}$$

Although there is no exact analytical formula for $\epsilon_{\rm xc}\left(n(\mathbf{r})\right)$[7], it is usually dealt with by numerically calculating it from QMC simulations, the most common of which is that performed by Ceperley and Alder [129]. In practice, to get use of the data obtained from QMC in standard DFT calculations, analytical forms of $\epsilon_{\rm xc}$ are parametrized and fitted against QMC simulations at different densities. A number of parameterization schemes are available, the one of Perdew and Zunger [130] being one of the most widely used schemes in the literature [113].

The LDA scheme is very commonly used in the literature due to its simplicity and, surprisingly, its ability to provide good results in many cases, including systems whose density is not slowly varying with position. The success of LDA may be explained through the fact that this approximation predicts the cor-

[7] Actually, the exchange part has a closed form expression, but it is the correlation part that is not generally known.

rect charge of the missing electron in the exchange-correlation hole, and it only approximates the *shape* of the hole [131, 132].

However, LDA has some well known limitations and failures. For instance, it generally overestimates the binding energy of molecules and solids [133], which results in underestimating the bond lengths and lattice constants and overestimating the bulk moduli of solids [134]. Also, LDA fails sometimes in predicting the equilibrium crystal structure of materials, as in the case of Fe [135]. Moreover, LDA fails to predict the insulating nature of some transition metal oxides such as FeO and CoO [136], where it predicts that they are metals.

In spite of these limitations however, we believe that LDA can still be sufficiently accurate for the purpose of the calculations provided in this thesis, where we are not mainly interested in the absolute values of the properties that we are calculating (like the refractive indices or the band gaps), but rather in the *trends* that these properties show under the effect of some structural perturbations. We shall be using this approximation in the DFT calculations presented throughout this thesis, unless otherwise mentioned.

The generalized gradient approximation

There are a number of attempts to go beyond LDA. The most straightforward idea is the so-called generalized gradient approximation (GGA), where the non-uniform density of the system at point $\mathbf{r}_0$ is approximated by a Taylor expansion around that point:

$$n(\mathbf{r}) = n(\mathbf{r}_0) + (\mathbf{r} - \mathbf{r}_0)\nabla n + \frac{1}{2}(\mathbf{r} - \mathbf{r}_0)^2\nabla^2 n + \dots , \tag{3.20}$$

and hence the exchange-correlation energy per electron $\epsilon_{\rm xc}$ is made dependent on the density *and* its gradients:

$$E_{\rm xc}[n(\mathbf{r})] \approx E_{\rm xc}^{\rm GGA}[n(\mathbf{r})] = \int n(\mathbf{r})\epsilon_{\rm xc}\left(n(\mathbf{r}), |\nabla n(\mathbf{r})|, \nabla^2 n(\mathbf{r}), \cdots\right) d\mathbf{r} , \tag{3.21}$$

where only the first derivative dependence is usually kept in the equation above.

There exist different parameterization schemes of $\epsilon_{\rm xc}\left(n(\mathbf{r}), |\nabla n(\mathbf{r})|\right)$, including the B88 [137], the PW91 [138], and the PBE [139] schemes.

The GGA, however, is not always better than the LDA. It also needs to be used with care due to its known limitations. For example, the GGA generally underestimates the binding energy, resulting in the overestimation of the lattice constants and underestimation of the bulk moduli of solids, in contrast to the LDA [133, 134].

Hybrid functionals

The exchange part E_{x} of the exchange-correlation functional can be directly expressed in terms of the orbitals ψ_i instead of the density n, in view of the Hartree-Fock theory (HF):

$$E_{\mathrm{x}} = -\frac{1}{2}\sum_{i,(j\neq i)}\int \frac{\psi_i^*(\mathbf{r})\psi_j^*(\mathbf{r}')\psi_j(\mathbf{r})\psi_i(\mathbf{r}')}{|\mathbf{r}-\mathbf{r}'|}\,d\mathbf{r}d\mathbf{r}'\,. \tag{3.22}$$

This expression is often referred to as the *exact-exchange* energy. In the original theory of Hartree and Fock, the orbitals ψ_i represent single-electron orbitals, from which the wavefunction of the system is built up by evaluating the Slater determinant [140], which guarantees the anti-symmetry of the wavefunction and hence the Pauli principle.

It was suggested that one can overcome some of the limitations of the LDA or the GGA functionals by "mixing" with them a portion of the exact exchange $E_{\mathrm{x}}^{\mathrm{HF}}$ [141], thus forming a *hybrid* functional. For this purpose, the Kohn-Sham orbitals are used in Eq. 3.22 instead of the HF orbitals.

This mixing, although it sounds empirical, provides a surprising success over LDA or GGA in many cases. It is, however, more computationally demanding than the normal approach.

Several mixing schemes are available that differ in the mixing ratio and the functional used. For example, the PBE0 hybrid functional [142] is defined by

$$E_{\mathrm{xc}}^{\mathrm{PBE0}} = aE_{\mathrm{x}}^{\mathrm{HF}} + (1-a)E_{\mathrm{x}}^{\mathrm{PBE}} + E_{\mathrm{c}}^{\mathrm{PBE}}\,, \tag{3.23}$$

where the subscripts x and c correspond to the exchange and the correlation parts respectively. The mixing parameter a is pre-set to 1/4, as determined from perturbation theory [143].

Another hybrid functional to mention is the HSE functional [144], which is defined as in Eq. 3.23, but uses a screened Coulomb potential to calculate the

exchange interactions and separates the long range and short range interactions via the use of an error function. The HSE functional further suggests that the long-range exchange interactions of the HF and the PBE functionals are small and tend to cancel out, thus the HSE functional is defined by neglecting them and hence can be expressed as

$$E_{\mathrm{xc}}^{\mathrm{HSE}} = aE_{\mathrm{x}}^{\mathrm{HF,SR}}(\omega) + (1-a)E_{\mathrm{x}}^{\mathrm{PBE,SR}}(\omega) + E_{\mathrm{x}}^{\mathrm{PBE,LR}}(\omega) + E_{\mathrm{c}}^{\mathrm{PBE}}, \qquad (3.24)$$

where a is the mixing parameter and ω is a parameter that governs the range of the interactions.

A common choice for the parameters a and ω is to set them to 0.25 and 0.11 respectively, and the corresponding functional is referred to as HSE06 [145]. It was shown that this choice works well in many systems. For example, it was successful in predicting accurate defect levels in diamond, Ge and Si for a variety of defect centers [146].

3.3.4 Bloch's theorem

We have shown in the previous sections how density functional theory within the Kohn-Sham formulation has circumvented the problem of many-body interactions by embedding the interaction effects into the exchange correlation functional, for which very good approximations are available.

For macroscopic systems however, the problem of dealing with a gigantic number of electrons, that could be infinite for extended systems, has not been addressed yet in the presentation above; one still needs to solve an infinite number of single particle Schrödinger equations, which is clearly not practical.

Fortunately, for crystalline systems, the entire bulk can be built up by infinitely repeating a single "unit cell" along the three translation vectors. One can cleverly takes advantage of the periodicity of the system in order to circumvent the problem of explicitly solving a gigantic number of single particle Schrödinger equations. In fact, this is achieved by the virtue of Bloch's theorem [147], from which one can map the electrons in the entire system to those in a single primitive unit cell. In what follows, we shall provide a basic derivation to this theorem and highlight its consequences in practical solutions to the Kohn-Sham equations. Alternative proofs can be found in Ref. [147].

Within the independent-electron picture, since the system under study is periodic, then the effective potential that the electrons feel within the system V_{eff} (see Eq. 3.16) has to have the same periodicity of the crystal structure of the system:

$$V_{\text{eff}}(\mathbf{r}+\mathbf{R}) = V_{\text{eff}}(\mathbf{r})\,, \tag{3.25}$$

where $\mathbf{R}$ is a general Bravais lattice vector:

$$\mathbf{R} = m_1\mathbf{a}_1 + m_2\mathbf{a}_2 + m_3\mathbf{a}_3\,, \tag{3.26}$$

with $\{\mathbf{a}_i\}$ being the three primitive vectors defining the primitive cell, and $\{m_i\}$ are some integers.

One can define a translational operator $\widehat{T}_{\mathbf{R}}$, that operates on an arbitrary function $f(\mathbf{r})$ by shifting its argument by $\mathbf{R}$:

$$\widehat{T}_{\mathbf{R}} f(\mathbf{r}) \equiv f(\mathbf{r}+\mathbf{R})\,. \tag{3.27}$$

It can be shown that the operator $\widehat{T}_{\mathbf{R}}$ commutes with the periodic Hamiltonian of the system $\widehat{H}(\mathbf{r})$ by noticing that:

$$\widehat{T}_{\mathbf{R}}\widehat{H}(\mathbf{r})\psi(\mathbf{r}) = \widehat{H}\left(\mathbf{r}+\mathbf{R}\right)\psi\left(\mathbf{r}+\mathbf{R}\right) = \widehat{H}(\mathbf{r})\widehat{T}_{\mathbf{R}}\psi(\mathbf{r})\,, \tag{3.28}$$

which holds for an arbitrary wavefunction $\psi(\mathbf{r})$, hence: $\widehat{T}_{\mathbf{R}}\widehat{H} = \widehat{H}\widehat{T}_{\mathbf{R}}$.

Similarly, it can also be shown that the translational operators $\widehat{T}_{\mathbf{R}}$, $\widehat{T}_{\mathbf{R}'}$ commute with each other for two different Bravais lattice vectors $\mathbf{R}$ and $\mathbf{R}'$, respectively:

$$\widehat{T}_{\mathbf{R}'}\widehat{T}_{\mathbf{R}}\psi(\mathbf{r}) = \widehat{T}_{\mathbf{R}'}\psi(\mathbf{r}+\mathbf{R}) = \psi(\mathbf{r}+\mathbf{R}+\mathbf{R}')\,, \tag{3.29}$$

$$\Rightarrow \widehat{T}_{\mathbf{R}'}\widehat{T}_{\mathbf{R}} = \widehat{T}_{\mathbf{R}}\widehat{T}_{\mathbf{R}'} = \widehat{T}_{\mathbf{R}'+\mathbf{R}}\,. \tag{3.30}$$

This implies that the Hamiltonian $\widehat{H}$ along with all the translation operators $\widehat{T}_{\mathbf{R}}$ share simultaneous eigenstates ψ:

$$\widehat{H}\psi = E\psi\,, \tag{3.31a}$$

$$\widehat{T}_{\mathbf{R}}\psi = c_{\mathbf{R}}\psi\,, \tag{3.31b}$$

with E and $c_{\mathbf{R}}$ being the corresponding eigenvalues.

On the other hand, the periodic boundary conditions imply:

$$\int |\psi(\mathbf{r}+\mathbf{R})|^2 d\mathbf{r} = \int |\psi(\mathbf{r})|^2 d\mathbf{r}\,, \tag{3.32a}$$

$$\Rightarrow \int |c_{\mathbf{R}}\psi(\mathbf{r})|^2 d\mathbf{r} = \int |\psi(\mathbf{r})|^2 d\mathbf{r}\,, \tag{3.32b}$$

$$\Rightarrow |c_{\mathbf{R}}|^2 = 1\,. \tag{3.32c}$$

Hence, $c_{\mathbf{R}}$ can be conveniently written as

$$c_{\mathbf{R}} = e^{2\pi i \chi_{\mathbf{R}}}\,, \tag{3.33}$$

for some real $\chi_{\mathbf{R}}$.

In view of Eq. 3.26, one notices that the operator $\widehat{T}_{\mathbf{R}}$ can be written as

$$\widehat{T}_{\mathbf{R}} = (T_{\mathbf{a}_1})^{m_1} (T_{\mathbf{a}_2})^{m_2} (T_{\mathbf{a}_3})^{m_3}\ . \tag{3.34}$$

In other words, $\widehat{T}_{\mathbf{R}}$ can be thought of as m_i successive translations along each of the primitive cell directions $\mathbf{a}_i$. Thus, utilizing Eq. 3.33, the eigenvalues $c_{\mathbf{R}}$ can be written as

$$c_{\mathbf{R}} = (c_{\mathbf{a}_1})^{m_1} (c_{\mathbf{a}_2})^{m_2} (c_{\mathbf{a}_3})^{m_3} = e^{2\pi i\left(m_1\chi_{\mathbf{a}_1}+m_2\chi_{\mathbf{a}_2}+m_3\chi_{\mathbf{a}_3}\right)}\,. \tag{3.35}$$

By defining a basis of dual vectors $\{\mathbf{b}_j\}$, such that $\mathbf{a}_i \cdot \mathbf{b}_j = 2\pi\delta_{ij}$, one can re-write the argument of the exponent of the equation above as follows:

$$(\chi_{\mathbf{a}_1}\mathbf{b}_1 + \chi_{\mathbf{a}_2}\mathbf{b}_2 + \chi_{\mathbf{a}_3}\mathbf{b}_3)\cdot(m_1\mathbf{a}_1 + m_2\mathbf{a}_2 + m_3\mathbf{a}_3) \equiv \mathbf{k}\cdot\mathbf{R}\,. \tag{3.36}$$

It turns out that $\mathbf{b}_i$ are nothing but the reciprocal lattice primitive vectors that are defined by

$$\mathbf{b}_1 = \frac{2\pi}{\Omega}\, \mathbf{a}_2 \times \mathbf{a}_3\,, \tag{3.37a}$$

$$\mathbf{b}_2 = \frac{2\pi}{\Omega}\, \mathbf{a}_3 \times \mathbf{a}_1\,, \tag{3.37b}$$

$$\mathbf{b}_3 = \frac{2\pi}{\Omega}\, \mathbf{a}_1 \times \mathbf{a}_2\,, \tag{3.37c}$$

with $\Omega = \mathbf{a}_1 \cdot (\mathbf{a}_2 \times \mathbf{a}_3)$ being the volume of the primitive cell in real space. The vector $\mathbf{k}$, appearing in Eq. 3.36, is a general reciprocal lattice vector, usually referred to as a wave vector. Therefore, the eigenvalues $c_{\mathbf{R}}$ are expressed as

$$c_{\mathbf{R}} = e^{i\mathbf{k}\cdot\mathbf{R}}\,. \tag{3.38}$$

Hence:

$$\widehat{T}_{\mathbf{R}}\psi_{\mathbf{k}}(\mathbf{r}) = \psi_{\mathbf{k}}(\mathbf{r}+\mathbf{R}) = e^{i\mathbf{k}\cdot\mathbf{R}}\psi_{\mathbf{k}}(\mathbf{r})\,. \tag{3.39}$$

The equation above is one of the possible expressions of Bloch's theorem. This states that although the single-particle eigenstates in a periodic effective potential are *not* periodic, they only differ by a phase factor from one unit cell to another.

The wave vector $\mathbf{k}$ introduced by Bloch's theorem defines the concept of the "crystal momentum" of the electron. This concept is better understood through analogy with a system with perfect translational symmetry (like a system of free non-interacting electrons). In such a system, the momentum operator commutes with the Hamiltonian operator, hence, the electronic wave-functions are also eigenstates to the momentum operator and thus the wave vector $\mathbf{k}$ directly represents the momentum of the electron $\mathbf{p}$ (with a factor of $\hbar$ that equals unity in atomic units.), which is conserved. However, in the system for which the effective potential is only periodic "modulo $\mathbf{R}$", the Hamiltonian no longer commutes with the momentum operator, since it lacks perfect translational symmetry. Therefore, the wave vector $\mathbf{k}$ in this case does not represent the actual momentum of the electron, but it rather conventionally represents a *crystal momentum*, that is conserved only modulo a primitive cell of reciprocal space.

Bloch's theorem can be expressed in an alternative way. Let us introduce the function $u_{\mathbf{k}}(\mathbf{r})$ that is defined as follows:

$$\psi_{\mathbf{k}}(\mathbf{r}) = u_{\mathbf{k}}(\mathbf{r}) e^{i\mathbf{k}\cdot\mathbf{r}} , \tag{3.40}$$

then, from Eq. 3.39, one can find:

$$\begin{aligned} &\psi_{\mathbf{k}}(\mathbf{r}+\mathbf{R}) = u_{\mathbf{k}}(\mathbf{r}+\mathbf{R}) e^{i\mathbf{k}\cdot\mathbf{r}} e^{i\mathbf{k}\cdot\mathbf{R}} = e^{i\mathbf{k}\cdot\mathbf{R}} \psi_{\mathbf{k}}(\mathbf{r}) , \\ &\Rightarrow \psi_{\mathbf{k}}(\mathbf{r}) = u_{\mathbf{k}}(\mathbf{r}+\mathbf{R}) e^{i\mathbf{k}\cdot\mathbf{r}} . \end{aligned} \tag{3.41}$$

Eqs. 3.40 and 3.41 implies that $u_{\mathbf{k}}(\mathbf{r})$ has exactly the same periodicity of the crystal structure:

$$u_{\mathbf{k}}(\mathbf{r}+\mathbf{R}) = u_{\mathbf{k}}(\mathbf{r}) . \tag{3.42}$$

The importance of Bloch's theorem in the form of Eqs. 3.40 and 3.42 can be seen by substituting Eq. 3.40 into the Kohn-Sham equation (Eq. 3.16), which yields:

$$-\frac{1}{2} \left(\nabla + i\mathbf{k}\right)^2 u_{\mathbf{k}}(\mathbf{r}) + V_{\text{eff}}\, u_{\mathbf{k}}(\mathbf{r}) = \varepsilon_{\mathbf{k}} u_{\mathbf{k}}(\mathbf{r}) , \tag{3.43}$$

where the phase factor $e^{i\mathbf{k}\cdot\mathbf{r}}$ has cancelled out, and it is only the periodic part of the electronic wavefunction $u_{\mathbf{k}}(\mathbf{r})$ that satisfies the eigenvalue problem above.

It can be easily shown that the phase $e^{i\mathbf{k}\cdot\mathbf{R}}$ is invariant if $\mathbf{k}$ is translated by a reciprocal lattice vector $\mathbf{G} = \ell_1\mathbf{b}_1 + \ell_2\mathbf{b}_2 + \ell_3\mathbf{b}_3$, for some integers $\{\ell_i\}$. Hence the possible values of $\mathbf{k}$ are restricted within a primitive cell in the reciprocal lattice. This conventionally taken to be the Wigner-Seitz cell in the reciprocal space, which is referred to as a Brillouin zone (BZ).

Because of the periodicity of $u_{\mathbf{k}}(\mathbf{r})$, it follows that the solutions can be restricted to a single primitive cell in the system. However, one should consider, in principle, all possible values of the wave vector $\mathbf{k}$ as the physical properties of the system, like the electronic density, are generally obtained through integrating the solutions over the entire BZ.

Since $\mathbf{k}$ appears only as a parameter in the Hamiltonian of Eq. 3.43, then the solutions $u_{\mathbf{k}}(\mathbf{r})$ for different values of $\mathbf{k}$ are completely decoupled. Thus, the problem of solving "infinitely" many Kohn-Sham equations for an infinite

bulk periodic system has been mapped to a problem of solving Eq. 3.43 within a single primitive cell only, but for infinitely many $\mathbf{k}$ points. Although this does not sound good in reducing the computational effort, it can be shown (as will be discussed in a later section) that one can choose a finite number of $\mathbf{k}$ points in reciprocal space for which to calculate the eigenstates and eigenvalues that result in a very good approximation to the actual integrations over the full Brillouin zone.

In Eq. 3.43, for each possible value of $\mathbf{k}$, there exist many discrete eigenvalues $\varepsilon_{\mathbf{k}}$ and eigenvectors $u_{\mathbf{k}}(\mathbf{r})$ that can be labelled by an index n; $\varepsilon_{n,\mathbf{k}}$ and $u_{n,\mathbf{k}}(\mathbf{r})$ (one can think about an analogues example of the well-known electron in a box problem). The energy levels $\varepsilon_{n,\mathbf{k}}$ that are lowest in energy will be occupied by the ground state electrons within the primitive cell (with each level being doubly occupied if the electrons are spin degenerate). So, if there is an even number $2N$ of electrons in the primitive cell, then the first N (or $2N$ if there is no spin degeneracy) energy levels are occupied by the electrons, and the rest are empty. Each energy level $\varepsilon_{n,\mathbf{k}}$ is usually referred to as a *band* energy, and the plot of $\varepsilon_{n,\mathbf{k}}$ as a function of the wave vectors $\mathbf{k}$ is referred to as the *band structure* of the material.

3.4 Technical details

3.4.1 Choosing a basis set

A further step that is needed to numerically solve the Kohn-Sham equations is to expand the unknown electronic orbitals $\psi_{n,\mathbf{k}}$ in a complete set of known basis functions[8]. Due to the periodicity of $u_{n,\mathbf{k}}(\mathbf{r})$, the most straightforward choice would be the orthonormal plane wave (PW) basis set:

$$\varphi_{\mathbf{G}}(\mathbf{r}) = \frac{1}{\sqrt{\Omega}} e^{i\mathbf{G}\cdot\mathbf{r}}\,, \tag{3.44}$$

where $u_{n,\mathbf{k}}(\mathbf{r})$ can be Fourier expanded as follows:

$$u_{n,\mathbf{k}}(\mathbf{r}) = \frac{1}{\sqrt{\Omega}} \sum_{\mathbf{G}} c_{n,\mathbf{k}}(\mathbf{G}) e^{i\mathbf{G}\cdot\mathbf{r}}\,, \tag{3.45}$$

[8]There is an alternative real-space technique that uses finite differences or finite elements to solve the Kohn-Sham equations [148].

with $c_{n,\mathbf{k}}(\mathbf{G})$ being the Fourier coefficients. The orbitals $\psi_{n,\mathbf{k}}(\mathbf{r})$ can then be expressed as (see Eq. 3.40):

$$\psi_{n,\mathbf{k}}(\mathbf{r}) = \frac{1}{\sqrt{\Omega}} \sum_{\mathbf{G}} c_{n,\mathbf{k}}(\mathbf{G}) e^{i(\mathbf{k}+\mathbf{G})\cdot\mathbf{r}} \,. \tag{3.46}$$

where the summation runs over the reciprocal space lattice vectors $\mathbf{G}$.

Although there exist other possible choices of the basis set, such as Gaussian functions and atomic orbitals, the choice of a planewave basis set has the advantage of mathematical simplicity. In addition, their periodicity naturally fits in with extended periodic systems. Plus, it is, in principle, a "complete set", i.e. it spans all the Hilbert space, so basically any orbital $u_{n,\mathbf{k}}$ can be expressed in terms of a Fourier series.

One can obtain a useful and elegant expression of the Kohn-Sham equations in reciprocal space by substituting the solutions in the form of Eq. 3.46 into Eq. 3.16, multiplying by $\frac{1}{\sqrt{\Omega}} e^{-i(\mathbf{k}+\mathbf{G}')}$, and integrating over the volume of the primitive cell Ω:

$$\begin{aligned} &\frac{1}{2} \sum_{\mathbf{G}} c_{n,\mathbf{k}}(\mathbf{G}) (\mathbf{k}+\mathbf{G})^2 \int_{\Omega} \frac{1}{\Omega} e^{i(\mathbf{G}-\mathbf{G}')\cdot\mathbf{r}} d\mathbf{r} \\ &+ \frac{1}{\Omega} \int_{\Omega} V_{\text{eff}}(\mathbf{r}) \sum_{\mathbf{G}} c_{n,\mathbf{k}}(\mathbf{G}) e^{i(\mathbf{G}-\mathbf{G}')\cdot\mathbf{r}} d\mathbf{r} = \varepsilon_{n,\mathbf{k}} \sum_{\mathbf{G}} c_{n,\mathbf{k}}(\mathbf{G}) \int_{\Omega} \frac{1}{\Omega} e^{i(\mathbf{G}-\mathbf{G}')\cdot\mathbf{r}} d\mathbf{r} \,. \end{aligned} \tag{3.47}$$

Since $V_{\text{eff}}(\mathbf{r})$ is also periodic, it can be expressed in terms of Fourier components as

$$V_{\text{eff}}(\mathbf{r}) = \sum_{\mathbf{G}''} \widetilde{V}_{\text{eff}}(\mathbf{G}'') e^{i\mathbf{G}''\cdot\mathbf{r}} \,. \tag{3.48}$$

By utilizing the orthonormality of the plane waves:

$$\frac{1}{\Omega} \int_{\Omega} e^{i(\mathbf{G}-\mathbf{G}')\cdot\mathbf{r}} \, d\mathbf{r} = \delta_{\mathbf{G},\mathbf{G}'} \,, \tag{3.49}$$

and substituting Eq. 3.48 into Eq. 3.47 we get:

$$\sum_{\mathbf{G}'} \left(\frac{1}{2}(\mathbf{k}+\mathbf{G}')^2 \delta_{\mathbf{G},\mathbf{G}'} + \widetilde{V}_{\text{eff}}(\mathbf{G}-\mathbf{G}') \right) c_{n,\mathbf{k}}(\mathbf{G}') = \varepsilon_{n,\mathbf{k}} c_{n,\mathbf{k}}(\mathbf{G}) \,, \tag{3.50}$$

or in a more compact form:

$$\sum_{\mathbf{G}'} H_{\mathbf{k}}(\mathbf{G},\mathbf{G}') c_{n,\mathbf{k}}(\mathbf{G}') = \varepsilon_{n,\mathbf{k}} c_{n,\mathbf{k}}(\mathbf{G}) \,. \tag{3.51}$$

This matrix equation can be solved by diagonalizing the Hamiltonian matrix $H_{\mathbf{k}}(\mathbf{G},\mathbf{G}')$. One of the disadvantages of the PW basis set is that, in principle, the sum over reciprocal lattice vectors in Eq. 3.46 requires an infinite number of terms to represent the wavefunction exactly. Since in practice it impossible to tackle an infinite matrix $H_{\mathbf{k}}(\mathbf{G},\mathbf{G}')$, usually one is interested in truncating the summation at some $\mathbf{G} = \mathbf{G}_{\text{max}}$. For this purpose, a cutoff energy E_{cut} is defined as follows:

$$E_{\text{cut}} \equiv \frac{1}{2}\mathbf{G}^2_{\text{max}} \,. \tag{3.52}$$

Convergence tests must be performed to choose what suitable value of E_{cut} should be used for the specific problem at hand. A suitable value would be such that if E_{cut} is increased by ΔE_{cut}, the physical quantity that one is interested in calculating (such as the total energy) would change by less than a designated acceptable tolerance.

Normally, very large numbers of planewaves are required to accurately represent the wavefunctions. This can be significantly decreased, however, when the pseudopotential formalism is used. This point shall be discussed in Sec. 3.4.3.

Even with the use of pseudopotentials, the size of the matrix $H_{\mathbf{k}}(\mathbf{G},\mathbf{G}')$ is usually too large to directly diagonalize it. There exist robust techniques to deal with this problem of which full details is out of the scope of this thesis.

Despite the fact that planewaves are periodic and extended over the system (in contrast with other basis such as Gaussians, which are localized and centered on specific atomic species), non-periodic systems that are localized in nature (such as defects or surfaces) may also be simulated with planewave DFT calculations. One usually circumvents the problem by increasing the size

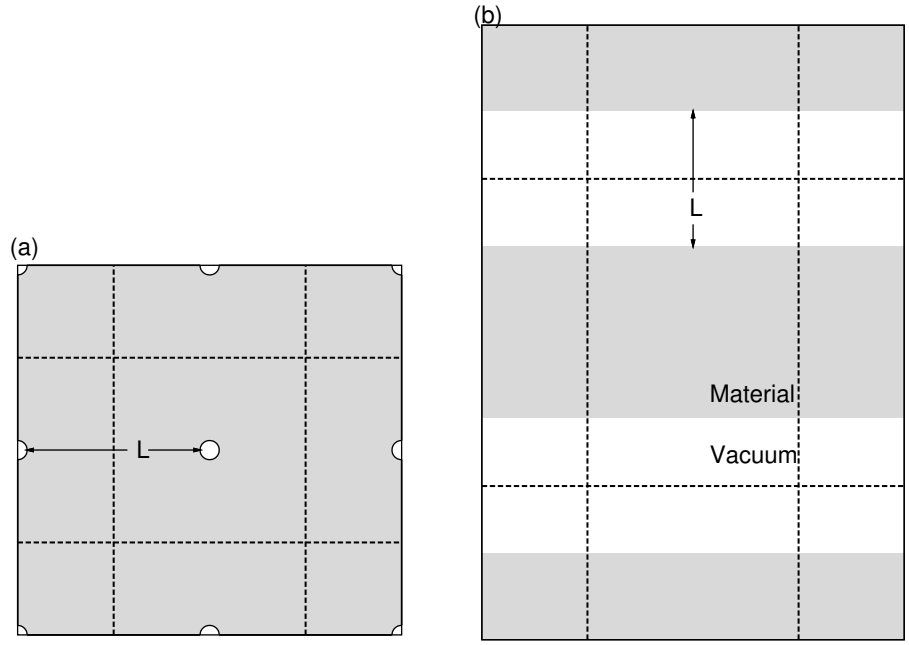


Figure 3.1: Schematic diagram of a periodic simulation cell (bounded by the dashed line) that includes **(a)** a defect, and **(b)** a surface. The use of periodic boundary conditions imposes fictitious interactions between the defect or the surface with its periodic images. The characteristic length (L) should be large enough to reduce the interactions and to converge the correct physical quantity that one is interested in.

of the simulation cell, or introducing a vacuum layer in order to reduce the spurious interactions between the defect centre (or the surface) and its periodic images, as shown Fig 3.1. This is called the "supercell approximation".

3.4.2 K-point sampling

As pointed out in Sec. 3.3.4, when Bloch's theorem is applied in periodic systems, the calculation of some physical properties can involve integration in the reciprocal space over the Brillouin zone. For instance, the electronic density, within the Kohn Sham formalism, is obtained via Eq. 3.17 if one would sum over the entire real space, but in view of Bloch's theorem, it can alternatively be calculated by

$$n(\mathbf{r}) = \sum_n \frac{1}{\Omega_{\mathrm{BZ}}} \int_{\mathrm{BZ}} f_n \, |\psi_{n,\mathbf{k}}(\mathbf{r})|^2 d\mathbf{k} \,, \tag{3.53}$$

where $\Omega_{\rm BZ}$ is the volume of the Brillouin zone, related to the real space volume by $\Omega_{\rm BZ} = (2\pi)^3/\Omega$, and the summation runs through the band index n, with f_n being the occupation of the $n^{\rm th}$ band.

Obviously, the continuous integration over $\mathbf{k}$ cannot be calculated exactly, since this requires the knowledge of analytical dependence of $\psi_{n,\mathbf{k}}(\mathbf{r})$ on the wave vector $\mathbf{k}$, and infinitely many $\mathbf{k}$ points are needed for this purpose.

In practice, the evaluation of BZ integrations are usually performed within the special-point method [149, 150], where the integration over $\mathbf{k}$ is approximated by a summation over a selected set of "special" k-points that belong to the BZ:

$$\frac{1}{\Omega_{\rm BZ}} \int_{\rm BZ} f(\mathbf{k}) d\mathbf{k} \approx \frac{1}{N_k} \sum_{\mathbf{k}} f(\mathbf{k}) \,, \tag{3.54}$$

where N_k is the total number of k-points. This is often referred to as BZ sampling, or k-point sampling, and is justified if the integrand $f(\mathbf{k})$ is smooth and does not rapidly change over $\mathbf{k}$.

The most common way of choosing the special points was proposed by Monkhorst and Pack (MP) [150]. Within the MP scheme, the BZ is sampled by a homogeneous mesh of $N_p \times N_r \times N_s$ k-points $\{\mathbf{k}_{prs}\}$ that are equally-spaced, and can be expressed by

$$\mathbf{k}_{prs} = u_p \mathbf{b}_1 + u_r \mathbf{b}_2 + u_s \mathbf{b}_3 \,, \tag{3.55}$$

where $\{u_\alpha\}$ is a set of N_α numbers defined by

$$u_\alpha = \frac{2\alpha - N_\alpha - 1}{2N_\alpha} \quad (\alpha = 1, \cdots, N_\alpha) \,, \tag{3.56}$$

with $\alpha \in \{p, r, s\}$, and N_α is the number of k-points along the α direction.

Obviously, larger values of the integers $\{N_\alpha\}$ (that lead to a denser MP mesh), implies more accurate approximation to the BZ integration. The choice of the density of the MP mesh is usually determined by investigating the convergence of the properties of interest, much like the choice of $E_{\rm cut}$. One should note however that whilst the total energy of the system is variational with $E_{\rm cut}$, this is not the case with the k-point grid density.

The summation over all the k-points in the MP mesh can usually be equivalently performed by summing over almost half of the points only. This is

achieved by exploiting time-reversal symmetry and the Bloch theorem [113]. This is explained as follows: in the absence of a magnetic field, the Hamiltonian of the system is invariant under time reversal. It follows that if ψ is an eigenfunction of the Hamiltonian, then so is its complex conjugate ψ^*, with the same eigenvalue. On the other hand, according to Bloch's theorem (Eq. 3.39), both of the equations below must hold:

$$\widehat{T}_{\mathbf{R}}\psi_{-\mathbf{k}}(\mathbf{r}) = \psi_{-\mathbf{k}}(\mathbf{r}+\mathbf{R}) = e^{-i\mathbf{k}\cdot\mathbf{R}}\,\psi_{-\mathbf{k}}(\mathbf{r})\,, \tag{3.57a}$$

$$\widehat{T}_{\mathbf{R}}\psi^*_{\mathbf{k}}(\mathbf{r}) = \psi^*_{\mathbf{k}}(\mathbf{r}+\mathbf{R}) = e^{-i\mathbf{k}\cdot\mathbf{R}}\,\psi^*_{\mathbf{k}}(\mathbf{r})\,, \tag{3.57b}$$

where Eq. 3.57a is obtained by setting $\mathbf{k} \to -\mathbf{k}$ in Eq. 3.39, and Eq. 3.57b is obtained by taking the complex conjugate of both sides of Eq. 3.39. This means that both $\psi_{-\mathbf{k}}(\mathbf{r})$ and $\psi^*_{\mathbf{k}}(\mathbf{r})$ are degenerate states of the translation operator and have the same $\mathbf{k}$ dependence, as deduced from Bloch's theorem. This implies that the eigenvalues $\varepsilon_{-\mathbf{k}}$ and $\varepsilon_{\mathbf{k}}$ are also equal (an equality usually referred to as Kramers theorem [151]). Thus, for any $-\mathbf{k}$ in the BZ, it suffices to find the complex conjugate of the eigenstate at the wave vector $\mathbf{k}$, leading to almost halving the computational effort.

Moreover, exploiting the point group symmetries of the crystal can further reduce the number of k-points in the MP mesh at which Eq. 3.50 needs to be solved. Usually, the integrand $f(\mathbf{k})$ has the same value for all k-points that are symmetry related. Hence, one can convert the summation over the full BZ into a summation over a reduced wedge of the BZ (usually referred to as the irreducible Brillouin zone (IBZ)) that only contain k-points which are not symmetry related:

$$\frac{1}{N_k}\sum_{\mathbf{k}_{\mathrm{MP}}\in\mathrm{BZ}} f(\mathbf{k}_{\mathrm{MP}}) = \sum_{\mathbf{k}_{\mathrm{MP}}\in\mathrm{IBZ}} w_{\mathbf{k}_{\mathrm{MP}}} f(\mathbf{k}_{\mathrm{MP}})\,, \tag{3.58}$$

where the weight $w_{\mathbf{k}_i}$ for the k-point $\mathbf{k}_i$ is defined by the ratio between the number of k-points that are symmetry related to $\mathbf{k}_i$ (usually referred to as the *star* of $\mathbf{k}_i$), and the total number of k-points in the MP mesh.

3.4.3 Pseudopotentials

It is well known that valence electrons have the dominant role in determining the majority of physical properties of solids, as opposed to the core electrons that are strongly bound to the nucleus and almost insensitive to the chemical environment. This motivates the idea that one can, in one way or another, keep only the valence electrons in practical DFT calculations, and "merge" the core electrons with the nucleus by using an effective "pseudopotential". Indeed, this is the basic idea of the pseudopotential (PP) approximation [152–154]. The advantage of the PP approximation over the all-electron calculations is that it can minimize the computational effort to a great extent, as shall be discussed later in this section.

Within the PP approximation, the strong external Coulomb potential of the nuclei V_{ext} (See Eqs. 3.15 and 3.16) is replaced by a weaker potential V_{pp} in a pre-defined core region, and the all-electron Kohn-Sham eigenstates ψ^{ae} are replaced by "pseudo" eigenstates ψ^{pp}. The Kohn-Sham equations (Eq. 3.16) are then solved for the pseudo valence states only, with the redefined effective potential:

$$V_{\text{eff}}(\mathbf{r}) \equiv \int \frac{n(\mathbf{r}')}{|\mathbf{r}-\mathbf{r}'|} d\mathbf{r}' + V_{\text{pp}}(\mathbf{r}) + \frac{\delta E_{\text{xc}}[n(\mathbf{r})]}{\delta n} \,. \tag{3.59}$$

Outside the core region (which is usually characterised by a cutoff core radius r_{c}), the eigenstates ψ^{ae} and ψ^{pp} are required to be identical (See Fig 3.2 for more clarification). The pseudopotential V_{pp} and the pseudo wavefunctions ψ^{pp} are constructed so that the "pseudo" eigenvalues match the all-electron Kohn-Sham eigenvalues.

As pointed out earlier, the PP approximation is very useful in reducing the computational effort. On the one hand, it is obvious that decreasing the number of electrons by removing the core states can dramatically decrease the computational demand (especially for systems consisting of large atoms). For example, in the case of BTO, the primitive cell contains 102 electrons, but this number can be reduced to just 40 electrons should the PP approximation be used, where 62 core electrons are discarded from explicit calculation.

On the other hand, due to the strong ionic potential, the all-electron valence states experience rapid oscillations within the core region ($r < r_{\text{c}}$), see Fig. 3.2. These oscillations are necessary to maintain the orthogonality between the

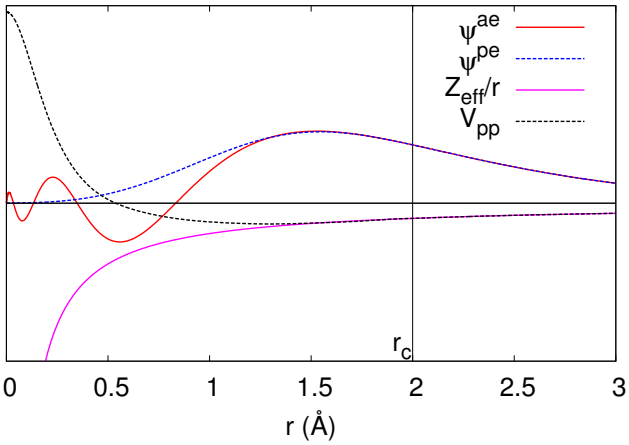


Figure 3.2: Illustration to the all-electron method versus the PP approximation method. In the core region ($r < r_c$), the strong ionic potential $Z_{\rm eff}/r$ is replaced by a weaker pseudopotential $V_{\rm PP}$, and the multi-node oscillatory wavefunction $\psi^{\rm ae}$ is replaced by a smooth nodeless pseudo wavefunction $\psi^{\rm PP}$. Beyond the designated cutoff radius r_c, $\psi^{\rm PP}$ and $\psi^{\rm ae}$ must agree. The wavefunction shown in this figure corresponds to the Ba 5s orbital. The pseudopotential is generated via the OPIUM code [4].

valence and the core states (as required by Pauli exclusion principle) [155]. The consequence of the oscillatory behaviour, however, is that an extremely large number of planewaves is needed to represent the valence states. Within the PP approximation, the core states are "removed" and hence the valence states no longer need the oscillations to maintain orthogonality with the core states, and are therefore much smoother. Thus, the number of the required planewaves is significantly reduced. This is another way in which PP approximation can serve in reducing the computational effort.

The mathematical form of the PP should be chosen so that the scattering properties of the nucleus and the core electrons for the all-electron valence wavefunctions are reproduced for the pseudo wavefunctions. Therefore, since the scattering properties are dependent on the angular momentum of the valence wavefunctions, the pseudopotential must also be constructed so that it is angular momentum dependent. Then the most general form for a pseudopotential can be expressed as [155]

$$V_{\rm pp} = \sum_{lm} |Y_{lm}\rangle \, V_l \, \langle Y_{lm}| \,, \tag{3.60}$$

where Y_{lm} are the spherical harmonics, and V_l is the PP corresponding to the angular momentum l. Such a general form of a pseudopotential is referred to as a *non-local* PP, with respect to l, as opposed to a *local* PP where the values of V_l are equal for all angular momenta l.

Pseudopotentials are usually generated based on *ab initio* calculations, in which case they are often referred to as *ab initio* pseudopotentials [153]. Within this scheme, the PP of a certain atomic species is constructed based on atomic DFT calculations. In brief, an all-electron calculation is first performed for a single atom, at a reference electronic configuration, to find $\psi^{\rm ae}$ and the eigenvalues. $\psi^{\rm pp}$ is then constructed so that it matches $\psi^{\rm ae}$ for $r > r_{\rm c}$, and is nodeless for $r < r_{\rm c}$. Once $\psi^{\rm pp}$ is constructed, the radial Schrödinger equation is inverted to find the *screened* potential $\widetilde{V}_l$, using the all-electron eigenvalues, and is then unscreened by subtracting the Hartree and the exchange-correlation energies.

As has just been pointed out, the pseudo wavefunction $\psi^{\rm pp}$ within the core region ($r < r_{\rm c}$) is constructed so that it is nodeless. There is, however, no unique choice for the form of $\psi^{\rm pp}$ inside the core region. In fact, one can use this "freedom" of choice to make the PP as *soft* as possible (i.e. to minimize the required cutoff energy of the planewave expansion). Several schemes are available in the literature for the description of the pseudo wavefunction in the core region. Examples can be found in Refs. [156–159].

The above-mentioned *ab initio* pseudopotentials are generated based on *atomic* calculations. However, one would usually need the PP to perform calculations for different systems, such as molecules or bulk solids. A good pseudopotential is one that is *transferabale*, i.e., though generated for a single atom, it can describe the the atom in different chemical environments. Hamann *et al* [156] suggested some criteria for the generation of a PP so that excellent transferability can be achieved: 1. The all-electron eigenvalues of the valence electrons must agree with the PP eigenvalues. 2. The pseudo wavefunction, its logarithmic derivative, and the energy derivative of its logarithmic derivate, must agree with the all-electron wavefunction and its corresponding derivatives for $r > r_{\rm c}$, respectively. 3. Both $\psi^{\rm ae}$ and $\psi^{\rm pp}$ must give the same total charge

in the core region:

$$\int_0^{r_c} |\psi^{PP}| r^2 dr = \int_0^{r_c} |\psi^{ae}| r^2 dr \,. \tag{3.61}$$

The latter condition is referred to as *norm-conservation*. In fact, norm conserving PP are guaranteed to reproduce, to first order, the energy dependence of the scattering properties due to the nucleus [155]. It is worth noting that norm conserving PP can also be extended so that they correctly describe the scattering properties to second order [160].

The general form of a PP given by Eq. 3.60 is computationally inefficient in practice. In fact, within planewave DFT calculations, the number of integrals required scales as the square of the number of plane waves. This is a consequence of the fact that the PP in the form Eq. 3.60, although non local in the angular coordinates, is local in the radial coordinate, so sometimes referred to as *semi–local*. This problem is most widely circumvented by using the Kleinman-Bylander (KB) fully non-local separable from of the PP [161]:

$$V_{pp}^{KB} = V_{loc} + \sum_{lm} \frac{|\delta V_l \, \psi_{lm}^{PP}\rangle\langle\psi_{lm}^{PP} \, \delta V_l|}{\langle\psi_{lm}^{PP}|\delta V_l|\psi_{lm}^{PP}\rangle} \,, \tag{3.62}$$

where V_{loc} is an arbitrary local potential that is usually chosen to be equal V_l for a chosen l, $\delta V_l \equiv V_l - V_{loc}$, and ψ_{lm}^{PP} are the eigenstates of the pseudo Hamiltonian. The advantage of this formalism is that the computational effort now scales linearly with the number of planewaves.

The condition of norm conservation obviously limits the freedom of the choice of $\psi^{PP}\,(r < r_c)$. Due to this constraint, $\psi^{PP}\,(r < r_c)$ cannot be always constructed to be much smoother than $\psi^{ae}\,(r < r_c)$, which results in only a minor decrease in the size of the plane wave basis set in the PP calculations compared to the all-electron calculations. This is mostly pronounced in atomic species containing highly localized valence states (like the first row atoms, e.g., O $2p$ states). In contrast to the norm-conserving PP, Vanderbilt developed another method to generate "ultra-soft" pseudopotentials where the norm conservation condition is relaxed, while retaining the correct scattering properties, to first order, which ensures good transferability of the potential. This allows construction of softer pseudo wavefunctions in the core region and thus lowers the basis set size [162].

3.5 The virtual crystal approximation

In many condensed matter systems, making alloys and solid solutions is important. The most pronounced advantage is that the properties of the alloy, such as the mechanical, magnetic, electronic, or optical properties, can be controlled by varying the composition [113].

The simulation of such systems, within the theoretical framework described so far, can be tricky, however. Perhaps the most straightforward idea is to approach the problem by considering a simulation "supercell" consisting of all the atomic species of the mixed materials, as shown in Fig. 3.3 for the case of $Ba_xSr_{1-x}TiO_3$. Examples of using the supercell approach can be found in Refs. [89, 91, 92, 163–170], where it has been used to investigate the structural, electronic, and optical properties of different solid solutions. The difficulty of such an approach lies in the fact that the supercell can be very large, especially if one is interested in dilute concentrations of the alloying elements. This leads to a dramatic increase in the computational effort, as the computational time scales cubically with the system size for conventional planewave DFT calculations.

This problem can be circumvented and approached differently by appealing to approximations that average over disorder. The most common of these are the coherent potential approximation (CPA) [171, 172] and the virtual crystal approximation (VCA) [173, 174]. We shall focus on the latter approach as it is the one that we use in this thesis.

Consider a solid solution consisting of two distinct atomic species A and B, at given concentrations, that form the lattice, or sub-lattice, of the system. The VCA replaces the original crystal by a hypothetical crystal in which the two species A and B are replaced by a "pseudo" atom C, that is assumed to have a weighted average of the properties of A and B, with the relative weights determined by the relative concentrations of A and B in the solid solution. The symmetry of the sub lattice formed by either the A or B atoms is retained by the sub lattice of the pseudo atom, and the crystal potential of the pseudo lattice is just the weighted average crystal potential of the individual sub lattices of A and B.

Within the PP approximation, the VCA is implemented by averaging the pseudopotentials of the A and B atoms with the desired mixing ratio, and

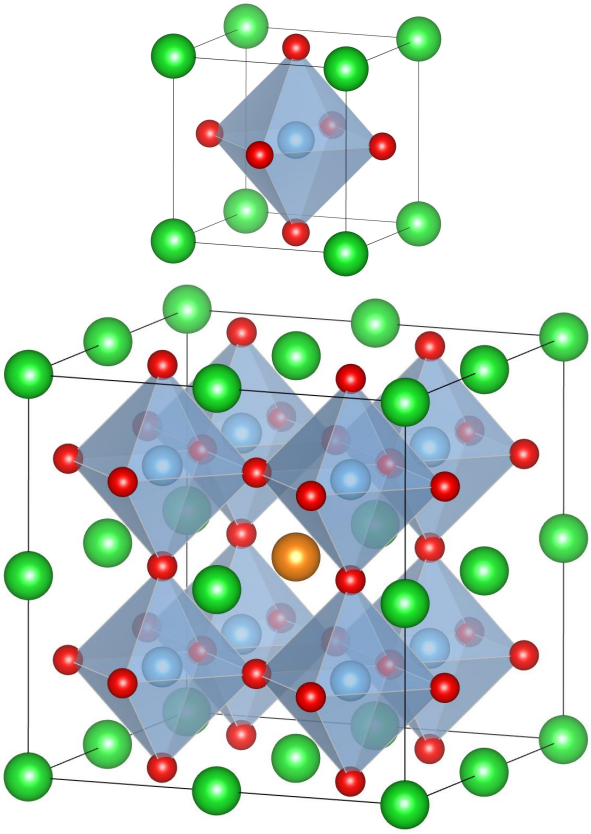


Figure 3.3: **(Top):** The simulation cell that corresponds to pure single crystal bulk cubic BTO. **(Bottom):** A supercell formed by a $2 \times 2 \times 2$ cubic extension of the BTO primitive cell. In this supercell, one of the Ba atoms is replaced by a Sr atom, forming the solid solution of $Ba_{0.875}Sr_{0.125}TiO_3$. Larger supercells are needed for more dilute concentrations of Sr. Green, orange, blue and red atoms correspond to Ba, Sr, Ti and O species, respectively.

assigned to the pseudo atom C. There is no unique way of doing this however, and it is far from straightforward with the fully non-local separable form of KB described in Sec. 3.4.3. Consider a solid solution described by the stoichiometric formula $A_\alpha B_\beta$, where α and β are the mixing ratios adding up to one. One averaging method to mention [175] is to construct two independent pseudopotentials $V_{\rm PP}^A$ and $V_{\rm PP}^B$ for the atomic species A and B, respectively. Then the VCA pseudopotential $V_{\rm PP}^{AB}$ is constructed as follows:

$$V_{\rm PP}^{AB} = \alpha V_{\rm PP}^A + \beta V_{\rm PP}^B \,, \tag{3.63}$$

where this averaging is performed for each angular momentum channel. It is clear from Eq. 3.62 that the KB non-local form requires the knowledge of the eigenstates of the pseudo Hamiltonian in order to construct the non-local corrections. Within this method, $V_{\rm PP}^{AB}$ is used to solve the radial Schrödinger equation to obtain the corresponding pseudo wavefunctions that are used in turn to construct the non-local PP.

Another method to mention [175] is designed to guarantee that the electronic properties of the pseudo atom are represented accurately. This is achieved by requiring that the all-electron eigenvalues of the pseudo atom ε_{nl}^{AB} resemble the correct linear average of the eigenvalues of the parent atoms ε_{nl}^A and ε_{nl}^B. That is:

$$\varepsilon_{nl}^{AB} = \alpha \varepsilon_{nl}^A + \beta \varepsilon_{nl}^B \,. \tag{3.64}$$

The pseudopotentials are then mixed according to:

$$V_{\rm PP}^{AB} = \alpha' V_{\rm PP}^A + \beta' V_{\rm PP}^B \,, \tag{3.65}$$

where the mixing parameters α' and β' are generally different from α and β, and tuned such that Eq. 3.64 is fulfilled.

Mixing schemes can also be generalized to be valid for ultra-soft pseudopotentials or heterovalent atoms. More details can be found in Refs. [176, 177].

The VCA method that has been used in the current work is the one implemented in the ABINIT code, unless stated otherwise. This implementation is quite simple and straightforward, and can be expressed as [178]

$$
\begin{aligned}
V_{\mathrm{pp}}^{AB} &= \alpha V_{\mathrm{loc}}^{A} + \beta V_{\mathrm{loc}}^{B} \\
&+ \sum_{lm} \frac{|\alpha\delta V_l^A \, \psi_{lm}^{\mathrm{PP},A}\rangle\langle\psi_{lm}^{\mathrm{PP},A} \, \alpha\delta V_l^A|}{\langle\psi_{lm}^{\mathrm{PP},A}|\alpha\delta V_l^A|\psi_{lm}^{\mathrm{PP},A}\rangle} \\
&+ \sum_{lm} \frac{|\beta\delta V_l^B \, \psi_{lm}^{\mathrm{PP},B}\rangle\langle\psi_{lm}^{\mathrm{PP},B} \, \beta\delta V_l^B|}{\langle\psi_{lm}^{\mathrm{PP},B}|\beta\delta V_l^B|\psi_{lm}^{\mathrm{PP},B}\rangle} \, .
\end{aligned}
\tag{3.66}
$$

Although the use of the VCA may dramatically reduce the computational effort, it has a drawback that information regarding the lattice ordering or the effect of atomic configurations of the dopant atoms in the host material is lost. VCA calculations, therefore, should always be compared against supercell calculations to justify their validity.

3.6 Geometry optimization

In order to accurately describe a certain physical property of a specific system, one is often required to perform the simulations at the equilibrium structure of the system. For instance, in order to calculate the refractive index of bulk BTO, one should consider the simulation cell to be at its equilibrium lattice constants and the atoms to be at equilibrium sites. Thus, geometry optimization (the process of seeking the equilibrium structure that minimizes the total energy of the system[9]) is an important step that is either required for its own sake, or is a pre-requisite of other sets of calculations.

In principle, the minimum energy structure of a system corresponds to the atomic configuration at which the forces acting on each individual atom in the system[10] vanishes, in addition to all the components of the stress tensor. The

[9] At a temperature of 0 K, and in the absence of external pressure, the equilibrium structure is associated with the minimization of the total energy of the system. The Helmholtz free energy or the enthalpy are indeed the thermodynamic potentials that are to be minimized if the calculations are performed under finite temperature or pressure, respectively. Most generally, one is interested in minimizing the Gibbs free energy should the calculations be performed at finite temperature and pressure.

[10] It should be noted that the opposite is not true. Vanishing forces corresponds generally to a "stationary" state of the energy, which could be a local maximum, a local minimum, or a saddle point. An example to mention is the paraelectric phase of BTO at low temperatures, where atoms occupy high symmetry sites resulting in vanishing forces, whilst the system is not at an energy minimum.

calculation of forces and stresses within the Kohn-Sham formalism of DFT for local density functionals is well established. A detailed description can be found in Refs. [113, 179–182].

The calculation of the quantum mechanical forces traditionally follows a formulation referred to as the "Hellmann-Feynman" theorem, a brief description of which shall be given in what follows.

The dependence of the total energy $E = \langle\Psi|\widehat{H}\Psi\rangle$ of a system of Hamiltonian $\widehat{H}$ and normalized eigenstate Ψ on some parameter λ can be described by

$$\frac{\partial E}{\partial \lambda} = \frac{\partial}{\partial \lambda}\langle\Psi|\widehat{H}\Psi\rangle = \langle\frac{\partial\Psi}{\partial\lambda}|\widehat{H}\Psi\rangle + \langle\Psi|\frac{\partial\widehat{H}}{\partial\lambda}\Psi\rangle + \langle\Psi|\widehat{H}\frac{\partial\Psi}{\partial\lambda}\rangle\,. \tag{3.67}$$

Since the Hamiltonian is a Hermitian operator (see for example Ref. [183]), then:

$$\langle\Psi|\widehat{H}\frac{\partial\Psi}{\partial\lambda}\rangle = \langle\widehat{H}\Psi|\frac{\partial\Psi}{\partial\lambda}\rangle\,. \tag{3.68}$$

Also, as we have pointed out earlier, the invariance of the Hamiltonian under time reversal leads to Ψ and Ψ^* being degenerate eigenstates of $\widehat{H}$, sharing the same eigenvalue E:

$$\widehat{H}\Psi = E\Psi\,, \tag{3.69a}$$

$$\widehat{H}\Psi^* = E\Psi^*\,. \tag{3.69b}$$

Hence, substituting Eqs. 3.68 and 3.69 into Eq. 3.67 gives:

$$\begin{aligned}\frac{\partial E}{\partial\lambda} &= E\left(\langle\frac{\partial\Psi}{\partial\lambda}|\Psi\rangle + \langle\Psi|\frac{\partial\Psi}{\partial\lambda}\rangle\right) + \langle\Psi|\frac{\partial\widehat{H}}{\partial\lambda}|\Psi\rangle \\ &= E\frac{\partial}{\partial\lambda}\langle\Psi|\Psi\rangle + \langle\Psi|\frac{\partial\widehat{H}}{\partial\lambda}\Psi\rangle \\ &= \langle\Psi|\frac{\partial\widehat{H}}{\partial\lambda}\Psi\rangle\,.\end{aligned} \tag{3.70}$$

where the first term in the second line vanishes since $\langle\Psi|\Psi\rangle = 1$.

Eq. 3.70 is a generalized form of the Hellmann-Feynman theorem. Its usefulness is in that the derivative of the total energy with respect to the parameter λ directly transfers to a derivative of the Hamiltonian, which is relatively easy to evaluate in practice.

Forces and stresses can be evaluated using the general expression given in Eq. 3.70. Generally, the force $\mathbf{F}_\alpha$, acting on some atom α in the system occupying the position $\mathbf{R}_\alpha$, can be expressed as

$$\mathbf{F}_\alpha = -\frac{\partial E}{\partial \mathbf{R}_\alpha} = -\langle\Psi|\frac{\partial H}{\partial \mathbf{R}_\alpha}|\Psi\rangle\,, \tag{3.71}$$

where the latter equality is a direct application to Eq. 3.70, with the parameter λ is replaced by the atomic position.

Similarly, the macroscopic stress tensor $S_{\alpha\beta}$ can be expressed as

$$S_{\alpha\beta} = -\frac{1}{\Omega}\frac{\partial E}{\partial \epsilon_{\alpha\beta}}\,, \tag{3.72}$$

where $\epsilon_{\alpha\beta}$ is the strain experienced by the system, which is defined as the amount by which the space is scaled. That is, if $\mathbf{r}$ and $\mathbf{r}'$ are general points in the system before and after the application of strain ϵ, respectively, then the two points are related by

$$r'_\alpha = (\delta_{\alpha\beta} + \epsilon_{\alpha\beta})\, r_\beta\,, \tag{3.73}$$

where the summation convention has been used, and the Greek subscripts refer to the Cartesian components. Expressions for the stress tensor that are used in practice have been derived and explained in details in Refs. [181, 182, 184].

It is obvious that Eq. 3.70 is true subject to the condition that Ψ is an exact eigenstate to the Hamiltonian. In practice, Ψ cannot be expressed exactly due to the incompleteness of the basis set used to expand the wavefunctions (a complete basis set often means that infinite terms has to be included in the expansion). As a result, the terms containing the wavefunction derivative in Eq. 3.70 do not necessarily vanish, and their contribution is usually referred to as *Pulay* forces or stresses [185].

Pulay contributions clearly vanish in the limit of a complete basis set. It should also be noted that if there is no explicit dependence of Ψ on λ, this will

also lead to vanishing the Pulay contributions. For example, since planewaves are extended and independent of the atomic positions, Pulay forces vanish despite the incompleteness of the basis set. This is a great advantage of the planewaves over local basis sets such as Gaussians or atomic orbitals.

In order to reduce the effect of Pulay stresses, larger values than the converged E_{cut} should be used. A 30% increase of the cutoff energy is usually adequate to give reliable stresses, and in the context of geometry optimization, this increase should restore the coincidence between the minimum energy and the zero stress structures.

Technically, the process of seeking the optimized structure by minimizing the total energy, the forces and the stresses, can follow different iterative optimization algorithms. These can range from naive and simple methods, such as the steepest descent algorithm, to more complicated and robust methods, such as the conjugate gradient algorithm or the quasi-Newtonian Broyden-Fletcher-Goldfarb-Shanno algorithm (BFGS) [186]. The latter method is used throughout this work to perform structural optimizations, unless stated otherwise.

Chapter 4

Effect of strain and alloying on the electronic structure of BTO and STO

4.1 Overview

As pointed out in Sec. 1.4.1, properties of materials (in particular BTO and STO) in thin film form can significantly differ from those of the bulk, due to the presence of a number of factors that include the mismatch strain and defects. Furthermore, we have pointed out in Sec. 1.1 that the properties of BTO and STO may also be tuned by means of doping and alloying, due to the amenability of these materials to a variety of dopant additions.

Our interest in this thesis is about how the aforementioned factors can influence, in particular, the electronic and optical properties of BTO and STO and their solid solutions, and more specifically, how the effect of these factors compare with each other, qualitatively and quantitatively, and hence, what could be the most dominant factor in tuning the optical properties of these materials.

As discussed in detail in Chapter 2, spectroscopic ellipsometry, which is the most commonly used experimental technique in characterizing the optical properties of thin films, is subject to a number of problems that can affect the reliability of its results. In addition, it is not very clear, within this method, how to disentangle the effects of individual factors that could influence the

properties in question of BTO/STO thin films. Therefore, the investigation of the problem from the perspective of first-principles theory and simulations can help move a step forward in answering the questions addressed above and deepen the knowledge about this problem.

Our investigations in this chapter shall be dedicated to the study, from first-principles, of strain-induced changes and alloying effects on the electronic properties of BTO, STO and their solid solutions. We find that the bandgap of these systems shows interesting features as a function of strain, where it decreases at low strains and increases at high strains. The trend of the bandgap with respect to the increasing concentration of Sr in BST also shows a non-monotonic behaviour, where it decreases and increases at low and high concentrations, respectively. We shall explain these features in detail in terms of the strain-induced changes in the magnitude and the direction of the spontaneous polarization of these systems. We also propose in this chapter a "space condition" for ferroelectricity. This condition states that the ferroelectric polarization component along a specific crystallographic direction cannot be induced unless the lattice vector along that direction is longer than a critical value.

This chapter can be thought of as a link to the next chapter, where we investigate there the strain and alloying effects on the optical properties of BST.

The calculation of the energy gap of materials, within the framework of DFT, is to be discussed first in the next section, where we address the limitations of the methodology we are using.

4.2 The band gap problem in DFT

The fundamental energy band gap of an insulating or semiconducting material is given by the difference between the first ionization energy I and the first electron affinity A of the material [187]. The ionization energy is the energy required to take out an electron from the material from the highest valence state and place it infinitely away from the material. Thus, for a system constituting initially of N electrons, $I(N)$ is given by

$$I(N) = E(N-1) - E(N)\,, \tag{4.1}$$

where $E(N)$ is the total energy of the system with N electrons, and $E(N-1)$ is the total energy of the system after a removal of an electron.

Similarly, the electron affinity is the energy required to add an electron to the material by placing it at the bottom of the conduction states. So, for a system constituting initially of N electrons, A is given by

$$A(N) = E(N) - E(N+1)\,. \tag{4.2}$$

where $E(N+1)$ is the total energy of the system after an addition of a single electron.

The energy band gap E_{g} of the system can then be expressed as

$$E_{\mathrm{g}} = I - A = E(N+1) + E(N-1) - 2E(N)\,. \tag{4.3}$$

As pointed out in Chapter 3, density functional theory is a ground state theory. In principle, the Hohenberg-Kohn theory within the Kohn-Sham formalism guarantees that the ground state energy and the ground state density of the system are exact. One might think then that E_{g} can also, in principle, be calculated exactly within DFT, as it is a difference between ground state energies. It turns out, however, that this is not true. It is well known that DFT underestimates the band gaps of insulators and semiconductors [188, 189].

Indeed, this problem is attributed to a derivative discontinuity that the exchange-correlation functional E_{xc} experiences when the number of electrons in the system changes from $N-\delta$ to $N+\delta$ for integer N, with δ being a positive infinitesimal change. This can be better understood through Janak's theorem [190], which relates the derivative of the total energy with respect to the occupancy f_i of the i^{th} Kohn-Sham eigenstate to its eigenvalue ε_i:

$$\varepsilon_i = \frac{\delta E}{\delta f_i}\,. \tag{4.4}$$

Within the Kohn-Sham formalism, E can be expressed according to Eqs. 3.8, 3.9 and 3.10. For the sake of simplicity, let the eigenvalues be conventionally sorted in an ascending order (so that ε_N and ε_{N+1} correspond to the energies of the highest occupied and the lowest unoccupied states). The ionization energy and the electron affinity can then be expressed in terms of the eigenvalues as follows [188]:

$$I(N) = -\int_0^1 \varepsilon_N(N-1+f)df = -\varepsilon_N(N-\delta)\,, \tag{4.5a}$$

$$A(N) = -\int_0^1 \varepsilon_{N+1}(N+f)df = -\varepsilon_{N+1}(N+\delta)\,, \tag{4.5b}$$

where the latter equality in Eq. 4.5 holds due to the fact that the eigenvalues ε_i are independent of f_i over range of integral.

For a real system, the number of electrons tends to be infinitely large[1] ($N \to \infty$), thus the addition or removal of an electron only infinitesimally affects the ground state density $n(\mathbf{r})$. However, this is not the case for the effective potential V_{eff} (see the definition in Eq. 3.15), where it has been shown that it is subject to a finite positive shift C besides an infinitesimal change. Indeed, this is attributed to the fact that the functional derivative of E_{xc} (i.e., the exchange-correlation potential) is subject to this discontinuity when the number of electrons in the system increases through N:

$$\left.\frac{\delta E_{\text{xc}}}{\delta n}\right|_{N+\delta} - \left.\frac{\delta E_{\text{xc}}}{\delta n}\right|_{N-\delta} = C\,. \tag{4.6}$$

The jump in the effective potential is then reflected in the eigenvalues, where they are subject to the same additive shift upon the change of the number of electrons. Thus, Eq. 4.5b can be re-written as

$$A(N) = -\varepsilon_{N+1}(N+\delta) = -\varepsilon_{N+1}(N) + C\,, \tag{4.7}$$

therefore, the band gap can be expressed as

$$\begin{aligned} E_{\text{g}} &= I(N) - A(N) \\ &= \varepsilon_{N+1}(N) - \varepsilon_N(N) + C \\ &= E_{\text{g}}^{KS} + C\,, \end{aligned} \tag{4.8}$$

where E_{g}^{KS} is the Kohn-Sham band gap. Thus, it is inherent[2] in Kohn-Sham

[1] In this context, we are referring specifically to solids rather than molecules.

[2] We would like here to reiterate the point that it is not actually the approximation of E_{xc} (such as the LDA) that is in full charge of underestimating the gap, but rather it is the formalism of the Kohn-Sham DFT that does not correctly take into account the quasiparticle

DFT that the band gap is underestimated, and the amount of the underestimation is given by the derivative discontinuity C, even with the exact functional.

Different approaches exist for the correction of the Kohn-Sham band gap. As has been shown from the work of Sham and Schlüter, the discontinuity C can be expressed in terms of the electron self energy Σ [189]. However, the calculation of the latter quantity lies beyond DFT. Currently, the common method of approximating Σ, and hence correcting the Kohn-Sham band gap is the *GW* approximation method [191, 192]. A detailed description of the *GW* method is, however, beyond the scope of this thesis.

The band gap correction can be alternatively performed through the *scissor shift method*, which, effectively, rigidly shifts the conduction bands towards higher energies [193]. This shift can be constant, or wavevector or energy dependent. The magnitude of the shift can be determined based on *GW* calculations [194], or just chosen to reproduce the experimental band gap (in which case it is an empirical correction).

Fortunately, despite the band gap error in DFT, we are not interested in this thesis in the absolute value of the gap or quantities related to it (such as the refractive index). Rather, we are interested in the trends that these quantities show as a function of some structural perturbations, as discussed earlier in this chapter. We expect these trends to be robust, as confirmed in Ref. [195], where the strain-induced changes in the GW gaps were reported to show similar trends to the DFT-LDA trends. Therefore, the DFT-LDA band gaps shall be reported throughout in this thesis, unless stated otherwise.

4.3 The simulation of epitaxial strain

The simulation of a *real* thin film, along with its characteristic structural complexities, is obviously out of reach, in the sense that an extremely large simulation cell would be required. Traditionally, the problem of investigating the properties of thin films is approached, from first-principles, by considering *bulk* material and introducing one or more of the structural perturbations that are mentioned above such as strain or defects (e.g., see [75]). This approach has the virtue of disentangling the individual effects of each perturbation, allowing

self energy, as discussed in the main text.

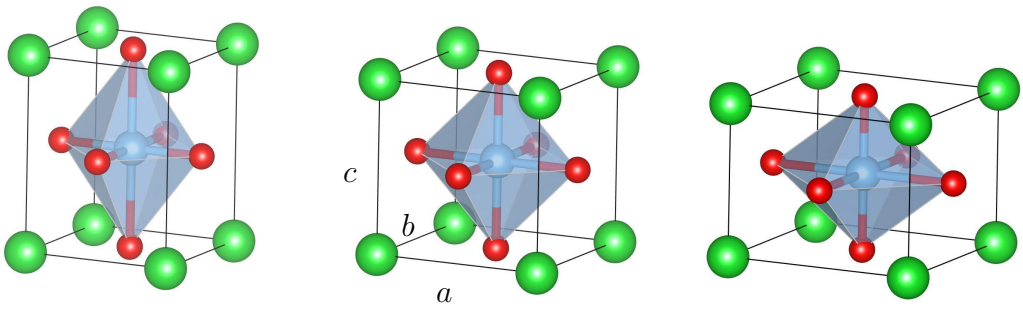


Figure 4.1: Illustration of the application of biaxial strain on a cubic perovskite unit cell. **(Middle):** Strain-free system. **(Left):** System under compressive strain. **(Right):** System under tensile strain. The amount of strain is exaggerated for illustration purposes.

a quantitative comparison between them.

Epitaxial strain might be the most pronounced factor that makes thin films differ from the bulk, as discussed in Sec. 1.4.1. Considering the [001] growth direction, epitaxial strain is mimicked by introducing biaxial strain on the (001) plane to the bulk material. This is practically achieved by straining the in-plane lattice parameters a and b (see Fig. 4.1), with the amount of strain ϵ defined by

$$\epsilon = \frac{a - a_0}{a_0} \times 100\% \,, \tag{4.9}$$

where a and a_0 are the strained and strain-free lattice parameters along the [100] direction, respectively. Our simulations can be thought of as an approximation to the experimental perspective, where the strained lattice parameter a is determined by the lattice parameter of the substrate for a coherent epitaxial growth.

Assuming a growth on a substrate whose ab plane is square, the in-plane lattice parameters are constrained to be equal and orthogonal. The out-of-plane lattice parameter c is then allowed to fully relax, while constrained to be perpendicular to the (001) plane. Unless stated otherwise, all the ionic degrees of freedom are also fully relaxed without constraints. Therefore the cubic or tetragonal symmetry is imposed on all the lattices considered in this chapter.

It is worth noting that one should not confuse the strain-free lattice parameter a_0, appearing in the above equation, with the lattice parameter of

the fully relaxed bulk system at 0 K. The former is determined by relaxing the system under the constraints mentioned above. In other words, a_0 is the lattice parameter that minimizes the total energy of the system subject to the aforementioned constraints.

In connection to real systems, the simulated systems that we are considering here can then be thought of as being generated by taking a single unit cell from the deep interior of the "real" film and infinitely periodically repeating it in space [75].

4.4 Computational details

The DFT calculations in this chapter were performed with the plane-wave abinit package [123–125]. The local density approximation (LDA) was used to approximate the exchange and correlation functional. Extended norm-conserving pseudopotentials were used, in which the Ba $5s$, Ti $3s$ and O $2s$ electrons are all treated as valence states. A high energy cutoff of 55 Ha ($\sim$ 1500 eV) was used in order to reduce the effect of Pulay stresses (see Sec. 3.6). The integration over the Brillouin zone was performed by summing over a dense Monkhorst-Pack k-point mesh of size $9 \times 9 \times 9$, in order to obtain accurate forces. DFT-LDA converged lattice parameters were adopted throughout, unless stated otherwise. The BFGS algorithm was used to relax the ionic and the cell degrees of freedom so that the force on each ion was less than 0.05 meV/Å and the relaxed component of the stress tensor was less than 0.01 GPa.

Once the self consistent Kohn-Sham density and potential have been determined, the energy eigenvalues are calculated on a denser mesh of k-points along special symmetry directions in the Brillouin Zone via a non-self consistent calculation in order to obtain the band structure of the system, from which the direct and the indirect Kohn-Sham band gaps are determined.

System	quantity	this work	(DFT-LDA) Ref. [197]	Experiment
BTO	a	3.94	3.96	4.00 [30]
	B	199	196	195 [198]
	$E_{\mathrm{g}}^{\mathrm{i}}$	1.80	1.92	3.20 [199]
	$E_{\mathrm{g}}^{\mathrm{d}}$	1.89	1.98	
STO	a	3.84	3.86	3.90 [200]
	B	208	222	179 [198]
	$E_{\mathrm{g}}^{\mathrm{i}}$	1.89	2.04	3.25 [201]
	$E_{\mathrm{g}}^{\mathrm{d}}$	2.22	2.36	3.75 [201]

Table 4.1: The lattice constants a (in Å), the bulk moduli B (in GPa), and the direct $E_{\mathrm{g}}^{\mathrm{d}}$ and indirect $E_{\mathrm{g}}^{\mathrm{i}}$ gaps (in eV) of BTO and STO, as compared between the present work and literature results.

4.5 Structure and electronic structure of BTO and STO

In Table 4.1, the structural and electronic properties of the cubic paraelectric phases of BTO and STO are compared with similar DFT-LDA results in the literature, and with the available experimental values. These calculations were performed in our previous work [196]. The lattice constants, the bulk moduli and the energy gaps show a good agreement to similar calculations performed in the literature. However, the lattice constants and the bulk moduli are underestimated and overestimated, respectively, as compared with experiment, which is a well-known limitation of the DFT-LDA approach (see Sec. 3.3.3). The energy gaps are underestimated by about 40%, which is also expected as discussed in Sec. 4.2.

The electronic band structures of BTO and STO, as obtained from DFT-LDA calculations, are depicted in Fig. 4.2, where we show only the highest occupied (mainly of O $2p$ character) and the lowest unoccupied (mainly of Ti $3d$ character) states. The band structure of these materials is well-known and has already been investigated in our previous work [196] and in the literature (e.g., see Ref. [197]). As can be noticed from Fig. 4.2, the valence band maximum

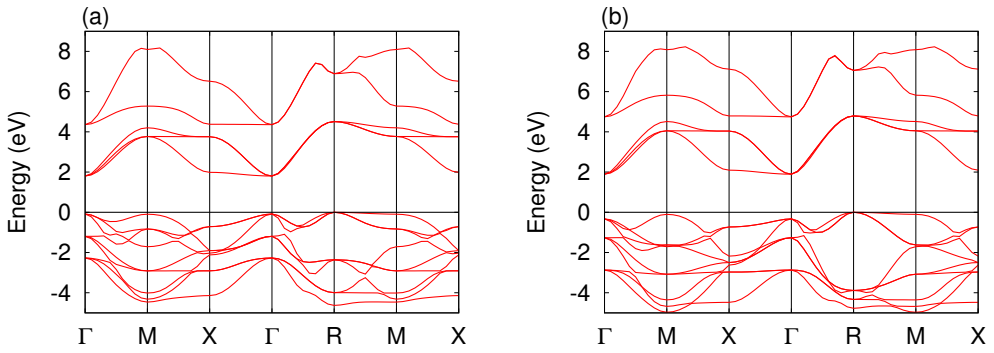


Figure 4.2: The calculated electronic band structure of BTO (a) and STO (b) along high symmetry directions in the Brillouin zone. The highest valence and the lowest conduction states are only shown. The valence band maximum is set at zero energy.

is found at the R point in the Brillouin zone, whilst the conduction band minimum is found at Γ, making the gap of these materials indirect.

4.6 Effect of strain on the electronic properties of BTO

The strain-induced changes of the direct gap E_g^d (also referred to as the optical gap) and the indirect gap E_g^i of BTO are depicted in Fig. 4.3. We have adopted a wide range of strain from -4% to 4%. One should note, however, that the values of strain toward the extrema of this range are quite high, and it is likely that in reality the film would relieve such strains, for instance, through forming dislocations. In this case, the maximum value of strain that a thin film can sustain is governed by the interplay between the strain energy and dislocations energy densities, with the specific material and the thickness of the film playing crucial role in determining the value [202]. However, it is possible, in principle, for sufficiently thin films to accommodate these high values of strain, and perovskite or non-perovskite substrates that could induce such strains already exist commercially[3] [202, 203].

[3]In Refs. [202, 203], a wide range of commercially available substrates are listed with lattice parameters ranging from $\sim 3.7 - 4.2$ Å. It should be noted, however, that these substrates are not abundant enough to generate the strain resolution that we have adopted in our study.

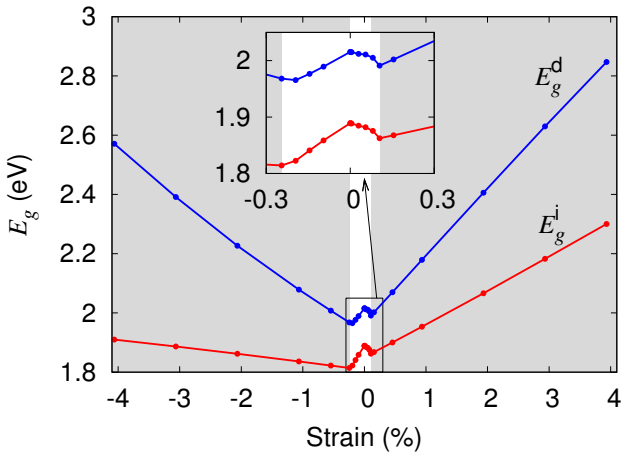


Figure 4.3: Effect of epitaxial strain on the direct ($\Gamma - \Gamma$) and the indirect ($R - \Gamma$) bandgaps of pure BTO, represented by the blue and the red curves, respectively. The region surrounded by the rectangle is enlarged in the inset. The unshaded region highlights the range of strain where the gap is decreased by increasing strain. The opposite trend is highlighted by the shaded region.

Fig. 4.3 shows that BTO remains an indirect gap material throughout the entire range of strain considered. This is in contrast to some materials, such as Ge, which undergoes a change in its band gap from indirect to direct at certain types and values of strain [204].

Both direct and indirect gaps show the same qualitative trend as a function of strain. However, there is an interesting feature in Fig. 4.3 that demands explanation. Starting from the unstrained system (0%), an increase in biaxial strain (whether tensile or compressive) results in a decrease in E_g^i and E_g^d (unshaded region in Fig. 4.3). Beyond -0.25% compressive and 0.1% tensile strain, the trend is reversed (shaded region) and gaps increase. Furthermore, the change in E_g is almost linear with respect to strain in each region.

Explanation of the anomalous feature

Beyond the unshaded region, the gaps start to increase almost linearly, with E_g^d showing a greater rate of increase than E_g^i. This can be attributed to the fact that the energy of the valence band[4] at Γ is much more strongly affected

[4]We maintain consistency in the calculation of the band edges at all values of strains by aligning the most deep isolated semicore states that correspond to Ti 3s with the corre-

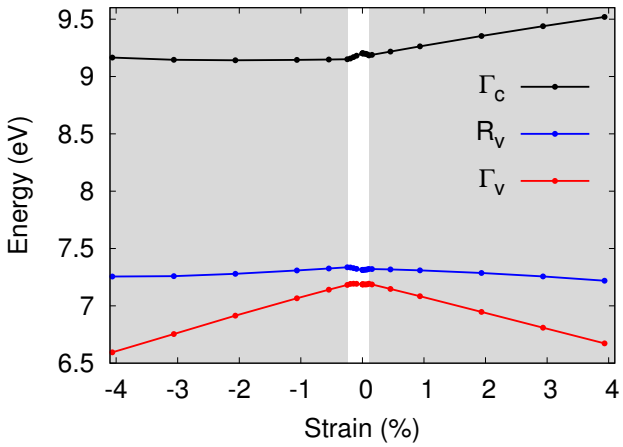


Figure 4.4: Strain-induced changes in the band edges of BTO at Γ and R. The v and c subscripts refer to the valence and the conduction bands, respectively.

by strain than the energy of the valence band maximum at R, which is almost constant (see Fig. 4.4).

The difference in the trend of E_g between the unshaded and shaded regions that is evident in Fig. 4.3 can be explained in relation to the direction of the spontaneous polarization of the material that is induced by the displacements of the Ti and O atoms off their high-symmetry (or ideal) sites. We quantify the magnitude and the direction of the atomic displacements by the quantity $\mathbf{Q}$, defined as

$$\mathbf{Q} \equiv \sum_i q_i \, \mathbf{r}_i \tag{4.10}$$

where the integer i runs over each ion in the unit cell, q_i is the formal charge of the i^{th} ion and $\mathbf{r}_i$ is its position with respect to the Ba ion (that is set at the origin).

The quantity $\mathbf{Q}$, should not be understood to give the "correct" magnitude of the spontaneous polarization of the material, where the latter is rigorously defined and calculated within the framework of the modern theory of polarization (see Chapter 1). However, $\mathbf{Q}$ *does* describe the relevant changes in the magnitude and direction of atomic displacements (and hence the polarization) as a function of strain.

sponding states of the strain-free system.

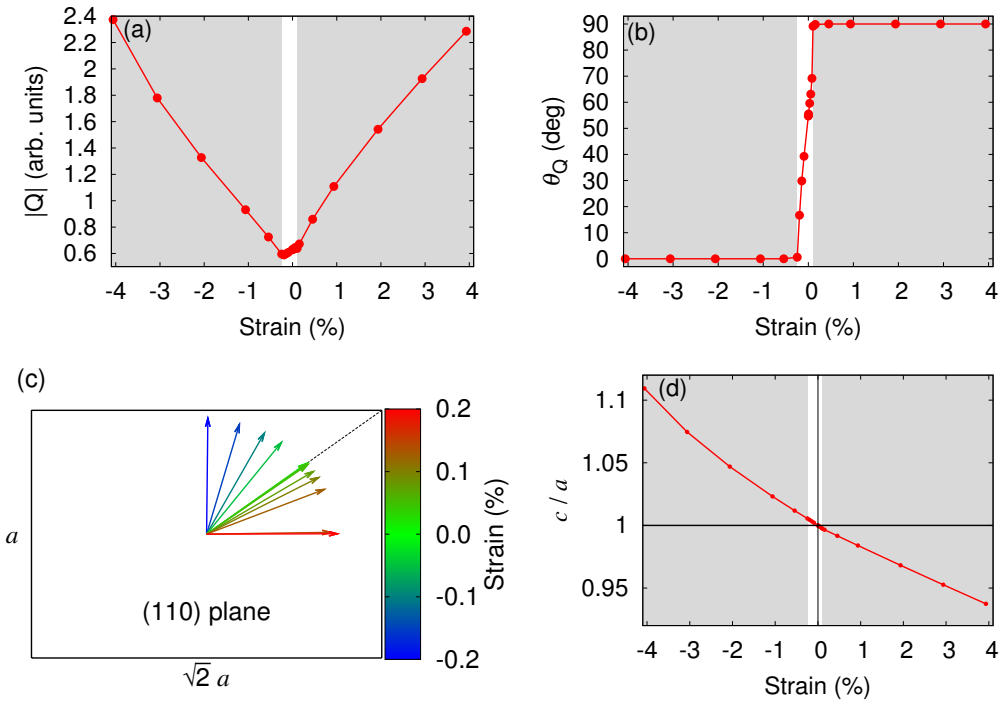


Figure 4.5: The magnitude (a) and the direction (b) of **Q**, defined in Eq. 4.10, for pure BTO. The angle θ_Q is measured from the c axis. Panel (c) illustrates the rotation of the polarization vector for the values of strains represented by the unshaded region, where the magnitude is exaggerated for clarity. The relative dimensions of the (110) plane correspond to the strain-free structure. The corresponding vector of the strain-free system is extrapolated by the dashed line. Panel (d) shows the c/a ratio of the system as a function of strain.

The magnitude and the direction (with respect to the c axis) of **Q** ($|\mathbf{Q}|$ and θ_Q, respectively) are plotted in Figs. 4.5a and 4.5b, respectively. Fig. 4.5a indicates that the spontaneous polarization of BTO can be greatly enhanced by means of epitaxial strain, which is in agreement with the experiment [72], as pointed out in Sec. 1.4.1.

Fig. 4.5b shows clearly that the range of strains within the unshaded region corresponds to a transition from a pure out-of-plane (i.e., along the c-axis, represented by the left shaded area) to a pure in-plane (right shaded area) state of polarization. From Fig. 4.5a it is seen that the rate of change of the magnitude of **Q** in the unshaded region (low strain) also differs from that in the shaded region (high strain), where it varies much faster in the latter. As depicted in Fig. 4.5c, the transition state involves a smooth rotation of

the polarization vector from the [001] to the [110] direction, where it lies in the (110) plane throughout the transition. It turns out that this transition directly affects and explains the different qualitative trend of the band edges and, therefore, the band gap of the material at the corresponding values of strains represented by the unshaded region.

It can be noticed that the direction of the polarization vector can be correlated with the tetragonality of the system. Fig. 4.5d shows how the ratio c/a is affected by strain. For high compressive strains, this ratio is relatively high, inducing a a pure out-of-plane polarization. The opposite is true for high tensile strains. However, in the region of small strains (the unshaded region), the system is almost cubic[5] with c/a being close to unity. In particular, at the 0% strain the lattice is perfectly cubic and the polarization vector points towards the [111] direction. This apparent relation between the polarization direction and the tetragonality of the system shall be investigated in more detail in Sec. 4.7.1.

Comparison with the literature

Our calculations of the polarization direction as a function of epitaxial strain are in a qualitative agreement with the first-principles work that is performed in Ref. [205], but they are in contradiction with the effective-Hamiltonian based work in Ref. [206], in which the polarization vector in the unshaded region is reported to lie in the (101) plane.

In spite of the qualitative agreement with Ref. [205], we should point out that our calculations differ in the unit cell structure in the range of strains described by the unshaded region. In our calculations, we considered a [001] growth direction normal to the substrate, which in turn imposes a constraint that the c parameter is normal to the (001) plane, restricting the lattice to cubic/tetragonal symmetry. In Ref. [205], this constraint is relaxed allowing the c parameter incline with respect to the (001) plane, leading to a monoclinic lattice structure. In the shaded region, however, our structures are in full agreement with Ref. [205].

[5]The reader should note that by "cubic" (here and throughout) we refer to the fact that all the lattice constants are equal and orthogonal. More rigorously, taking into account the atomic displacements, the crystal system of BTO at 0% strain is actually classified as being rhombohedral with the $R3m$ space group. The term "tetragonal" is also used in the same context in this thesis.

Strain	$\Delta E_{\mathrm{g}}^{\mathrm{i}}$	$\Delta E_{\mathrm{g}}^{\mathrm{d}}$
−4%	0.021	0.556
−3%	−0.002	0.376
−2%	−0.027	0.211
−1%	−0.053	0.063
0%	0.000	0.000
1%	0.064	0.164
2%	0.177	0.390
3%	0.293	0.614
4%	0.411	0.832

Table 4.2: The changes (in eV) in the direct and the indirect gaps of BTO as affected by epitaxial strain. The differences are calculated with respect to the gaps of BTO as 0% strain. All strains considered in this table belong to the shaded region depicted in Fig. 4.3.

The "width" of the unshaded region, as predicted by our calculations, also differs from the corresponding region in Ref. [205]. We believe that this is strongly influenced by the value of the lattice constant that is adopted for the strain-free system, as shall be discussed in Sec. 4.7.1. The difference in the computational details lead to a small difference in the converged lattice constants that, in turn, affect the width of the unshaded region.

Quantifying the changes in E_{g}

In order to have a clearer idea about the extent to which the BTO bandgaps might be engineered by means of strain, we quantify the strain-induced changes in the bandgaps in Table 4.2. The indirect gap shows a negligible change at negative strains, while it shows an increase up to ~ 0.4 eV at 4% strain. In contrast, the optical gap is strongly affected by both compressive and tensile strains, showing an increase of up to ~ 0.5 eV and ~ 0.8 eV at -4% and 4%, respectively.

It is noteworthy to highlight that both compressive and tensile strains have a qualitatively similar effect on the bandgap of BTO, in the sense that they both widen the gap. For instance, our results suggest that an increase of 0.2 eV

in the optical gap can be achieved by depositing BTO either on a compressive substrate with $\epsilon \approx -2\%$, or alternatively on a tensile substrate with $\epsilon \approx 1.2\%$. This suggests that, for the purpose of engineering the gap of BTO, the already available compressive substrates could replace some unavailable tensile substrates, or vice versa, since they would produce the same effect on the bandgap. It should be noted, however, that the anisotropy of the film is not the same in the two strain regimes, as quantified by the refractive index and the birefringence of the material; this shall be discussed in the next chapter.

Furthermore, the rate of decrease/increase in the bandgap is different for compressive and tensile strains, as can be noticed in Fig. 4.3. This shall be discussed in detail in the following section, where we study the strain-induced changes in the gaps of pure STO.

4.7 Effect of strain on STO bandgaps

The direct and indirect gaps of pure STO, as affected by epitaxial strain, are depicted in Fig. 4.6. Similar to BTO, STO remains an indirect gap material throughout all the considered values of strain.

The qualitative trends of the gaps of STO are similar to those of BTO. For moderate strains ranging between -1.2% and 0.95% (which are illustrated by the unshaded region in Fig. 4.6), the gaps decrease following a piecewise linear behaviour. Beyond this region, the gaps start to increase at a higher rate.

The origin of the existence of the two regions

In contrast to the gaps of BTO, the discontinuities that are observed in the case of STO have a different physical origin, though it is still linked to the spontaneous polarization of the system. Indeed, in the case of STO, the unshaded region corresponds also to a transition from an out-of-plane (along [001]) to an in-plane (along [110]) polarization state, as depicted in Fig. 4.7. However, the transition involves a complete inhibition of the ferroelectricity of the material rather than a smooth rotation of the polarization vector. This result suggests that this strain-induced ferroelectric transition is of a displacive nature rather than an order-disorder nature (see Sec. 1.3.2).

These results are not surprising actually, since strain-free BTO is a well-

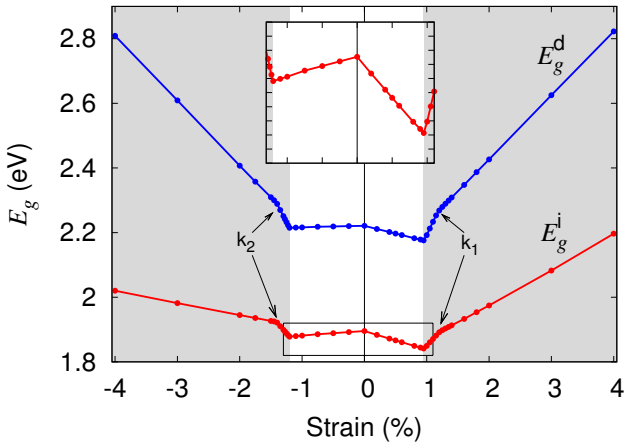


Figure 4.6: Effect of epitaxial strain on the direct ($\Gamma - \Gamma$) and the indirect (R$-\Gamma$) bandgaps of pure STO, represented by the blue and the red curves, respectively. Region surrounded by the rectangle is enlarged in the inset. The unshaded and shaded regions highlight the strain ranges within which the gap decreases and increases, respectively. k_1 and k_2 indicate observed kinks in the gaps within the tensile and compressive strains range, respectively.

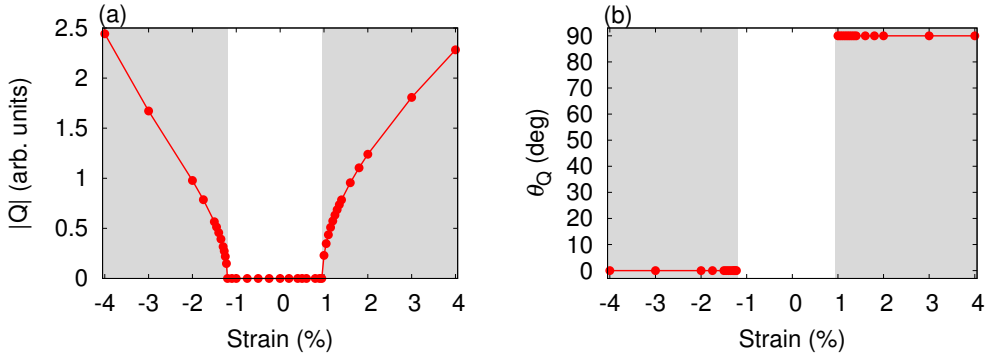


Figure 4.7: The magnitude (a) and direction (b) of **Q**, defined in Eq. 4.10, for pure STO.

known ferroelectric material, in contrast to STO that is not ferroelectric even at low temperatures (see Sec. 1.2.1 and 1.2.2), which is completely consistent with our results. In addition, Fig. 4.7 shows the role of epitaxial strain in inducing ferroelectricity in STO, which is also consistent with experiment (see Sec. 1.4.1 and Ref. [34]). On the other hand, the role of the atomic displacements (and hence polarization) in widening the gap in STO is confirmed by the work in Ref. [195], where it is attributed to the fact that the ferroelectric distortions lower the symmetry of the system and thus allow orbital mixing between the lowest conduction bands (mainly of Ti $3d$ character) and the highest valence bands (mainly of O $2p$ character).

Interpretation of the trend in E_{g} within the unshaded region

As depicted in Fig. 4.8a, unstrained STO has a perfect cubic symmetry with a c/a ratio equal to unity. The cubic symmetry is broken with the application of strain. Interestingly, this suggests that breaking the cubic symmetry does not necessarily imply the breaking of the inversion symmetry of the system (since atoms are in their high symmetry positions for all values of strain in the unshaded region), and it is possible, in principle, for a perovskite to adopt a tetragonal phase with a $P4/mmm$ symmetry while not showing spontaneous polarizaion.

It turns out, then, that the reduction in the direct and indirect band gaps of STO due to strain in the unshaded region can be attributed to the lowering of the symmetry of the system. This is explained in view of breaking the degeneracy of the valence and the conduction bands. To further clarify it; due to the cubic symmetry at 0% strain, the highest valence and lowest conduction band edges are three-fold degenerate. When the cubic symmetry is lowered to the tetragonal symmetry, these states are split into a singlet and a doublet state, resulting in a reduction in the bandgap on both sides of the strain-free point. This is also in agreement with the analysis in Ref. [195].

Although this interpretation explains the reduction in the band gap due to strains in the unshaded region, it does not clearly account for the different *rates* of decrease in E_{g} between compressive and tensile strains, as depicted in the inset of Fig. 4.6, where it is steeper at positive (tensile) strains.

As shown in Fig. 4.8, epitaxial strain does not only distort the cubic sym-

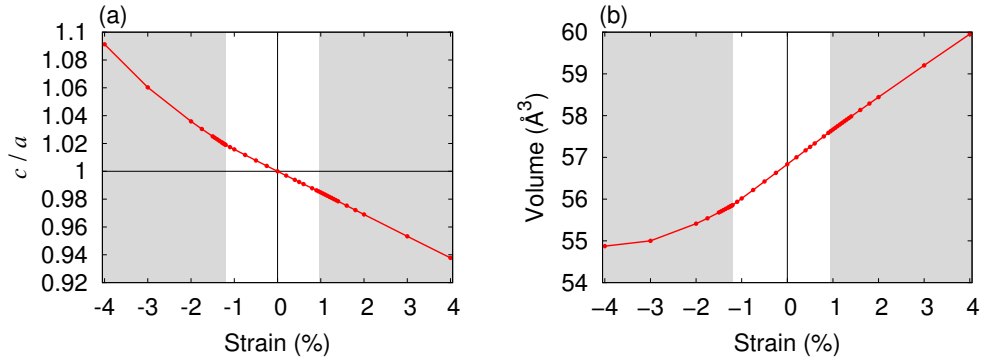


Figure 4.8: Effect of epitaxial strain on the tetragonality ratio (a) and the volume per unit cell (b) of pure STO.

metry, but it induces an overall change in the volume of the system as well. Our attempt to explain the different gradients in E_g as a function of strain is based on disentangling the effects of the changes in the tetragonality and the volume on the bandgap of the system. We achieve this by expanding E_g in a Taylor series, treating the reduced[6] volume $\widetilde{V}$ and the tetragonality $\eta \equiv c/a$ as order parameters:

$$\begin{aligned} E_g(\widetilde{V},\eta) &= E_g^0 + \left.\frac{\partial E_g}{\partial \eta}\right|_{\widetilde{V}} (\eta - \eta^0) + \left.\frac{\partial E_g}{\partial \widetilde{V}}\right|_{\eta} \left(\widetilde{V} - \widetilde{V}^0\right) + \dots , \\ &\equiv E_g^0 + \Delta^{\eta} + \Delta^{\widetilde{V}} + \dots , \end{aligned} \tag{4.11}$$

where $E_g^0 \equiv E_g(\widetilde{V}^0, \eta^0)$, η^0 and $\widetilde{V}^0$ are the tetragonality and the reduced volume of the system at 0% strain, respectively[7], and the derivatives are evaluated at 0% strain. Our approximation is to keep only the first-order terms in the expansion above, neglecting the higher order and cross partial derivatives.

The evaluation of the first-order derivatives is performed by taking the gradient of the best fit line to the relevant DFT results that are shown in Fig. 4.9 (only the indirect gap gradients are shown). In Fig. 4.9a, the tetragonality of the system is varied while the volume is held constant at $\widetilde{V}^0$ (i.e., volume-conserving biaxial strain is applied). In Fig. 4.9b, the volume of the system is

[6]For convention, we deal with a dimensionless (or reduced) volume $\widetilde{V} \equiv V/V^0$, where V is the volume per unit cell of the system at an arbitrary strain, and V^0 is the corresponding volume per unit cell at 0% strain.

[7]Obviously, η^0 and $\widetilde{V}^0$ are equal to one.

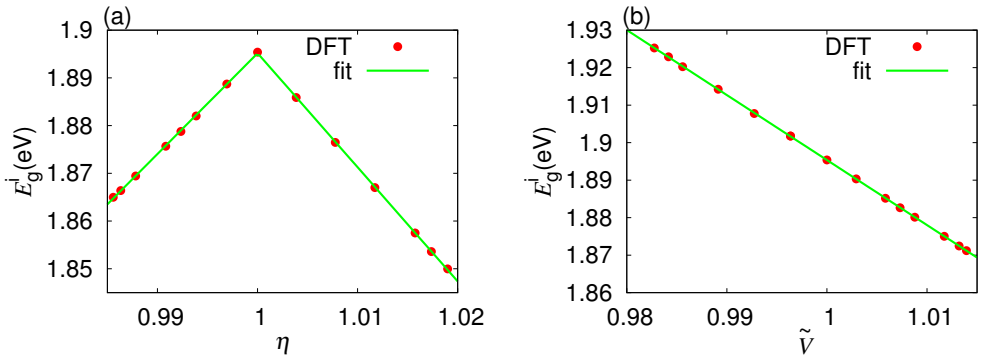


Figure 4.9: The data sets and the corresponding fits that are used to evaluate $\partial E_g/\partial\eta$ (a) and $\partial E_g/\partial\widetilde{V}$ (b) that appear in Eq. 4.11. The data points are obtained from DFT calculations. $\widetilde{V}$ and η are held fixed in (a) and (b), respectively. The slopes of the best fit lines are tabulated in Table 4.3. All data correspond to pure STO system.

varied while maintaining the cubic symmetry throughout (i.e., isotropic strain is applied). In both cases, the values of η and $\widetilde{V}$ considered are such that they lie within the same range of the corresponding values in the unshaded region of Fig. 4.8.

The excellent fit that is achieved in Fig. 4.9 increases the reliability in the evaluated gradients, and the linear trends support the approximation of keeping only the first order terms in the Taylor expansion.

The values of the first-order partial derivatives, as evaluated from the slopes of the best-fit lines shown in Fig. 4.9, are tabulated in Table 4.3. In contrast to $\partial E_g/\partial\widetilde{V}$, which is defined for all $\widetilde{V}$ in the considered domain, $\partial E_g/\partial\eta$ is not well-defined at η^0, where it experiences a jump discontinuity. Therefore, we tabulate in Table 4.3 both the left and right derivatives (that correspond to tensile and compressive strains, respectively), and compressive and tensile strains are treated separately in Eq. 4.11 by using the corresponding values of the derivatives.

We compare in Fig. 4.10 the strain-induced changes in the band gap of STO that are obtained directly from DFT calculations to the corresponding gaps that are calculated from the approximation of Eq. 4.11. The good reproduction of the DFT gaps indicates the success of our approach in approximating the changes in the gaps of STO at moderate strains. In addition, it also suggests that the effects of volume and tetragonality on E_g are almost decoupled and,

	Indirect gap		Direct gap	
	$\epsilon < 0$	$\epsilon > 0$	$\epsilon < 0$	$\epsilon > 0$
$\left.\frac{\partial E_g}{\partial \eta}\right\|_{\widetilde{V}}$	-2.39	2.11	-1.06	2.28
$\left.\frac{\partial E_g}{\partial \widetilde{V}}\right\|_{\eta}$	-1.73		-0.94	

Table 4.3: The numerical values of the Taylor expansion coefficients appearing in Eq. 4.11, calculated from the best-fit lines shown in Fig. 4.9. The corresponding gradients of both E_g^i and E_g^d are quoted. The slopes are given in units of eV. All data correspond to pure STO system.

to a very good approximation, are additive.

In view of this approximation, it is straightforward to account for the different rates by which E_g decreases in the two strain regimes. As indicated in Fig. 4.10, both $\widetilde{V}$ and η tend to decrease the gap at positive strains, whilst they oppose each other at negative strains, with $\widetilde{V}$ tending to open the gap. This immediately leads to a greater rate of reduction in the gap at positive strains since the effects of $\widetilde{V}$ and η are cooperative.

One might think to expand the above discussion to approximate E_g at higher strains by including the spontaneous polarization of the material as another order parameter in Eq. 4.11. Indeed, we have tried this by representing the polarization with the quantity $\mathbf{Q}$ (defined in Eq. 4.10), but it turned out that polarization is strongly coupled with volume and tetragonality, and treating it as an additional additive effect fails to reproduce the gaps at higher strains. In other words, it is essential to consider higher-order cross partial derivative terms in Eq. 4.11 to accurately represent the effect of polarization, but this was beyond the scope of this study.

When the strain-induced ferroelectric distortions are inhibited, one would observe the disappearance of the shaded region in Fig. 4.6 and the gaps would continue to decrease with increasing strain, as could be understood from our earlier discussion. This is also confirmed by the work in Ref. [195]. In which case, the obtained gaps from Eq. 4.11 show a slight deviation to the DFT gaps at higher values of strains. This actually could be attributed to the fact that

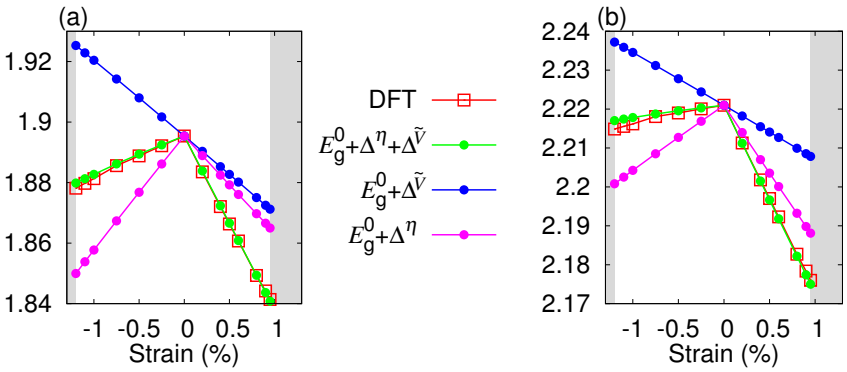


Figure 4.10: A comparison of the strain-induced changes in E_g^i (a) and E_g^d (b) between direct DFT calculations (red) and Eq. 4.11 (green). The individual effects of the volume and the tetragonality are also illustrated by the blue and purple curves, respectively. Energies are given in units of eV. All data correspond to pure STO system.

the trend of E_g with strain is not perfectly linear, and the accuracy of Eq. 4.11 could be improved by including higher-order terms in Eq. 4.11.

Interpretation of the "kinks" in E_g as a function of strain.

Lastly, having discussed the main features that are observed in the trend of E_g as a function of strain in Fig. 4.6, namely; 1. the sudden increase in the band gap at the boundary between the unshaded and the shaded regions, and 2. the different rates of decrease in the gap within the unshaded region, we would like to comment on the "kinks" that are indicated by the labels k_1 and k_2 in Fig. 4.6. These can be understood by considering the strain-induced changes in the energies of the lowest conduction states.

We show in Fig. 4.11 the lowest three conduction bands at selected values of tensile strains[8]. These bands are of Ti $3d$ character and, more explicitly, they have t_{2g} symmetry with the d_{xy}, d_{yz} and d_{xz} states represented by the blue, red and green curves, respectively. At the strain-free point, Fig. 4.11a indicates a full degeneracy of these states at Γ due to the cubic $Pm\bar{3}m$ symmetry, as explained earlier. Within the range of strain that is represented by the unshaded region, the symmetry is lowered to tetragonal $P4/mmm$, and Fig. 4.11b shows that the three-fold degeneracy is hence broken with the split-

[8] A similar discussion applies for compressive strains, whose effect is not shown.

ting off of the d_{xy} state from the d_{yz} and d_{xz} states, which remain degenerate. When the strain is further increased beyond the unshaded region, the symmetry is lowered to $Amm2$ due to the breaking of inversion symmetry that is induced by the ferroelectric distortion, and this is reflected on the splitting of the d_{yz} and d_{xz} states, as shown in Fig. 4.11c. This splitting is further increased with increasing strain, and at a critical value of $\epsilon \approx 1.2\%$, the d_{yz} state crosses the d_{xy} state, as depicted in Fig. 4.11d. At higher values of strain, the d_{yz} state becomes the lowest conduction state at Γ, replacing the d_{xy} state (Fig. 4.11e), leading to a different rate of increase in E_{g}, and hence inducing the aforementioned kink at the crossing point (labelled k_1). It should also be pointed out that the valence states at Γ also experience such crossing at almost the same value of strain, while no crossing is observed at R.

The corresponding kink at compressive strains (k_2) is also attributed to a band crossing at the corresponding strain. However, it should be noted that compressive strains do not break the degeneracy between the d_{yz} and d_{xz} states, so they cross the d_{xy} state *together* at the "kink".

Quantifying the changes in E_{g}

Much as in BTO, the results in Table 4.4 indicate that epitaxial strain could be a promising means by which the gaps of STO can be tuned, in spite of small quantitative differences between the effects on the two systems.

The results suggest that the direct gap can be tuned "more easily" than the indirect gap: $E_{\mathrm{g}}^{\mathrm{d}}$ can be increased by as much as ~ 0.6 eV at 4% strain, compared to an increase of only ~ 0.3 eV shown by $E_{\mathrm{g}}^{\mathrm{i}}$. Compressive strains have less effect on the gaps, however: a highly compressive strain of -4% only opens $E_{\mathrm{g}}^{\mathrm{i}}$ by ~ 0.13 eV, while $E_{\mathrm{g}}^{\mathrm{d}}$ experiences an increase of ~ 0.59 eV.

At moderate strains (within the unshaded region in particular, which covers larger values of strains as compared to BTO), the gaps show a small decrease of less than ~ 0.1 eV.

It is worth noting that these trends are subject to a little modification depending on the lattice parameter adopted for the strain-free structure and, hence, implicitly on the XC functional used. This issue is discussed in the next section.

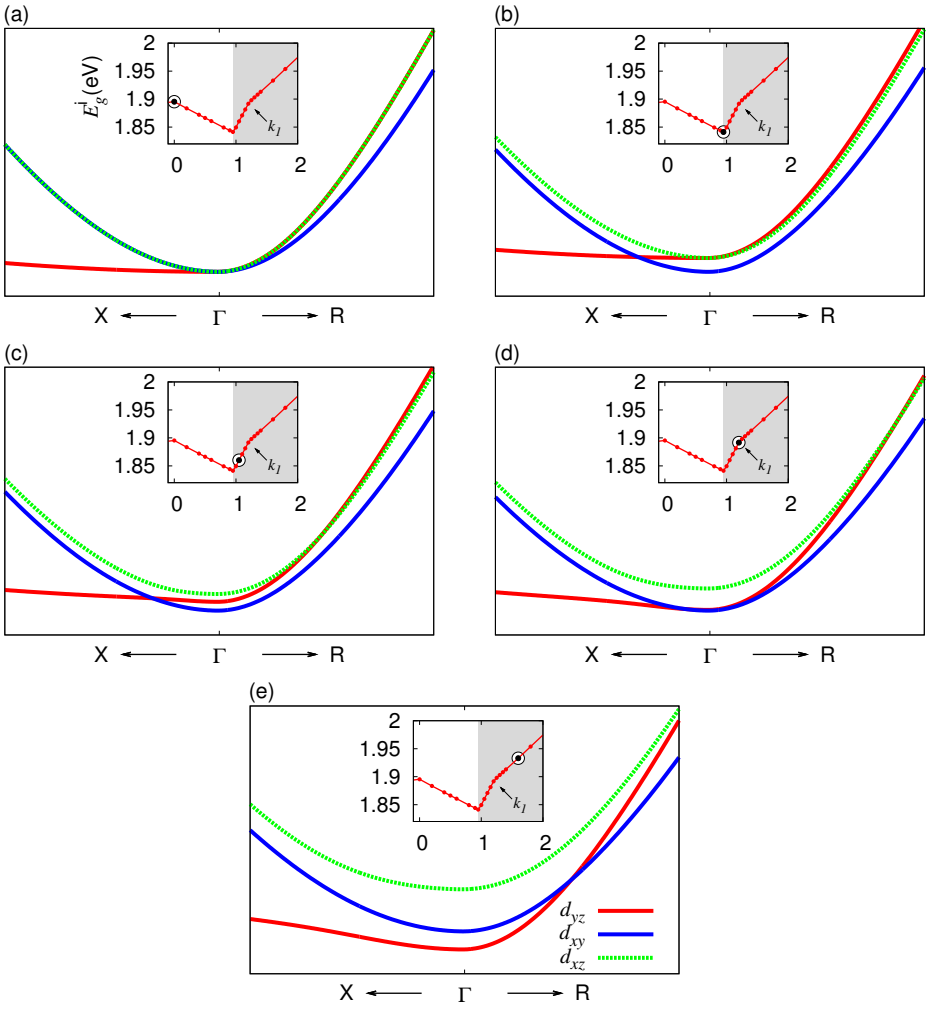


Figure 4.11: The lowest three Ti $3d$ conduction states at selected values of tensile strains. The curve of $E_{\rm g}^{\rm i}$ versus strain is shown in the inset, where we have circled the corresponding point for which the states are shown. The minima of the states at Γ are all set to the same reference for convenience. An extremely high resolution of k-points along the X−Γ−R path is used to allow a straightforward disentangling of the bands.

Strain	$\Delta E_{\mathrm{g}}^{\mathrm{i}}$	$\Delta E_{\mathrm{g}}^{\mathrm{d}}$
-4%	0.125	0.588
-3%	0.086	0.388
-2%	0.049	0.186
-1%	-0.014	-0.005
0%	0.000	0.000
1%	-0.046	-0.029
2%	0.079	0.205
3%	0.187	0.404
4%	0.301	0.602

Table 4.4: The changes (in eV) in the direct and the indirect gaps of STO as affected by epitaxial strain. The differences are calculated with respect to the gaps of STO as 0% strain.

4.7.1 Comparison with the work in the literature

There exist several first-principles studies in the literature regarding the strain induced changes in the structure and energy gaps of cubic STO. However, there exist some discrepancies in the results of these investigations, where some of them are in qualitative agreement with our results, and others are not. On the one hand, in Refs. [207, 208], STO is reported to undergo phase transitions as a function of epitaxial strain similar to the transitions that our results show. However, the "width" of the paraelectric (unshaded) region is different in these two studies and, at the same time, they both differ from our results. On the other hand, no region of biaxial strain in which the system is paraelectric is reported to be present in Ref. [195]; instead they observe the ferroelectric distortion for even the smallest value of the strain they considered.

Indeed, we attribute these discrepancies to the small differences in the equilibrium lattice constant a_0 of strain-free STO that is adopted in these studies. In Table 4.5, we compare the values and give the critical strains at which the ferroelectric transition is induced.

The width of the paraelectric (unshaded) region shows a clear correlation to the value of a_0, where it covers higher values of strains as a_0 gets lower. At first glance, the study in Ref. [195] seems to violate this trend since the

Study	a_0 (Å)	critical strain (%)		critical a (Å)
		$\epsilon < 0$	$\epsilon > 0$	
Ref. [208]	3.87	-0.1	0.3	3.882
Ref. [195]	3.864	–	–	–
Ref. [207]	3.855	-0.75	0.54	3.876
This work	3.845	-1.2	0.95	3.881

Table 4.5: The equilibrium DFT-LDA lattice parameter of strain-free STO a_0 and the critical values of compressive and tensile strains at which the ferroelectric transition is induced. The data are obtained from three different references and compared to this work. We explicitly quote the corresponding values of the strained in-plane lattice parameter a in the last column.

width of the paraelectric region apparently vanishes, despite the fact that the corresponding a_0 is lower than that of Ref. [208], with the latter study showing a finite width of the region. However, we believe that the strain resolution that is adopted in Ref. [195] (steps of 0.5%) is not fine enough for the paraelectric region to appear, and that the same trend would be observed if smaller strains were considered.

This trend can be explained in view of the well-known correlation between the ferroelectricity of the system and its size (see Sec. 1.3.3 and Refs. [51, 209, 210]). For instance, it was shown in Ref. [51] that when BTO undergoes a decrease in its *volume* as a response to a compressive *isotropic* strain, the ferroelectricity of the system is consequently decreased until it is completely inhibited below a critical volume. On the other hand, ferroelectricity is enhanced when the volume is increased. Similar behaviour is also shown for other perovskites.

"Space" condition for ferroelectricity

The idea of the existence of a critical volume for the appearance of ferroelectricity is generalized in our next discussion in order to account for the application of "biaxial" rather than "isotropic" strain. We propose a necessary, but not sufficient, condition (which we refer to as a "space" condition) that ferroelectricity along a certain crystallographic direction ([100], [010] or

[001]) is induced only above a critical value of the *lattice constant* (which shall be denoted with an asterisk) along that direction. The relevant polarization component can then be enhanced by increasing the value of the corresponding lattice parameter. So, instead of correlating the "total" polarization vector of the system with the "volume" of the system, we correlate the individual projections of the polarization vector along the a, b, and c directions with the "lengths" of the corresponding lattice vectors[9].

For epitaxially strained STO, the space condition suggests that the in-plane ferroelectricity is only induced when the a (and consequently, b) lattice parameters become longer than a critical value, above which ferroelectricity is "simultaneously" induced along *both* [100] and [010] directions, resulting in a total polarization vector pointing towards the [110] direction.

Indeed, the different expectations in the literature of the width of the paraelectric region (See Table 4.5) can be straightforwardly explained in view of the discussion above. In the last column of Table 4.5, we quote the critical value of the a lattice parameter at which the in-plane ferroelectricity is induced. One notices that all studies (including ours) give almost the same critical value of $a^* \approx 3.88$ Å with small discrepancies of order ~ 0.5 mÅ, which supports the proposed idea of the space condition. Having almost the same critical lattice constant, it is then obvious how the different values of a_0 used in these studies result in different values of the critical strain.

The out-of-plane ferroelectric transition at compressive strains may also be interpreted in view of the space condition. As shown in Fig. 4.8a, compression of the (001) plane causes the c lattice parameter to increase. When c becomes long enough, ferroelectricity is induced along the [001] direction. Interestingly, our calculations indicate that the critical value is $c^* \approx 3.87$ Å, which is almost equal to a^* for in-plane polarization.

Although we are not aware of the values of c^* for Refs. [207,208], we believe that they almost equal to the value that we quoted. In fact, if we use our value of the slope[10] of c/a as a function of strain, as shown in Fig. 4.8a, in order to

[9]It should be pointed out that the "space" condition that we are discussing here is relevant in the context of ferroelectricity induced by atomic displacements. It has been shown that the general correlation between system size and ferroelectricity becomes the opposite at very high pressure, in which case it has been shown that ferroelectricity can be *enhanced* when the system size is further *decreased*. In the latter case, ferroelectricity is believed to have a distinct physical origin [211].

[10]In the unshaded region of Fig. 4.8a, the curve shows a linear behaviour with a constant

Strain type	a^*(Å)	c^*(Å)	V^*(Å^3)
Isotropic (tensile)	3.89	3.89	59.1
Biaxial volume-conserving (compressive)	3.82	3.88	56.8
Biaxial (compressive)	3.80	3.87	55.8
Biaxial (tensile)	3.88	3.82	57.6

Table 4.6: The critical values (denoted by an asterisk) of a, c, and the volume V at which the ferroelectric transition occurs in STO under different strain regimes.

extrapolate c^* in Refs. [207, 208], we find that it is almost equal to 3.87 Å, in agreement with our result.

We further support the idea of the space condition by considering two fictitious systems. In system 1, we apply an isotropic tensile strain to cubic STO, and in system 2, we apply a volume-conserving compressive strain (that is, when the (001) plane is compressed, the c lattice constant is increased such that it reproduces the volume of cubic strain-free STO). In both systems the ions are only allowed to relax along the [001] direction, while holding the other degrees of freedom fixed.

We quote in Table 4.6 the values of the critical lattice constants of the two systems at which the ferroelectric transition takes place. For comparison, we quote also the corresponding critical values of biaxially strained STO at the two boundaries between the unshaded and the shaded regions. For both fictitious systems, one finds that the polarization along the [001] direction is "switched on" at almost the same critical value of the lattice parameter $c^* \approx 3.88 \pm 0.01$ Å, which also agrees with the value that we find for biaxially compressively strained STO. The in-plane polarization is induced also at almost the same critical value of the corresponding lattice constant $a^* = 3.88$ Å (see the last row of Table 4.6), as discussed earlier.

The above results strongly support the idea of the space condition, and in particular, the point that it is the length of the lattice constant in a specific direction (rather than the volume of the system) that determines whether the system polarizes along that direction. Indeed, one can see in Table 4.6 that

slope.

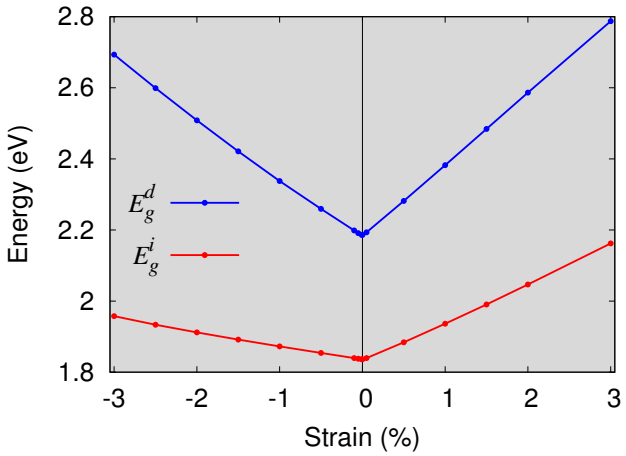


Figure 4.12: Strain-induced changes in the bandgaps of STO at the experimental lattice parameters.

the ferroelectric transition shows no apparent correlation to the volume of the system, where it can range between 55.8 Å^3 to 59.1 Å^3 for different strain regimes.

One can notice that the value of the critical lattice parameter of STO (3.88 ± 0.01 Å) is almost equal to its experimental lattice constant at 0 K (which equals 3.890 Å [212]). This suggests that for the "real" system, ferroelectricity would be induced in STO even for a tiny amount of strain, and the unshaded region that the curve of E_g versus strain shows would consequently disappear. To confirm this, we consider STO under a negative homogeneous pressure so that its lattice constant in the DFT calculation is equal to the experimental lattice constant of 3.89 Å. The amount of the applied pressure required is ~ -6.5 GPa. Similar investigations are then carried out for the strain-induced changes in the bandgaps of the system. Fig. 4.12 shows indeed that the unshaded region has now disappeared and the ferroelectric transition (that widens the gap of the system) is induced for even tiny amounts of strain.

Interestingly, when the experimental lattice parameters are adopted for STO, the bandgaps show a greater tunability as a function of strain. The induced changes in the gaps that we have quoted earlier when a $\pm 4\%$ strain is applied can now be achieved with more modest strains of $\sim \pm 3\%$.

In this section, we have restricted our study on the high temperature phase of STO and did not take into account the effect of the rotations of the oxy-

gen octahedra (see Sec. 1.2.2). This effect has been investigated in Ref. [195], where it is reported that it tends to open the gap of the system, much like the ferroelectric distortion modes. It is, however, worth expanding the investigations of these rotations by studying there dependence on the size of the system, but this is left to a future work.

Explaning the strain-induced changes in the structure of BTO within the concept of the space condition

One may extrapolate the discussion of the space condition to further understand the strain-induced changes in the polarization direction of BTO that give rise to the unshaded and shaded regions in that system (see Fig. 4.5). As we discussed in Sec. 4.6, the unshaded region in BTO involves a "rotational" transition of the polarization from [001] to [110] directions. Within the shaded region of compressive strains, no in-plane component of the polarization is observed. Similarily, within the shaded region of tensile strains, no out-of-plane component of the polarization is observed. In view of the concept of the space condition, this can be attributed to the fact that the in-plane and the out-of-plane lattice constants are not long enough to support polarizations along [110] and [001], respectively, in the corresponding regions. On the negative strain side, in-plane polarization is induced at a critical value of $a^* \approx 3.93$ Å. Similarily, on the tensile strain side, out-of-plane polarization is induced at an equal critical value of $c^* \approx 3.93$ Å.

Within the unshaded region of BTO, both a and c lattice parameters are *above* the critical value, leading to the polarization vector having components along both [001] and [110] in the corresponding region. In contrast, both a and c are *below* their critical value in the unshaded region of STO (with the LDA lattice constant), leading to a vanishing polarization within the corresponding region. This suggests that, in contrast to STO, when the experimental lattice parameters are adopted for BTO, one would expect an increase in the width of the unshaded region. So, one may conclude that "moderate" epitaxial strains have opposite effects on BTO and STO: they would tend to close the gap in the former, and opens it in the latter.

It is noteworthy to highlight the point that the critical lattice constant of STO differs from that of BTO. Actually, we do not believe that the critical

value is "universal": different materials could generally show different critical values. The sizes of the ions in the system could play a crucial role in determining the critical lattice constant, as inspired by the Goldschmidt criteria (see Sec. 1.3.1).

We should point out that whilst the concept of the space condition provides a very consistent explanation of the behaviour of BTO and STO (and their solid solutions, as shall be seen in the next section), in order to draw a more general conclusion about its validity in other similar systems, it would be worth performing similar studies for other perovskite oxides. This is beyond the scope of this thesis and is left to a future work.

4.8 Effect of alloying on E_g of BST solid solutions

In the previous two sections of this chapter, we investigated how epitaxial strain could tune the band gaps of BTO and STO. In this section, we shall investigate another possible means by which to tune the gap, namely, the alloying of BTO and STO. The virtual crystal approximation (see Sec. 3.5) shall be used in this section to represent solid solutions of BST.

4.8.1 Structural properties of BST

Checking the validity of VCA

Before carrying out our investigations for BST systems, we begin by testing the validity of the VCA. We do so by considering a particular system of $Ba_{0.5}Sr_{0.5}TiO_3$ under a compressive biaxial strain of -3%. This system is studied within two approaches: 1. by using the VCA on a single unit cell, and 2. by considering a $1 \times 1 \times 2$ supercell that is shown in Fig. 4.13, which gives rise to a 50% atomic concentration of Ba and Sr species. Full relaxation of the ionic degrees of freedom and the c lattice parameter is performed. The out-of-plane lattice constant, the atomic displacements, the energy gaps and the total pressure are quoted in Table 4.7, as obtained from the two approaches. It can be noticed that the VCA for this system reproduces to a very good extent all the considered physical quantities that are obtained from the supercell

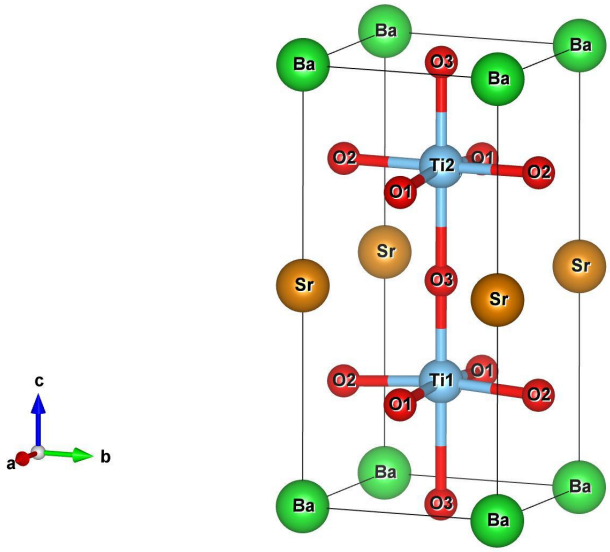


Figure 4.13: A supercell of $1 \times 1 \times 2$ unit cells corresponding to $Ba_{0.5}Sr_{0.5}TiO_3$ at -3% strain, used as a reference to check the validity of the VCA approach.

approach. This suggests that VCA can be used with confidence to represent the structural and electronic properties of BST solid solutions. The VCA is further tested in the next chapter for different concentrations and different atomic ordering of Sr in BST.

Structure of BST

As obtained from the VCA approach, the lattice constants of free-standing BST films at different Sr content are tabulated in Table 4.8. The corresponding values of pure BTO and STO are also quoted for comparison. It is evident that the lattice constant of BST decreases monotonically and almost linearly with the increase of Sr content, obeying to a large extent Vegard's law [213, 214]. This is in agreement with previous experimental results for bulk [215, 216] and thin film [217] BST. Similar results are also obtained from a previous first-principles study [178], in which the VCA was also used.

4.8.2 Strain induced changes in E_g of BST

We show in Fig. 4.14 the effect of epitaxial strain on the direct and the indirect energy gaps of BST at Sr concentrations of 25%, 50% and 75%. The trend of

Quantity	VCA	supercell
c (Å)	4.017	4.014
ΔTi	0.012	0.011
$\Delta O_{1,2}$	−0.023	−0.027
ΔO_3	−0.023	−0.026
E_g^i	1.95	1.93
E_g^d	2.43	2.45
Pressure (GPa)	8.95	8.46

Table 4.7: A comparison between the VCA and the supercell approaches for a selected set of physical quantities corresponding to the $Ba_{0.5}Sr_{0.5}TiO_3$ system. The atomic displacements are given in fractional coordinates. The subscripts of the O atoms refer to the arrangement in Fig. 4.13. For the supercell calculation, the value reported for c is half the supercell lattice parameter in the [001] direction, and the atomic displacements in the two unit cells that make up the supercell are averaged to maintain consistency in comparison.

Sr content	a_0(Å)	a_0^{Vegard}(Å)
0%	3.941	3.941
25%	3.918	3.917
50%	3.896	3.893
75%	3.872	3.869
100%	3.845	3.845

Table 4.8: The equilibrium lattice constant a_0 of BST at 0% strain as affected by Sr concentration. The values are obtained from the VCA approach. The interpolated lattice constants according to Vegard's law are shown in the last column for comparison.

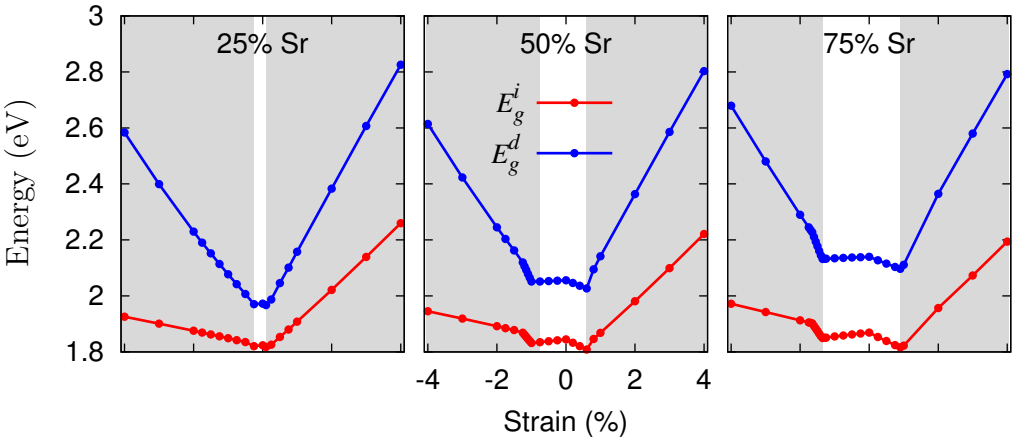


Figure 4.14: Strain-induced changes in the direct and the indirect energy gaps of BST at different Sr content. Sr concentration is printed on each panel.

E_g that these systems show are very similar to the corresponding trends in pure BTO and STO, where all systems show a qualitatively similar feature around the strain-free point (highlighted by the unshaded area in Fig. 4.14), indicating a transition region at the corresponding values of strain. The quantitative changes in E_g due to strain for these systems are also similar.

Indeed, the investigation of the atomic displacements of these systems (which are represented by the quantity $\mathbf{Q}$, defined by Eq. 4.10) as a function of strain, indicates that the transition region (the unshaded region) corresponds to a paraelectric phase (see Fig. 4.15), much like the case of pure STO. The same discussion about the features in the E_g curve of STO holds here.

Space condition revisited

One can notice that the unshaded region in Fig. 4.15 covers a narrower range of strains as the Sr content decreases. Interestingly, we find that for each one of the three systems considered above, the paraelectric/ferroelectric transition at compressive and tensile strains occurs at the same critical value of c and a (to within less than 0.01 Å), respectively, further supporting the concept of the space condition discussed above. We can see in Table 4.9 that the values of the critical lattice parameters show a monotonic decrease with the increase of Sr content in BST. Unlike the decrease of the equilibrium lattice constant of these systems (see Table 4.8), the critical lattice parameters do not show

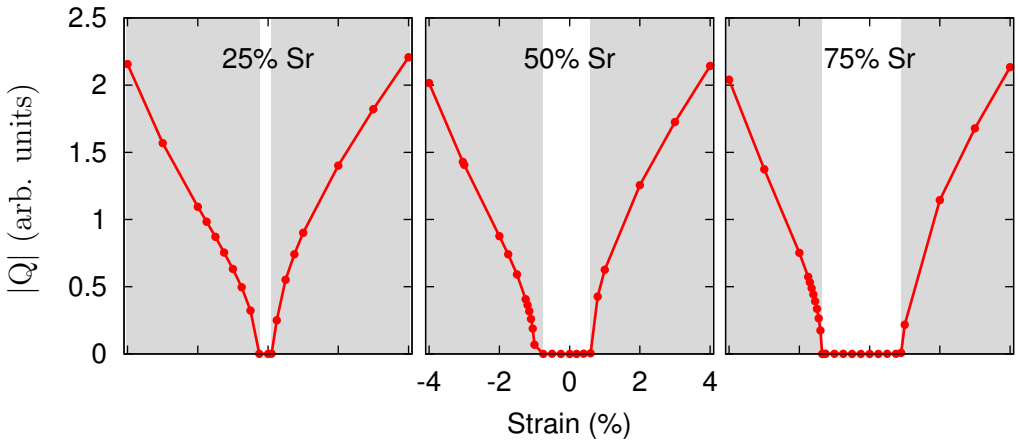


Figure 4.15: Effect of strain on the magnitude of the atomic displacements of BST that are represented by the quantity **Q**, defined in Eq. 4.10. Each panel corresponds to a different Sr concentration in BST.

a linear trend as a function of composition. The difference in a^* between the systems with 25% and 50% of Sr is negligible, while the difference between the systems with 75% and 100% Sr content reaches ~ 0.02 Å.

As pointed out earlier, a^* is less than a_0 for pure BTO. One notices in Table 4.9, however, that a^* is greater than a_0 for all Sr concentrations that are equal to and above 25%. A transition point is thus expected to occur at an intermediate concentration of Sr below 25%. This has a direct influence on the behaviour of the bandgaps of BST as a function of Sr content, as shall be discussed in the next section.

4.8.3 Effect of Sr content of the gaps of BST

As we have pointed out in Sec. 4.5, the indirect energy gaps of BTO and STO are almost equal, as predicted by our DFT calculations, which are also confirmed by the experimental measurements. The direct gap is different, however, with STO showing a greater value.

If Vegard's law holds for the gaps of the system, one would expect then that E_g^i is almost invariant with the change in the Sr content, while E_g^d shows a monotonic linear increase. However, this expectation is not borne out by our DFT calculations. As depicted in Fig. 4.16, both E_g^i and E_g^d show a non-monotonic behaviour where they decrease linearly with increasing Sr content

Sr content	a_0(Å)	a^*(Å)
0% (BTO)	3.941	3.93
25%	3.918	3.92
50%	3.896	3.92
75%	3.872	3.90
100% (STO)	3.845	3.88

Table 4.9: The values of the critical lattice parameter a^* ($\approx c^*$), at which the ferroelectric transition occurs, of BST system at different Sr concentrations. The equilibrium lattice parameters are also indicated for reference.

up to a critical value of $\sim 15\%$, beyond which they linearly increase.

This behaviour can be understood in connection with the corresponding phase of BST at 0% strain at different Sr content. Within the Sr concentrations that are represented by the shaded region in Fig. 4.16, the system adopts a ferroelectric phase, just like BTO, while for the higher concentrations of Sr (represented by the unshaded region in the figure) the system has a paraelectric phase.

However, using the argument of the space condition (see Sec. 4.7.1), one would expect that the critical Sr concentration at which the ferroelectric/paraelectric transition occurs would fall at higher value than what DFT-LDA calculations predict. This can be explained as follows. According to the concept of the space condition, BST system at 0% strain is ferroelectric if its equilibrium lattice constant is greater than its critical lattice parameter (see Table. 4.9). Our DFT-LDA calculations predict that at a critical Sr concentration of $\sim 15\%$, the equilibrium and the critical lattice parameters are equal, therefore, the ferroelectric/paraelectric transition occurs at this particular concentration. However, since DFT-LDA underestimates the equilibrium lattice constant, the equality to the critical lattice parameter is then expected to occur at higher concentrations of Sr.

On the other hand, the behaviour of the energy gap with Sr content in BST is also believed to be sensitive to the strain state of the system, since epitaxial strain can enhance the spontaneous polarization and, therefore, can change the value of the critical Sr content.

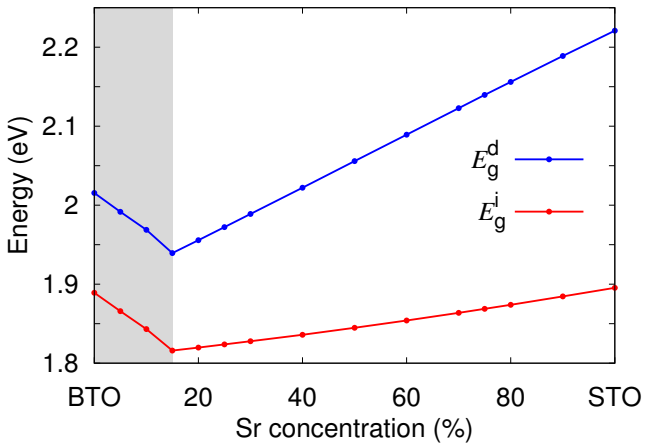


Figure 4.16: Effect of Sr concentration on the direct and the indirect gaps of free-standing BST thin films. The shaded region highlights the range of concentrations for which the gaps are decreased.

Interestingly, experimental measurements of bulk BST at room temperature indicate that below a critical Sr content of $\sim$ 30%, the ferroelectric tetragonal phase of the system is preferred [215]. On the other hand, thin film BST deposited on Pt/MgO substrate [217] shows a higher critical Sr content of 56%, below which the ferroelectric phase is adopted.

Tailoring the energy gaps of BST by means of alloying could be promising. Whilst the energy gaps are opened when epitaxial strain is applied[11], the gaps can be closed by varying the Sr composition in BST solid solutions, reaching a minimum value at a critical Sr concentration. The magnitude of the decrease is not large however: the indirect gaps of BTO and STO can be decreased by as much as $\sim$ 0.1 eV, while the direct gap of STO can be decreased by $\sim$ 0.2 eV.

4.9 Summary

In this chapter we performed detailed investigations of the effect of epitaxial strain and alloying on the electronic structure and the bandgaps of BTO, STO, and BST solid solutions.

[11] This holds unless the atomic distortions are suppressed (which is not very clear how to be achieved technologically).

We showed that within a strain range of ±4%, the optical gap of BTO and STO can be opened by up to ~ 0.8 and ~ 0.6 eV, respectively, while the indirect gap exhibits a weaker effect due to strain. On the other hand, we found that alloying does not tune the gaps of BST as much, where we showed that by varying the Sr content in BST, the direct gaps of pure BTO and STO can be lowered by ~ 0.1 and ~ 0.2 eV, respectively, while the indirect gap can be closed by as much as ~ 0.1 eV for both systems.

We showed that the energy gaps of BST do not show a monotonic behaviour with the application of strain, where the trend of E_g with respect to strain exhibit different behaviours between low and high strains. At low positive and negative strains, the gaps decrease with the increasing strain, while they open again when the strain becomes higher than a critical value.

The investigations of these features suggested that they are linked to the polarization state of the system, which can be tuned by means of strain. At high positive and negative strains, the systems maintain a spontaneous polarization along the [110] and [001] directions, respectively. At low strains, the systems transition between the two polarization directions. However, BST systems differ in the nature of the transition. For pure BTO and up to a critical Sr content of $\sim 15\%$ in BST, the polarization vector adopts a smooth rotation between the two directions while almost maintaining a constant amplitude. For higher Sr concentrations up to pure STO, the transition state involves a complete inhibition of ferroelectricity.

The ferroelectric transition at a critical value of strain was understood through the proposed concept of a "space" condition for ferroelectricity, which states that the ferroelectric polarization component of a system along one of the crystallographic directions of [100], [010] or [001], which is induced by the atomic displacements, only occurs if the lattice parameter along that direction is longer than a critical value, which is system dependent. The concept of the space condition explained also the different reports in the literature about the "width" of the transition region in STO.

The above DFT-LDA results suggest that STO (and BST below the critical Sr concentration) adopt a certain transition phase as a function of epitaxial strain within which the cubic symmetry of the system is broken without breaking the inversion symmetry. However, we found that the critical lattice parameter of STO is almost equal to its experimental lattice constant, thus,

when the calculations were done at the experimental lattice constant, the transition region disappeared and the ferroelectricity of the system was induced even for tiny amounts of strain. In contrast, the space condition suggested that the transition region of BTO (and BST below the critical Sr concentration) could increase to cover a wider range of strains when the experimental lattice constant is adopted.

We showed that when the atoms are frozen at their ideal sites, the STO gap decreases when strain is applied due to the degeneracy breaking of the highest occupied and lowest unoccupied states that follow the breaking of the cubic symmetry of the strain-free system. The decrease in the gap, however, occurs at higher rate for tensile strains than for compressive strains. This was explained by disentangling the effects of the changes in the volume and tetragonality of the system. The two effects were shown to be additive, to an excellent approximation, at relatively low values of strain. At positive strains, both changes in volume and tetragonality cooperate in decreasing the gap, while at negative strains the two effects oppose each other. This immediately explains the higher rate of decrease for the bandgap of STO as a function of tensile strain, as compared to compressive strain.

The virtual crystal approximation was used in this chapter to represent the alloying of BST. The VCA was tested against a supercell of size $1 \times 1 \times 2$ for a 50% Sr content at -3% strain. Both approaches gave a very good agreement in the energy gaps, the relaxed lattice parameter c, the atomic displacements and the total pressure of the system.

The direct and indirect energy gaps of strain-free BST were found to violate Vegard's law (unlike the lattice constant of the alloy) and follow a non-monotonic behaviour with the increase of the Sr content, adopting a minimum value at a critical Sr content of $\sim 15\%$. This behaviour was attributed to the phase of the system at the strain-free point, which is ferroelectric below the critical concentration and paraelectric above. According to the concept of the space condition, the value of the critical concentration is believed to become higher when the experimental lattice parameters are used, but this is not tested.

Further work that is suggested by the present results and discusion includes:

- Investigations of the low temperature phase of STO that involves the tilting of the oxygen octahedra.

- Treating the volume and the tetragonality as order parameters in approximating the bandgap of the system can be generalized to include the effect of the spontaneous polarization of the system, in order to successfully reproduce the gaps of the ferroelectric phase.
- The concept of the space condition can be investigated for other similar systems to draw a firm conclusion about its validity and generality.

Chapter 5

Effect of strain and alloying on the optical properties of BTO and STO

5.1 Overview

In this chapter, we investigate different possible means by which the optical properties (the refractive index, in particular) of BTO, STO and their solid solutions may be tuned. We shall mainly focus on these materials in thin-film form and study the effect of epitaxial strain. In addition, we also investigate the effect of Sr content in BST, and compare it to the effect of strain. Other effects such as ferroelectric distortions and atomic confgurations of Sr in BST are also studied.

We find that epitaxial strain provides a promising means for refractive index modulation, where it can decrease the refractive index of BTO and STO by $\sim 4\%$ and induce a birefringence of up to ~ 0.14. Strain-induced ferroelectric distortions are found to have the dominant role in decreasing the refractive index of these materials, as compared to the strain-induced changes of the lattice vectors. We also find that increasing the Sr content in BST can decrease the refractive index of BTO by the same amount as strains of $\sim \pm 2\%$ may induce. On the other hand, we find that the refractive index of BST shows almost no dependence of the arrangements of the Sr atoms in the supercell.

As in Chapter 4, the VCA will be used to represent the alloying of BST.

To our knowledge, there is no previous work that assesses the validity of the VCA in calculating the refractive index of BST. Hence, we shall test the VCA against the supercell approach, justifying its validity by comparing against supercell results.

Many results in this chapter are strongly linked to the outcomes of the previous chapter, so the reader is advised to go through the preceding chapter first in order to get a more comprehensive understanding.

In the next section, we shall briefly describe the theoretical framework within which the optical properties can be obtained from density functional theory calculations.

5.2 Theoretical framework

In this section, we give a brief description of the relevant equations via which the dielectric function and the refractive index are calculated, based on DFT calculations. Detailed derivations can be found in e.g., Ref. [218].

The interaction between electromagnetic waves and materials[1] can be described by the polarization $\mathbf{P}$ of the material that is induced by the electric field $\mathbf{E}$ of the incoming wave:

$$P^{\alpha}(\omega) = \chi^{\alpha\beta}(\omega)E^{\beta}(\omega) + \text{nonlinear terms}\,, \tag{5.1}$$

where the Greek superscripts denote the Cartesian components, and summation convention is adopted. $\chi^{\alpha\beta}$ is the $\alpha\beta$ component of the linear susceptibility tensor and ω is the energy of the electromagnetic wave.

With the presence of the electromagnetic field of the incoming wave, the momentum operator of the j^{th} electron in the system is generalized to

$$-i\nabla_j \rightarrow -i\nabla_j - \mathbf{A}\,, \tag{5.2}$$

where $\mathbf{A}$ is the vector potential of the magnetic field $\mathbf{B}$, defined by

$$\mathbf{B} = \nabla \times \mathbf{A}\,, \tag{5.3}$$

[1] Only the *electronic* response of the material is considered in this thesis. In general, low energy light can also interact with materials through atomic vibrations.

and its time derivative is related to the electric field **E** as

$$\mathbf{E} = -\frac{\partial \mathbf{A}}{\partial t}\,. \tag{5.4}$$

The single particle Hamiltonian of the system is then given by

$$\widehat{H} = \frac{1}{2}\sum_{j}\left(i\nabla_j + \mathbf{A}\right)^2 + V_{\text{eff}}(\mathbf{r})\,. \tag{5.5}$$

Within the framework of perturbation theory, the linear susceptibility χ in terms of the Kohn-Sham eigenstates is given by [218]

$$\chi^{\alpha\beta}(\omega) = \frac{1}{\Omega}\sum_{mn\mathbf{k}} f_{nm}\frac{r^{\alpha}_{nm}(\mathbf{k})r^{\beta}_{mn}(\mathbf{k})}{\omega_{mn}(\mathbf{k}) - \omega - i\gamma}\,, \tag{5.6}$$

where Ω is the volume of the unit cell and the summation runs over the wave vectors $\mathbf{k}$ and the band indices m and n of the Kohn-Sham eigen states $|n\mathbf{k}\rangle$. The prefactor $f_{nm} \equiv f_n - f_m$ is defined as the difference between the Fermi occupation factors f of the n^{th} and the m^{th} bands, respectively, where f has a value of 0 (for unoccupied states) or 2 (for occupied[2] states) at 0 K. $\omega_{mn}(\mathbf{k})$ is the difference between the eigenvalues of the m^{th} and the n^{th} states, respectively, at the wave vector $\mathbf{k}$, ω is the energy of the incoming light and γ is a smearing factor added to avoid singularities and broaden the calculated spectrum. $r^{\alpha}_{mn}(\mathbf{k})$ are the optical matrix elements that are defined by

$$r^{\alpha}_{mn}(\mathbf{k}) \equiv \langle m\mathbf{k}|r^{\alpha}|n\mathbf{k}\rangle\,, \tag{5.7}$$

where r^{α} is the α^{th} component of the position operator. The position matrix elements are often expressed in terms of the momentum matrix elements as follows[3]:

$$\mathbf{r}_{mn} = \frac{\langle m\mathbf{k}| - i\nabla_{r^{\alpha}}|n\mathbf{k}\rangle}{i\omega_{mn}}\,. \tag{5.8}$$

The energy dependent dielectric tensor $\varepsilon(\omega)$ is related to the linear susceptibility by

[2]Spin degeneracy is assumed.

[3]The relation between the position and the momentum matrix elements deviates from the form given by Eq. 5.8 when fully non-local pseudopotentials are used [219].

$$\varepsilon^{\alpha\beta}(\omega) \equiv \varepsilon_1^{\alpha\beta} + i\varepsilon_2^{\alpha\beta} = \delta^{\alpha\beta} + 4\pi\chi^{\alpha\beta}(\omega)\,, \tag{5.9}$$

where ε_1 and ε_2 are the real and imaginary parts of the dielectric function, respectively. The relation of ε to the refractive index of the material is given in Eq. 2.27, which is rewritten below:

$$N \equiv n + ik = \sqrt{\varepsilon}\,, \tag{5.10a}$$

$$\Rightarrow n = \frac{1}{\sqrt{2}}\sqrt{\sqrt{\varepsilon_1^2 + \varepsilon_2^2} + \varepsilon_1}\,, \tag{5.10b}$$

$$\Rightarrow k = \frac{1}{\sqrt{2}}\sqrt{\sqrt{\varepsilon_1^2 + \varepsilon_2^2} - \varepsilon_1}\,, \tag{5.10c}$$

where the Greek superscripts have been dropped for simplicity. The physical meaning of a diagonal component $n_{\alpha\alpha}$ of the refractive index of a material refers to the ratio between the speed in vacuum and the speed through the material of an electromagnetic wave polarized along the α direction.

The calculations of the optical matrix elements and the subsequent optical properties in this chapter are performed with the abinit package [123–125]. The technical details of the calculations performed in this chapter are similar to those adopted in the preceding chapter, apart from the k-point sampling. A dense Monkhorst-Pack mesh of $15 \times 15 \times 15$ k-points are used to obtain well-converged optical spectra. The summation in Eq. 5.6 includes a total of 13 unoccupied bands to converge the dielectric function in the energy range of $0-15$ eV.

The application of biaxial strain is also performed in the same manner as described in Chapter 4, namely, biaxial strain is applied on the *ab* plane of bulk unit cell, while the out-of-plane lattice parameter and the ionic degrees of freedom are all fully relaxed, constraining the lattice vectors to be orthogonal. In this chapter, we use the term "thin-film" BTO, STO, or BST to refer to the calculations of these systems under the aforementioned constraints.

Throughout this chapter, n_{xx} and n_{yy} refer to the in-plane components of the refractive index (i.e., along the strained plane), while n_{zz} corresponds to the out-of-plane component (i.e., along the direction in which the lattice

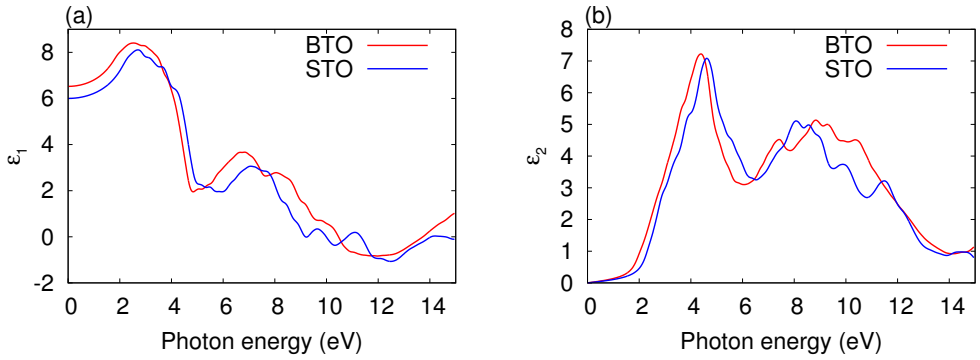


Figure 5.1: The calculated real (a) and imaginary (b) parts of the frequency dependent dielectric function of the high temperature phase of BTO (red) and STO (blue).

constant is allowed to relax).

5.3 Optical spectra of bulk BTO and STO

Before we begin our main investigations, we present in this section our calculated optical spectra of the high temperature phases of bulk BTO and STO. A comparison with other theoretical and experimental results is also presented. These results have already been presented in our previous unpublished work [196].

We show in Fig. 5.1 the real and imaginary parts of the dielectric function of pure BTO and STO, while in Fig. 5.2 we show the dispersion of the refractive index in the visible and near infrared range.

Our calculations overestimate the refractive index of BTO and STO as compared to experiment [220]. However, qualitative features are correctly reproduced, including the general form of the dispersion with wavelength and the relative differences between BTO and STO. The discrepancy between the calculated and the experimental indices can be largely attributed to the underestimation of the optical gap within DFT-LDA. Nonetheless, the *variation* of the calculated spectra due to structural perturbations such as strain and composition are expected to be robust, and the trends are not expected to significantly deviate from the "real" ones.

Our calculated dielectric function is also in good qualitative agreement with

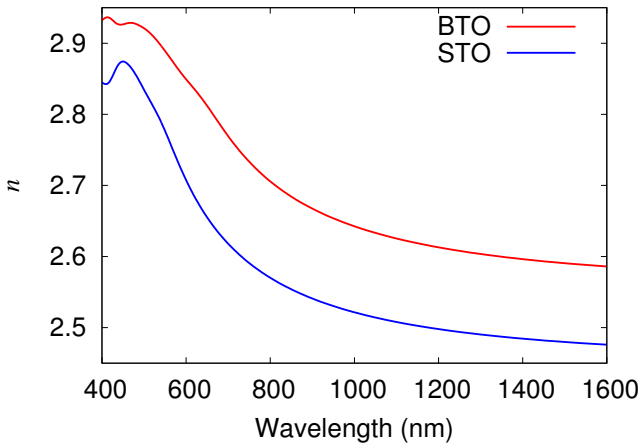


Figure 5.2: The calculated refractive index dispersion of bulk BTO (red) and STO (blue) at their high temperature phases.

other theoretical [85, 87] and experimental [221] works. The main difference with the experimental data is that the characteristic peaks in ε_2 are red shifted in our calculations, which is again a direct consequence of the underestimation of the true quasiparticle bandgap of the material.

5.4 Effect of strain on the refractive index of BTO

In this section, we shall study the effect of biaxial strain on the refractive index of pure BTO thin films. We shall also show the role of ferroelectric distortions in affecting the trends in refractive index with respect to applied strain.

The strain-induced changes in the xx and zz components of the refractive index of 1000 nm of fully-relaxed BTO are depicted in Fig. 5.3 by the solid red and blue curves, respectively. Due to the cubic/tetragonal symmetry of the lattice, n_{xx} and n_{yy} are identical, so only n_{xx} is shown in the figure. Similar behaviour is followed by the refractive index at other visible / near-infrared wavelengths, so we show only $n(\lambda = 1000 \text{ nm})$ as a representative example.

One can first notice that the three components of n of unstrained BTO are equal. This is a straightforward consequence of the isotropy of the system at the strain-free point, where it adopts a cubic lattice (with rhombohedral

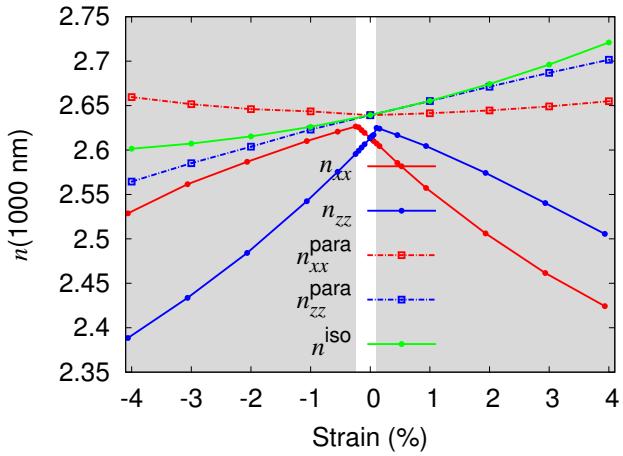


Figure 5.3: Strain-induced changes in the xx and zz components of the refractive index of ferroelectric and paraelectric BTO (represented by the solid and the dashed lines, respectively). The green line corresponds to paraelectric BTO under isotropic strain. The unshaded and shaded regions cover the same range of strains as in Fig. 4.5.

space group $R3m$) as discussed in Chapter 4. Uniaxial birefringence[4] is then introduced by the application of strain that breaks the cubic symmetry.

One can describe the trends of each of n_{xx} and n_{zz} with strain as being two piecewise approximately linearly decreasing functions with a "cusp" that is shifted off the strain-free point. The positions of the cusps of the n_{xx} and n_{zz} curves are located at the left and right boundaries of the unshaded region in Fig. 5.3, respectively. Interestingly, the unshaded region in Fig. 5.3 covers *exactly* the same range of strains as in Fig. 4.5. This suggests that the trend of the refractive index is also correlated with the magnitude and the direction of the spontaneous polarization of the material, much like the trends in the bandgap, discussed in Chapter 4.

Indeed, it can be noticed that n_{xx} and n_{zz} have their maximum value (i.e., at the cusp) just at the point where the polarization is induced along

[4]Birefringence refers to a property of certain materials in which the refractive index depends on the direction and the polarization of light propagation. Uniaxial birefringence refers to the case where one of the three diagonal components of the refractive index (usually referred to as the "extraordinary" component) is distinct from the other two (which are referred to as the "ordinary" components). The uniaxial birefringence is defined as the difference between the extraordinary and the ordinary components. Biaxial birefringence refers to the case where all the three components are distinct from each other. See Ref. [105] for more details.

the in-plane and out-of-plane directions, respectively. As the magnitude of the polarization along a certain direction increases, the component of the refractive index in that direction decreases correspondingly.

The in-plane components of the refractive index are also correlated with the out-of-plane polarization, and vice versa. That is, it can be noticed that the *in-plane* component n_{xx} is lowered within the left shaded region due to the increase of the *out-of-plane* polarization. A similar argument holds for n_{zz}.

We have shown so far how the decrease in the refractive index is correlated with the increase in the ferroelectric polarization. In order to get a more comprehensive understanding, we consider a system in which the atoms are frozen at their ideal high-symmetry sites throughout the entire range of strains (i.e., a paraelectric phase is imposed for all strains). This allows one to disentangle the effects of the changes in the volume and the tetragonality of the system from the effect of the atomic displacements. The corresponding refractive indices of this constrained system are represented by the dashed lines in Fig. 5.3. Interestingly, one can notice that the in-plane refractive index of this system n_{xx}^{para} is almost constant and insensitive to the value of the applied strain. In contrast, n_{zz}^{para} shows a monotonic trend throughout the range of strain studied. This suggests that the decrease in n_{xx} with strain is almost solely attributable to the increase in the magnitude of the ferroelectric polarization of the system. On the other hand, the trend in n_{zz} is affected in addition by changes in the structure of the system. In general, the changes in the refractive index due to ferroelectric distortion are much greater than those due to the variations in the volume and the tetragonality.

The general trend of the refractive index with strain can also be understood within the context of the changes in the optical gap of the material. Within the shaded region, one notices that the refractive index is always *decreasing* with increasing magnitude of strain, in contrast to the trend in E_{g} where it increases (see Fig. 4.3). This relation can be understood in view of Eq. 5.6, where one can notice the inverse relation between the transition energies ω_{mn}[5] and the optical spectrum. However, it should be noticed that this inverse relation is not generic and can be violated due to the presence of the optical matrix elements in the numerator of Eq. 5.6.

[5]Obviously, E_{g}^{d} is equivalent to the transition energy ω_{vc} at Γ, with v being the highest occupied state and c being the lowest unoccupied state.

In what we have presented above, one can conclude that strain can affect the refractive index in two ways: a direct way, in which the changes in the Bravais lattice vectors due to strain affect mainly the out-of-plane component; and an indirect way, where strain can enhance the spontaneous polarization of the material, which in turn lowers the refractive index. The latter effect was shown to have a stronger influence than the former.

One can notice in Fig. 5.3 that the birefringence of the material exhibits opposite trends between the compressive and tensile strain regimes in both the paraelectric and the ferroelectric phases; at compressive strains, the extraordinary out-of-plane component n_{zz} is lower than n_{xx}, while at tensile strains it is higher. One might, at the first glance, correlate this to the "length" of the corresponding lattice parameter along which the refractive index component is calculated. In other words, throughout the entire range of strains, the refractive index adopts a higher value along the "shortest" lattice vector. One might also try to support this argument by observing that n_{zz}^{para} increases as the c lattice parameter decreases.

However, one should be aware that this argument is not necessarily generic and can be contradicted in certain cases. For instance, consider a system of paraelectric BTO under isotropic strain (i.e., a system that is constrained to have cubic symmetry while only the volume changes, keeping the ions at the ideal high-symmetry sites). The corresponding refractive index of this system n^{iso} is illustrated in Fig. 5.3 by the green line. One can notice that n^{iso} follows the opposite trend, where it *increases* with the increase of the corresponding lattice parameters.

Therefore, it can be concluded that the correlation between a specific component of the refractive index of this material and the system size cannot be solely linked with the "length" of the lattice parameter along that direction, but rather the lengths of the lattice parameters in the other two directions could also play an important role in describing the relation. The coupling with the lengths of all three lattice parameters can lead to different trends of a certain component of the refractive index with the increase of the length of the corresponding lattice constant; it can increase, decrease or remain almost constant as in the cases of n^{iso}, n_{zz}^{para} and n_{xx}^{para}, respectively.

Strain	$\Delta n_{xx}(\%)$	$\Delta n_{zz}(\%)$	$n_{zz} - n_{xx}$
-4%	-3.24	-8.61	-0.14
-3%	-1.99	-6.88	-0.13
-2%	-1.02	-4.95	-0.10
-1%	-0.13	-2.72	-0.07
-0.25%	0.50	-0.69	-0.03
0%	0.00	0.00	0.00
0.1%	-0.23	0.44	0.02
1%	-2.15	-0.35	0.05
2%	-4.11	-1.50	0.07
3%	-5.81	-2.80	0.08
4%	-7.24	-4.13	0.08

Table 5.1: The percentage differences in the xx and the zz components of the refractive index of ferroelectric BTO at different values of epitaxial strain as compared to the corresponding values of unstrained BTO. The birefringence is quoted in the last column.

5.4.1 Quantifying the results

We explicitly quote in Table 5.1 the amounts by which the calculated refractive indices of BTO thin films can be tuned due to strain. It can be noticed that n_{zz} is more strongly affected by compressive strains, in contrast to n_{xx} which is affected more by tensile strains.

In general, epitaxial strain has a stronger effect on n_{zz} than n_{xx}. At high strains of $\pm 4\%$, n_{zz} decreases by $\sim -8.6\%$ and $\sim -4.1\%$ due to compressive and tensile strains, respectively. However, n_{xx} is decreased by $\sim -3.2\%$ and $\sim -7.2\%$ due to compressive and tensile strains, respectively. On the other hand, small compressive and tensile strains can induce a small increase in n_{xx} and n_{zz} of 0.5% and 0.44%, respectively. One should note that the range of strains within which the refractive index increases is expected to be larger if the experimental lattice parameters are adopted rather than the DFT-LDA equilibrium values. This is because the width of the unshaded region in Fig. 5.3 is expected to increase, which was discussed in detail in Chapter 4.

As for the birefringence of the material, the magnitude of the difference be-

tween the ordinary and the extraordinary components of the refractive index shows a monotonic increase with strain. As pointed out earlier, the birefringence is negative for compressive strains and positive for tensile strains. In general, applying a negative strain induces a slightly higher birefringence than applying a positive strain of the same magnitude, as shown in the last column of Table 5.1.

From an experimental perspective, these changes in the refractive index can be easily detected by methods such as prism coupling or spectroscopic ellipsometry (see Chapter 2). For example, thermally induced changes in the refractive index of BST thin films as small as 0.002 ($\sim 0.1\%$) are experimentally measured by the prism coupling method in Ref. [80]. These changes were found useful in tuning the surface plasmon resonance. In addition, in Ref. [81] the birefringence of BST thin films was tuned by means of an external electric field and a value up to 0.004 could be achieved, which makes the material be a potential candidate for optical waveguide applications. The strain-induced changes in refractive index and birefringence reported in Table 5.1 are an order of magnitude larger.

Therefore, epitaxial strain appears to be a very promising means by which the refractive index and the birefringence of BTO may be tuned, which can in turn be very useful in many applications.

5.5 Tuning the refractive index of STO with epitaxial strain

Similar investigations to those of the previous section are reported in this section for pure STO. We show in Fig. 5.4 the effect of epitaxial strain on the in-plane and out-of-plane components of the refractive index of STO, evaluated at a wavelength of 1000 nm. The apparent trends and the features in the curves can be explained within the same context as the trends for BTO, as shall be discussed below.

Fig. 5.4 is also divided into two regions, unshaded and shaded, with different behaviour of the refractive index observed within each region. This division matches exactly the division in Fig. 4.7, suggesting the strong influence of the ferroelectric distortions on the refractive index of STO, similar to the case of

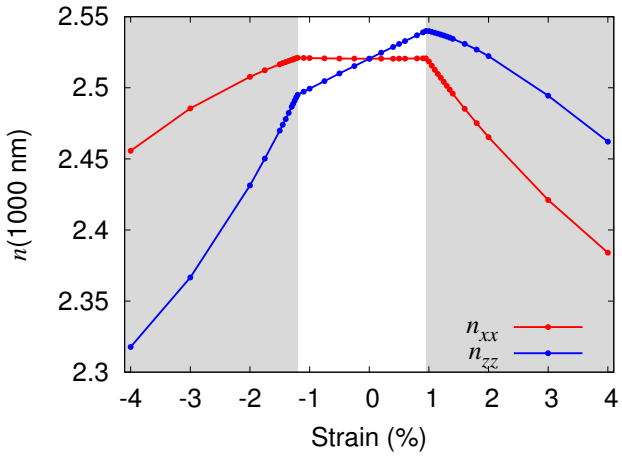


Figure 5.4: Strain-induced changes in the xx and zz components of the refractive index of STO thin films. The shaded region covers the same range of strains as in Fig. 4.6.

BTO discussed in Sec. 5.4.

Within the unshaded region of Fig. 5.4, where the application of strain breaks only the cubic symmetry of the lattice while maintaining atomic positions at their high symmetry sites (i.e., a paraelectric phase), n_{xx} and n_{zz} of STO have a very similar behaviour to the dashed lines in Fig. 5.3 that correspond to paraelectric BTO, and a similar interpretation for this trend holds here for the case of STO.

At higher strains, the refractive indices of STO within the shaded region monotonically decrease with increasing magnitude of strain, as in the case of BTO. This is also attributed to the ferroelectric transition that is induced in this region.

The birefringence of STO as a function of strain is also similar to BTO, being negative for compressive strains and positive for tensile strains.

Since the unshaded region is expected to disappear when the experimental lattice constants of STO are adopted, as discussed in Chapter 4, it follows that the trends of the refractive indices would also change; the expected behaviour is that they would be lowered as soon as strain is applied.

Table 5.2 indicates that for a given strain, the refractive index of STO is slightly less affected than the refractive index of BTO, while the strain-induced birefringence is approximately as large as that of BTO. However, this

Strain	$\Delta n_{xx}(\%)$	$\Delta n_{zz}(\%)$	$n_{zz} - n_{xx}$
-4%	-2.57	-8.04	-0.14
-3%	-1.39	-6.10	-0.12
-2%	-0.51	-3.54	-0.08
-1%	0.02	-0.84	-0.02
0%	0.00	0.00	0.00
1%	-0.08	0.77	0.02
2%	-2.19	0.07	0.06
3%	-3.94	-1.03	0.07
4%	-5.41	-2.31	0.08

Table 5.2: The percentage differences in the xx and the zz components of the refractive index of STO ferroelectric thin films at different values of epitaxial strains as compared to the corresponding values of free standing STO film. The birefringence is quoted in the last column.

conclusion is not expected to hold when the experimental lattice constants are adopted for STO, where the decrease in the refractive index due to strain is likely to be larger.

5.6 The refractive index of bulk BST

We first investigate in this section the effect of the atomic configurations of the Sr species on the refractive index of bulk BST solid solutions. We then address the validity of the VCA in the calculation of the refractive index of this material. Finally, we study the effect of Sr content on tuning the refractive index of strain-free BST thin films.

Effect of atomic configurations on the refractive index of bulk BST

We restrict our investigations in this section to bulk BST at 50% concentration of Sr (i.e., $Ba_{0.5}Sr_{0.5}TiO_3$). Obviously, there is no unique supercell representation of this system. Among the many possible choices, we consider three different configurations that are represented by the supercells shown in Fig. 5.5. The first configuration, $C^{(1)}$, is represented by a $1 \times 1 \times 2$ supercell,

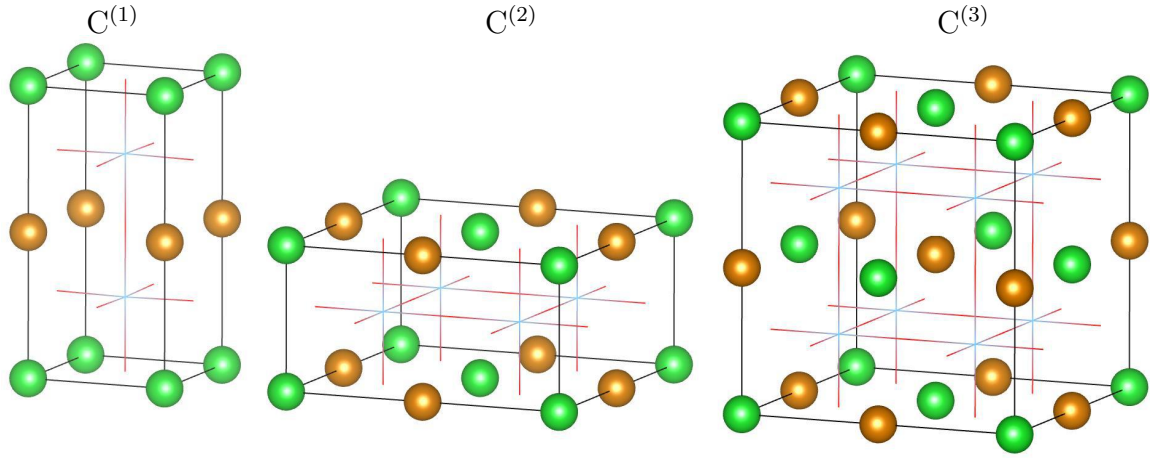


Figure 5.5: The corresponding configurations of Sr atom in BST at 50% concentration of Sr for which the refractive indices in Fig. 5.6 are calculated. Supercells of sizes $1 \times 1 \times 1$, $2 \times 2 \times 1$ and $2 \times 2 \times 2$ are used for the configurations $C^{(1)}$, $C^{(2)}$ and $C^{(3)}$, respectively. Ba and Sr species are represented by the green and orange atoms, respectively. Ti and O species are not shown for clarity.

and can be thought of as a layered structure with alternating BaO and SrO planes stacked along the z direction and separated by TiO_2 planes. The second configuration, $C^{(2)}$, is represented by a $2 \times 2 \times 1$ supercell, in which the Ba and Sr atoms are arranged in a checkerboard-like structure in the (110) plane. The third configuration, $C^{(3)}$, is represented by a larger $2 \times 2 \times 2$ supercell, and differs from $C^{(2)}$ in that the Ba and Sr species occupy alternate sites in the different (001) planes; it can be thought of as a three dimensional checkerboard structure[6].

The calculated refractive indices of these different configurations are shown in Fig. 5.6. Both $C^{(1)}$ and $C^{(2)}$ have a tetragonal space group symmetry of $P4/mmm$, so the xx and yy components of the refractive index are equivalent, while the zz component is distinct; we therefore show in Fig. 5.6 both the xx and the zz components of these two configurations. $C^{(3)}$, however, has a cubic $Fm\bar{3}m$ symmetry, so all components of the refractive index are equivalent; we therefore show only the xx component for this configuration.

[6]It should be pointed out that the supercells used to represent $C^{(2)}$ and $C^{(3)}$ are not primitive cells for these structures. We used larger supercells in order to render the comparison between these three configurations more straightforward.

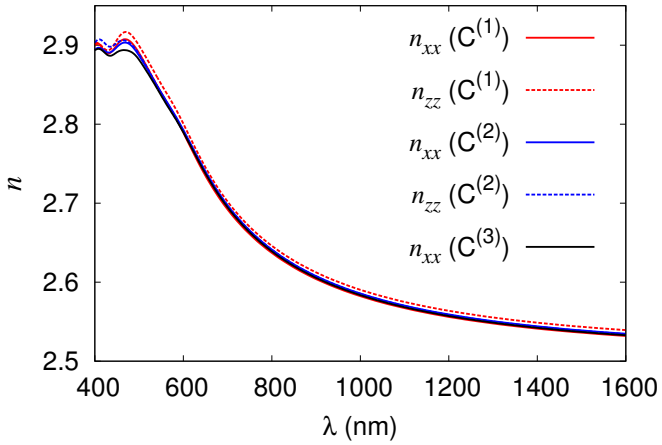


Figure 5.6: The refractive index of bulk $Ba_{0.5}Sr_{0.5}TiO_3$ for different atomic configurations of Sr atoms that are shown in Fig. 5.5. $C^{(3)}$ is isotropic, so only the xx component is shown.

It is evident from Fig. 5.6 that the refractive indices of $C^{(1)}$, $C^{(2)}$ and $C^{(3)}$ are almost identical to each other for the entire range of wavelengths considered. Also, despite the fact that $C^{(1)}$ and $C^{(2)}$ are in principle anisotropic, the xx and zz components of their refractive indices show only a negligible difference. This suggests that the refractive index of BST is not very sensitive to the atomic ordering of the Sr species in the material. This can be attributed to the fact that the optical transitions that are relevant for the calculated spectra within the considered range of wavelengths (400 to 1600 nm) are mainly the transitions from the highest occupied O $2p$ states to the lowest unoccupied Ti $3d$ states. These states are almost insensitive to the chemical environment of the Ba and Sr atoms in the system and, therefore, to their ordering.

The calculation of the refractive index with the VCA approximation used

The insensitivity of the refractive index to the atomic configurations of Ba and Sr in BST suggests that the use of approximations that average over disorder in representing the alloying of BST may provide a good representation of the material and reproduce the optical spectra obtained via the supercell approach.

We compare in Fig. 5.7 the refractive indices of bulk cubic paraelectric BST at different Sr contents as obtained from the VCA and the supercell

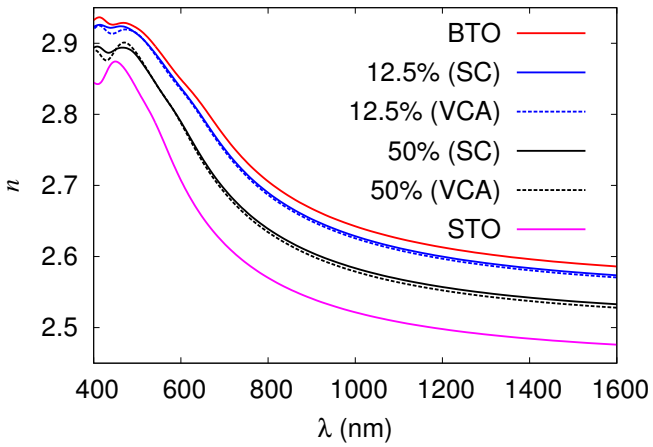


Figure 5.7: A comparison between the supercell (SC) approach and the virtual crystal approximation (VCA) approach in calculating the refractive index of bulk BST solid solutions in their cubic paraelectric phase. The supercells used in these calculations are shown in Fig. 5.8. The indicated percentage refers to the Sr content in BST. The refractive indices of pure BTO and STO are also shown for reference.

approaches. The supercells used are shown in Fig. 5.8.

As expected, excellent agreement between the two approaches is observed with both 12.5% and 50% Sr content in BST. Although we have not considered other concentrations, we believe that the agreement also holds for an arbitrary content of Sr. Therefore, we shall adopt the VCA approach in the investigations that follow, with a high degree of confidence.

Tuning the refractive index of BST solid solutions by means of alloying

We study in this section an alternative means by which the refractive index of BST may be tuned, namely, the effect of Sr concentration.

In Fig. 5.9, we show the refractive index, at 1000 nm, of unstrained BST thin films, at different Sr concentrations. We see that the refractive index shows a maximum at an Sr content of $\sim 15\%$. Either side of this value, the refractive index decreases with varying Sr content in an approximately linear manner. Once again, this can be attributed to the different phases of the material at the strain-free point, where it is paraelectric above the critical concentration and ferroelectric below (see Sec. 4.8.3). It can be noticed that

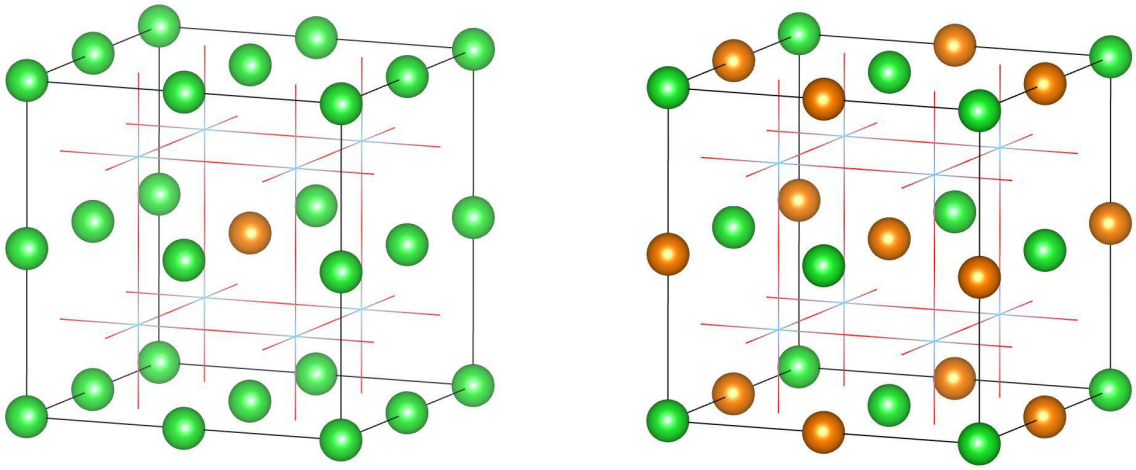


Figure 5.8: The supercells that are used for the calculations of the refractive indices of BST solid solutions at 12.5% (a) and 50% (b) Sr concentration. See Fig. 5.7. Ti and O species are not shown for clarity.

the general trend of the refractive index with Sr content opposes the trend in the direct gap of the system (see Fig. 4.16). The relation between the band gap and the refractive index has already been discussed earlier in Sec. 5.4. If the ferroelectric distortions are inhibited, one expects the refractive index to decrease monotonically with increasing Sr content, following a Vegard-like law even below Sr content of 15%.

The above results suggest that alloying can be a promising means to tune the refractive index of BST. Quantitatively, by increasing the Sr content in BST, the refractive index of pure BTO can be raised by up to $\sim 0.4\%$ around the critical Sr concentration, beyond which it can be lowered by $\sim 3.5\%$ in pure STO. As compared with the results in Table 5.1, alloying could lower the refractive index of BTO by as much as strains of $\sim \pm 1\% - \pm 2\%$ can do. Unlike alloying, however, strain can also induce strong birefringence.

The variations of the refractive index of BST with the Sr content were investigated in Ref. [79], where spectroscopic ellipsometry measurements for epitaxially grown BST films on a compressive substrate were performed. Although they reported a main trend that the refractive index tends to decrease with the increase of the Sr content, in agreement with our results, the detailed behaviour was not observed to be linear or monotonic, and deviates a lot from our results. The discrepancies between our results and those presented in

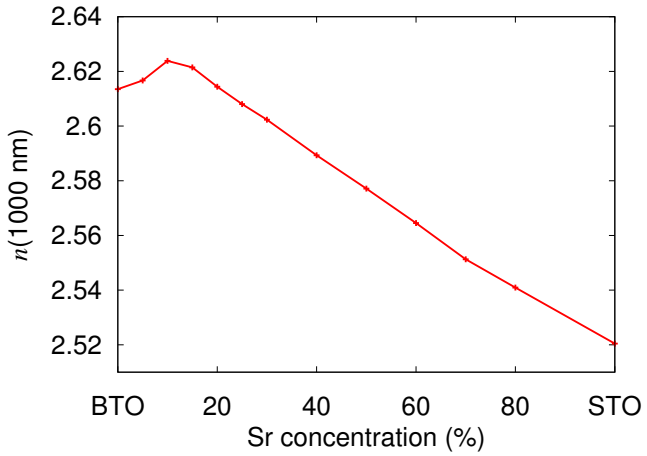


Figure 5.9: Effect of Sr content on the refractive index of free standing BST thin films.

Ref. [79] could be attributed to the fact that they considered *strained* BST films, while our results correspond to strain-free BST. The limitations of the spectroscopic ellipsometry technique (which are addressed in details in Chapter 2) could also play a role in the discrepancy.

Interestingly, one might argue that the trends in the refractive indices of BST as a function of Sr content may be attributed to the variation of the equilibrium lattice constant (see Table 4.8) rather than to the change in stoichiometry. In order to understand which effect dominates, we consider a system of cubic paraelectric BST at 50% concentration of Sr. We calculate the refractive index of this system at three different lattice constants, namely, at the lattice constant of pure BTO (a_{BTO}), pure STO (a_{STO}), and at its own equilibrium lattice constant. The refractive indices of these three cases are compared with those of pure paraelectric BTO and STO in Fig. 5.10.

It can be seen that the change in the stoichiometry has a much greater effect than the change in the lattice constant on the refractive index of the material. This conclusion does not hold for wavelengths lower than ~ 500 nm, but we expect that it would hold for the whole range of $400-1600$ nm if the band gaps of the systems were corrected, since the spectrum will then be blue shifted, as pointed out in Sec. 5.3.

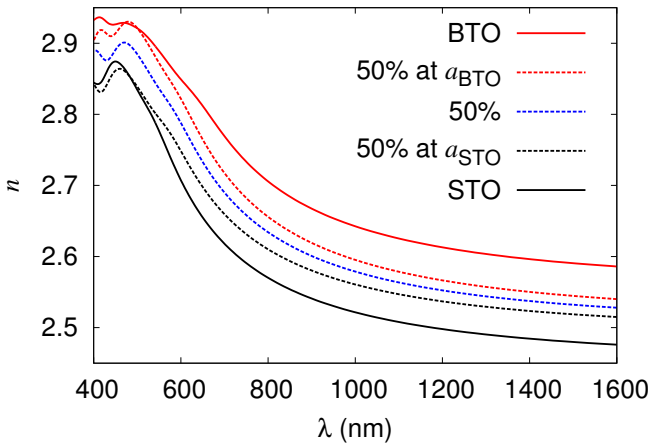


Figure 5.10: A comparison between the effects of volume and Sr content on the refractive index of BST. Bulk cubic paraelectric phase is adopted for all systems.

Strain-induced changes in the refractive index of BST solid solutions

The effect of strain on the refractive index of BST is very similar to the effects that have been investigated earlier for pure BTO and STO, where epitaxial strain generally lowers the refractive index of the materials mainly due to the induced ferroelectric transition. This is in agreement with the results in Ref. [73], where compressive substrates were found to lower the refractive index of $Ba_{0.5}Sr_{0.5}TiO_3$ thin films.

5.7 Summary

We studied in this chapter the effects of epitaxial strain and alloying on the refractive indices of BST solid solutions.

We found that epitaxial strain can provide a promising means for refractive index modulation, where strain-induced changes in both refractive index and birefringence could be greater than the reported changes in the literature induced by thermal and electro-optic effects. Quantitatively, we found that strains up to $\pm 4\%$ can lower the refractive index of BTO and STO by $3-4\%$ and can induce birefringence of up to ~ 0.14.

We found that strain can affect the refractive index directly and indirectly. The direct way refers to the strain-induced changes in the lattice vectors, and

consequently, the bond lengths. We found that these changes have almost no effect on the in-plane components of the refractive index, while they induce an almost linear change with strain in the zz component, which is lowered for compressive strains and raised for tensile strains. On the other hand, the indirect effect lies in the ferroelectric distortion that is induced by strain, which significantly lowers all the components of the refractive index.

On the other hand, we found that the variation of Sr content in BST can induce changes in the refractive index of pure BTO by the same amount as strains of $\sim \pm 2\%$ may induce. The refractive index of BST does not, however, show a linear trend with the Sr content, due to the existence of a critical Sr concentration at which the system undergoes a ferroelectric/paraelectric transition.

Furthermore, our results suggested that the refractive indices of BST solid solutions are almost insensitive to the atomic ordering of the Sr species. This was attributed to the fact that, within the visible and near infrared range, the relevant optical transitions are those that take place between the O $2p$ and the Ti $3d$ states, whereas the Ba and Sr states hardly affect the optical spectra.

The virtual crystal approximation was found to work very well, as it could reproduce, to very good accuracy, the spectra obtained with the supercell approach. This was tested for different Sr contents in BST. The success of the VCA is not unexpected, however, since we found that the atomic ordering is almost irrelevant for the refractive index of BST within the range of incident wavelengths of $400-1600$ nm.

Finally, our calculations suggested that the discrepancy between the refractive indices of BST solid solutions at different concentrations of Sr are mostly attributable to the change in the stoichiometry of the system rather than the change in the lattice parameter.

As in the preceding chapter, we restricted our study to the high temperature phase of STO and neglected the effects of rotations of the oxygen octahedra. This work could be extended in the future to include these effects and compare them with the results studied in this chapter.

Chapter 6

Effect of doping BTO with fluorine and nitrogen

6.1 Overview

In the last two chapters, we showed how the electronic and optical properties of BTO and STO may be tuned by forming a homogeneous solid solution. The promising results stimulate the investigation of other types of extrinsic substitutional dopants in BTO, and raise the questions of how would they compare to Sr, and to what extent could they affect the electronic and optical properties.

There exist a number of theoretical/experimental studies investigating the mechanisms and the effects of doping BTO and STO. A wide range of cationic dopants have been studied in the literature. Examples can be found in Refs. [222–225] and Refs. [226, 227] for experimental and first-principles studies, respectively. On the other hand, there are not as many studies about anionic dopants. The most common anionic dopants in BTO include fluorine (donor dopant), and nitrogen (acceptor dopant). Examples of experimental studies can be found for example in Refs. [228, 229].

In particular, Rao *et al* in Ref. [230] have studied the effect of co-substitution of F and N in powdered BTO. They have investigated the structural, electronic, ferroelectric and optical properties of the doped BTO both experimentally and from first-principles. Their results are interesting and promising; e.g., BTO shows an inhibition in ferroelectricity upon the dopant additions, and the pow-

der colour changes from white to green.

There exist, however, interesting questions that, to our knowledge, have not been investigated yet. For example, how does the co-substitution of F and N in BTO change its refractive index, as compared to Sr substitutions? What is the relevance of the arrangement of the dopant atoms in the host material and to what extent does it influence the refractive index and the band gap? How does biaxial strain affect the doped BTO in terms of its structural, electronic and optical properties? Furthermore, how does the concentration of F and N affect the above-mentioned properties?

In this chapter, we investigate, from first-principles, the questions posed above, attempt to shed more light on this material in thin-film form, and discuss the potential of anion doping as another possible means of tuning the optical properties of BTO.

The structural, electronic and optical properties of bulk $BaTiO_{2.8}F_{0.1}N_{0.1}$ are first investigated. We find that the most energetically favourable structure involves the dopant atoms forming a linear motif of F−Ti−N. We find also that the refractive index of the material shows a large dependence on the arrangement of the dopant atoms in the supercell; the component along the linear motif shows a greater value compared to the other components, indicating that doping BTO with F and N could be a promising means to tune the refractive index of the material. We find also that the refractive index can be further tuned by means of epitaxial strain. We finally investigate the effect of doping concentration and find that dilute concentrations have less effect on the electronic and optical properties of BTO, as might be expected.

6.2 Computational details

The DFT calculations in this chapter have been performed within the plane-wave CASTEP package. The calculations of the optical properties and the density of states were performed using the OptaDOS package [231, 232]. The local density approximation was used to approximate the exchange and correlation functional. CASTEP "On the fly" ultra-soft pseudopotentials, in which the Ba $5s$, Ti $3s$, O $2s$, F $2s$ and N $2s$ electrons are all treated as valence states, and a plane-wave energy cutoff of 40 Ha (1088 eV) were used throughout. The integration over the Brillouin zone has been performed by summing

over $7 \times 7 \times 7$, $4 \times 4 \times 4$ and $3 \times 3 \times 3$ Monkhorst-Pack k-point meshes for super-cell sizes of $1 \times 1 \times 1$, $2 \times 2 \times 2$ and $3 \times 3 \times 3$, respectively. Almost equivalent sampling was used for supercells of other shapes and sizes. DFT-LDA converged lattice parameters were adopted throughout. Unless stated otherwise, the ionic and the cell degrees of freedom were relaxed using the BFGS algorithm until the force on each atom was less than 0.5 meV/Å, and the relaxed components of the stress tensor were less than 0.06 GPa.

6.3 Properties of bulk $\mathbf{BaTiO_{2.8}F_{0.1}N_{0.1}}$

6.3.1 Structural properties

Firstly, $BaTiO_{2.8}F_{0.1}N_{0.1}$ shall be considered, in which F and N atoms have a concentration of $\sim 3.3\%$[1], as this is the concentration that has been experimentally synthesized in Ref. [230]. More dilute concentrations shall be investigated in Sec. 6.6. This concentration is approximately achieved, in the DFT calculations, by considering a 40-atom supercell of $2 \times 2 \times 2$ repetitions of the BTO primitive cell, in which two out of the 24 oxygen atoms are substituted by an F and an N atom[2]. This results in a total of $24 \times 23 = 552$ permutations of the possible sites of the dopant atoms. However, only seven of these sites (shown in Fig. 6.1) are symmetry inequivalent and shall be considered in this section. The corresponding atomic configurations shall be denoted by $C^{(1)}$, $C^{(2)}$ to $C^{(7)}$ throughout.

Description of the configurations

Conventionally, we have chosen to align the Ti−F bond along the c parameter in all configurations. The configurations $C^{(1)}$ to $C^{(7)}$ can then be characterized by the relative orientation of the Ti−N bond with respect to the Ti−F bond, and by the distance between the F and the N atoms. This information is summarized in Table. 6.1

[1] This concentration is defined as the ratio between the number of the F (or the N) atoms in the system and the total number of the O sites.

[2] This supercell gives slightly higher concentrations of F and N (i.e., $\sim 4\%$), resulting in a formula unit of $BaTiO_{2.75}F_{0.125}N_{0.125}$. For the sake of simplicity, we shall keep the formula $BaTiO_{2.8}F_{0.1}N_{0.1}$ to refer to the concentration given by the $2 \times 2 \times 2$ supercell.

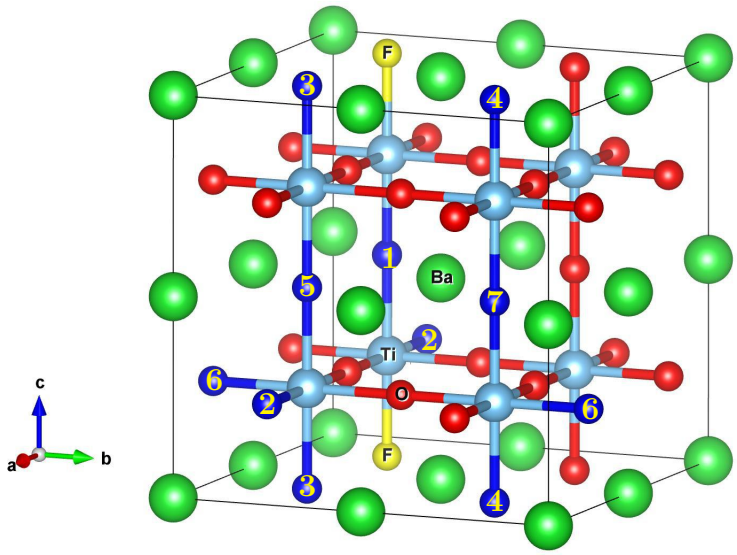


Figure 6.1: An illustration of the $2 \times 2 \times 2$ supercell used for the calculation of $BaTiO_{2.8}F_{0.1}N_{0.1}$. The positions of the seven nitrogen atoms (blue) with respect to the fluorine atom (yellow) indicate the seven symmetry inequivalent sites described in the main text. The corresponding labels are printed on each N atom.

Configuration	Ti−N bond alignment	F to N distance (Å)
$C^{(1)}$	c	4.04
$C^{(2)}$	a	2.81
$C^{(3)}$	c	3.93
$C^{(4)}$	c	5.59
$C^{(5)}$	c	5.61
$C^{(6)}$	b	4.84
$C^{(7)}$	c	6.88

Table 6.1: The interatomic distance between F and N, and the alignment of the Ti−N bond of the seven configurations shown in Fig. 6.1.

Configuration	a	b	c	α	β	γ	Volume	ΔE
$C^{(1)}$	7.86	7.86	8.06	89.97	89.97	90.00	498.61	0.000
$C^{(2)}$	7.94	7.89	7.97	89.96	89.96	89.96	498.89	0.514
$C^{(3)}$	7.87	7.90	8.03	89.94	89.96	89.98	499.28	0.519
$C^{(4)}$	7.89	7.89	8.03	89.95	89.95	89.97	499.48	0.554
$C^{(5)}$	7.88	7.90	8.03	89.94	89.97	89.98	499.27	0.552
$C^{(6)}$	7.88	7.95	7.98	89.94	89.98	89.96	499.29	0.603
$C^{(7)}$	7.89	7.89	8.01	89.95	89.95	89.97	499.25	0.598
BTO	7.91	7.91	7.91	89.92	89.92	89.92	495.56	–

Table 6.2: The structural parameters and the corresponding relative energies of the seven symmetry-inequivalent atomic configurations of the supercell of $BaTiO_{2.8}F_{0.1}N_{0.1}$ shown in Fig. 6.1. The relative energy ΔE (per $2 \times 2 \times 2$ supercell) is defined as $\Delta E = E_i - E_1$, where E_i is the energy of the i^{th} configuration with i running from 1 to 7, and E_1 is the total energy of $C^{(1)}$. The lattice parameters, the angles, the volumes and the energies are given in units of angstroms, degrees, Å^3 and eV, respectively. The corresponding calculated quantities of pure rhombohedral BTO are shown in the last row.

Energetics of the configurations

In order to study the energetics of these different configurations, we consider first the bulk fully-relaxed structures at 0 K, in contrast to the *ab initio* calculations performed in Ref. [230], where the experimental lattice parameter of cubic BTO (i.e., 4.00 Å, see table. 4.1) was used. Hence, the atomic positions and the lattice parameters are allowed to fully relax without constraints. We show in Table 6.2 the corresponding structural parameters of these configurations, along with the total energies with respect to the minimum energy configuration. The corresponding parameters of the low temperature rhombohedral phase of BTO are also shown in the table for comparison.

It is first noted that doping BTO with F and N with this concentration distorts the perfect rhombohedral structure and has an overall effect of a small volume increase of $\sim 3 - 4$ Å^3 per supercell. The symmetry breaking could be attributed to the change in the bonding character between Ti and the neighbouring anions, where the Ti−F bonding is of an ionic nature, while the

Ti−N bonding has a covalent nature, resulting in a large discrepancy in the bond lengths [230].

In agreement with Ref. [230], $C^{(1)}$ is the most energetically favourable. In this configuration, the F and N atoms congregate to form a linear chain of F−Ti−N, with a bond angle of almost exactly 180 degrees (relaxation slightly distorts the linear arrangement by ~ 0.7 degrees).

There are, however, some quantitative and qualitative differences between our results and those of Ref. [230], in particular with respect to the relative energies of the other configurations. For example, we found that $C^{(1)}$ is lower in energy, compared to the others, by about 0.5-0.6 eV, while they reported energy differences ranging between 0.16 eV to 0.55 eV for the configurations they tested (which are the same as the configurations we are testing here, apart from $C^{(3)}$ and $C^{(4)}$, which they did not consider). Besides this, our results also disagree with the energy ordering of the different configurations, where, for instance, we show that $C^{(6)}$ is the one of highest energy, while they reported $C^{(5)}$ to be higher in energy than $C^{(6)}$ by about 0.3 eV.

A key difference between our calculations and those of Ref. [230] is that we use fully relaxed structures, whereas they have fixed lattice parameters set to the experimental value of pure cubic BTO.

In order to ascertain whether this is an important contributory factor, it is worth considering that in our calculations the seven configurations can be divided into distinct groups that are very close in energy (differences of $O(10^{-3})$ eV). Each group is separated by a dashed horizontal line in Table 6.2. Some configurations that have very similar lattice parameters (e.g., $C^{(3)}$, $C^{(5)}$ and $C^{(7)}$) belong to different energy groups; on the other hand, $C^{(2)}$ and $C^{(3)}$ are very close in energy, despite the fact that their lattice parameters are not very similar. This immediately suggests that small changes in the shape and volume of the supercell are not the dominant factor in determining the relative energetics of the different configurations, but rather it is the internal atomic configuration. In fact, if we consider $C^{(1)}$ but fix its lattice constants at those of $C^{(4)}$, relaxing the ions only, the energy would increase by just ~ 6 meV (that is, $\sim 1\%$ of the current ΔE).

6.3.2 Electronic and optical properties

In Fig. 6.2, we show the corresponding refractive indices of each atomic configuration considered above. Unlike the case of BST solid solutions, which was discussed earlier in Chapter 5, the refractive index of the doped $BaTiO_{2.8}F_{0.1}N_{0.1}$ shows a significant dependence on the atomic configuration. This suggests that the VCA might not work well in this particular system. The components of the refractive index along the [100], [010], and [001] crystallographic directions are labeled by the xx, yy and zz subscripts, respectively.

One first notices in Fig. 6.2 that there exist some configurations for which the refractive indices are very similar. Indeed, these can be divided into three groups, group I (G I), which includes $C^{(1)}$, $C^{(4)}$ and $C^{(7)}$, group II (G II), which includes $C^{(2)}$ and $C^{(6)}$, and group III (G III), which includes $C^{(3)}$ and $C^{(5)}$. This can be explained in view of the relative orientations of the Ti−F and the Ti−N bonds within the same system (see Table 6.1). In all configurations, the Ti−F bond is aligned along the c direction . One can notice that for all configurations in G I and G III, the Ti−N bond is aligned along the c direction (i.e., parallel to the Ti−F bond), in contrast to the configuration of G II, where it is aligned along the a or the b directions. This suggests that the refractive index is more sensitive to the relative *alignments* of the bonds than to the relative *sites* of these bonds. The observed discrepancy between the refractive indices of G I and G III, however, is attributed to the symmetry breaking of the xy isotropy in G III, where one can notice the splitting in the xx and the yy components of the refractive index. Other than that, the refractive indices of G III would look similar to those of G I. In general, doping BTO with F and N induces a large anisotropy in the system leading to large birefringence, which could be uniaxial (such as configurations in G I) or biaxial (such as configurations in G II and G III), depending on the symmetry of the system.

On the other hand, the refractive indices of the distinct configurations show no obvious correlation to the total energy of the system. Configurations that are very close in energy (such as $C^{(6)}$ and $C^{(7)}$) can have very different refractive indices (see Figs. 6.2f and 6.2g).

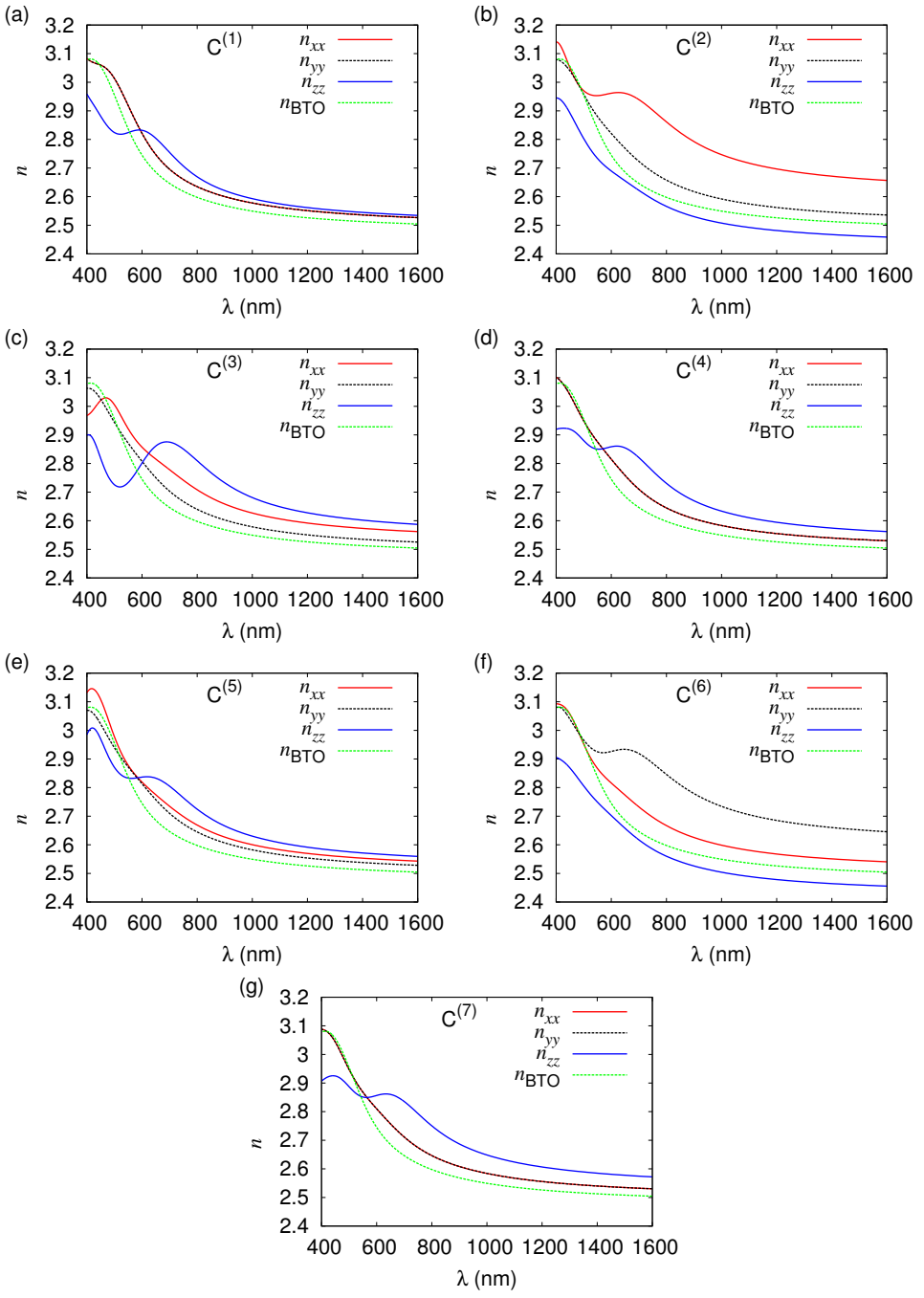


Figure 6.2: The three components of the refractive index that correspond to the seven symmetry-inequivalent atomic configurations of the F and N dopant atoms in $BaTiO_{2.8}F_{0.1}N_{0.1}$. Panels **(a)-(g)** correspond to configurations of $C^{(1-7)}$ shown in Fig. 6.1, respectively. The refractive index of pure rhombohedral BTO (green line) is shown on each panel for comparison.

Configuration	E_g	ΔE_g
$C^{(1)}$	1.71	−0.68
$C^{(2)}$	1.38	−1.01
$C^{(3)}$	1.48	−0.91
$C^{(4)}$	1.46	−0.93
$C^{(5)}$	1.46	−0.93
$C^{(6)}$	1.38	−1.01
$C^{(7)}$	1.42	−0.97
BTO	2.39	0.00

Table 6.3: The direct energy gaps (at Γ) of the seven configurations of $BaTiO_{2.8}F_{0.1}N_{0.1}$ depicted in Fig. 6.1. The corresponding bandgap of rhombohedral BTO is given in the last row. ΔE_g is the difference in the bandgap with respect to pristine BTO. All the energies are given in units of eV.

Electronic structure

The direct optical gaps (at Γ) of the seven different configurations are tabulated in Table 6.3. One can notice that doping BTO with N and F generally closes the gap. Different configurations show different effects on the gap. A maximum reduction of ~ 1 eV is observed in $C^{(2)}$ and $C^{(6)}$, while the gap of $C^{(1)}$ is lower than that of BTO by ~ 0.7 eV.

The decrease in the bandgap is attributed to the presence of the N $2p$ defect levels that are located in the gap at the top of the O $2p$ states near the Fermi level (see Figs. 6.3 and 6.4). This is confirmed by Ref. [230], where a similar band structure for cubic $BaTiO_{2.8}F_{0.1}N_{0.1}$ is presented. We show in Fig. 6.3 the band structures of the two extreme cases of $C^{(1)}$ and $C^{(6)}$ that correspond to the minimum and the maximum decrease in the bandgap with respect to BTO, respectively. The N states of $C^{(6)}$ are almost entirely isolated from the O states, explaining the greater decrease in the bandgap.

The calculation of the projected density of states (Fig. 6.4) also shows that the F $2p$ levels, in contrast to the N levels, are located at the bottom of the manifold of O $2p$ states, indicating that there is little or no hybridization with the bottom conduction bands corresponding to Ti $3d$ states. This supports the statement made earlier, that the Ti−F bond is of more ionic character than

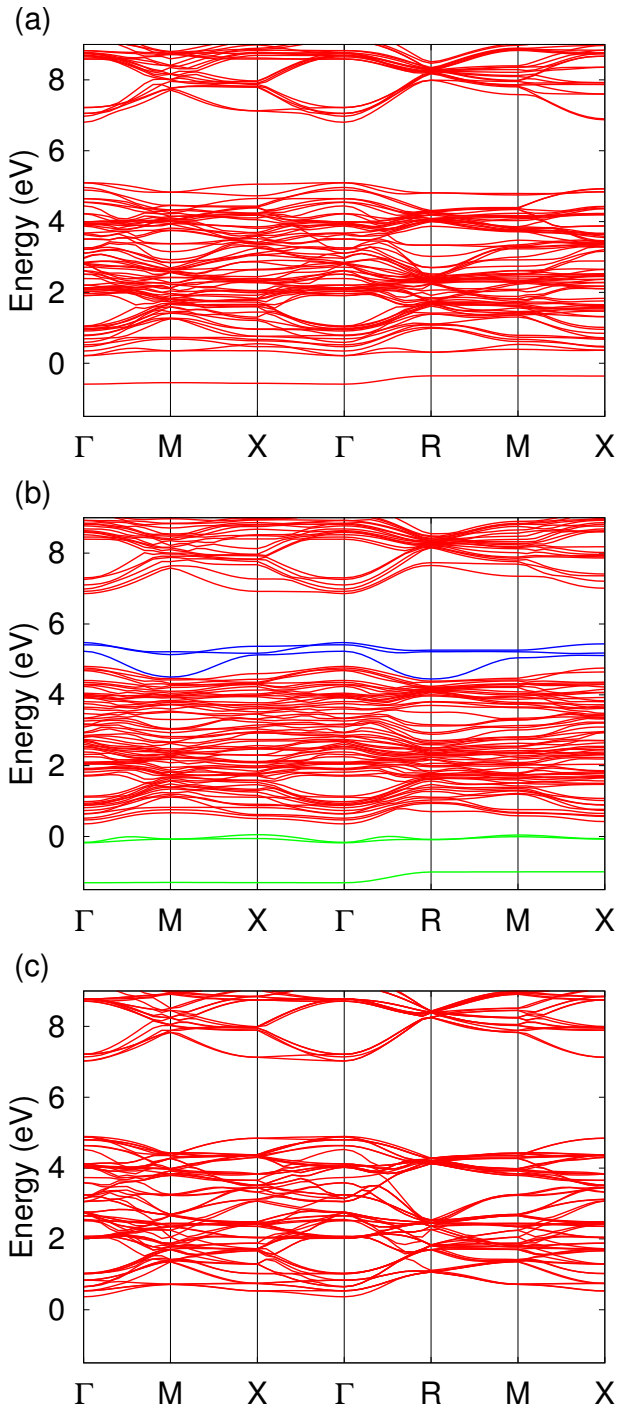


Figure 6.3: The calculated electronic band structures of **(a)** $C^{(1)}$ and **(b)** $C^{(6)}$ of $BaTiO_{2.8}F_{0.1}N_{0.1}$ as depicted in Fig. 6.1. Only the top valence and the bottom conduction states are shown. The corresponding band structure of pure rhombohedral BTO is also shown in panel **(c)** for comparison. The N and F states are coloured blue and green, respectively, in panel **(b).**

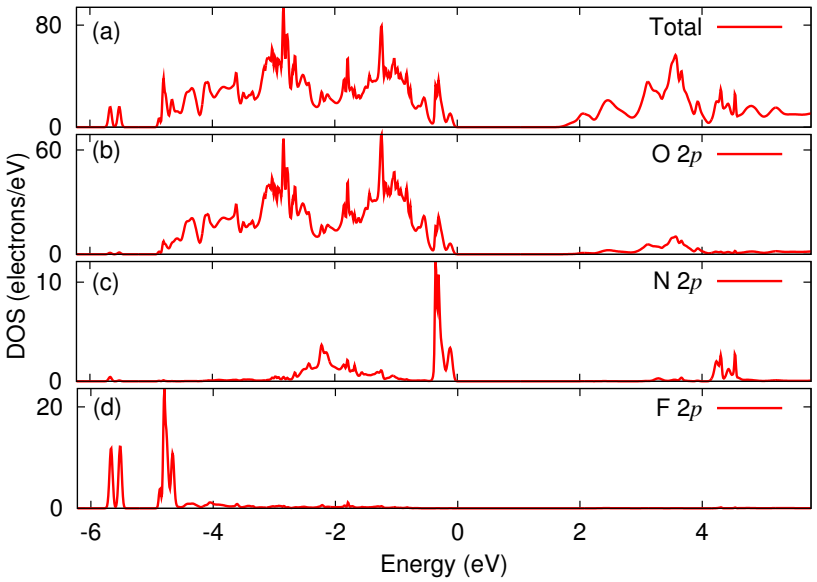


Figure 6.4: Total **(a)** and partial **(b)**−**(d)** electronic density of states of $BaTiO_{2.8}F_{0.1}N_{0.1}$ ($C^{(1)}$). Panels **(b)**, **(c)**, and **(d)** show the partial density of states of the O $2p$, N $2p$, and F $2p$ electrons, respectively. Energies are given with respect to the valence band maximum, which is set to zero.

the Ti−N bond.

6.4 Properties of thin film $\mathbf{BaTiO_{2.8}F_{0.1}N_{0.1}}$

We have shown in the previous section how the electronic and optical properties of BTO could be significantly changed after the co-substitution of F and N. However, the maximum change in the bandgap and the refractive index (given by $C^{(1)}$ and $C^{(6)}$) does not correspond to the atomic configuration that is minimum in energy. In fact, the difference between the lowest energy structure ($C^{(1)}$) and the one just above it is ~ 0.5 eV per $2 \times 2 \times 2$ supercell (20 times larger than k_BT at room temperature). This difference is quite high and suggests that the other configurations may not be present in the real material. The previous results, however, indicate the sensitivity of the refractive index of $BaTiO_{2.8}F_{0.1}N_{0.1}$ to distinct atomic configurations.

In essence, we are looking for external means to control the relative energetics of the different configurations. Inspired by earlier chapters, we con-

sider biaxial strain which may be realised experimentally in coherent thin-film growth on suitable substrates.

6.4.1 Structural properties

Our previous calculations in Sec. 6.3.1 (which are also in agreement with Ref. [230]) indicate that the dopant atoms of F and N favour a configuration in which they form a linear chain of F−Ti−N bonds ($C^{(1)}$). Thus, we shall consider this particular configuration in the calculations that follow.

When applying epitaxial biaxial strain, we adopt the same constraints that were adopted in chapters 4 and 5, where the in-plane lattice parameters (a and b) are held fixed and constrained to be equal, while the out-of-plane lattice parameter is allowed to relax. All the lattice parameters are kept orthogonal to each other (hence restricting the study to cubic/tetragonal lattices), and all the ions are allowed to relax as described in Sec. 6.2.

The amount of strain ϵ is given with respect to the strain-free pristine BTO, so, Eq. 4.9 is re-defined as follows:

$$\epsilon = \frac{a - a_0^{\mathrm{BTO}}}{a_0^{\mathrm{BTO}}} \times 100\% \tag{6.1}$$

where a_0^{BTO} is the lattice parameter of pure BTO, at 0% strain, under the above constraints. So, one can think of a thin film $BaTiO_{2.8}F_{0.1}N_{0.1}$ at 0% strain as corresponding to the case in which it is deposited on a pure cubic BTO substrate.

In the bulk rhombohedral or cubic lattice, all three directions (x, y and z) are symmetrically equivalent. However, this is not the case in the tetragonal lattice, where the in-plane directions (x and y) are symmetrically distinct from the z direction. Therefore, we consider two different configurations (illustrated in Fig. 6.5) at each value of strain, that correspond to the F−Ti−N chain being parallel (conveniently chosen to be along the y direction) and perpendicular (along the z direction) to the plane of strain, respectively. We shall be using the superscripts $\perp$ and $\parallel$ to refer to the configuration and physical quantities that correspond to the perpendicular and the parallel orientations, respectively.

The most energetically favourable orientation is dependent on the value of the applied strain. As illustrated in Fig. 6.6, $C^{(\perp)}$ is more stable for strains that range between -4% to $\sim 0.5\%$, beyond which $C^{(\parallel)}$ becomes lower in energy.

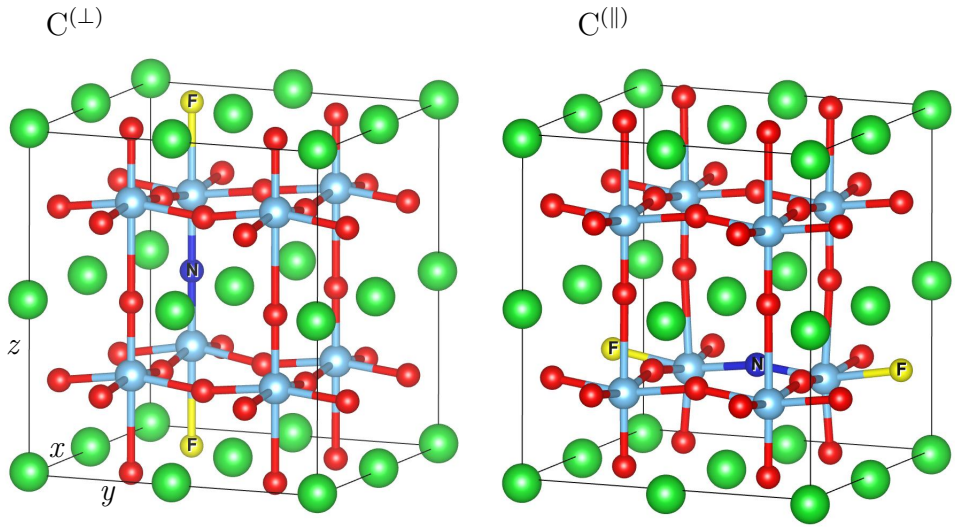


Figure 6.5: $BaTiO_{2.8}F_{0.1}N_{0.1}$ under compressive strain. Two symmetry-inequivalent alignments of the linear F−Ti−N motif are shown, one perpendicular $C^{(\perp)}$ and one parallel $C^{(\parallel)}$ to the strained (001) plane.

The energy difference between the two configurations depends monotonically on the value of strain. At moderate strains of $\pm 1\%$, the difference is about $0.1 - 0.2$ eV, while it vanishes at a tensile strain of $\sim 0.5\%$.

In Fig. 6.6 we also plot c/a for $C^{(\perp)}$ (black line) and note that the energy of $C^{(\perp)}$ becomes larger than that of $C^{(\parallel)}$ at almost the same point at which c/a becomes less than 1. This can be understood as follows: energetically, the linear F−Ti−N motif prefers to adopt the configuration that enables the F−N distance to be as large as possible. For compressive strains and tensile strains less than $\sim 0.5\%$ this is along the c-axis (unshaded region in Fig. 6.6); for tensile strains higher than $\sim 0.5\%$, it is in the in-plane direction.

So, one can conclude that when a single crystalline thin film of $BaTiO_{2.8}F_{0.1}N_{0.1}$ is deposited on a compressive substrate, it is more energetically favourable for the F−Ti−N chains to be oriented perpendicular to the substrate. However, when deposited on a tensile substrate the opposite is expected. This result is very relevant when one is interested in the optical properties of the deposited film, because the optical anisotropy is strongly influenced by the orientation of the F−Ti−N chain, as shall be discussed in the next section.

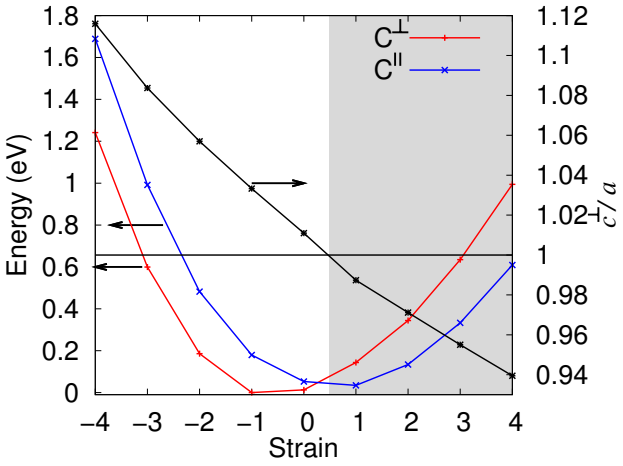


Figure 6.6: The total energy of the perpendicular (red) and the parallel (blue) configurations, depicted in Fig. 6.5, of strained $BaTiO_{2.8}F_{0.1}N_{0.1}$. The tetragonality ratio of $C^{(\perp)}$ ($c^{\perp}/a$) is also shown by the black curve. The energies are given with respect to the minimum point in the curves, which corresponds to $C^{(\perp)}$ at -1% strain. The shaded area corresponds to the range of strains where ($c^{\perp}/a$) is less than 1.

6.4.2 Electronic and optical properties

The three components of the refractive indices of $C^{(\perp)}$ and $C^{(\parallel)}$ are shown in Figs. 6.7, 6.8 and 6.9 for the visible and near infrared wavelength range. It can be first noticed that the xx component of the refractive index of both configurations shows only a negligible difference with respect to the refractive index of pure BTO at all values of strain considered[3]. Similarly, $n^{\perp}_{yy}$ and $n^{\parallel}_{zz}$ are nearly the same as in pure BTO. However, a substantial difference is observed in $n^{\perp}_{zz}$ (represented by the red curve in Fig. 6.9) and $n^{\parallel}_{yy}$ (represented by the blue curve in Fig. 6.8).

In fact, this large anisotropy appears to be strongly governed by the character of the bonds between the Ti cation and the neighbouring anions, along which the refractive index is determined. Along the x direction, the bonds are merely of Ti−O type in both configurations, similar to the case of pure BTO, resulting in $n^{\perp}_{xx}$, $n^{\parallel}_{xx}$ and n^{BTO}_{xx} being almost equal. On the other hand, an

[3]In this chapter, the refractive index of strained BTO differs slightly from that shown in Chapter 5. This is a consequence of the different computational details in this chapter that are adopted for both BTO and $BaTiO_{2.8}F_{0.1}N_{0.1}$ for consistency, leading to different equilibrium structural parameters for BTO. The qualitative behaviour is retained.

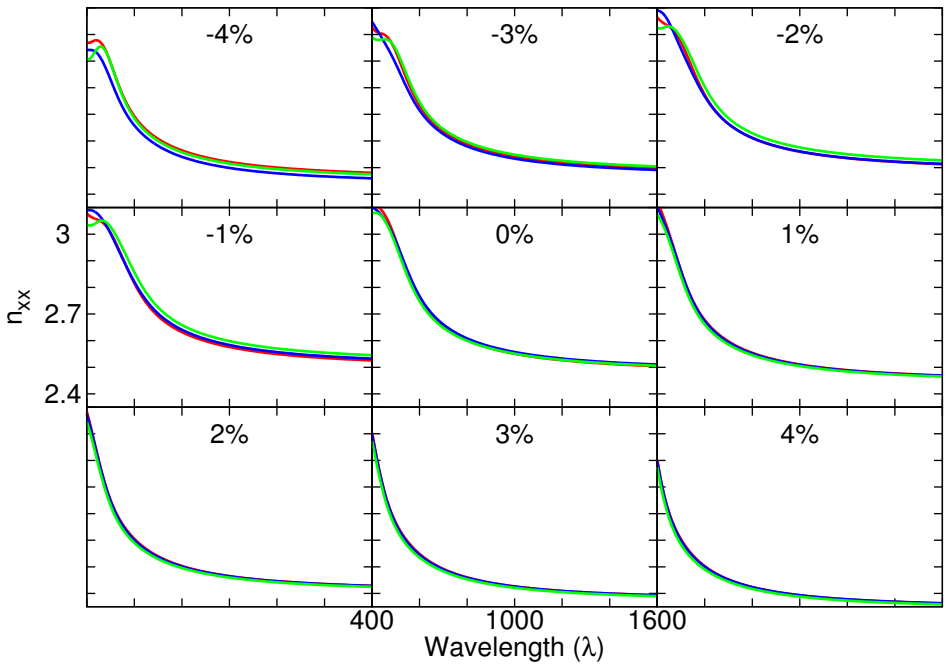


Figure 6.7: Effect of biaxial strain on the xx component of the refractive index of $BaTiO_{2.8}F_{0.1}N_{0.1}$ thin films. The refractive indices of $C^{(\perp)}$ and $C^{(\parallel)}$ (shown in Fig. 6.5) are illustrated by the red and blue curves, respectively. For comparison, the refractive index of pristine BTO is shown by the green curve. The value of strain is printed on each panel.

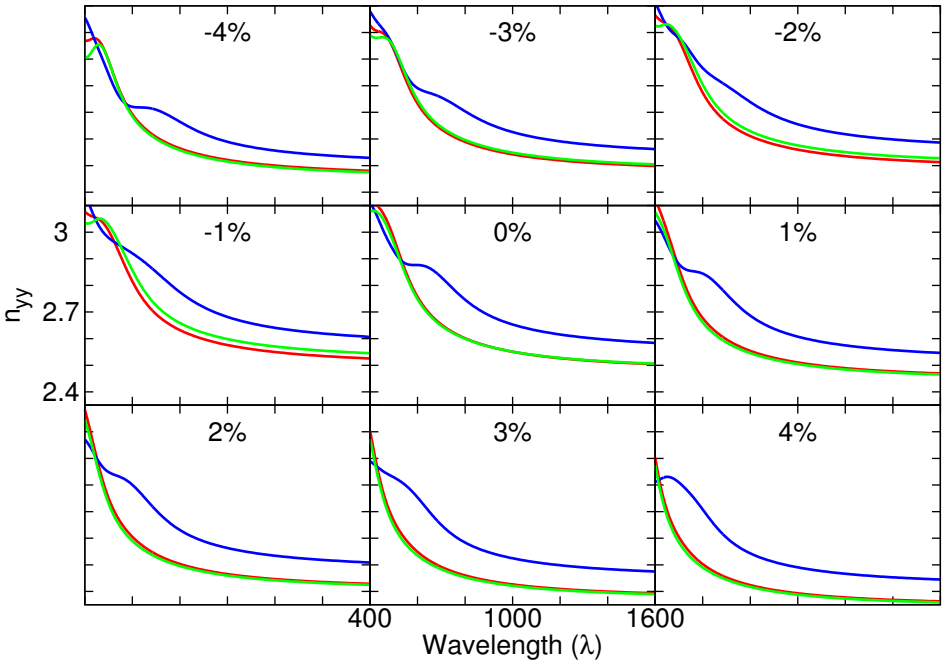


Figure 6.8: Effect of biaxial strain on the yy component of the refractive index of $BaTiO_{2.8}F_{0.1}N_{0.1}$ thin films. The refractive indices of the $C^{(\perp)}$ and $C^{(\parallel)}$ configurations (shown in Fig. 6.5) are illustrated by the red and blue curves, respectively. For comparison, the refractive index of pristine BTO is shown by the green curve. The value of strain is printed on each panel.

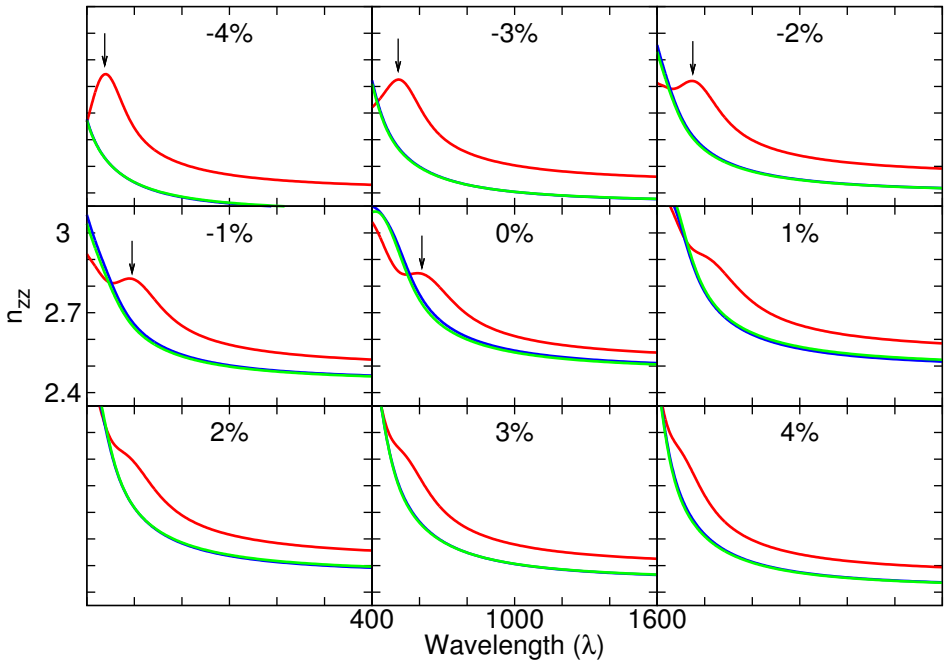


Figure 6.9: Effect of biaxial strain on the zz component of the refractive index of $BaTiO_{2.8}F_{0.1}N_{0.1}$ thin films. The refractive indices of $C^{(\perp)}$ and $C^{(\parallel)}$ configurations (shown in Fig. 6.5) are illustrated by the red and blue curves, respectively. For comparison, the refractive index of pristine BTO is shown by the green curve. The value of strain is printed on each panel. The black arrows indicate a characteristic peak in the refractive index of $C^{(\perp)}$.

F−Ti−N chain lies along the y direction for $C^{(\parallel)}$, in contrast to $C^{(\perp)}$ in which all the bonds are of Ti−O type along the y-direction; this results in both $n_{yy}^{\perp}$ and n_{yy}^{BTO} being almost equal, while $n_{yy}^{\parallel}$ is distinct. Similar arguments holds for the components along the z direction.

In view of the calculations of the refractive indices of bulk $BaTiO_{2.8}F_{0.1}N_{0.1}$ (Fig. 6.2), one can relate the enhancement of the refractive index component along the F−Ti−N chain (Fig. 6.8 (blue curve) and Fig. 6.9 (red curve)) to the presence of the Ti−N bond in particular, rather than the Ti−F bond. As shown in Figs. 6.2b and 6.2d (which correspond to $C^{(2)}$ and $C^{(4)}$, respectively), the refractive index component along the Ti−N bond is much higher than that of BTO, whilst the component along the Ti−F bond is lower. This may be related to the degree of bond covalency (and hence polarizability). This is greatest for the Ti-N bond; the Ti-F bond is more ionic, as pointed out earlier.

In Fig. 6.9, one can notice that $n_{zz}^{\perp}$ shows an anomalous peak at ∼500 nm, which gets more pronounced at high compressive strains. The corresponding values of $n_{zz}^{\parallel}$ and n_{zz}^{BTO} do not show this peak, however. This can be related to an extra characteristic peak in the absorption spectrum that is observed around this wavelength for this system (denoted by P_0 in Fig. 6.10). In fact, we found that the optical matrix elements of the highest occupied states of $C^{(\perp)}$ have a greater value than those of $C^{(\parallel)}$ and pure BTO, which indicate more allowed electronic transitions in the former case giving rise to the extra peak in the spectrum. It is worth pointing out that in Ref. [230], the measured absorbance of powdered $BaTiO_{2.8}F_{0.1}N_{0.1}$ also shows this characteristic peak at $\sim 400 - 500$ nm, explaining the colour change in the material.

In order to have a clearer idea of the effect of strain on $BaTiO_{2.8}F_{0.1}N_{0.1}$ thin films, we plot in Fig. 6.11 the refractive index (at a representative value of wavelength, chosen to be 1000 nm) as a function of the epitaxial strain. It is evident from Figs. 6.11a and 6.11b that the variation of the refractive index, as a function of strain, of both configurations of $BaTiO_{2.8}F_{0.1}N_{0.1}$ is similar to that of pure BTO, apart from an almost-constant shift in $n_{zz}^{\perp}$ and $n_{yy}^{\parallel}$, which has been discussed above.

As we have discussed in Chapter 5, BTO shows uniaxial birefringence as a function of strain as a consequence of the tetragonal symmetry, with the extraordinary axis being along the out-of-plane lattice parameter. In the case of $BaTiO_{2.8}F_{0.1}N_{0.1}$, the presence of the linear F−Ti−N chain plays an addi-

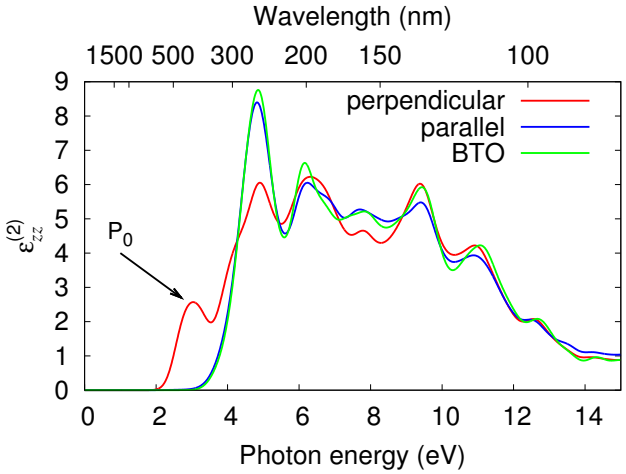


Figure 6.10: The zz component of the imaginary part of the dielectric constant $\varepsilon^{(2)}$ at a strain of -4% for $C^{(\perp)}$ (red curve) and $C^{(\parallel)}$ (blue curve). The corresponding curve of BTO is also shown by the green curve. $(\varepsilon^2_{zz})^{\perp}$ has an extra characteristic peak at ~ 400 nm, denoted by P_0.

tional role in determining the optical anisotropy of the system. As for $C^{(\perp)}$, the chain is already oriented along the extraordinary tetragonal axis, so it shows similar anisotropy to pure BTO where both $n^{\perp}_{xx}$ and $n^{\perp}_{yy}$ are equal. However, the linear F−Ti−N chain in $C^{(\parallel)}$ is oriented along the y axis. This leads to an extra degree of anisotropy, breaking the symmetry between the in-plane components of the refractive index, as shown in Fig. 6.11b.

One might argue, however, that in $C^{(\parallel)}$, the F−Ti−N chain is only *conventionally* oriented along the y axis. It could be equivalently oriented along the x axis leading to a symmetry-equivalent configuration. Therefore, it might be possible that both of the orientations coexist, leading back to the case of xy isotropy. However, we will show later in Sec. 6.5 that the F−Ti−N chains favour a configuration in which they are parallel to each other, and the coexistence of two perpendicular chains in two neighbouring $2 \times 2 \times 2$ supercells is energetically unfavourable.

At each value of strain in Fig. 6.11c, we show the refractive index (at 1000 nm) of the equilibrium configuration of $BaTiO_{2.8}F_{0.1}N_{0.1}$ at that strain, which we refer to as n^{eq} (see Fig. 6.6). The refractive index of pure BTO is also shown in the figure for comparison. It can be noticed that n^{eq}_{yy} and n^{eq}_{zz} are almost symmetric around the 0% strain point, meaning that compressive

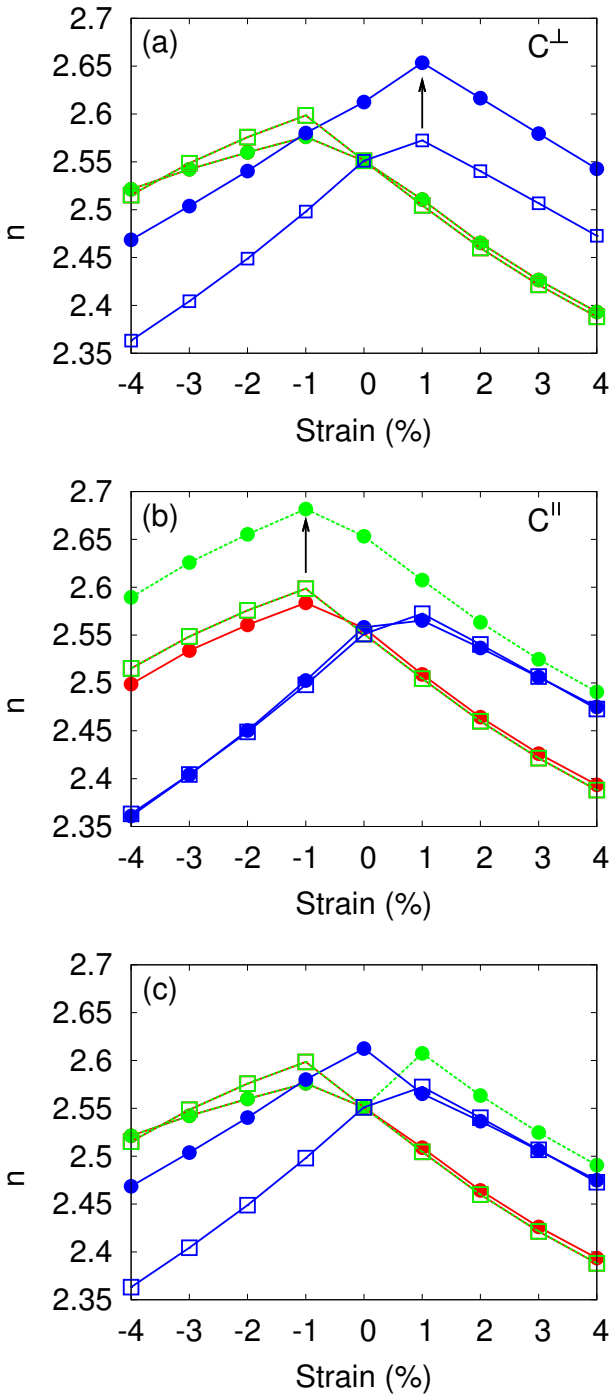


Figure 6.11: The refractive index (at 1000 nm) of $C^{(\perp)}$ **(a)** and $C^{(\parallel)}$ **(b)** (represented by solid circles) as affected by epitaxial strain. Panel **(c)** shows the refractive index of the lowest energy configuration at each value of strain, as given by Fig. 6.6. The xx, yy and zz components of the refractive index are represented by the red, green and blue curves, respectively. The refractive index of pristine BTO is also shown for comparison (represented by the open squares).

and tensile substrates have almost the same effect on tuning the refractive index of the material. n_{yy}^{eq} shows also a sudden drop at 0% strain, this is expected to be due to the transition from $C^{(\perp)}$ to $C^{(\parallel)}$ around this value of strain. n_{yy}^{eq} is expected to show a smoother variation if a higher resolution of strains is considered. It is worth noting that the material shows almost no birefringence at $\sim -1\%$ strain at 1000 nm, but that this does not hold for the entire dispersion, unlike the case of BTO at 0% strain, where it is truly isotropic by symmetry.

The question immediately arises to what quantitative extent the co-substitution of F and N in BTO thin films could affect its optical properties. For this purpose, we list in Table 6.4 the percentage differences between the three components of n^{eq} and n^{BTO} at 1000 nm. Interestingly, at 0% strain the out-of-plane component of the refractive index can be increased by $\sim 2.4\%$ upon doping, while the in-plane components are almost unchanged. For compressive strains, n_{zz} shows the greatest effect and can be raised by up to $\sim 4\%$ at high compression, whereas the other components are decreased by less than a percent at moderate strains. On the other hand, tensile strains mostly affect n_{yy} by increasing its value by $\sim 4\%$, while the effect on the other components is minor.

These results indicate that doping BTO with F and N could be a promising tool by which the refractive index of BTO can be dramatically changed along particular crystallographic directions. The optical properties can be further finely tuned by means of epitaxial strain. We can see that this anionic doping appears to have a stronger effect on the optical properties of BTO than the other means that have been discussed in Chapter 5, which include cationic doping with Sr and epitaxial strain.

6.5 Most stable configuration

In Sec. 6.3.1, we have investigated the energetics of all the symmetry-inequivalent configurations of the dopant species in bulk $BaTiO_{2.8}F_{0.1}N_{0.1}$. The results suggest that F and N are most favourably aligned in linear chains of F−Ti−N bonds. Thus, we focused on this particular configuration in our investigations in Sec. 6.4.1 and 6.4.2.

However, all the previous calculations have been performed on a supercell of $2 \times 2 \times 2$ size. This obviously limits the number of possible configurations that

Strain	$\Delta n_{xx}(\%)$	$\Delta n_{yy}(\%)$	$\Delta n_{zz}(\%)$
-4%	0.24	0.24	4.19
-3%	-0.25	-0.25	3.90
-2%	-0.62	-0.62	3.55
-1%	-0.86	-0.86	3.16
0%	-0.01	-0.01	2.40
1%	0.18	4.11	-0.28
2%	0.17	4.20	-0.15
3%	0.19	4.27	-0.03
4%	0.23	4.30	0.09

Table 6.4: The percentage difference in the refractive index Δn (at 1000 nm) between thin films of pristine BTO and the equilibrium structure of $BaTiO_{2.8}F_{0.1}N_{0.1}$ at each value of epitaxial strain.

could be investigated. Actually, the configurations that we have considered so far (in the last two sections) correspond to an ordered cubic array of linear chains of F−Ti−N that is infinitely repeated in space. It is more likely that in a real material (even at 0 K), the configuration might differ from this idealized picture.

In this section, we extend the size of the system allowing the investigation of more possible configurations, and try to draw a conclusion about the global energy minimum configuration. We shall also investigate how the optical properties might be affected.

The study is restricted, however, to the state of 0% strain[4], and all the configurations in this section are compared against $C^{(\perp)}$ depicted in Fig. 6.5a.

First, we consider seven distinct configurations (configurations a – f, depicted in Fig. 6.12) achieved by extending the system size along the y direction (perpendicular to the alignment of the F−Ti−N chain), making the supercell tetragonal of size $2 \times 4 \times 2$. None of these configurations can be realised using a $2 \times 2 \times 2$ supercell.

[4]The reader is reminded that the term 0% strain here means that the in-plane lattice parameters are fixed at those of pristine BTO, while the out-of-plane lattice parameter is fully relaxed under the constraint that it is orthogonal to the [110] plane. All the ionic degrees of freedom are fully relaxed.

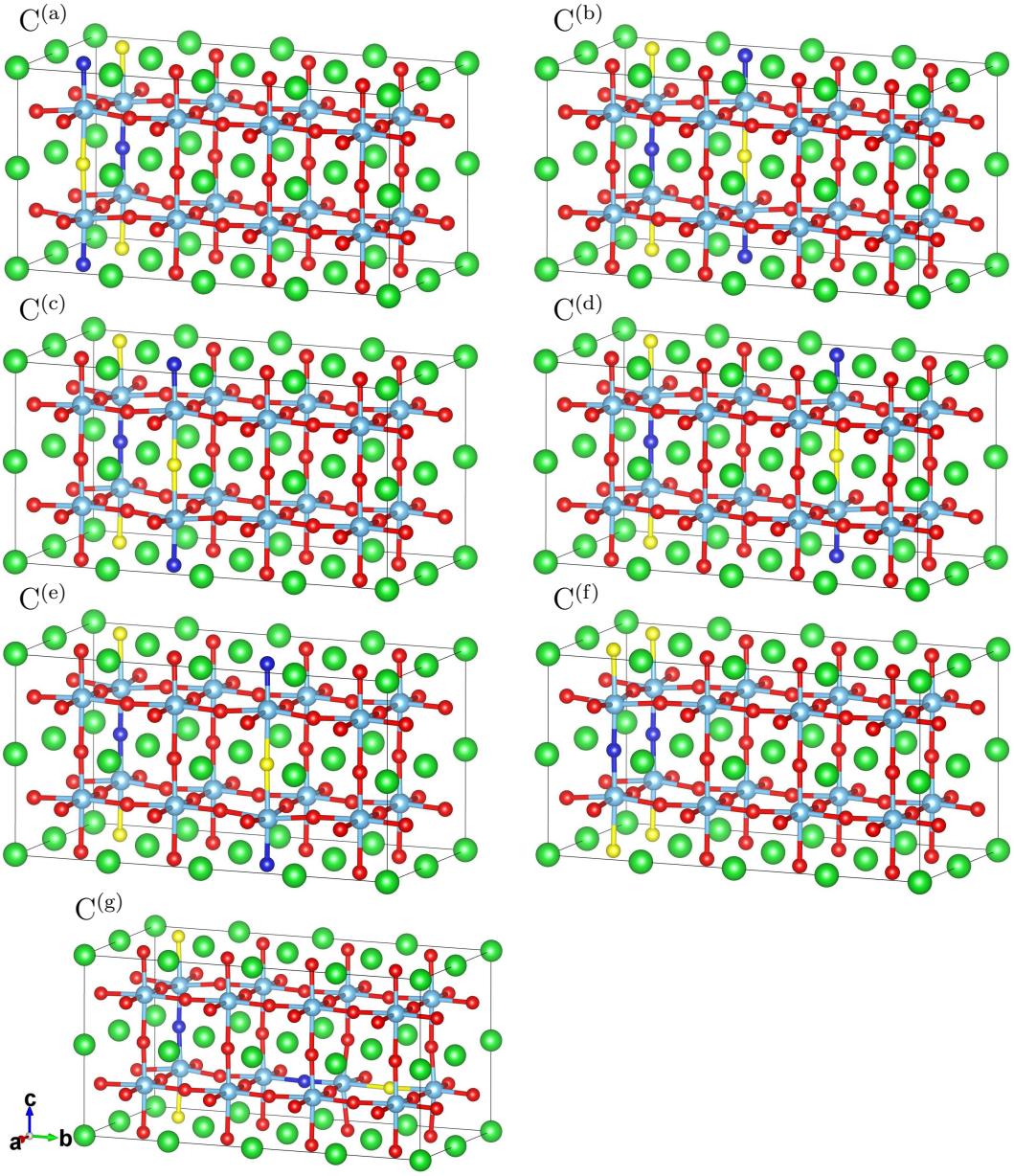


Figure 6.12: Seven symmetry-inequivalent atomic configurations of $BaTiO_{2.8}F_{0.1}N_{0.1}$ that are achieved by considering a $2 \times 4 \times 2$ supercell.

Configuration	ΔE (eV)
$C^{(a)}$	-0.028
$C^{(b)}$	-0.016
$C^{(c)}$	-0.013
$C^{(d)}$	-0.003
$C^{(e)}$	-0.003
$C^{(f)}$	-0.001
$C^{(g)}$	0.047

Table 6.5: The energy difference of $BaTiO_{2.8}F_{0.1}N_{0.1}$ between the configurations shown in Fig. 6.12 and $C^{(\perp)}$ shown in Fig. 6.5a at 0% strain. All configurations are more energetically favourable, apart from $C^{(g)}$. Energies are given per $2 \times 2 \times 2$ supercell.

Obviously, the number of symmetry-inequivalent configurations that exist in a $2 \times 4 \times 2$ supercell is far more than we have considered. However, we have excluded many configurations that are not expected to be energetically favourable, restricting our investigations to configurations that involve the F and N atoms forming a linear motif, leading to the presence of two linear F−Ti−N chains in the supercell. The seven configurations that we have selected differ only in the position and the alignment of the second chain, which has been introduced by the extension of the supercell, relative to the first.

In configurations a – e, we investigate the effect of the "inversion" of the second chain, where the F and the N atoms are put in opposite sites with respect to the first chain. The position of the second chain is then varied between the five symmetry-inequivalent possible positions in the supercell.

Table. 6.5 indicates that all these five configurations are more energetically favourable than $C^{(\perp)}$ represented by a $2 \times 2 \times 2$ supercell. Indeed, the fact that F and N atoms prefer to have opposite sites in the two chains can be explained within the same context that they favour a linear motif clustering. As pointed out in Ref. [230], N and F atoms have one fewer and one extra valence electron, respectively, compared to the O atom, so they behave in $BaTiO_{2.8}F_{0.1}N_{0.1}$ like an electron donor and acceptor, preferring to cluster together to lower the energy.

This also explains why the energies of the configurations $C^{(a)}$ to $C^{(e)}$ are monotonically increasing with the nearest neighbour distance between the two chains, which increases in ascending order from configuration (a) to configuration (e)[5], indicating that clustering of the chains is mostly favoured, lowering the energy by ~ 28 meV per $2 \times 2 \times 2$ supercell.

$C^{(f)}$ differs from $C^{(a)}$ in that the second chain has the same orientation of sites for F and N. As expected, this is less favourable than the opposite sites case, but it still lowers the energy with respect to $C^{(\perp)}$, though the energy difference is tiny (~ 1 meV).

Finally, we consider the case in which the second chain is not parallel to the first ($C^{(g)}$). Our calculations show that this case is quite unfavourable and raises the energy by about 47 meV (about two times k_BT at room temperature). This suggests that the chains favour being parallel to each other, as pointed out briefly in Sec. 6.4.2.

In order to build a more comprehensive idea about the "global" minimum energy configuration, we investigate another set of configurations constructed by extending the $2 \times 2 \times 2$ supercell along the z direction, i.e., along the F−Ti−N chain, forming a $2 \times 2 \times 4$ supercell. These are depicted in Fig. 6.13.

Similarly to the case of the $2 \times 4 \times 2$ supercell, these configurations differ in the location and the alignment of the second chain of F−Ti−N atoms. Thinking of this supercell as two $2 \times 2 \times 2$ sub-cells placed on top of each other, $C^{(\alpha)}$ corresponds to the case where the second chain is placed in the same sub-cell of the first chain, parallel and as close as possible to it. In contrast, the other four configurations (configurations β – ξ) correspond to the second chain being placed in the top sub-cell. The second chain is inverted only in configurations α, β and ξ.

Table 6.6 indicates that the first four configurations show a similar trend in the energy with respect to the position and the alignment of the second chain, suggesting that the chains favour being in opposite alignment and as close to each other as possible[6]. However, this trend is not followed by $C^{(\xi)}$, the energy of which is higher by ~ 0.35 eV than that of $C^{(\delta)}$, suggesting that it is highly unfavourable, despite the fact that the second chain is closer and inverted.

[5] $C^{(a)}$ and $C^{(b)}$ have the same nearest neighbour distance. However, the "coordination number" of $C^{(a)}$ is 2, which is twice as that of $C^{(b)}$.

[6] In this sense, the distance is measured between the two centering Ti atoms of the two chains.

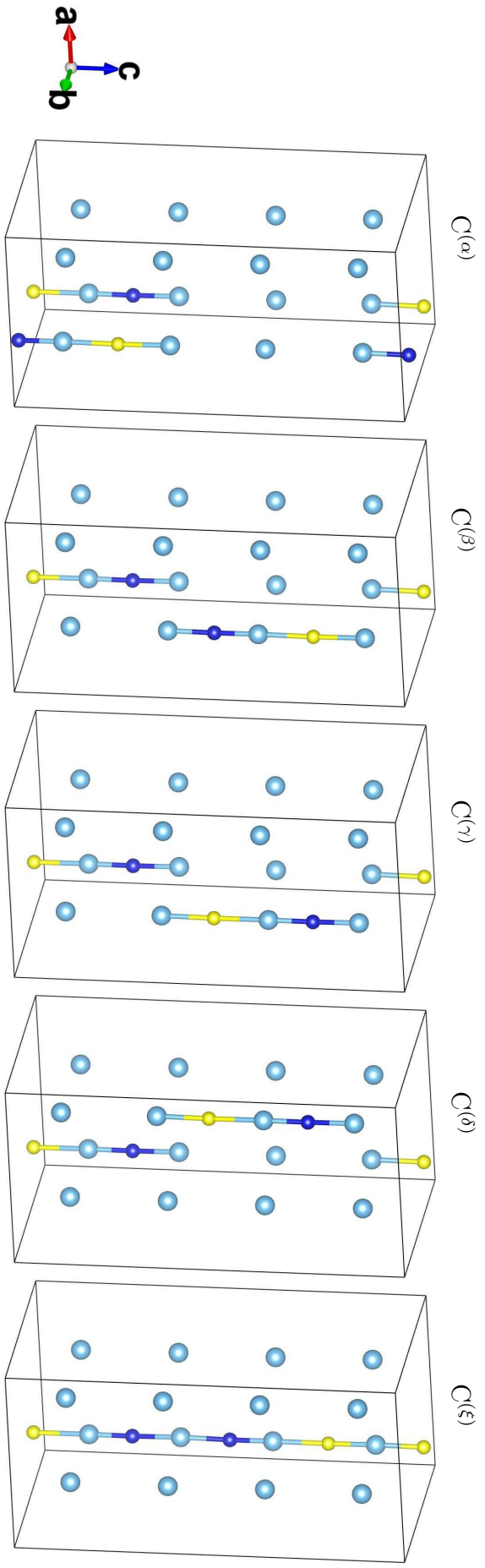


Figure 6.13: Five symmetry-inequivalent atomic configurations of $BaTiO_{2.8}F_{0.1}N_{0.1}$ constructed by considering a $2 \times 2 \times 4$ supercell. The Ba and the O atoms are not shown for clarity.

Configuration	ΔE (eV)
$C^{(\alpha)}$	0.014
$C^{(\beta)}$	0.039
$C^{(\gamma)}$	0.044
$C^{(\delta)}$	0.068
$C^{(\xi)}$	0.422

Table 6.6: The energy difference of $BaTiO_{2.8}F_{0.1}N_{0.1}$ between the configurations shown in Fig. 6.13 and $C^{(\perp)}$ shown in Fig. 6.5a at 0% strain. All configurations are less energetically favourable than $C^{(\perp)}$. Energies are given per $2 \times 2 \times 2$ supercell.

This can be attributed to the formation of new N−Ti−N and F−Ti−F linear bonds in $C^{(\xi)}$ that are energetically unfavourable.

On the other hand, Table 6.6 shows that all of these configurations are energetically less favourable than $C^{(\perp)}$. This can be explained by noticing that configurations α – δ involve breaking a F−Ti−N motif and replacing it with N−Ti−O and O−Ti−F chains.

The above investigations of the configurations of the $2 \times 4 \times 2$ and $2 \times 2 \times 4$ supercells result in the conclusion that it is likely in a real single crystal material at 0 K that the dopant atoms of F and N in BTO favour the formation of long linear chains of F−Ti−N−Ti−$\cdots$, and that these chains prefer to cluster with each other, with adjacent chains adopting opposite sites for F and N.

This picture might differ, however, at higher temperatures, where it is important to consider the configurational entropy to draw conclusions about the most stable configuration. In addition, at sufficiently high temperatures it may be possible that the system hops between one configuration and another, crossing the energy barrier between the two. These ideas, however, are beyond the scope of this work and are kept for future investigations.

6.5.1 Electronic and optical properties

Tables 6.5 and 6.6 show that the energy differences between the configurations of the $2 \times 4 \times 2$ and $2 \times 2 \times 4$ supercells are generally quite small. It is worth questioning, however, whether refractive index discrepancies are also small.

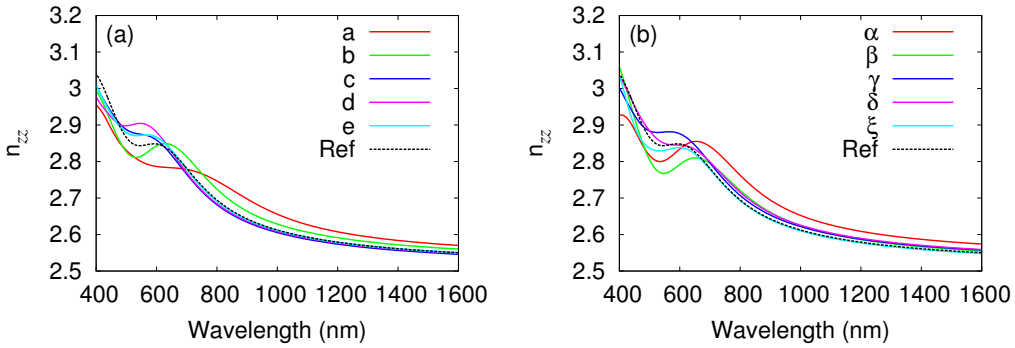


Figure 6.14: The zz component of the refractive indices of configurations a – e **(a)** and configurations α – ξ **(b)** referred to in the main text. $C^{(\perp)}$ of the $2 \times 2 \times 2$ supercell is represented by the dashed black line in the two panels for reference.

So, we calculate the refractive indices of configurations a – e (Fig. 6.14a) and configurations α – ξ (Fig. 6.14b), and compare them to the refractive index of $C^{(\perp)}$ of the $2 \times 2 \times 2$ supercell.

In view of the discussion in Sec. 6.4.2, one would not expect the refractive indices to show a lot of difference between these configurations. In fact, our calculations indicate that the xx and yy components of the refractive index are almost identical for all configurations (figures not shown). However, Fig. 6.14 indicates that the zz component shows some discrepancy compared to the reference configuration. This discrepancy is mostly pronounced around the characteristic peak that is discussed in Sec. 6.4.2 (indicated by the black arrow in Fig. 6.9). This can be linked to the nature of the optical transitions near the Fermi level and to the changes in the band gaps of these different configurations, where closing the band gap generally results in a red-shift in the peak. The corresponding values of E_g are tabulated in Table 6.7.

In particular, n_{zz} of the minimum energy configuration ($C^{(a)}$) shows a clear deviation from $n^{\perp}_{zz}$ (dashed black line in Fig. 6.14) throughout the whole spectrum, which is not very surprising as the corresponding bandgap shows a considerable decrease with respect to $E^{\perp}_g$. The deviation reaches a maximum increase of $\sim 2\%$ with respect to $n^{\perp}_{zz}$ at ~ 850 nm. Compared with pure BTO, it shows an increase of $\sim 4\%$ at 1000 nm, which is noticeably more than the $\sim 2.4\%$ that $n^{\perp}_{zz}$ shows (discussed earlier in Sec. 6.4.2). These results highlight the fact that relatively large changes in refractive index can be achieved

Configuration	E_g	ΔE_g	Configuration	E_g	ΔE_g
$C^{(a)}$	1.50	−0.89	$C^{(\alpha)}$	1.69	−0.70
$C^{(b)}$	1.76	−0.63	$C^{(\beta)}$	1.62	−0.77
$C^{(c)}$	1.79	−0.60	$C^{(\gamma)}$	1.81	−0.58
$C^{(d)}$	1.80	−0.59	$C^{(\delta)}$	1.80	−0.59
$C^{(e)}$	1.82	−0.57	$C^{(\xi)}$	1.63	−0.76
$C^{(\perp)}$	1.79	−0.6			
BTO	2.39	0.00			

Table 6.7: The direct energy gaps (at Γ) of the different configurations of $BaTiO_{2.8}F_{0.1}N_{0.1}$ at 0% strain depicted in Figs. 6.12 and 6.13. The corresponding bandgaps of $C^{(\perp)}$ and cubic BTO at 0% strain are given in the last two rows for comparison. ΔE_g is the difference in the bandgap with respect to BTO. All energies are given in units of eV.

upon doping, and that these changes are sensitive to the detailed atomic arrangement of the dopants. The consideration of further stable configurations in larger supercells might show further enhancements, but is beyond the scope of this study.

6.5.2 Refractive index averaging

Tables 6.5 and 6.6 show that the energy differences between some of the configurations studied above are quite small. Thus, one can argue that it might be possible for two or more different configurations to simultaneously exist when the material is synthesized. If this is the case, the effective refractive index of the material could be roughly predicted as the average of the refractive indices of the individual configurations. This idea of averaging over different configurations is quite common in predicting the properties of disordered systems (e.g., see Ref. [233]).

The aim of the calculations in this section is two fold. First, to study the idea of refractive index averaging, and second, to investigate the possibility of simplifying calculations of the refractive index of large systems.

As illustrated in Fig. 6.15, one can think of the $2 \times 4 \times 2$ supercell of $C^{(a)}$ as being composed of two $2 \times 2 \times 2$ adjacent sub-cells, one corresponding to

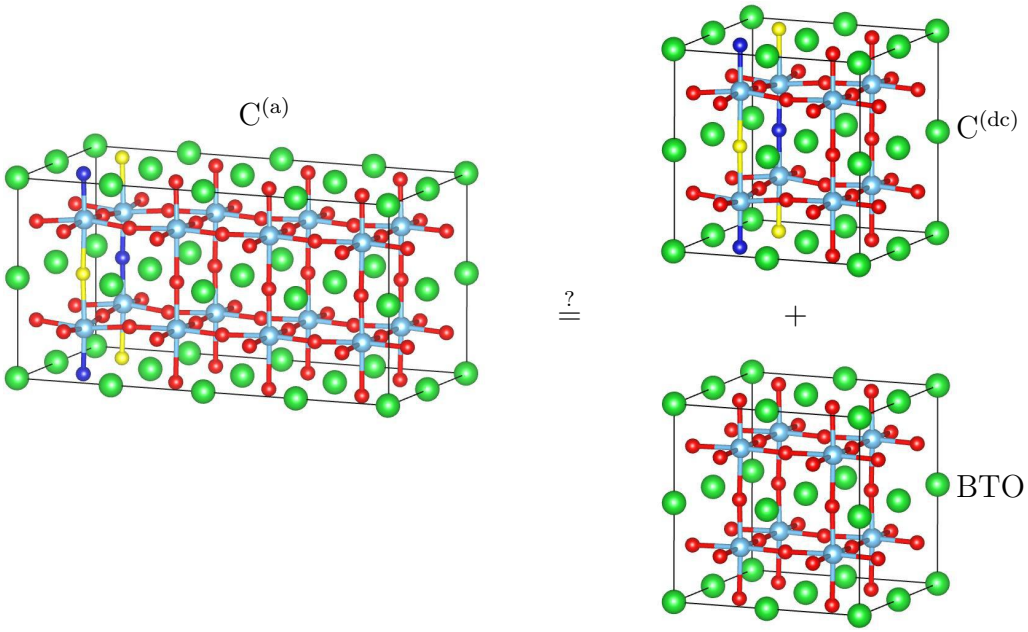


Figure 6.15: An illustrative figure addressing the possibility of reproducing the refractive index of the system on the left by averaging the refractive indices of the "sub-systems" on the right.

pure BTO, and the other corresponding to a doubly concentrated doping of F and N in BTO (which we will refer to by the superscript (dc)).

Each sub-cell is then treated individually and its corresponding refractive index is calculated. The refractive indices of the three systems depicted in Fig. 6.15 are shown in Fig. 6.16. In addition, we show also in the same figure the average of n^{BTO} and n^{dc}, which we denote $\bar{n}$. As for the xx and the yy components, the refractive indices of all systems are already very close to each other, so, it is trivial to have a good agreement between $\bar{n}$ and the refractive index of $C^{(a)}$ (which we denote n^{ca}). However, despite the large discrepancy between the zz components of the indices, one can notice, surprisingly perhaps, that the average refractive index of the two sub-cells reproduces, to a reasonable extent[7], the refractive index of the "parent" supercell of $C^{(a)}$.

This result suggests that it might be possible to predict, to a good approximation, the "effective" refractive index of a doped BTO system consisting of distinct co-existing configurations by averaging the refractive indices of each

[7]Quantitatively, the root mean square of the differences between n^{ca} and $\bar{n}$, within the considered range of wavelengths, is less than 0.02.

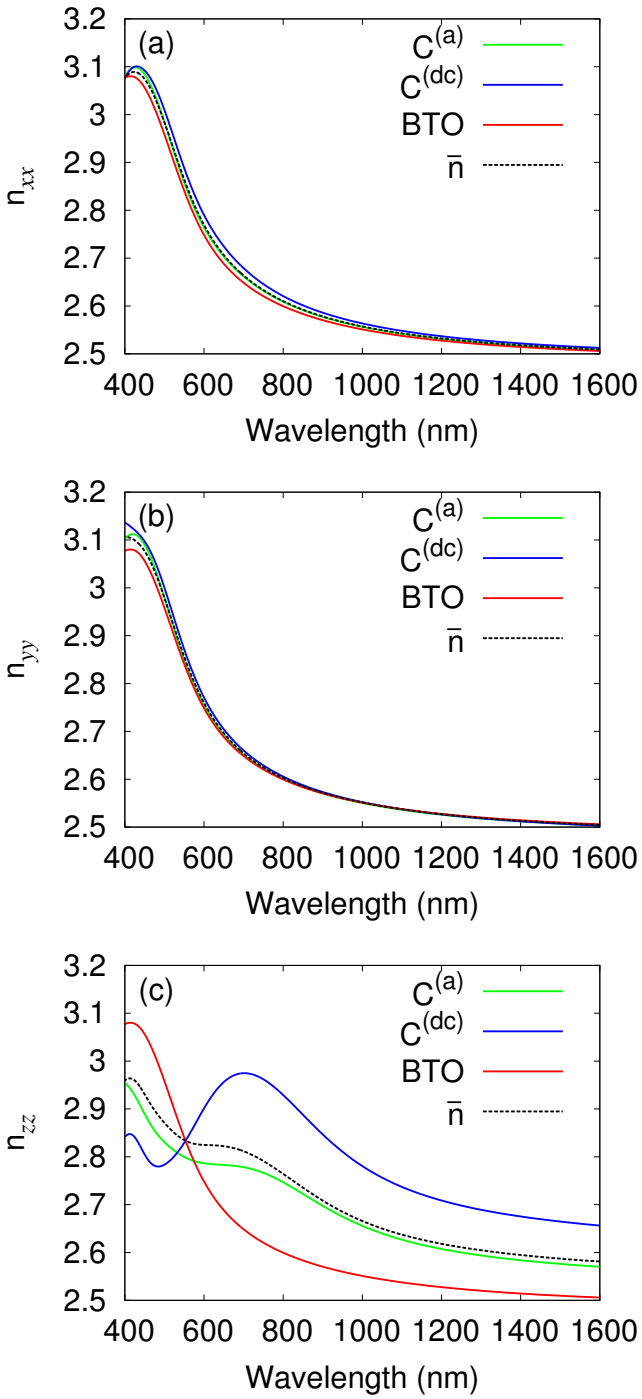


Figure 6.16: The three components of the refractive indices of the systems shown in Fig. 6.15. The averaged refractive index of $C^{(dc)}$ and pristine BTO, which we denote as $\bar{n}$, is represented by the dashed line.

individual configuration. Furthermore, this can help in saving a lot of computational time, as calculating the optical properties of the individual subsystems is much computationally cheaper than doing the same calculations for the bigger parent system.

We shall show in the next section how this idea might be utilized to predict the refractive index of more dilute concentrations of the dopant atoms.

6.6 Properties of bulk $BaTiO_{2.92}F_{0.04}N_{0.04}$

We have considered so far the structural, electronic and optical properties of bulk and thin-film $BaTiO_{2.8}F_{0.1}N_{0.1}$. Our investigations of BST solid solutions in Chapter 5 indicate that the concentration of the dopant atoms can play a major role in tuning the refractive index of the material. Thus, we shall consider in this chapter the effect on the optical properties of the concentration of F and N in BTO.

As pointed out earlier, the virtual crystal approximation is not expected to work well in reproducing the properties of anion doped BTO, as the atomic configuration has a considerable effect on the optical properties (see Fig. 6.2). This limits the range of concentrations that we consider, since the simulation of dilute concentrations is computationally expensive. On the other hand, we do not consider higher concentrations of the dopant atoms as we are not aware whether this is experimentally achievable.

Thus, we shall restrict our study in this chapter to a single concentration of $BaTiO_{2.92}F_{0.04}N_{0.04}$ ($\sim$ 1.3% of each of F and N), to develop a general idea of how the concentration of dopants affects the optical properties. This concentration is approximately[8] achieved by substituting two O atoms by F and N in a 135-atom $3 \times 3 \times 3$ supercell of BTO.

The bulk, fully relaxed[9] system is considered throughout this section. In a $3 \times 3 \times 3$ rhombohedral supercell of BTO, there exist a total of $81 \times 80 = 6480$

[8]Once again, a $3 \times 3 \times 3$ supercell of BTO with two O atoms substituted by F and N gives slightly lower concentrations of F and N than the formula $BaTiO_{2.92}F_{0.04}N_{0.04}$ describes (it actually gives a concentration of $1/81 \approx 1.2\%$), but we shall refer to it as such for the sake of simplicity.

[9]The force tolerance is made less strict for the calculations in this section; the force on each atom is guaranteed to be less than 7.5 meV/Å, which still about an order of magnitude better than the tolerance used in Ref. [230]. Total energies (per atom) are converged to a tolerance of ~ 0.1 μeV.

Concentration	ΔV (%)	Δa (%)	Δc (%)
$BaTiO_{2.8}F_{0.1}N_{0.1}$	0.62	−0.64	1.92
$BaTiO_{2.92}F_{0.04}N_{0.04}$	0.18	−0.26	0.73

Table 6.8: The changes in the volume and the lattice constants of pure BTO (in percent) due to doping of F and N at two different concentrations.

possible ways to occupy two vacant O sites with F and N atoms. However, only 11 among them are symmetry inequivalent. Our calculations show that in this dilute concentration, the N and F atoms prefer to cluster to each other forming a linear motif of F−Ti−N, as in the case of $BaTiO_{2.8}F_{0.1}N_{0.1}$. The second energetically favourable configuration is higher in energy by ~ 0.28 eV per $3 \times 3 \times 3$ supercell (or equivalently, ~ 0.08 eV per 40-atom supercell). This indicates that the energies of the different configurations are much closer to each other than are those of $BaTiO_{2.8}F_{0.1}N_{0.1}$ (Table 6.2). All the investigations below, however, are restricted to the lowest energy configuration.

Smaller changes in the structure of pure BTO due to doping are observed when the doping concentration is lowered, as might be expected. The changes in the volume and the lattice parameters are alluded to in Table 6.8.

We compare in Fig. 6.17 the refractive indices of bulk $BaTiO_{2.92}F_{0.04}N_{0.04}$, $BaTiO_{2.8}F_{0.1}N_{0.1}$ ($C^{(1)}$), and pure BTO. Similar to the structural parameters, the refractive index of BTO is also less affected when the doping is diluted. This could be a direct consequence of the smaller change in the direct band gap with respect to BTO. The direct gap of $BaTiO_{2.92}F_{0.04}N_{0.04}$ is 1.89 eV, which is lower by ~ 0.5 eV than the gap of BTO, whereas the gap of $BaTiO_{2.8}F_{0.1}N_{0.1}$ is lower by ~ 0.7 eV (see Table 6.3).

It can also be seen that the anomalous peak in the zz component of the refractive index present at ~ 600 nm in the more highly concentrated system has almost disappeared in the less highly concentrated system. Actually, the zz component of the imaginary part of the dielectric function of $BaTiO_{2.92}F_{0.04}N_{0.04}$ no longer shows a feature around the corresponding wavelength. This suggests that the change in the colour of BTO does not occur at low doping concentration, but rather when a critical concentration of the dopant atoms is reached.

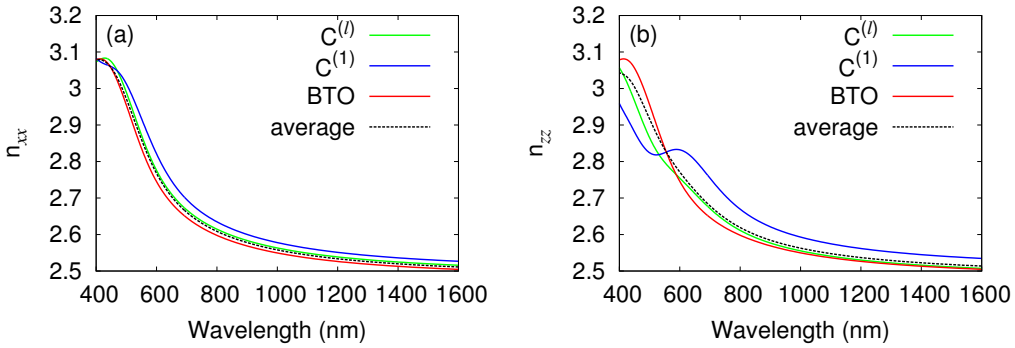


Figure 6.17: Effect of the concentration of F and N on the xx **(a)** and zz **(b)** components of the refractive index. $C^{(l)}$ refers to the system of low dopant concentrations of $BaTiO_{2.92}F_{0.04}N_{0.04}$. The weighted average of refractive index of $C^{(1)}$ and BTO is represented by the dashed line.

We conclude this section by revisiting the idea of the average refractive index discussed in the previous section. The supercell of $BaTiO_{2.92}F_{0.04}N_{0.04}$ can be thought of as consisting of a $2\times2\times2$ sub-cell of $BaTiO_{2.8}F_{0.1}N_{0.1}$ ($C^{(1)}$), plus 19 5-atom unit cells of pure BTO. Our conjecture is that the refractive index of $BaTiO_{2.92}F_{0.04}N_{0.04}$ can be reproduced by averaging[10] the refractive indices of $BaTiO_{2.8}F_{0.1}N_{0.1}$ and pure BTO.

Fig. 6.17 shows that the weighted average of pristine BTO and $BaTiO_{2.8}F_{0.1}N_{0.1}$ gives a very good approximation to the index of $BaTiO_{2.92}F_{0.04}N_{0.04}$. This, on the one hand, supports the idea of averaging the refractive index, and, on the other hand, suggests a general behaviour of the refractive index of doped BTO, that it varies almost linearly with the concentration of the dopant atoms, following a Vegard-like law. However, a firm conclusion about this cannot be drawn yet, and calculations of some intermediate concentrations would be required to support the suggested behaviour. This is left, however, for future work.

6.7 Summary

In this chapter we have investigated the effect of co-substitution of F and N in BTO on the structural, electronic and optical properties. Bulk $BaTiO_{2.8}F_{0.1}N_{0.1}$

[10]The average is weighted by the corresponding size of each sub-system. Namely, $BaTiO_{2.8}F_{0.1}N_{0.1}$ and pure BTO are given weights of 8/27 and 19/27, respectively.

was considered first, with different symmetry-inequivalent atomic configurations of the dopant atoms. It was shown that F and N doping breaks the rhombohedral symmetry of BTO and slightly increases the volume of the system. The energetics of different configurations showed that F and N atoms favour the formation of a linear motif of F−Ti−N, and that the other possible configurations are higher in energy by at least ~ 0.5 eV per $2 \times 2 \times 2$ supercell. The energy differences between the different configurations were attributed mainly to the atomic ordering itself, rather than to the structural changes induced by each individual configuration.

In contrast with the BST system, the refractive index of bulk $BaTiO_{2.8}F_{0.1}N_{0.1}$ shows a significant dependence on the atomic configuration of the dopant atoms, suggesting that the virtual crystal approximation is not reliable to study this particular disorder. It was shown that the discrepancies in the refractive index between different atomic configurations can be attributed to the relative alignment of the Ti−F and the Ti−N bonds in the system, rather than the relative sites of these bonds in the supercell.

As compared to pristine bulk BTO, the co-substitution of F and N has the general effect of increasing its refractive index. This is attributed to the closing of the band gap of the material due to the presence of the N $2p$ levels on top of the O $2p$ valence states in the doped material.

Next, we considered $BaTiO_{2.8}F_{0.1}N_{0.1}$ in thin film form by investigating the effect of biaxial strain on the material. We restricted the investigations to the minimum energy configuration which has a linear F−Ti−N motif in the supercell. We showed that for compressive strains the motif favours alignment along the out-of-plane direction, whereas in-plane alignment is favoured for tensile strains, with the transition between the two occurring approximately at 0.5% strain. This is linked to the tetragonality of the system that is induced and controlled by strain; we showed that the motif prefers to be aligned along the longest available lattice direction.

We have shown that the refractive index of thin film $BaTiO_{2.8}F_{0.1}N_{0.1}$ exhibits a considerable anisotropy. Namely, the component along the Ti−N bond has a pronouncedly higher value than the other components. This is attributed to the covalent character of this bond that gives it greater polarizability compared to Ti−O and Ti−F bonds, leading to the increase in the dielectric function and the refractive index. Compared to pure BTO, we showed that thin

film $BaTiO_{2.8}F_{0.1}N_{0.1}$ displays an increase in the refractive index of $\sim 2.40\%$ at 0% strain, which can be increased further to $\sim 4\%$ by means of strain. This is larger than the effect of Sr alloying in thin film BST, hence suggesting another promising means of tuning the refractive index of BTO.

Furthermore, we investigated more dopant configurations that are only accessible by increasing the supercell size. Restricting the study to the unstrained state, we considered 12 configurations obtained by considering supercells of sizes $2 \times 4 \times 2$ and $2 \times 2 \times 4$. The results indicated that it is highly likely that the most energetically favourable configuration involves the presence of long linear chains of F−Ti−N−Ti−$\cdots$ parallel to each other and clustering together with opposite sites of F and N in the neighbouring chains. As for the optical properties, the minimum energy configuration, among the ones we investigated, showed the greatest difference compared to BTO, suggesting that the real material indeed has a substantially modified refractive index compared to pure BTO.

We then studied the idea of refractive index averaging, where we showed that the refractive index of a large "parent" supercell may be obtained, to a reasonable approximation, by averaging over the refractive indices of the "constituent" sub-systems. This suggested, on the one hand, a less computationally expensive means to calculate the optical properties of large systems, and on the other hand, a reasonable approximation to the refractive index of a disordered material that involves coexistence of different atomic configurations.

Finally, we investigated the effect of the dopant concentration by considering bulk $BaTiO_{2.92}F_{0.04}N_{0.04}$. As in the higher concentration case, we showed that the N and the F atoms like to cluster with each other to form a linear motif of F−Ti−N. As might be expected, we found that the structural, electronic and optical properties are less different to those of pure BTO when the concentration is lowered. The results also indicated that BTO may only undergo a colour change when the doping concentration reaches a critical value.

We found that the idea of the refractive index averaging can be used to predict the refractive index of bulk $BaTiO_{2.92}F_{0.04}N_{0.04}$, to a very good approximation. This might suggest a linear behaviour of the refractive index of $BaTiO_{3-2x}F_xN_x$ with the concentration of F and N atoms, allowing the prediction of the refractive index at more dilute concentrations.

Chapter 7

Conclusions

In the present work, we have comprehensively investigated, from first principles, the effects of structural perturbations such as epitaxial strain, alloying, ferroelectric distortions, anionic substitutions and atomic ordering, on the electronic and optical properties of BTO, STO and BST solid solutions.

We began this thesis with a description of the experimental technique, spectroscopic ellipsometry (SE), which is the most widely used method in characterizing the optical properties of thin solid films. We focused in our description on the limitations of this technique. We showed that obtaining an excellent fit to the measured data does not necessarily imply a reliability in the predicted structural and optical models of the film and, therefore, in the calculated optical spectra. We explicitly calculated the refractive index of a $Ba_{0.5}Sr_{0.5}TiO_3$ film deposited on an MgO substrate by fitting the raw SE measurements, adopting different models for the film structure. We showed that, although an excellent fit is obtained for all the considered models, considerable discrepancies in the calculated refractive indices are observed, with non-physical behaviour of the refractive index of the film in some cases. These limitations in the SE method motivate the calculations of the optical properties of BST films from first principles.

Since the simulation of *real* thin films is computationally intractable, due to the need for a very large simulation cell, thin films under epitaxial mismatch strain due to growth on a substrate were mimicked by considering the *bulk* material subject to an in-plane biaxial strain that corresponds to the strain induced by the substrate. Furthermore, the alloying of Ba and Sr in BST has been simulated using the virtual crystal approximation, the accuracy of which

was tested against the supercell approach. A very good reproduction of the lattice constants, energy gaps and optical properties has been obtained.

We started by investigating strain-induced changes in the energy gaps of BTO and STO, since these changes are believed to have a strong impact on the optical properties. The DFT-LDA gaps were adopted in this thesis. In spite of the fact that DFT underestimates the true quasiparticle bandgap of insulators and semiconductors, we expect the *trends* of the gaps with respect to strain and other structural perturbations to be robust. We showed that the direct and the indirect gaps of both BTO and STO exhibit interesting features as a function of epitaxial strain; moderate strains were shown to decrease the gaps of these systems, whereas high strains were shown to increase the gaps. Quantitatively, high strains of $\pm 4\%$ induced an increase in the gaps of BTO and STO by up to ~ 0.8 and ~ 0.6 eV, respectively. We explained these features in terms of strain-induced changes in the magnitude and the direction of the spontaneous polarization of the material. For high strains, the increase in the gaps of both BTO and STO was attributed to the increase in the ferroelectric polarization that is induced by strain. On the other hand, the decrease in the gap of BTO at lower strain magnitudes is correlated with a homogeneous rotation of the polarization vector from the [001] to the [110] direction as strain is varied from the compressive to the tensile regimes, while in the case of STO, the decrease is linked to a complete inhibition of ferroelectricity within the corresponding range of strain.

We also introduced a vector generalisation of the space condition previously applied to polarization in BTO and STO. The vectorial space condition states that the component of the polarization along [100], [010] or [001] in BTO, STO and their solid solutions is zero unless the lattice parameter along the same axis is larger than a system-dependent critical value.

In STO, we found that in the absence of the ferroelectric distortions, the gap decreases at higher rate as a function of tensile strain than compressive strain. We successfully accounted for this behaviour by disentangling the effects of the strain-induced changes in the volume and the tetragonality of the system, where we found that both effects cooperate in decreasing the gap for tensile strains, while they oppose each other for compressive strains. This analysis is also expected to hold for BST at an arbitrary Sr content.

The effect of Sr content in BST was also investigated, where a critical

Sr content was observed, below which the gap increases with increasing Sr concentration, and above which the opposite trend is observed. This trend was correlated with the space condition discussed above.

We then investigated in Chapter 5 the effects of strain, alloying, and atomic configuration on the refractive indices of BTO, STO and BST. The refractive indices of BTO and STO were also shown to exhibit interesting features as a function of strain. It was found that these features correlate with the features that are observed in the optical gaps of these systems as a function of strain. We found that strain-induced enhancement of ferroelectricity of the system has a major effect in lowering the refractive index: strains up to $\pm 4\%$ can lower the refractive index of these materials by $\sim 8\%$, and can induce birefringence of up to ~ 0.14, which indicates that strain is a very promising means by which the refractive index of these materials may be tuned. On the other hand, a much smaller effect on the refractive index is observed when the ferroelectricity of the material is inhibited.

In comparison to strain, increasing the Sr content in BST from 0% to 100% was shown to lower the refractive index of BTO by the same amount as strains of $\sim 2\%$, while the configurational ordering of the Ba and Sr ions in BST was shown to be irrelevant for the refractive index of the material in the visible and the near infrared range.

Finally, we investigated in Chapter 6 another means by which the refractive index of BTO may be tuned; namely, the co-substitution of fluorine and nitrogen. Unlike the case of alloying with Sr, the refractive index of the anionic codoped BTO was found to show significant dependence on the ordering of the dopant atoms, leading to the inapplicability of the VCA approach. Detailed investigations of the energetics of different orderings using different supercell sizes have suggested that the F and N atoms cluster to form linear motifs of F$-$Ti$-$N chains. These chains in turn were found to align and cluster, with the F and N atoms occupying opposite sites in the neighbouring chains.

It was observed that the refractive index of codoped BTO exhibits a large increase in the component along the F$-$Ti$-$N chain, whereas the other two components show only a negligible difference compared to pure BTO.

We also investigated the effect of epitaxial strain on the refractive indices of codoped BTO. It was found that strain affects the refractive index primarily because it changes the thermodynamically stable orientation of the F-Ti-N

chains, which prefer to be aligned with the largest lattice parameter. For compressive strains the largest lattice parameter is out-of-plane, whereas for tensile strains it is in-plane. As a result, the out-of-plane component of the refractive index of codoped BTO shows an increase of between $\sim 2.4\%$ and $\sim 4.2\%$ with respect to pure BTO when the system is compressively strained from 0% up to -4%, while the other two components show only a negligible change. For tensile strains, however, the in-plane component that is along the F−Ti−N chain shows an almost constant increase of $\sim 4\%$ with respect to the corresponding component of pure BTO, while the other two components show only a small change.

Although strain and Sr alloying generally *lower* the refractive index of BTO (except at low Sr content up to $\sim 15\%$), doping with F and N generally *increases* one component of the refractive index of BTO, keeping the other two almost unchanged. On top of doping, epitaxial strain can also serve as an additional effect to further tune the refractive index of doped BTO.

We have also investigated the effect of the doping concentration. The effect of doping on the refractive index of BTO was found to increase with the dopant concentration.

We have also studied the idea of "refractive index averaging", where the refractive index of lightly doped BTO could be approximated, to a very good extent, by averaging the refractive indices of pure BTO and doped BTO at high concentrations. This idea suggests that the variations of the refractive index of doped BTO exhibit a linear trend with the concentration of the dopant atoms, thus allowing the estimation of the optical spectra for more dilute systems.

7.1 Future work

The present investigations of the optical properties of BST thin films have been performed by considering *bulk* materials, while the effect of the substrate is mimicked by introducing biaxial strain. Although this approximation allows one to investigate the effect of epitaxial strain on the electronic and optical properties, other factors that could have a major influence are neglected. These include surface effects, dislocations, grain boundaries, point defects and strain gradients.

The investigations of these effects makes it necessary to consider larger su-

percells, that could make the conventional density functional theory approach impractical. Alternative approaches might involve the use of linear scaling DFT methods [127], in which the computational time scales linearly with the system size (as compared with the cubic scaling of conventional DFT). Alternatively, atomistic simulations can be a promising approach, in which the electronic effects are described by a force field, usually fitted against first principles results to reproduce the forces, stresses and energies [234]. The virtue of these simulations is that one can consider extremely large systems (composed of tens of thousands of atoms), but losing the information about the electrons in the system could make the investigations of the optical properties tricky.

In our investigations throughout this thesis, we considered conventional DFT with the local density approximation for the calculations of the electronic and optical properties of BST. Due to the well-known band gap problem in the DFT approach, the absolute values of the calculated quantities (namely, the band gaps and the refractive indices) are subject to a systematic quantitative error. Although we expect that the *trends* of these quantities are reliable, the use of more accurate methods (such as GW calculations [191,192]) to calculate the bandgap and other excitation properties could be useful.

The investigations of strain effects have only considered one type of strain, i.e., biaxial strain applied to the (110) plane, which is consistent with the epitaxial strain that is experienced by films grown along the [001] direction on a mismatched substrate. Other growth directions can induce biaxial strain on different crystallographic planes, the effects of which, to our knowledge, are not known yet.

We have restricted our investigations to the high temperature phase of STO, neglecting the effects of the antiferrodistortive modes. A comprehensive study of these effects on the optical properties of BST films would be a key avenue of further work.

Finally, the promising results that have been obtained for the $BaTiO_{3-2x}F_xN_x$ system suggest investigations of the effects of other types of anionic and cationic dopants on tuning the electronic and optical properties of BTO.

Bibliography

[1] Stojanovic, B., Jovalekic, C., Vukotic, V., Simoes, A., and Varela, J. A. (2005) *Ferroelectrics* **319(1)**, 65–73.

[2] Dubourdieu, C., Bruley, J., Arruda, T. M., Posadas, A., Jordan-Sweet, J., Frank, M. M., Cartier, E., Frank, D. J., Kalinin, S. V., Demkov, A. A., et al. (2013) *Nature Nanotechnology* **8(10)**, 748–754.

[3] Dai, Z., Wang, Z. L., Duan, X., and Zhang, J. (1996) *Applied Physics Letters* **68(22)**, 3093–3095.

[4] Opium code website http://opium.sourceforge.net/.

[5] Valasek, J. (1921) *Phys. Rev.* **17(4)**, 475.

[6] ULUDOĞAN, M. and ÇAĞIN, T. (2006) *Turkish Journal of Physics* **30(4)**, 277–285.

[7] Rabe, K. M., Ahn, C. H., and Triscone, J.-M. (2007) Physics of ferroelectrics: a modern perspective, volume **105**, Springer, .

[8] Lines, M. and Glass, A. Principles and applications of ferroelectrics and related materials, 1977 (1977).

[9] Sawyer, C. B. and Tower, C. H. Feb 1930 *Phys. Rev.* **35**, 269–273.

[10] Resta, R. (1992) *Ferroelectrics* **136(1)**, 51–55.

[11] King-Smith, R. and Vanderbilt, D. (1993) *Physical Review B* **47(3)**, 1651.

[12] Dawson, L. H. Apr 1927 *Phys. Rev.* **29**, 532–541.

[13] Resta, R. (2003) *Modelling and Simulation in Materials Science and Engineering* **11(4)**, R69.

[14] Bin-Omran, S. (2008) Properties of ferroelectric ultrathin films from first principles, ProQuest.

[15] Samara, G. A. (2001) *Solid State Physics* **56**, 239–458.

[16] Deb, K. K., Hill, M. D., and Kelly, J. F. (1992) *J. Mater. Res.* **7**, 3296.

[17] Baettig, P., Schelle, C. F., LeSar, R., Waghmare, U. V., and Spaldin, N. A. (2005) *Chem. Mater.* **17**, 1376.

[18] Catalan, G., Noheda, B., McAneney, J., Sinnamon, L., and Gregg, J. (2005) *Phys. Rev. B* **72(2)**, 020102.

[19] Bednorz, J. G. and Müller, K. A. (1988) *Reviews of Modern Physics* **60**, 585.

[20] Fergus, J. W. (2007) *Sensors and Actuators B* **123**, 1169.

[21] Bain, A. K., Jackson, T. J., Koutsonas, Y., Cryan, M., Yu, S., Hill, M., Varrazza, R., Rorison, J., and Lancaster, M. J. (2007) *Ferroelectric Letters* **34**, 149.

[22] Dicken, M. J., Sweatlock, L. A., Pacifici, D., Lezec, H. J., Bhattacharya, K., and Atwater, H. A. (2008) *Nano Lett.* **8**, 4048.

[23] Petraru, A., Schubert, J., Schmid, M., and Buchal, C. (2002) *Appl. Phys. Lett.* **81**, 1375.

[24] Chen, H., Yang, C., Wang, B., Ji, H., and Zhang, J. (2009) *J. Appl. Phys.* **105**, 034112.

[25] Li, S. Z., Yang, Y. Q., Liu, L., Liu, W. C., and Wang, S. B. (2008) *Physica B* **403**, 2618.

[26] Im, J., Auciello, O., Baumann, P., Streiffer, S., Kaufman, D., Krauss, A., et al. (2000) *Appl. Phys. Lett.* **76(5)**, 625–627.

[27] Kingon, A., Streiffer, S., Basceri, C., and Summerfelt, S. (1996) *MRS Bulletin* **21(07)**, 46–52.

[28] Bussmann-Holder, A. (2012) *Journal of Physics: Condensed Matter* **24(27)**, 273202.

[29] Kwei, G., Lawson, A., Billinge, S., and Cheong, S. (1993) *The Journal of Physical Chemistry* **97(10)**, 2368–2377.

[30] Evarestov, R. A. and Bandura, A. V. (2012) *Journal of Computational Chemistry* **33**, 1123.

[31] Glaister, R. and Kay, H. (1960) *Proceedings of the Physical Society* **76(5)**, 763.

[32] Müller, K. and Burkard, H. (1979) *Phys. Rev. B* **19(7)**, 3593.

[33] Itoh, M., Wang, R., Inaguma, Y., Yamaguchi, T., Shan, Y.-J., and Nakamura, T. (1999) *Phys. Rev. Lett.* **82(17)**, 3540.

[34] Haeni, J., Irvin, P., Chang, W., Uecker, R., Reiche, P., Li, Y., Choudhury, S., Tian, W., Hawley, M., Craigo, B., et al. (2004) *Nature* **430(7001)**, 758–761.

[35] Bednorz, J. and Müller, K. (1984) *Phys. Rev. Lett.* **52(25)**, 2289.

[36] Fleury, P., Scott, J., and Worlock, J. (1968) *Phys. Rev. Lett.* **21(1)**, 16.

[37] Cohen, R. E. (1992) *Nature* **358(6382)**, 136–138.

[38] Cochran, W. (1961) *Advances in Physics* **10(40)**, 401–420.

[39] Bersuker, I. (1966) *Physics Letters* **20(6)**, 589–590.

[40] Cohen, R. E. (1993) *Ferroelectrics* **150(1)**, 1–12.

[41] Takesada, M., Itoh, M., and Yagi, T. (2006) *Phys. Rev. Lett.* **96(22)**, 227602.

[42] Shigenari, T. and Abe, K. (2008) *Ferroelectrics* **369(1)**, 117–126.

[43] Yashima, M. and Komatsu, T. (2009) *Chemical Communications* **(9)**, 1070–1072.

[44] Itoh, K., Zeng, L., Nakamura, E., and Mishima, N. (1985) *Ferroelectrics* **63(1)**, 29–37.

[45] Ravel, B., Stern, E., Vedrinskii, R., and Kraizman, V. (1998) *Ferroelectrics* **206(1)**, 407–430.

[46] Harada, J., Axe, J. D., and Shirane, G. Jul 1971 *Phys. Rev. B* **4**, 155–162.

[47] Zalar, B., Laguta, V. V., and Blinc, R. (2003) *Phys. Rev. Lett.* **90(3)**, 037601.

[48] Zhong, W., Vanderbilt, D., and Rabe, K. (1995) *Phys. Rev. B* **52(9)**, 6301.

[49] Hashimoto, T. and Moriwake, H. (2014) *Molecular Simulation* **(ahead-of-print)**, 1–7.

[50] Fallon, J. PhD thesis Imperial College London (2014).

[51] Cohen, R. and Krakauer, H. (1990) *Phys. Rev. B* **42(10)**, 6416.

[52] Kinase, W., Nakamura, K., and Harada, K. (2001) *Ferroelectrics* **259(1)**, 175–180.

[53] Miura, K., Azuma, M., and Funakubo, H. (2011) *Materials* **4(1)**, 260–273.

[54] Xiang, H., Wang, P., Whangbo, M.-H., and Gong, X. (2013) *Phys. Rev. B* **88(5)**, 054404.

[55] Ishikawa, K., Yoshikawa, K., and Okada, N. Apr 1988 *Phys. Rev. B* **37**, 5852–5855.

[56] Bean, C. and Livingston, J. (1959) *J. Appl. Phys.* **30(4)**, S120–S129.

[57] Slack, J. and Burfoot, J. (1971) *Journal of Physics C: Solid State Physics* **4(8)**, 898.

[58] Yashima, M., Hoshina, T., Ishimura, D., Kobayashi, S., Nakamura, W., Tsurumi, T., and Wada, S. (2005) *J. Appl. Phys.* **98(1)**, 014313.

[59] Nuraje, N., Su, K., Haboosheh, A., Samson, J., Manning, E. P., Yang, N.-l., and Matsui, H. (2006) *Advanced Materials* **18(6)**, 807–811.

[60] Ishikawa, K., Nomura, T., Okada, N., and Takada, K. (1996) *Jpn. J. Appl. Phys.* **35(9S)**, 5196.

[61] Zhong, W., Jiang, B., Zhang, P., Ma, J., Cheng, H., and Yang, Z. (1993) *Journal of Physics: Condensed Matter* **5(16)**, 2619.

[62] De Keijser, M., Dormans, G., Van Veldhoven, P., and De Leeuw, D. (1991) *Appl. Phys. Lett.* **59(27)**, 3556–3558.

[63] Fong, D. D., Stephenson, G. B., Streiffer, S. K., Eastman, J. A., Auciello, O., Fuoss, P. H., and Thompson, C. (2004) *Science* **304(5677)**, 1650–1653.

[64] Zhong, W., Wang, Y., Zhang, P., and Qu, B. (1994) *Phys. Rev. B* **50(2)**, 698.

[65] Stachiotti, M. (2004) *Appl. Phys. Lett.* **84(2)**, 251–253.

[66] Junquera, J. and Ghosez, P. (2003) *Nature* **422(6931)**, 506–509.

[67] Meyer, B. and Vanderbilt, D. (2001) *Phys. Rev. B* **63(20)**, 205426.

[68] Lee, H.-G. and Kim, H.-G. (1990) *J. Appl. Phys.* **67(4)**, 2024–2028.

[69] Sato, H. and Naito, M. (1997) *Physica C: Superconductivity* **274(3)**, 221–226.

[70] Gan, Q., Rao, R., Eom, C., Garrett, J., and Lee, M. (1998) *Appl. Phys. Lett.* **72(8)**, 978–980.

[71] Wang, J., Neaton, J., Zheng, H., Nagarajan, V., Ogale, S., Liu, B., Viehland, D., Vaithyanathan, V., Schlom, D., Waghmare, U., et al. (2003) *Science* **299(5613)**, 1719–1722.

[72] Choi, K. J., Biegalski, M., Li, Y., Sharan, A., Schubert, J., Uecker, R., Reiche, P., Chen, Y., Pan, X., Gopalan, V., et al. (2004) *Science* **306(5698)**, 1005–1009.

[73] Lei, D., Kéna-Cohen, S., Zou, B., Petrov, P., Sonnefraud, Y., Breeze, J., Maier, S., and Alford, N. (2012) *Optics Express* **20(4)**, 4419–4427.

[74] Nix, W. D. (1989) *Metallurgical Transactions A* **20(11)**, 2217–2245.

[75] Dieguez, O. and Vanderbilt, D. (2008) *Phase Transitions* **81(7-8)**, 607–622.

[76] Dawber, M., Rabe, K., and Scott, J. (2005) *Reviews of Modern Physics* **77(4)**, 1083.

[77] Tenne, D. A., Farrar, A. K., Brooks, C. M., Heeg, T., Schubert, J., Jang, H. W., Bark, C. W., Folkman, C. M., Eom, C. B., and Schlom, D. G. (2010) *Applied Physics Letters* **97(14)**, –.

[78] Dejneka, A., Tyunina, M., Narkilahti, J., Levoska, J., Chvostova, D., Jastrabik, L., and Trepakov, V. (2010) *Physics of the Solid State* **52(10)**, 2082–2089.

[79] Wang, G., Zhang, Y., Mao, C., Dong, X., and Chu, J. (2007) *Appl. Phys. Lett.* **91(6)**, 061104–061104.

[80] Xin, J., Hui, K., Wang, K., Chan, H., Ong, D., and Leung, C. (2012) *Applied Physics A* **107(1)**, 101–107.

[81] Wang, D.-Y., Chan, H. L. W., and Choy, C. L. (2006) *Applied optics* **45(9)**, 1972–1978.

[82] Hu, Z., Wang, G., Huang, Z., Meng, X., Shi, F., and Chu, J. (2003) *Jpn. J. Appl. Phys.* **42(3R)**, 1400.

[83] Hu, Z., Wang, G., Huang, Z., Meng, X., Zhao, Q., and Chu, J. (2004) *Applied Physics A* **78(5)**, 757–760.

[84] Tian, H., Luo, W., Pu, X., He, X., Qiu, P., Ding, A., Yang, S., and Mo, D. (2001) *Journal of Physics: Condensed Matter* **13(18)**, 4065.

[85] Sanna, S., Thierfelder, C., Wippermann, S., Sinha, T. P., and Schmidt, W. G. (2011) *Phys. Rev. B* **83**, 054112.

[86] Ahuja, R., Eriksson, O., and Johansson, B. (2001) *J. Appl. Phys.* **90**, 1854.

[87] Gupta, G., Nautiyal, T., and Auluck, S. (2004) *Phys. Rev. B* **69**, 052101.

[88] Samantaray, C., Sim, H., and Hwang, H. (2004) *Physica B* **351**, 158.

[89] Zhu, Z. Y., Zhang, H. Y., Tan, M., Zhang, X. H., and Han, J. C. (2008) *J. Phys. D: Appli. Phys.* **41**, 215408.

[90] Khenata, R., Sahnoun, M., Baltache, H., Rérat, M., Rashek, A. H., Illes, N., and Bouhafs, B. (2005) *Solid State Communications* **136**, 120.

[91] Jiang-Ni, Y., Zhi-Yong, Z., Jun-Feng, Y., and Zhou-Hu, D. (2010) *Chin. Phys. B* **19**, 017101.

[92] Xin-Yin, Z., Yue-Hua, W., Min, Z., Na, Z., Sai, G., and Qiong, C. (2011) *Chin. Phys. Lett.* **28**, 067101.

[93] Azzam, R. M. and Bashara, N. M. (1987) Ellipsometry and polarized light, North-Holland. sole distributors for the USA and Canada, Elsevier Science Publishing Co., Inc. .

[94] Fujiwara, H. (2007) Spectroscopic ellipsometry: principles and applications, John Wiley & Sons.

[95] Tompkins, H. and Irene, E. A. (2005) Handbook of ellipsometry, William Andrew.

[96] Drude, P. (1887) *Annalen der Physik* **268(12)**, 584–625.

[97] Drude, P. (1888) *Annalen der Physik* **270(7)**, 489–531.

[98] Vedam, K. (1998) *Thin Solid Films* **313314(0)**, 1 – 9.

[99] Jellison, G. E., Boatner, J. L. A., Lowndes, D. H., McKee, R. A., and Godbole, M. (1994) *Applied Optics* **33**, 6053.

[100] Yang, S.-H., Mo, D., Tian, H.-Y., Luo, W.-G., Pu, X.-H., and Ding, A.-L. (2002) *Physica Status Solidi (a)* **191(2)**, 605–612.

[101] Zelezny, V., Chvostová, D., Pajasová, L., Jelínek, M., Kocourek, T., Danis, S., and Valvoda, V. (2010) *Journal of Optoelectronics and Advanced Materials* **12(3)**, 538–541.

[102] Yin, Y., Ye, H., Zhang, C., Shen, W., and Liu, X. (2009) *J. Appl. Phys.* **106(7)**, 074103.

[103] Chvostova, D., Železnỳ, V., Pajasova, L., Šimek, D., Jelinek, M., and Matěj, Z. (2008) *Ferroelectrics* **370(1)**, 126–131.

[104] Griffiths, D. J. and College, R. (1999) Introduction to electrodynamics, volume **3**, Prentice hall Upper Saddle River, NJ.

[105] Born, M. and Wolf, E. (1999) Principles of optics: electromagnetic theory of propagation, interference and diffraction of light, Cambridge University Press.

[106] Sellmeier, W. (1871) *Annalen der Physik und Chemie* **219(6)**, 272–282.

[107] Suzuki, I., Ejima, M., Watanabe, K., Xiong, Y.-M., and Saitoh, T. (1998) *Thin Solid Films* **313**, 214–217.

[108] Hu, Z., Wang, G., Huang, Z., Meng, X., and Chu, J. (2003) *Semiconductor Science and Technology* **18(6)**, 449.

[109] Aspnes, D. E., Theeten, J. B., and Hottier, F. Oct 1979 *Phys. Rev. B* **20**, 3292–3302.

[110] Ppa, Z., Budai, J., Hanyecz, I., Csontos, J., and Toth, Z. (2014) *Thin Solid Films* **571, Part 3(0)**, 562 – 566 6th International Conference on Spectroscopic Ellipsometry (ICSE-VI).

[111] Jones, R. C. (1941) *J. Opt. Soc. Am* **31(7)**, 488–493.

[112] Lei, D. et al. Private Communication.

[113] Martin, R. M. (2004) Electronic structure: basic theory and practical methods, Cambridge University Press.

[114] Foulkes, W., Mitas, L., Needs, R., and Rajagopal, G. (2001) *Reviews of Modern Physics* **73(1)**, 33.

[115] Fock, V. (1930) *Zeitschrift für Physik* **61(1-2)**, 126–148.

[116] Hohenberg, P. and Kohn, W. Nov 1964 *Phys. Rev.* **136**, B864–B871.

[117] Kohn, W. and Sham, L. J. Nov 1965 *Phys. Rev.* **140**, A1133–A1138.

[118] Born, M. and Oppenheimer, R. (1927) *Annalen der Physik* **389(20)**, 457–484.

[119] Car, R. and Parrinello, M. (1985) *Phys. Rev. Lett.* **55(22)**, 2471.

[120] Kresse, G. and Hafner, J. (1993) *Phys. Rev. B* **47(1)**, 558.

[121] Pisana, S., Lazzeri, M., Casiraghi, C., Novoselov, K. S., Geim, A. K., Ferrari, A. C., and Mauri, F. (2007) *Nature Materials* **6(3)**, 198–201.

[122] Giannozzi, P., Baroni, S., et al. (2009) *Journal of Physics: Condensed Matter* **21(39)**, 395502 (19pp).

[123] Gonze, X. et al. (2009) *Computer Physics Communications* **180(12)**, 2582–2615.

[124] Gonze, X. (2005) *Zeitschrift für Kristallographie* **220(5/6/2005)**, 558–562.

[125] Gonze, X. et al. (2002) *Computational Materials Science* **25(3)**, 478–492.

[126] Clark, S. J., Segall, M. D., Pickard, C. J., Hasnip, P. J., Probert, M. J., Refson, K., and Payne, M. (2005) *Z. Kristall.* **220**, 567–570.

[127] Mostofi, A. A., Haynes, P. D., Skylaris, C.-K., and Payne, M. C. (2007) *Molecular Simulation* **33(7)**, 551–555.

[128] Kresse, G. and Furthmüller, J. Oct 1996 *Phys. Rev. B* **54**, 11169–11186.

[129] Ceperley, D. M. and Alder, B. J. Aug 1980 *Phys. Rev. Lett.* **45**, 566–569.

[130] Perdew, J. P. and Zunger, A. May 1981 *Phys. Rev. B* **23**, 5048–5079.

[131] Sutton, A. P. (1993) Electronic structure of materials, Oxford University Press.

[132] Jones, R. O. and Gunnarsson, O. (1989) *Reviews of Modern Physics* **61(3)**, 689.

[133] Filippi, C., Singh, D. J., and Umrigar, C. J. Nov 1994 *Phys. Rev. B* **50**, 14947–14951.

[134] Liou, B.-T. (2008) *Jpn. J. Appl. Phys.* **47(5R)**, 3350.

[135] Wang, C. S., Klein, B. M., and Krakauer, H. Apr 1985 *Phys. Rev. Lett.* **54**, 1852–1855.

[136] Terakura, K., Oguchi, T., Williams, A. R., and Kübler, J. Oct 1984 *Phys. Rev. B* **30**, 4734–4747.

[137] Becke, A. D. Sep 1988 *Phys. Rev. A* **38**, 3098–3100.

[138] Perdew, J. P. and Wang, Y. Jun 1992 *Phys. Rev. B* **45**, 13244–13249.

[139] Perdew, J. P., Burke, K., and Ernzerhof, M. Oct 1996 *Phys. Rev. Lett.* **77**, 3865–3868.

[140] Slater, J. C. Nov 1929 *Phys. Rev.* **34**, 1293–1322.

[141] Becke, A. D. (1993) *The Journal of Chemical Physics* **98(2)**, 1372–1377.

[142] Adamo, C. and Barone, V. (1999) *The Journal of Chemical Physics* **110(13)**, 6158–6170.

[143] Perdew, J. P., Ernzerhof, M., and Burke, K. (1996) *The Journal of Chemical Physics* **105(22)**, 9982–9985.

[144] Heyd, J., Scuseria, G. E., and Ernzerhof, M. (2003) *The Journal of Chemical Physics* **118(18)**, 8207–8215.

[145] Krukau, A. V., Vydrov, O. A., Izmaylov, A. F., and Scuseria, G. E. (2006) *The Journal of Chemical Physics* **125(22)**, 224106–224106.

[146] Deák, P., Aradi, B., Frauenheim, T., Janzén, E., and Gali, A. Apr 2010 *Phys. Rev. B* **81**, 153203.

[147] Ashcroft, N. W. and Mermin, N. D. (1976) Solid State Physics, Harcourt College Publisher.

[148] Beck, T. L. (2000) *Reviews of Modern Physics* **72(4)**, 1041.

[149] Chadi, D. J. and Cohen, M. L. Dec 1973 *Phys. Rev. B* **8**, 5747–5753.

[150] Monkhorst, H. J. and Pack, J. D. Jun 1976 *Phys. Rev. B* **13**, 5188–5192.

[151] Madelung, O. (1995) Introduction to solid-state theory, volume **2**, Springer Science & Business Media.

[152] Phillips, J. C. and Kleinman, L. (1959) *Phys. Rev.* **116(2)**, 287.

[153] Yin, M. and Cohen, M. L. (1982) *Phys. Rev. B* **25(12)**, 7403.

[154] Cohen, M. L. and Heine, V. (1970) *Solid State Physics* **24**, 37–248.

[155] Payne, M. C., Teter, M. P., Allan, D. C., Arias, T., and Joannopoulos, J. (1992) *Reviews of Modern Physics* **64(4)**, 1045.

[156] Hamann, D., Schlüter, M., and Chiang, C. (1979) *Phys. Rev. Lett.* **43(20)**, 1494.

[157] Kerker, G. (1980) *Journal of Physics C: Solid State Physics* **13(9)**, L189.

[158] Troullier, N. and Martins, J. (1990) *Solid State Communications* **74(7)**, 613–616.

[159] Rappe, A. M., Rabe, K. M., Kaxiras, E., and Joannopoulos, J. (1990) *Phys. Rev. B* **41(2)**, 1227.

[160] Shirley, E. L., Allan, D. C., Martin, R. M., and Joannopoulos, J. (1989) *Phys. Rev. B* **40(6)**, 3652.

[161] Kleinman, L. and Bylander, D. (1982) *Phys. Rev. Lett.* **48(20)**, 1425.

[162] Vanderbilt, D. (1990) *Phys. Rev. B* **41(11)**, 7892.

[163] Li, D., Zhang, X., Zhu, Z., and Zhang, H. (2011) *Solid State Sciences* **13**, 1731.

[164] Moriwake, H., Fisher, C. A. J., and Kuwabara, A. (2009) *Jpn. J. Appl. Phys.* **48**, 09KC03.

[165] Gao, L. H., Ma, Z., and Fan, Q. B. (2011) *J Electroceram* **27**, 114.

[166] Jiang-Ni, Y. and Zhi-Yong, Z. (2010) *Acta Phys. Chim. Sin.* **26**, 751.

[167] Jiang-Ni, Y., Zhi-Yong, Z., Jun-Feng, Y., and Wu, Z. (2009) *Chin. Phys. Lett.* **26**, 017107.

[168] Jiang-Ni, Y. and Zhi-Yong, Z. (2009) *Chinese Physics B* **18**, 2945.

[169] Zhi-Yong, Z., Jiang-Ni, Y., and Fu-Chun, Z. (2007) *Chinese Physics* **16**, 2791.

[170] Zhao, X., Wang, Y., amdMin Zhang, Q. C., and Zhao, N. (2012) *Computational Materials Science* **54**, 119.

[171] Soven, P. (1967) *Phys. Rev.* **156**, 809.

[172] Wołoszyn, M. and Maksymowicz, A. Z. (2002) *TASK Quarterly: scientific bulletin of Academic Computer Centre in Gdansk* **6**, 669–680.

[173] Nordheim, L. (1931) *Annalen der Physik* **401(5)**, 607–640.

[174] De Gironcoli, S., Giannozzi, P., and Baroni, S. (1991) *Phys. Rev. Lett.* **66(16)**, 2116.

[175] Ramer, N. J. and Rappe, A. M. (2000) *Journal of Physics and Chemistry of Solids* **61**, 315.

[176] Bellaiche, L. and Vanderbilt, D. (2000) *Phys. Rev. B* **61**, 7877.

[177] Yu, C.-J. and Emmerich, H. (2007) *Journal of Physics: Condensed Matter* **19(30)**, 306203.

[178] Ghosez, P., Desquesnes, D., Gonze, X., and Rabe, K. M. (2000) *AIP Conf. Proc.* **535**, 102.

[179] Hellmann, H. (1937) *Franz Deutsche, Leipzig.*

[180] Feynman, R. P. (1939) *Phys. Rev.* **56(4)**, 340.

[181] Nielsen, O. and Martin, R. M. (1983) *Phys. Rev. Lett.* **50(9)**, 697.

[182] Nielsen, O. and Martin, R. M. (1985) *Phys. Rev. B* **32(6)**, 3780.

[183] Liboff, R. L. (2003) Introductory quantum mechanics, Addison-Wesley.

[184] Nielsen, O. and Martin, R. M. (1985) *Phys. Rev. B* **32(6)**, 3792.

[185] Francis, G. and Payne, M. (1990) *Journal of Physics: Condensed Matter* **2(19)**, 4395.

[186] Press, W. H. (2007) Numerical recipes 3rd edition: The art of scientific computing, Cambridge University Press.

[187] Perdew, J. P. (1985) *International Journal of Quantum Chemistry* **28(S19)**, 497–523.

[188] Perdew, J. P. and Levy, M. (1983) *Physical Review Letters* **51(20)**, 1884.

[189] Sham, L. and Schlüter, M. (1983) *Physical Review Letters* **51(20)**, 1888.

[190] Janak, J. (1978) *Physical Review B* **18(12)**, 7165.

[191] Hedin, L. (1965) *Physical Review* **139(3A)**, A796.

[192] Aulbur, W. G., Jönsson, L., and Wilkins, J. W. (1999) *Solid State Physics* **54**, 1–218.

[193] Godby, R., Schlüter, M., and Sham, L. (1988) *Physical Review B* **37(17)**, 10159.

[194] Levine, Z. H. and Allan, D. C. (1991) *Physical Review B* **43(5)**, 4187.

[195] Robert F. Berger, C. J. F. and Neaton, J. B. (2011) *Phys. Rev. Lett.* **107**, 146804.

[196] AlSaei, J. (2011) A thesis submitted in partial fulfillment of the requirements for the degree of Master of Science of Imperial College London, unpublished.

[197] Piskunov, S., Heifets, E., Eglitis, R., and Borstel, G. (2004) *Computational Materials Science* **29(2)**, 165–178.

[198] Fischer, G. J., Wang, Z., and Karato, S. (1993) *Physics and Chemistry of Minerals* **20(2)**, 97–103.

[199] Wemple, S. (1970) *Physical Review B* **2(7)**, 2679.

[200] Abramov, Y. A., Tsirelson, V., Zavodnik, V., Ivanov, S., and Brown, I. (1995) *Acta Crystallographica Section B: Structural Science* **51(6)**, 942–951.

[201] Van Benthem, K., Elsässer, C., and French, R. (2001) *Journal of applied physics* **90(12)**, 6156–6164.

[202] Schlom, D. G., Chen, L.-Q., Eom, C.-B., Rabe, K. M., Streiffer, S. K., and Triscone, J.-M. (2007) *Annu. Rev. Mater. Res.* **37**, 589–626.

[203] Schubert, J., Trithaveesak, O., Petraru, A., Jia, C., Uecker, R., Reiche, P., and Schlom, D. (2003) *Applied Physics Letters* **82(20)**, 3460–3462.

[204] Tahini, H., Chroneos, A., Grimes, R., Schwingenschlögl, U., and Dimoulas, A. (2012) *Journal of Physics: Condensed Matter* **24(19)**, 195802.

[205] Diéguez, O., Tinte, S., Antons, A., Bungaro, C., Neaton, J., Rabe, K. M., and Vanderbilt, D. (2004) *Phys. Rev. B* **69(21)**, 212101.

[206] Pertsev, N., Zembilgotov, A., and Tagantsev, A. (1998) *Phys. Rev. Lett.* **80(9)**, 1988.

[207] Antons, A., Neaton, J., Rabe, K. M., and Vanderbilt, D. (2005) *Phys. Rev. B* **71(2)**, 024102.

[208] Lin, C.-H., Huang, C.-M., and Guo, G. (2006) *J. Appl. Phys.* **100(8)**, 084104.

[209] Samara, G., Sakudo, T., and Yoshimitsu, K. (1975) *Phys. Rev. Lett.* **35(26)**, 1767.

[210] Sanjurjo, J., Lopez-Cruz, E., and Burns, G. (1983) *Phys. Rev. B* **28(12)**, 7260.

[211] Kornev, I. A., Bellaiche, L., Bouvier, P., Janolin, P.-E., Dkhil, B., and Kreisel, J. (2005) *Phys. Rev. Lett.* **95(19)**, 196804.

[212] Bilc, D., Orlando, R., Shaltaf, R., Rignanese, G.-M., Íñiguez, J., and Ghosez, P. (2008) *Phys. Rev. B* **77(16)**, 165107.

[213] Vegard, L. (1921) *Zeitschrift für Physik A Hadrons and Nuclei* **5(1)**, 17–26.

[214] Denton, A. R. and Ashcroft, N. W. (1991) *Physical Review A* **43(6)**, 3161.

[215] McQuarrie, M. (1955) *Journal of the American Ceramic Society* **38(12)**, 444–449.

[216] Wu, L., Chen, Y.-C., Chen, L.-J., Chou, Y.-P., and Tsai, Y.-T. (1999) *Japanese Journal of Applied Physics* **38(9S)**, 5612.

[217] Abe, K. and Komatsu, S. (1995) *J. Appl. Phys.* **77(12)**, 6461–6465.

[218] Sharma, S. and Ambrosch-Draxl, C. (2004) *Physica Scripta* **2004(T109)**, 128.

[219] Read, A. J. and Needs, R. J. Dec 1991 *Phys. Rev. B* **44**, 13071–13073.

[220] Bass, M., Van Stryland, E., Williams, D., and Wolfe, W. (1995) Handbook of optics, Volume II: Devices, Measurements, and Properties, McGraw-Hill, Inc. .

[221] Cai, M.-Q., Yin, Z., and Zhang, M.-S. (2003) *Appl. Phys. Lett.* **83**, 2805.

[222] Chan, H. M., HARMER, M. R., and SMYTH, D. M. (1986) *Journal of the American Ceramic Society* **69(6)**, 507–510.

[223] Murillo, A. G., Romo, F. C., Hernández, M. G., García, O. B., Nava, A. M., Sánchez, S. P., and Vela, A. F. (2009) *Materials Transactions* **50(7)**, 1850–1854.

[224] Kumar, Y., Ahamad Mohiddon, M., Srivastava, A., and Yadav, K. (2009) *Indian Journal of Engineering and Materials sciences* **16(6)**, 390.

[225] Wang, L., Sakka, Y., Shao, Y., Botton, G. A., and Kolodiazhnyi, T. (2010) *Journal of the American Ceramic Society* **93(9)**, 2903–2908.

[226] Iwazaki, Y., Suzuki, T., Mizuno, Y., and Tsuneyuki, S. (2012) *Physical Review B* **86(21)**, 214103.

[227] Sharma, V., Pilania, G., Rossetti Jr, G., Slenes, K., and Ramprasad, R. (2013) *Physical Review B* **87(13)**, 134109.

[228] Makovec, D., Drofenik, M., and Baker, J. (2003) *Journal of the American Ceramic Society* **86(3)**, 495–500.

[229] Müller, T., Großmann, T., and Abicht, H.-P. (2009) *Journal of Physics and Chemistry of Solids* **70(7)**, 1093–1097.

[230] Kumar, N., Pan, J., Aysha, N., Waghmare, U. V., Sundaresan, A., and Rao, C. (2013) *Journal of Physics: Condensed Matter* **25(34)**, 345901.

[231] Morris, A. J., Nicholls, R. J., Pickard, C. J., and Yates, J. R. (2014) *Computer Physics Communications* **185(5)**, 1477–1485.

[232] Yates, J. R., Wang, X., Vanderbilt, D., and Souza, I. May 2007 *Phys. Rev. B* **75**, 195121.

[233] Berlijn, T., Lin, C.-H., Garber, W., and Ku, W. May 2012 *Phys. Rev. Lett.* **108**, 207003.

[234] Tangney, P. and Scandolo, S. (2002) *The Journal of Chemical Physics* **117(19)**, 8898–8904.

[235] Abeles, F. (1950) *J. Phys. Radium* **11(7)**, 310–314.

[236] Gibson, M. and Frejlich, J. (1984) *Applied Optics* **23(12)**, 1904_1–1906.

[237] Tien, P. (1971) *Applied Optics* **10(11)**, 2395–2413.

[238] Ulrich, R. and Torge, R. (1973) *Applied Optics* **12(12)**, 2901–2908.

[239] Kersten, R. T. (1975) *Optics Communications* **13(3)**, 327–329.

[240] Metricon corporation website http://www.metricon.com.

[241] Adams, A., Schinke, D., and Capio, C. (1979) *Journal of the Electrochemical Society* **126(9)**, 1539–1543.

Appendices

Appendix A

Experimental methods

In this appendix we give a brief review of two experimental techniques that are used for the characterization of the optical properties of thin films. Namely, the Abelés method and the prism coupling method.

A.1 Abelés method

The Abelés method [235, 236] is one of the simplest methods for determining the refractive indices of thin films. This method is based on the concept of the Brewster angle [105, p. 45]. When a light beam travels in a medium of refractive index n_0 and is incident on a surface of another medium of refractive index n_1, both the reflected and the transmitted beams generally have all the possible components of the electric field that the incoming light initially contains. At a certain angle of incidence, the reflected light becomes linearly polarized and contains only the electric field component that is perpendicular to the plane of incidence. This particular angle is called the Brewster angle and it occurs when the transmitted and the reflected beams are at right angles. The Brewster angle is a property of the two media, that is, it only depends on the refractive indices of the two media.

Considering the special case of linearly polarized incoming light with the electric field vector parallel to the plane of incidence, then at the Brewster angle all the light will be perfectly transmitted and nothing will be reflected.

This simple concept can be applied to the air/film/substrate system (see Fig 2.3) to determine the film refractive index. The trick is that when the

incoming light has a parallel polarization state, and if it is incident at the Brewster angle of the air/film interface, then the reflected light from the system will have the same reflectance whether or not the film is deposited on the substrate. So by comparing the "brightness" of the reflected light from a bare substrate and from one coated by the film as a function of the angle of incidence, one can find the Brewster angle as the angle at which the two intensities are equal.

This technique has a number of known limitations. For instance, it is limited to transparent films and substrates (i.e., non-absorbent with real refractive index). In addition, it does not depend on the thickness of the film and is not sensitive to the refractive index of the substrate. A number of improvements have been developed, however, to improve its accuracy [236].

A.2 Prism coupling technique

The prism coupling (PC) technique [237–239] was first adopted in the early 1970s. It is an indirect method and can be used to determine both the refractive index of the film and its thickness.

The theory behind this method is more complicated than that of the Abelés method. The main idea is to use a prism to couple an incident laser beam to a thin film of material that acts as a planar waveguide for the light, at particular values for the incident angle.

Practically, the film is first clamped into the base of the prism allowing a narrow air gap between them (so this method requires a physical contact applied to the film). A laser beam is then incident on the base of the prism. Normally, the laser beam would be totally reflected back from the prism base (since the refractive index of the prism is greater than that of the air) exiting the prism where it can be detected by a photo detector. At certain special values of the incident angle, however, the laser beam can "tunnel" through the air gap and into the film, and propagate through the film that acts as an optical waveguide. As a consequence, the intensity of the reflected light will strongly drop, and hence the characteristic angle of incidence can be identified.

This coupling occurs under the fulfilment of the condition that the phase velocity of the laser beam through the prism in the direction parallel to its base (parallel to the film), which we will call the x-direction, is equal to the phase

velocity of the propagation mode through the waveguide (the film). Generally, the film has many waveguide modes. The excitation of these modes can be achieved by varying the phase velocity of the laser beam in the x direction in order to successively match the phase velocities of the corresponding modes, fulfilling the condition above mentioned. This is achieved in practice by simply varying the angle of incidence.

The refractive index of the film and its thickness are obtained as follows. First, the propagation constant (a constant describing how the amplitude and the phase of the wave changes as it travels through the medium) of a specific coupling mode can be readily found experimentally (relative to the propagation constant of free space) from knowledge of the refractive index of the prism and the corresponding angle of incidence at which the mode is excited. On the other hand, this relative propagation constant can be calculated theoretically from the waveguide dispersion equation. This equation involves a set of constants that are either known or can be measured independently, such as the refractive index of the substrate and the polarization state of the laser beam. Along with these constants, it also involves two more parameters that correspond to the refractive index of the film and its thickness. These two parameters can then be calculated so that both the theoretical and the experimental propagation constants match. It is therefore necessary to excite at least two modes in order to find both the refractive index and the thickness of the film. Usually, more than two independent measurements are involved in the calculations of these two desired quantities in order to increase the accuracy of and confidence in the results.

From the description above, it is clear that the refractive index of the film is calculated at a single light frequency, which is the frequency of the monochromatic laser beam. One way of calculating the dispersion of the refractive index of the film at a range of frequencies is to repeat the measurements for two or more laser beams of different wavelengths. Such multiple measurements can then be used to fit a continuous dispersion [240].

As mentioned above, this technique is based on the fact that the film is used as a waveguide. This requires that the index of the film is higher than that of its adjacent layers (the substrate below and the air gap above) in order to allow total internal reflection of the light propagating through the film. It has been shown, however, that this technique can also be extended to a

non-waveguiding case where the index of the substrate is higher than the film index [241].

The prism coupling method is limited to films of thickness no less than $\sim 100 - 200$ nm [240], below which the refractive index cannot be calculated. This is because the number of waveguide modes of the film depends on its thickness. If the thickness is below a certain threshold then no modes can be supported. If only one mode is supported, then *either* the refractive index *or* the thickness of the film can be calculated provided that the other is known from other sources.

One of the disadvantages of the prism coupling method is that it involves contact between the film and the prism, so in certain situations it can be destructive.

The accuracy of this technique is reported to be very high, however. The Metricon company [240] reports that with the manufactured Model (2010/M), the refractive index can be calculated with an absolute accuracy down to $\pm$ 0.0001.

Appendix B

Permissions

In the following pages we include copies of all permission documents that we received from the publishers to reproduce the images shown in Figs. 1.1 and 1.4.

Copyright Clearance Center RightsLink®

Home | Account Info | Help | Live Chat



Title: Ferroelectric Properties of Mechanically Synthesized Nanosized Barium Titanate

Author: B. D. Stojanovic, C. Jovalekic, V. Vukotic, et al

Publication: Ferroelectrics

Publisher: Taylor & Francis

Date: Jul 1, 2005

Copyright © 2005 Taylor & Francis

Logged in as:
Jawad Alsaei

LOGOUT

Thesis/Dissertation Reuse Request

Taylor & Francis is pleased to offer reuses of its content for a thesis or dissertation free of charge contingent on resubmission of permission request if work is published.

BACK | CLOSE WINDOW

Copyright © 2015 Copyright Clearance Center, Inc. All Rights Reserved. Privacy statement. Terms and Conditions.
Comments? We would like to hear from you. E-mail us at customercare@copyright.com

NATURE PUBLISHING GROUP LICENSE TERMS AND CONDITIONS

Jun 01, 2015

This is a License Agreement between Jawad Alsaei ("You") and Nature Publishing Group ("Nature Publishing Group") provided by Copyright Clearance Center ("CCC"). The license consists of your order details, the terms and conditions provided by Nature Publishing Group, and the payment terms and conditions.

All payments must be made in full to CCC. For payment instructions, please see information listed at the bottom of this form.

License Number	3640540417494
License date	Jun 01, 2015
Licensed content publisher	Nature Publishing Group
Licensed content publication	Nature Nanotechnology
Licensed content title	Switching of ferroelectric polarization in epitaxial BaTiO3 films on silicon without a conducting bottom electrode
Licensed content author	Catherine Dubourdieu, John Bruley, Thomas M. Arruda, Agham Posadas, Jean Jordan-Sweet, Martin M. Frank
Licensed content date	Sep 29, 2013
Volume number	8
Issue number	10
Type of Use	reuse in a dissertation / thesis
Requestor type	academic/educational
Format	print and electronic
Portion	figures/tables/illustrations
Number of figures/tables/illustrations	1
High-res required	no
Figures	Figure 1 | TEM and in-plane X-ray diffraction of BaTiO3/SrTiO3/silicate/SiO2 stacks. a, TEM images emphasizing the interface between SrTiO3 and BaTiO3 films. Edge dislocations are observed at the interface.
Author of this NPG article	no
Your reference number	None
Title of your thesis / dissertation	Theory and simulation of electronic and optical properties of thin film barium strontium titanate
Expected completion date	Jun 2015
Estimated size (number of pages)	230
Total	0.00 GBP
Terms and Conditions	

Terms and Conditions for Permissions

Nature Publishing Group hereby grants you a non-exclusive license to reproduce this material for this purpose, and for no other use,subject to the conditions below:

1. NPG warrants that it has, to the best of its knowledge, the rights to license reuse of this material. However, you should ensure that the material you are requesting is original to Nature Publishing Group and does not carry the copyright of another entity (as credited in the published version). If the credit line on any part of the material you have requested indicates that it was reprinted or adapted by NPG with permission from another source, then you should also seek permission from that source to reuse the material.

2. Permission granted free of charge for material in print is also usually granted for any electronic version of that work, provided that the material is incidental to the work as a whole and that the electronic version is essentially equivalent to, or substitutes for, the print version.Where print permission has been granted for a fee, separate permission must be obtained for any additional, electronic re-use (unless, as in the case of a full paper, this has already been accounted for during your initial request in the calculation of a print run).NB: In all cases, web-based use of full-text articles must be authorized separately through the 'Use on a Web Site' option when requesting permission.

3. Permission granted for a first edition does not apply to second and subsequent editions and for editions in other languages (except for signatories to the STM Permissions Guidelines, or where the first edition permission was granted for free).

4. Nature Publishing Group's permission must be acknowledged next to the figure, table or abstract in print. In electronic form, this acknowledgement must be visible at the same time as the figure/table/abstract, and must be hyperlinked to the journal's homepage.

5. The credit line should read:
   Reprinted by permission from Macmillan Publishers Ltd: [JOURNAL NAME] (reference citation), copyright (year of publication)
   For AOP papers, the credit line should read:
   Reprinted by permission from Macmillan Publishers Ltd: [JOURNAL NAME], advance online publication, day month year (doi: 10.1038/sj.[JOURNAL ACRONYM].XXXXX)

   Note: For republication from the *British Journal of Cancer,* the following credit lines apply.
   Reprinted by permission from Macmillan Publishers Ltd on behalf of Cancer Research UK: [JOURNAL NAME] (reference citation), copyright (year of publication)For AOP papers, the credit line should read:
   Reprinted by permission from Macmillan Publishers Ltd on behalf of Cancer Research UK: [JOURNAL NAME], advance online publication, day month year (doi: 10.1038/sj.[JOURNAL ACRONYM].XXXXX)

6. Adaptations of single figures do not require NPG approval. However, the adaptation should be credited as follows:

   Adapted by permission from Macmillan Publishers Ltd: [JOURNAL NAME] (reference citation), copyright (year of publication)

   Note: For adaptation from the *British Journal of Cancer,* the following credit line applies.
   Adapted by permission from Macmillan Publishers Ltd on behalf of Cancer Research UK: [JOURNAL NAME] (reference citation), copyright (year of publication)

7. Translations of 401 words up to a whole article require NPG approval. Please visit http://www.macmillanmedicalcommunications.com for more information.Translations of up to a 400 words do not require NPG approval. The translation should be credited as follows:

   Translated by permission from Macmillan Publishers Ltd: [JOURNAL NAME] (reference citation), copyright (year of publication).

   Note: For translation from the *British Journal of Cancer,* the following credit line

applies.
Translated by permission from Macmillan Publishers Ltd on behalf of Cancer Research UK: [JOURNAL NAME] (reference citation), copyright (year of publication)

We are certain that all parties will benefit from this agreement and wish you the best in the use of this material. Thank you.

Special Terms:

v1.1

Questions? customercare@copyright.com or +1-855-239-3415 (toll free in the US) or +1-978-646-2777.

AIP PUBLISHING LLC LICENSE
TERMS AND CONDITIONS

Jun 01, 2015

All payments must be made in full to CCC. For payment instructions, please see information listed at the bottom of this form.

License Number	3640541190171
Order Date	Jun 01, 2015
Publisher	AIP Publishing LLC
Publication	Applied Physics Letters
Article Title	Link-up of 90° domain boundaries with interface dislocations in BaTiO3/LaAlO3
Author	Z. R. Dai,Z. L. Wang,X. F. Duan, et al.
Online Publication Date	May 27, 1996
Volume number	68
Issue number	22
Type of Use	Thesis/Dissertation
Requestor type	Student
Format	Print and electronic
Portion	Figure/Table
Number of figures/tables	1
Title of your thesis / dissertation	Theory and simulation of electronic and optical properties of thin film barium strontium titanate
Expected completion date	Jun 2015
Estimated size (number of pages)	230
Total	0.00 USD

Terms and Conditions

AIP Publishing LLC -- Terms and Conditions: Permissions Uses

AIP Publishing LLC ("AIPP"") hereby grants to you the non-exclusive right and license to use and/or distribute the Material according to the use specified in your order, on a one-time basis, for the specified term, with a maximum distribution equal to the number that you have ordered. Any links or other content accompanying the Material are not the subject of this license.

1. You agree to include the following copyright and permission notice with the reproduction of the Material:"Reprinted with permission from [FULL CITATION]. Copyright [PUBLICATION YEAR], AIP Publishing LLC." For an article, the copyright and permission notice must be printed on the first page of the article or book chapter. For photographs, covers, or tables, the copyright and permission notice may appear with the Material, in a footnote, or in the reference list.
2. If you have licensed reuse of a figure, photograph, cover, or table, it is your responsibility to ensure that the material is original to AIPP and does not contain the copyright of another entity, and that the copyright notice of the figure, photograph, cover, or table does not indicate that it was reprinted by AIPP, with permission, from another source. Under no circumstances does AIPP, purport or intend to grant permission to reuse material to which it does not hold copyright.
3. You may not alter or modify the Material in any manner. You may translate the Material into another language only if you have licensed translation rights. You may not use the Material for promotional purposes. AIPP reserves all rights not specifically granted herein.
4. The foregoing license shall not take effect unless and until AIPP or its agent, Copyright Clearance Center, receives the Payment in accordance with Copyright Clearance Center Billing and Payment Terms and Conditions, which are incorporated herein by reference.

5. AIPP or the Copyright Clearance Center may, within two business days of granting this license, revoke the license for any reason whatsoever, with a full refund payable to you. Should you violate the terms of this license at any time, AIPP, AIP Publishing LLC, or Copyright Clearance Center may revoke the license with no refund to you. Notice of such revocation will be made using the contact information provided by you. Failure to receive such notice will not nullify the revocation.
6. AIPP makes no representations or warranties with respect to the Material. You agree to indemnify and hold harmless AIPP, AIP Publishing LLC, and their officers, directors, employees or agents from and against any and all claims arising out of your use of the Material other than as specifically authorized herein.
7. The permission granted herein is personal to you and is not transferable or assignable without the prior written permission of AIPP. This license may not be amended except in a writing signed by the party to be charged.
8. If purchase orders, acknowledgments or check endorsements are issued on any forms containing terms and conditions which are inconsistent with these provisions, such inconsistent terms and conditions shall be of no force and effect. This document, including the CCC Billing and Payment Terms and Conditions, shall be the entire agreement between the parties relating to the subject matter hereof.

This Agreement shall be governed by and construed in accordance with the laws of the State of New York. Both parties hereby submit to the jurisdiction of the courts of New York County for purposes of resolving any disputes that may arise hereunder.

Questions? customercare@copyright.com or +1-855-239-3415 (toll free in the US) or +1-978-646-2777.